Atom Probe Tomography Analysis of Near Surface, Low Concentration Impurities in Single Crystal Silicon



James Owen Douglas

Linacre College

University of Oxford

A thesis submitted for the degree of

Doctor of Philosophy

Hilary Term 2017

Abstract

Advances in semiconductor device manufacture have led to modern nanoelectronic devices incorporating features with dimensions less than ten nanometres, fabricated within tens of nanometres of silicon substrate surfaces. To refine materials processing and optimise the correlation between fabricated nanostructures and device performance, high resolution characterisation techniques, such as atom probe tomography (APT), are required. In this thesis, surface sensitive specimen preparation methodologies for APT, utilising focused ion beam techniques using metal capping layers and low energy milling, were developed. This resulted in a reproducible method of precisely placing a metal/silicon interface at the apex of an APT nanoscale tip. This approach was utilised to characterise the surface regions of two silicon material systems with technological applications.

Low concentration, low energy phosphorus ion implantation is currently being investigated for fabrication of qubit arrays for large scale quantum computers. APT was used to investigate phosphorus implantation depth accuracy. 14 kV phosphorus ions with predicted peak concentrations between 0.1 and 0.2 at.% and peak depths of ~ 22 nm were implanted into planar substrates and pre-fabricated silicon posts. Measured profiles matched well with simulation but showed a reduced peak concentration and an extended tail region, likely from ion channelling.

Phosphorus diffusion is used to getter transition metals, particularly iron, to the surfaces of silicon solar cell material, however, the exact physical mechanism underpinning this is not well understood. Secondary ion mass spectrometry depth profiles were previously used to propose the interaction of oxide particles formed near the surface. In this study, single crystal silicon substrates were contaminated with pure iron and subjected to an industrially-relevant phosphorus diffusion process. APT analyses showed oxygen-rich regions in direct contact with silicon phosphide precipitates, confirming a heterogeneous distribution of oxygen in the surface regions. This can be used to inform processing conditions for modern silicon photovoltaics.

Preface

The work presented in this doctoral thesis has been carried out at the Department of Materials, University of Oxford from January 2013 to February 2017, under the supervision of Professor Michael Moody and Dr Paul Bagot. All of the research carried out for this thesis is original and where the work of others has been included it has been clearly referenced and acknowledged. All figures reproduced from journal articles and books have been used with permission from the respective copyright owner. No part of this thesis has been submitted for a degree at this, or any other university.

The following papers, presentations and posters were based on the work in this thesis.

Published journal papers

"Optimisation of sample preparation and analysis conditions for Atom Probe Tomography characterisation of low concentration surface species", **J. O. Douglas**, P. A. J. Bagot, B. C. Johnson, D. N. Jamieson and M. P. Moody. *Semiconductor Science and Technology*, 31 084004, 2016.

"Comparing the Consistency of Atom Probe Tomography Measurements of Small-Scale Segregation and Clustering Between the LEAP 3000 and LEAP 5000 Instruments". T. L. Martin, A. J. London, B. Jenkins, S. E. Hopkin, **J. O. Douglas**, P. D. Styman, P. A. J. Bagot and M. P. Moody. *Microscopy and Microanalysis*, vol. 23, no. 2, pp. 227–237, 2017.

Invited Colloquia

"*Atom Probe Tomography: 3D materials characterisation on the atomic scale*", presented at the School of Physics, University of Melbourne, February 23rd, 2016.

Conference presentations and posters

1) "*Atom probe tomography analysis of surface species: The effect of capping layer selection and analysis conditions on measurement of low concentration, near surface phosphorus implantation profiles in single crystal silicon*", **J. O. Douglas**, P. A .J. Bagot, B. C. Johnson, D. N. Jamieson and M.P. Moody. European APT workshop, Oxford, UK, 2016. Oral Presentation.

2) "*APT analysis of low concentration, near surface phosphorus implantation in single crystal silicon for quantum computing applications."* **J. O. Douglas**, P. A .J. Bagot, B. C. Johnson, D. N. Jamieson and M.P. Moody. Atom Probe Tomography and Microscopy, Gyeongju, South Korea. 2016. Oral Presentation.

3) "*Atom Probe Tomography of surface and near-surface features: Sample preservation and analysis techniques*". **J. O. Douglas**, G. F. Martins, A. B. Siddique, J. D. Murphy, P. R. Wilshaw, D. N. Jamieson, P. A. J. Bagot, M. P. Moody. European APT workshop, Leoben, Austria, 2015, Oral Presentation.

4) "*Applications of Atom Probe Tomography to silicon solar energy materials – 3D characterisation on the atomic scale*". **J. O. Douglas**, G. F. Martins, A. B. Siddique, J. D. Murphy,P. R. Wilshaw, P. A. J. Bagot, M. P. Moody. Supergen Supersolar Technical Meeting, University of Bath, UK, 2015. Oral Presentation.

5) "*Atom Probe analysis of sub-surface phosphorus implantation profiles in silicon*" **J. O. Douglas**, P. A. J. Bagot, M. P. Moody. Microscopy of Semiconducting Materials (MSM), University of Cambridge, UK, 2015, Oral Presentation.

6) "*Atom Probe analysis of iron and oxygen co-clustering of transition metal contaminated single crystal silicon subjected to Phosphorus Diffusion Gettering*", **J. O. Douglas**, G. F. Martins, A. B. Siddique, J. D. Murphy, P. R. Wilshaw, P. A. J. Bagot, M. P. Moody. Gettering and Defect Engineering in Silicon Technology (GADEST), Bad Staffelstein, Germany, 2015. Oral Presentation.

7) "*Atom Probe Tomography and Microscopy 2014, Preliminary APT Characterisation of Low Dose Phosphorus Implantation in Single Crystal Silicon*." **J. O. Douglas,** P. A. J. Bagot, D. N. Jamieson and M. P. Moody. Atom Probe Tomography and Microscopy, Stuttgart, Germany, 2014. Poster Presentation.

Acknowledgements

Whilst I did write all the words in this thesis, getting them all in the right order would not have been possible without a great deal of help from a large number of people. Professor Michael Moody and Dr Paul Bagot (along with their respective furry overlords) have been exemplary supervisors and it is highly unlikely that I would have been able to complete my DPhil without their support and guidance. Thanks also go to Professor John Murphy and Professor David Jamieson for providing the theoretical framework for my research.

Some specific contributions should also be acknowledged: George Martins and Abu Saddique Bakr for their assistance with iron contamination and phosphorus diffusion. Professor Andrew Watt for first kindly coating my initial samples with nickel and then allowing me access to his thermal evaporator, without which my project would have been much more difficult. Dr Stella Pedrazzini for our productive games of playing "Pass the Brain", Alan Xu for introducing me to the Temple of Iron and especially Megan Carter and Dr Ben Jenkins for reading my thesis and correcting my (many) typographical errors. Jenni, Brian and Michal for sharing the honour of being Michael's "Fantastic Four" set of DPhil students, for which I would almost certainly have the title of "Mr Fibtastic". I would also like to thank my parents for their unconditional support during my academic career, I'll find a way of paying you back one day. Thank you to the whole of team RAPTOR, past and present. You've made the entire process so much nicer with constant support, cake, coffee, more cake and many group outings. Finally, I would like to thank Ellie for being there during every stage of my DPhil, from the application to the submission process via the "thesis goblin" stage. I am forever grateful. This thesis was brought to you via the music of K. Perry and T. Swizzle. No puns were harmed in the making of this manuscript.

Contents

1 **Introduction……1**

1.1 Characterisation of low concentration, near surface phosphorus ion implantation profiles in single crystal silicon…….2

1.2 Characterisation of surface regions of iron contaminated, phosphorus diffusion gettered single crystal silicon……...……...3

1.3 Thesis structure…….5

2 **Literature Review……...9**

2.1 **Semiconductors ……...9**

2.1.1 Silicon ……....10

2.1.2 Doping of silicon……....10

2.1.3 Crystal defects……11

2.1.4 Single crystal silicon ……. 12

2.1.5 Multicrystalline silicon……. 14

2.1.6 Impurities in silicon……... 15

2.2 **Ion implantation for nanoelectronic devices…… 16**

2.2.1 Nanoscale electronic devices……..17

2.3 Diffusion doping……..29

2.2.2 Quantum Computing……. 19

2.2.3 Requirements of quantum computing devices……...20

2.2.4 Potential qubit species……21

2.2.5 Bottom up and top down fabrication methods……... 21

2.2.6 Ion implantation for quantum device fabrication……... 24

2.2.7 Characterisation of low concentration implants…… 25

2.3.1 Silicon solar cells…….……. 30

2.3.2 Effect of iron in silicon photovoltaics ……..……32

2.3.3 Gettering……..…….. 34

2.3.4 Gettering of iron in silicon photovoltaics……...…….. 37

2.3.5 Phosphorus diffusion gettering……..……37

2.3.6. Oxygen and iron co-clustering ……..……42

2.4 Characterisation techniques …….....44

2.4.1 Scanning Electron Microscopy…….. 45

2.4.2 Scanning Electron Microscopy Energy Dispersive X-ray Spectroscopy….. 45

2.4.3 Focused Ion Beam ……46

2.4.4 Transmission Electron Microscopy and Scanning Transmission Electron Microscopy…….. 46

2.4.5 Transmission Electron Microscopy Energy Dispersive X-ray Spectroscopy 47

2.4.6 (Scanning) Transmission Electron Microscopy Elastic Electron Loss Spectroscopy ……..……. 48

2.4.7 Secondary Ion Mass Spectrometry ……..……..49

2.4.8 Nanoscale characterisation of surface regions ……...52

2.5 Atom probe …….53

2.5.1 Field Ion Microscopy…… 53

2.5.2 Atom Probe Tomography (APT) ……...58

2.5.3 Laser pulsed atom probe tomography…… 60

2.5.4 Focused Ion Beam (FIB) based sample preparation…….. 64

2.5.6 Atom probe analysis of semiconductor materials ……..67

3 Surface sensitive Focused Ion Beam sample preparation and APT analysis ……...70

3.1. Standard approach to Focused Ion Beam sample preparation ……70

3.1.1 Known artefacts affecting APT surface analysis ……...71

3.1.2 Current state of atom probe FIB based sample preparation ……..72

3.1.3 Optimisation of FIB for surface sensitive applications ……... 75

3.1.4 Atom probe analysis of surface regions …….. 76

3.2 Surface preservation and delineation…….…..80

3.2.1 Thermal evaporation of nickel and cobalt capping layers …….80

3.2.2 E-beam and FIB deposition of protective layers via Gas Injection System 85

3.2.3 Surface sensitive FIB milling of lift out samples ……89

3.2.4 FIB Sample preparation of flat top silicon micro posts ……...91

3.3 Optimisation of atom probe analysis parameters ……..……94

3.3.1 Parameters for yield……..……94

3.3.2 Optimisation of detection rate ……...…….. 95

3.3.3 Optimisation of laser energy ……96

3.3.4 Optimisation of pulse frequency…….. 97

3.4.5 Optimisation of base temperature…….. 97

3.4.6 Analysis limiting artefacts……... 98

4. Atom probe analysis of low concentration, near surface of ion implantation of phosphorus in single crystal silicon ……...99

4.1 Description of analysis approach ……99

4.2 Analysis using LEAP 3000X HR ……104

4.2.1 Analysis of implanted micro post with nickel capping layer. Predicted peak phosphorus concentration 0.2 at.%.……...……...104

4.2.2 Analysis of lift out sample with nickel capping layer. Predicted peak phosphorus concentration 0.2 at.%.……...……...125

4.2 Analysis using LEAP 5000X R ……133

4.2.1 Analysis of implanted micro post with cobalt capping layer. Predicted peak phosphorus concentration 0.2 at.%. Laser energy 50 pJ ……133

4.2.2 Analysis of implanted micro post with cobalt capping layer. Predicted peak phosphorus concentration 0.2 at.%. Laser energy 25 pJ.……144

4.2.2 Comparison of concentration profiles from atom probe analyses using 50 pJ and 25 pJ laser pulse energies..…….....153

4.3 Comparison between analyses of LEAP 3000X HR and LEAP 5000X R ……155

4.4 Analysis of effect of Rapid Thermal Anneal (RTA) processing…… 157

4.4.1 Analysis of implanted micro post with cobalt capping layer. RTA. Predicted peak phosphorus concentration 0.2 at.%. Laser energy 50 pJ. …….157

4.4.2 Comparison of phosphorus profiles between as-implanted implanted micro posts and RTA micro posts. ……..163

4.5 Discussion……...167

4.5.1 Use of implanted micro posts as analogues for planar substrates. …..……167

4.5.2 Limits of detection……... 168

4.5.3 Phosphorus species……..… 169

4.5.4 Comparison between LEAP 3000X HR and LEAP 5000 XR systems….. 170

4.5.5 Comparison with Stopping and Range of Ions in Matter simulations …….170

4.5.6 Capping layer requirements ……171

4.5.7 Summary ……..…173

4.6 Future work…… 208

5 Atom probe analysis of iron contaminated, phosphorus diffused silicon…….…… 176

5.1 Description of analysis approach……..… 176

5.1.1 Substrate selection, iron contamination and phosphorus diffusion …...…...178

5.2 Atom probe analyses using LEAP 5000X R of iron contaminated silicon …...…180

5.2.1 Atom probe analysis of iron contaminated, phosphorus diffused silicon. Laser energy 50 pJ ...……..181

5.1.1.1 Transmission electron microscopy of iron contaminated, phosphorus diffused silicon …….193

5.1.1.2 Analysis of silicon phosphide precipitates ……194

5.2.2 Atom probe analysis of iron contaminated, phosphorus diffused silicon. Laser energy 75 pJ. ……..… 209

5.2 Atom probe analyses using LEAP 5000X R of uncontaminated silicon…….. 214

5.2.1 Atom probe analysis of uncontaminated, phosphorus diffused silicon. Laser energy 75 pJ. …….……. 214

5.3 Discussion…….. 218

5.3.1 Silicon phosphide precipitates ……218

5.3.2 Oxygen rich regions ……..……..220

5.3.3 Atom probe identification of potential iron species ……...222

5.3.4 Phosphorus diffusion gettering mechanisms ……..…223

5.3.5 Future work……224

6 Conclusions …….227

Appendix A Focused Ion Beam lift out parameters…… 230

Appendix B Phosphorus Ion Implantation parameters ……231

Scattering and Range of Ions in Matter (SRIM) simulation parameters……..……232

Appendix C Comparison between APT and SRIM phosphorus profiles from implanted micro post with predicted 0.1 at.% peak phosphorus concentration….....……233

Comparison between APT measured phosphorus profile of implanted micro posts with predicted 0.1 at.% and 0.2 at.% peak phosphorus concentrations and lift out with 0.2 at.% peak phosphorus concentration…….……235

Appendix D Cross sectional SEM analyses of iron contaminated, phosphorus diffused silicon substrates with their phosphorus silicate glass layer removed…….....……236

Cross sectional SEM analyses of phosphorus diffused silicon substrates with no intentional iron contamination with their phosphorus silicate glass layer intact……..…238

Cross sectional SEM analyses of phosphorus diffused silicon substrates with their phosphorus silicate glass intact, processed using spin coating…..…….……241

Appendix E SIMS analysis of phosphorus profiles in phosphorus diffused silicon substrates with and without their phosphorus silicate glass layers intact……..…..….243

Comparison between APT and SIMS analyses of phosphorus profiles in phosphorus diffused silicon substrates with/without their phosphorus silicate glass layers intact…..…….....248

Appendix F Atom probe analysis of iron contaminated, phosphorus diffused silicon with no silicon phosphide precipitates present. Laser energy 50 pJ ……..…250

APT analysis of heterogeneous oxygen rich regions found at the silicon surface…….252

References…….253

1. Introduction

The work in the thesis is based around the application of Atom Probe Tomography (APT) to the analysis of low concentration species at surface and near surface regions (within tens of nm) in single crystal silicon. APT is a materials characterisation technique that is used to give 3D chemical and spatial information from nanoscale volumes, with concentration limits in the ppm range (depending on dataset sizes) and resolution up to 0.2 nm in the analysis direction [1]. Originally restricted to 1D analysis of highly conductive metals and alloys [2], advances in atom probe instrumentation (including increased fields of field and UV laser pulsing [3]) have allowed the analysis of semiconductor materials [4] and entire nanoelectronic devices [5]. Advances have also been made in Focused Ion Beam (FIB) sample preparation, allowing site specific analysis of selected nanoscale regions [6]. This specificity of analysis, combined with its unique 3D capabilities, has shown APT to be a valuable characterisation tool for nanoscale volumes [7].

A systematic approach to surface analysis, involving adaptions to standard FIB based sample preparation and optimisation of atom probe analysis parameters, was applied to two related but distinct silicon based material systems. The first involves characterisation of low concentration, near surface phosphorus ion implantation profiles in single crystal silicon. Direct implantation into pre-fabricated silicon support structures was also carried out in order to determine if this would be a viable analogue for planar substrates. The second involves characterisation of the surface regions of iron contaminated, phosphorus diffusion gettered silicon in order to determine if there was any nanoscale, heterogeneous segregation of phosphorus, oxygen and iron that can be linked to understanding the mechanisms of phosphorus diffusion gettering.

1.1 Characterisation of low concentration, near surface phosphorus ion implantation profiles in single crystal silicon

The vast majority of modern computing is based on silicon semiconductor integrated circuits (ICs). These are fabricated through a series of selective doping, deposition and etching stages on a single crystal silicon substrate in order to form a 2D (and now often 3D) structure with precisely controlled electronic properties [8]. Nanoscale spatial control over dopant position is required and the high control over dopant placement that ion implantation can give leads to it being a standard doping technique for ICs [9].

Modern nanoelectronic devices are now of the size where the position of individual dopant atoms within certain features can have measurable effects on the device's electronic behaviour. The physical limitations of the materials and fabrication techniques are also rapidly being reached [10]. In order to bypass this and further reduce device sizes, there is a great interest in the use of single atom electronics [11].

Quantum effects are noticeable at the length scales used in modern nanoelectronics and single atoms have been used as quantum bits or 'qubits' to take advantage of their unique properties [12]. Ionised phosphorus atoms in an isotopically enriched ^{28}Si matrix currently hold the record for the amount of time for which quantum information can be stored at both cryogenic and room temperatures [13]. Whilst test structures using single or small clusters of phosphorus are generally fabricated through Scanning Tunnelling Microscopy (STM) based methods [14], this is not readily scalable to the ~ 10^6 qubit arrays required for a viable quantum computer [15]. Ion implantation is being investigated as a method by which large numbers of ions can be precisely placed at the depths and spacing required for a viable quantum computing array [16]. The standard semiconductor depth profiling technique of Secondary Ion Mass Spectrometry (SIMS) has not been able to give sufficient

compositional information to inform implantation models [17] and APT is being investigated as a potential alternative nanoscale characterisation technique. Direct implantation into prefabricated supports alongside those planar substrates is being attempted in order to reduce FIB sample preparation time.

1.2 Characterisation of surface regions of iron contaminated, phosphorus diffusion gettered single crystal silicon

Transition metal species, especially iron, are a major cause of recombination in silicon photovoltaic materials and this reduces the efficiency of silicon solar cells when they are present [18]. These impurities are not generally present in sufficient quantities to cause issues in electronic grade single crystal silicon wafers, however these are expensive and are generally only used in applications where maximised efficiency is worth the increased cost. For the majority of applications, it is more economical to use larger areas of lower efficiency material rather than small areas of higher efficiency material. For these, solar grade single crystal silicon [19] and multicrystalline silicon are often used [20] due to their reduced cost. A diffusive distribution of transition metals, particularly iron, throughout the bulk of the material is more damaging to efficiency than if they are highly segregated to small, discrete, regions [21]. Therefore, in order to improve the efficiency of these contaminated materials, transition metals can be segregated away from the bulk in a process known as gettering. Phosphorus diffusion gettering simultaneously forms the n-type emitter region of the solar cell whilst segregating transition metals from the bulk into the phosphorus rich surface regions [22].

The mechanism of phosphorus diffusion gettering is not precisely known but has been proposed to be linked to the creation of vacancies during the diffusion process [23]. This causes the precipitation of nanoscale oxide particles, to which iron segregation is energetically favoured, and, as iron has been shown to increase the precipitation rate of oxygen, the oxide particle formation process can occur again [24]. This proposal is based upon SIMS analysis of spatially overlapping oxygen and iron depth profiles within tens of nm of the surface in iron contaminated, phosphorus diffused silicon. Oxygen precipitates have also been observed to be spatially segregated to silicon phosphide precipitates [25] and it has been proposed by that interstitials generated by the formation of silicon phosphide precipitates at the surface of phosphorus diffused silicon can be involved in the gettering process [26].

In order to experimentally determine if there is nanoscale, heterogeneous distribution of oxygen and iron at the surfaces of iron contaminated, phosphorus diffused silicon, the local composition of nanoscale regions at the surface of iron contaminated, phosphorus diffused silicon is required. APT is a technique that has the potential to determine the extent of nanoscale, co-segregation of phosphorus, oxygen and iron within tens of nm of the surfaces of such materials.

1.3 Thesis structure

In Chapter 2, an overview will be given of the use of silicon in modern electronics. The role of impurities and dopants will be discussed and two applications given where nanoscale characterisation such as APT is required. The background of both phosphorus diffusion gettering of iron in silicon and of ion implantation of phosphorus in silicon will be presented. The limitations of current characterisation techniques for these material systems will be discussed.

In Chapter 3, the process of optimising FIB based sample preparation for surface sensitive analysis of single crystal silicon through the use of ex-situ deposited capping layers and low energy milling will be presented.

In Chapter 4, APT analyses from phosphorus ion implanted silicon substrates will be presented and discussed. Comparisons of phosphorus implantation profiles for 14 kV P^+ with peak concentrations of 0.2 at.% are made between those obtained from pre-fabricated silicon micro posts and planar liftouts. The effect of laser energy, laser wavelength and detection efficiency on the observed phosphorus implantation profile are shown. Comparisons in phosphorus concentration distributions from silicon microposts and planar substrates that have been subjected to Rapid Thermal Annealing are also made.

In Chapter 5, APT analyses from iron contaminated, phosphorus diffused substrates will be presented and discussed. The identity of overlapping mass spectra peaks to be those containing iron rather than silicon or carbon is discussed, particularly in relation to the effect of varied laser energies.

Finally, conclusions will be given in Chapter 6 on how this work has given insight into the material systems studied and advanced sample preparation for surface analysis of low concentration species using APT.

A number of appendices have been included which give technical information that would otherwise interrupt the flow of this thesis or highlight specific aspects of the analysis that may be of interest to the reader.

Appendix A details the precise Focused Ion Beam sample preparation parameters for the Zeiss NVision40 Focused Ion Beam/Scanning Electron Microscope that were used in this thesis to prepare atom probe specimens of surface sensitive materials.

Appendix B shows the details of Stopping and Range of Ions in Matter simulation parameters for 14 kV P^+ ions in single crystal silicon with predicted peak concentrations of 0.2 at.%, 0.1 at.% and 0.01 at.%.

Appendix C shows the atom probe analysis of a pre-fabricated single crystal silicon micro post that had been implanted with 14 kV P^+ ions to a predicted peak concentration of 0.1 at.%. This was the single viable dataset obtained from those materials implanted to such a dose and so comparisons between implanted micro posts and planar substrates and thermal treatments could not be made. It is therefore included in this appendix as it indicates a reasonable lower limit of detection of phosphorus for phosphorus implanted silicon samples processed and analysed within this thesis.

Appendix D contains comparisons between planar and cross-sectional electron micrographs of various silicon substrates that had been processed using phosphorus diffusion gettering using gas phase and liquid phase dopants. This shows that the

topography of these surfaces are not homogeneous, especially those from the liquid phase dopants, and may influence the local phosphorus concentration.

Appendix E compares SIMS and APT depth profiles of phosphorus in phosphorus diffusion gettered silicon substrates that have been processed in a similar manner to those shown in Chapter 5.

Appendix F shows APT analysis of non-uniform concentrations of oxygen at the surface of iron contaminated, phosphorus diffusion gettered silicon samples where no silicon phosphide precipitates are present.

All atom probe and electron microscopy preparation for samples shown in this thesis was carried out using the dual beam Focused Ion Beam/Scanning Electron Microscope (FIB/SEM) Zeiss NVision40 system at the David Cockayne Centre for Electron Microscopy at the Department of Materials, University of Oxford, UK.

All atom probe analyses of samples shown in this thesis was carried out by the author using the Local Electrode Atom Probe (LEAP) 3000X HR and LEAP 5000X R atom probe systems at the Oxford Atom Probe Research Group, Department of Materials, UK. Transmission Electron Microscopy (TEM) samples were fabricated by the author under the supervision of Dr Mohsen Danaie and the TEM analysis was made by Dr Danaie using the Atomic Resolution Microscope 200 aberration correction TEM at the David Cockayne Centre for Electron Microscopy.

Ion implantation of phosphorus into single crystal silicon micro post arrays and subsequent Rapid Thermal Anneal (RTA) was carried out by Dr Brett Johnson and Professor David Jamieson of University of Melbourne, using the facilities at the Department of Electronic Materials Engineering at the Australian National University. The iron diffusion of silicon

substrates was carried out by Dr George Martins at the University of Oxford. The phosphorus diffusion was performed by Abu Saddique Bakr at the furnace facilities at Tetreon, Surrey, UK. The Secondary Ion Mass Spectrometry (SIMS) sample preparation was carried out by Abu Saddique Bakr and the SIMS analysis was performed at Aystorm Scientific, Cheshire, UK under his supervision.

2. Literature Review

2.1 Semiconductors

Semiconductors are defined as materials that have their Fermi level between the valence band and conduction band; this allows them to act as either insulators or conductors depending on their temperature. Increased temperature allows promotion of electrons from the valence band to the conduction band and so will increase conductivity, whilst a reduction in temperature reduces the number of electrons promoted to the conduction band and so reduces conductivity. The most commonly used intrinsic semiconductor material, that does not require dopants in order to behave as a semiconductor, is silicon [8]. Whilst the semiconducting behaviour of bulk silicon is of interest, it has limited uses in electronics when in its pure form. However, silicon can be made extremely electronically versatile through the introduction of impurities.

Extrinsic semiconductors have had their electrical properties altered through the addition of specific impurities, referred to as dopants, that change the numbers of electrons and holes available for conduction. Through selectively doping regions with species that can contribute electrons or holes, n-doping or p-doping respectively, and arranging these doped regions in specific spatial configurations in 2D or 3D, a wide range of electronic behaviours can be made possible in micron scale and nanoscale volumes. Due to the range of potential electronic properties and behaviours that can be fabricated from them, extrinsic semiconductor materials in the form of doped silicon substrates are widely used in electronic devices and are the basis for the integrated circuits (ICs) that are the heart of modern computing [10].

ICs are found in virtually every single electronic device that has been produced in the last few decades and the vast majority of these have been fabricated using selectively doped silicon [8].

2.1.1 Silicon

Silicon is the most commonly used semiconducting material in ICs for a number of reasons. It is a highly abundant element in the Earth's crust and can be purified through a number of methods to form the extremely pure crystal structure and rigorous compositional purity requirements of modern ICs. It has an atomic density of 5 x 10^{22} at/cm^3. It forms a native oxide layer within seconds in ambient cleanroom conditions [27] (~28ºC, average humidity 42 %) and can be made to form a cohesive, insulating and stable oxide layer through exposure to oxygen in dry or wet conditions at high temperatures. The thickness and quality of this oxide layer can be controlled through well understood temperature dependencies duringprocessing [28]. The conductivity and electronic behaviour of silicon can be altered across many orders of magnitude through specific spatial distributions and concentrations of impurities. The control and characterisation of these impurities has been a prominent area in semiconductor research and industrial processing [8].

2.1.2 Doping of silicon

An important distinction should be made between 'dopants' and 'impurities'. Dopants are those species present that have been deliberately placed in the semiconductor material in order to achieve specific electronic properties. Impurities are those species that are either present within the material prior to processing or have been unintentionally introduced

during processing and can affect electronic properties in an unpredictable or undesired manner [29].

In order for silicon IC devices to have predictable electronic properties, control of impurities and the crystal structure of the material is extremely important. Dopants in silicon are chosen based on their ability to occupy a substitutional site in a silicon lattice without causing excessive strain and whilst also supplying additional charge carriers to the material.

As silicon is a Group IV element, the elements that are most suited to readily take a substitutional lattice point within the silicon lattice that have a similar atomic radius are those from Group III and Group V. Dopants from Group V, such as phosphorus, have one extra valence electron than silicon and so will contribute an extra electron to the conduction band, resulting in an n^- type material. Dopants from Group III, such as boron, have one fewer valence electron than silicon and so the replacement of a silicon atom with a boron atom will result in the loss of one electron for conduction; this negative charge is often referred to as a 'hole'[8].

2.1.3 Crystal defects

Crystallographic defects in silicon, such as grain boundaries and dislocations, are features that disrupt the crystal structure and can act as regions of impurity segregation. Due to improvements in manufacturing single crystal substrates for IC applications, extended defects have been virtually removed and are now only an issue in the multicrystalline silicon used extensively in silicon photovoltaics. The presence of extended defects can drastically change the electronic properties of the material in a non-systematic manner and

therefore make the properties of individual devices harder to predict and reduces reproducibility between devices [21]. This effect is through the segregation of impurities, such as transition metals, to these extended defects. This can increase recombination, limit diffusion lengths and thus can influence electronic behaviour.

A range of common crystallographic defects are shown in Figure 2.1.

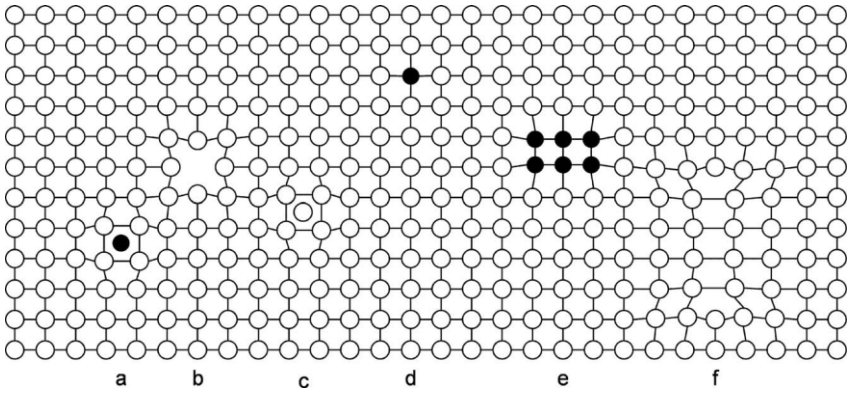


Figure 2.1 - Examples of common defects in a crystal: (a) interstitial impurity atom, (b) vacancy, (c) self-interstitial atom, (d) substitutional impurity atom (dopant), (e) precipitate of impurity atoms (cluster), (f) vacancy cluster/pair of dislocations [30].

2.1.4 Single Crystal Silicon

The majority of high quality single crystal silicon is fabricated using the Czochralski method [8] (Figure 2.2), where single boules of silicon are slowly drawn out of a melt using a seed crystal to ensure particular crystal orientation [31].

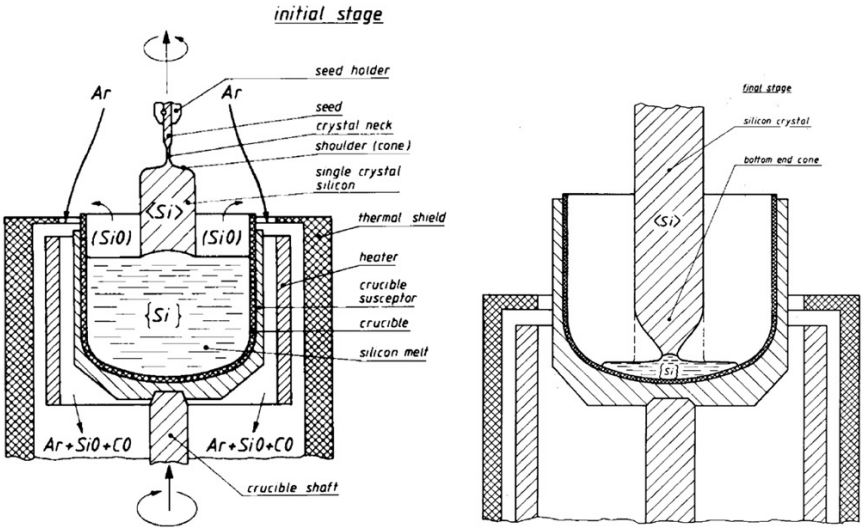


Figure 2.2 – The Czochralski growth method of silicon [31].

The slow solidification process 'freezes' out impurities and allows for extremely high purity crystals with virtually no extended defects, although oxygen containing point defects and intrinsic point defects such as vacancies and interstitials still remain. Despite this, there are still impurities within the material that can cause issues further down the processing route. Oxygen is one of the main contaminants (with an average concentration of 10^{18} at/cm^3 or 0.0002 at.%) for Czochralski silicon; mainly diffusing in from the silica crucible walls [32]. For those applications which require lower oxygen concentrations and increased resistivity [33], Float Zone silicon is used [1]. Float Zone silicon wafers cannot be fabricated in the large sizes that are possible with Czochralski silicon and so Czochralski silicon wafers are predominantly used for most industrial applications [34].

Uniform doping of silicon materials can be carried out during the silicon crystallisation stage of fabrication where dopant containing materials are mixed into the raw silicon feedstock [35]. After solidification, these silicon boules are sawn into wafers and polished to an extremely high surface uniformity. Processing costs to go from a blank wafer to a fully functioning device do not increase appreciably with increased wafer size (although

capital costs do) and therefore by increasing the size of the wafers whilst reducing the size of devices, the cost per device can be dramatically reduced [36].

Despite the size of Czochralski produced boules increasing dramatically since initial commercial fabrication methods, with the largest current industry standard diameter now at 300 mm, there are limitations on the size of these boules. Therefore for those applications requiring large numbers of larger surface silicon wafers than can be provided by the Czochralski process and that may not require the same level of purity and structural control as ICs, such as in photovoltaics [37], other silicon fabrication methods are used [31]. Multicrystalline (MC) silicon wafers can be formed in larger sizes and in greater numbers than those made through the Czochralski method although at the cost of increased impurity contamination and without a single crystal structure.

2.1.5 Multicrystalline silicon

There a number of methods by which MC silicon is made [31] but one of the most common is through melting feedstock silicon in a large crucible before allowing it to cool into a large ingot which can then be sawn into usable wafers. The non-uniform cooling prevents the formation of a uniform single crystal and instead the resulting crystal is made of many individual crystals of various sizes (Figure 2.3).

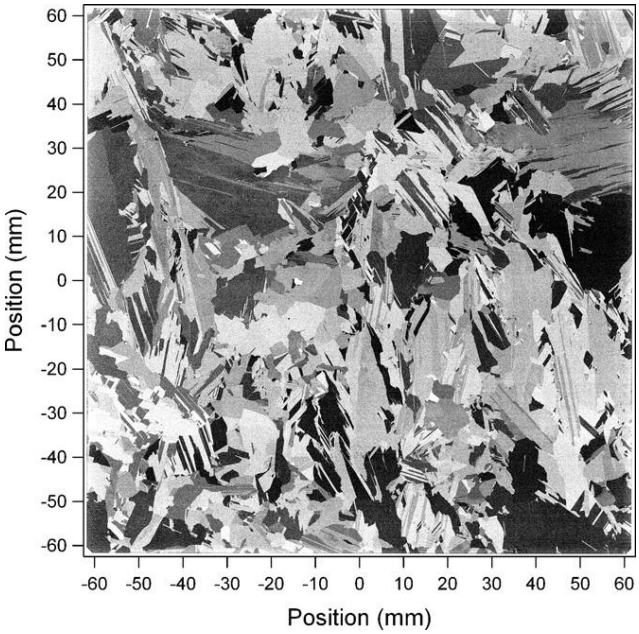


Figure 2.3 – Optical micrograph of cross section of MC wafer. Note mm variation in size and shape of silicon grains [22].

This prevents the use of MC silicon for many modern IC applications as the devices will have a large variation in impurities and crystallographic defects within and between them and so will have a large variation in electronic behaviour [37]. The resulting ingot contains a large amount of impurities that were present from the feedstock and that have diffused in through the walls of the crucible [38]. A typical application of MC silicon is in the fabrication of MC solar cells. Although the overall efficiency of the cell is reduced by the presence of crystallographic defects and impurities, such as transition metals [39], the overall impact is mitigated by the reduction in cost of materials and fabrication.

2.1.6 Impurities in silicon

A major type of impurities that can cause issues with electronic behaviour in MC silicon are transition metals [40], present both in the initial silicon feedstock and from diffusion in from the crucible walls during the casting process [41]. These metals are found in interstitial, substitutional and precipitate forms depending on their type, concentration and

location within the ingot [42] and the thermal history of the material [43]. They can also frequently be found bound to various crystallographic features such as grain boundaries and dislocations or as complexes with intrinsic point defects. The control of contamination and impurities in silicon materials and devices has been driven by requirements for improved device uniformity and yield, with increasingly stringent restrictions [8]. For the creation of nanoscale structured semiconductor devices with defined regions of required electronic properties, a high level control over the concentration and distribution of both impurities and dopants is required.

In this thesis, two silicon material systems are analysed. The first involves the precise placement of dopants through ion implantation into silicon. The second involves surface segregation of impurities through diffusion doping of silicon. In order to give context to both, they are addressed separately in this literature review.

2.2 Ion Implantation for nanoelectronic devices

Ion implantation is a standard method used to introduce dopants into a specific volume of material, whereby ions of the dopant species of interest are accelerated through a high potential difference towards the target material [44]. This beam of ions can then be directed with high accuracy over specific regions using a combination of physical apertures and magnetic focussing lenses. The regions to be implanted are often defined through open spaces in a photolithographic mask however, bulk doping can also be carried out though ion implantation as the total dose can be easily controlled [8].

Although implantation depth is largely controlled by the accelerating potential difference, when implanting into crystalline materials, the crystal orientation can also have a

significant effect in the form of ion channelling [45]. This is where ions travel further into a material than would be expected from the given accelerating voltage and occurs when their trajectory is aligned to open regions through specific crystallographic orientations. In order to reduce this effect, a pre-amorphisation stage can be used [46].

For modern surface based devices, increasingly low implantation energies are required in order to ensure that the peak in implant concentration is closer to the surface [47]. For very shallow surface implants of light species, such as boron, the minimum controllable implant depth may be greater than is required for the device and so implantation using complex ion species is used [48]. This is where the ion of interest is combined with other, heavier, species which can then be used to increase the mass of the incident ion [30]. Plasma based ion implantation is now also used to give extremely shallow, uniform, implants. This is achieved through exposing the surface to be implanted to a plasma containing the dopant ions of interest [49]. Ion implantation damages the crystal structure of the silicon substrates, therefore this must be repaired prior to further processing in order to prevent subsequent changes to the electronic properties of the material. After ion implantation, thermal processing is then carried out in order to both repair the lattice damage and also activate the as-implanted interstitial dopants by allowing them to move towards a substitutional lattice point [50].

Thermal treatments are an integral part of semiconductor processing; they are used to control dopant diffusion behaviour in various stages of device fabrication. A variety of thermal treatments are used according to the requirements of the particular processing stage, with temperature and time being the two key parameters [8]. Prolonged, low temperature annealing is used to diffuse dopants deep into the bulk of the material, with the extent and concentration distribution profile being determined by the initial surface concentration and the length of time at the temperatures used. For those applications where

it is important that the dopants do not move more than nanoscale distances, extremely short ‘spike’ or ‘flash’ Rapid Thermal Anneals (RTA) with rapid cool downs can be used [30].

2.2.1 Nanoscale electronic devices

As devices have decreased in size, small differences in local concentrations and distributions have a correspondingly increasing effect on device performance and reproducibility [51]. The location of individual atoms within key regions can have measurable effects on device function. As modern devices are located at the very surface of substrates, there is an increased requirement for high resolution characterisation that is able to give structural [52] and compositional information for nanoscale surface regions with extremely low concentrations [53].

There have been significant increases in the number density of transistors on modern IC devices over the last few decades (Figure 2.4) [54]. Modern nanoscale electronic devices and IC fabrication methods are rapidly approaching the physical limits dictated by the materials used [55].

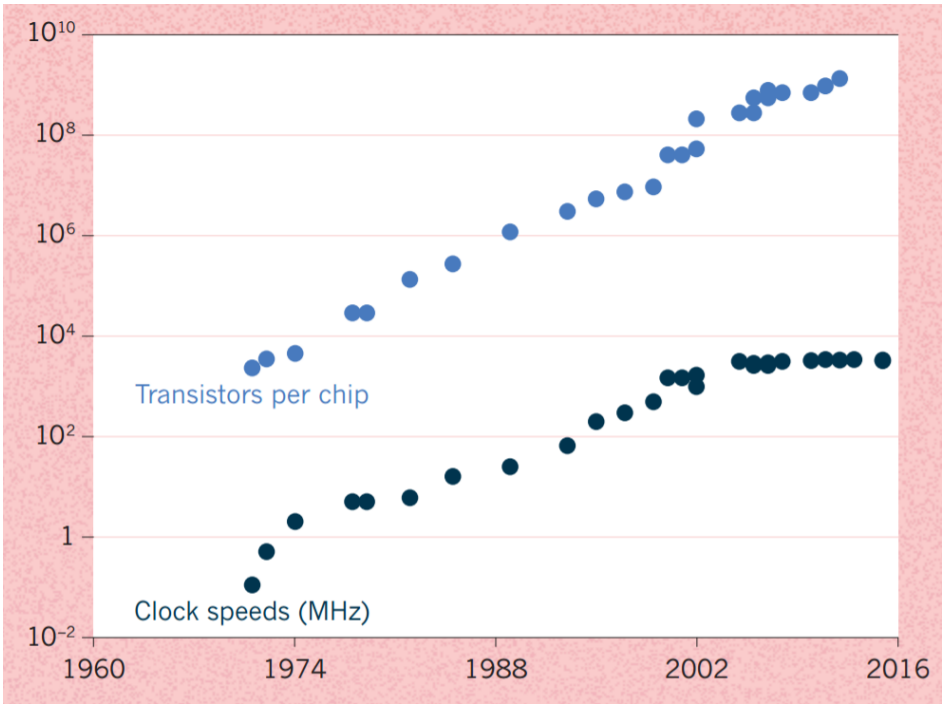


Figure 2.4 – Comparison of increases in transistor density and clock speed for integrated circuits from 1960 to 2016 [54]

There has been significant research into the potential use of single atom electronics in order to extend these limits [16]**.** This increased interest to the semiconductor community is due to their potential in potentially breaking the trend of Moore's Law [56] and removing the fundamental limitations of current IC technology [57]. The direct characterisation and interaction of single atoms within a material or surface can be implemented using nanoscale and atomic scale technique, such as Scanning Tunnelling Microscopy (STM) [58]. Scanning Transmission Electron Microscopy (STEM) has also been explored in the fabrication and analysis of single atom electronics [59]. Single atom electronics can also be used to take advantage of the quantum nature of these structures in order to allow for non-classical computing that would otherwise be impossible [60]. Such an application is the manipulation of single atoms as a quantum bit or 'qubit' [61].

2.2.2 Quantum computing

Quantum computing relies on utilising the quantum behaviour of single atoms, or small clusters of atoms, to perform computational processes that are otherwise impossible using classical computation [62]. An in-depth description of quantum computing and the theory governing their interaction and manipulation is outside the scope of this literature review and so only a brief overview will be given. Instead emphasis will be given to the material characterisation challenges associated with fabricating qubits, in particular those involving the fabrication of large scale qubit arrays [63].

There are a large number of engineering and technical challenges in both fabricating arrays and optimising their manipulation. A major requirement of these devices is the positioning of the qubits within the extremely strict spatial limits required in addition to meeting the number density criteria [12]. Classical computing uses differences in voltage or current within specific sections of an electronic device to denote a 1 (high voltage/current – on) signal or 0 (low voltage/current – off). This information is encoded into a binary unit or bit. Quantum computing uses quantum bits or "qubits" instead of bits. Whereas classical bits have two states (1 or 0), qubits can be in a superposition of the two. With **n** additional qubits, the number of states increases as $2^{\mathbf{n}}$, showing that the computational power of a computing array increases dramatically with large arrays [64] [63].

2.2.3 Requirements of quantum computing devices

Both the fabrication and testing of quantum devices require extreme control over the immediate environment of the qubit in order to maximise the signal to noise ratio [65]. This is typically carried out by ensuring there are no other potential sources of signal

interaction that can interfere with the manipulation of the qubit [12]. This is achieved through a combination of extremely low temperature, provided by dilution fridges, and precise control of the structure and composition of the material surrounding the qubit [66].

Qubits are manipulated through their spin state via microwave pulses. In order for this manipulation to be possible, qubits are required to be in a half integer spin state. By placing half integer spin qubits into an extremely high purity matrix of integer spin material [67], only the qubits will respond to the microwave input and the signal to noise ratio from those qubits can be raised to more readily detectable levels. For a viable quantum computer, an array of these qubits is required ($\sim 10^6$) [15]. These qubits must be within a specific coherence distance of each other in order to interact, which is on the order of a few nm [12]. Current fabrication models for quantum computing devices consist of integrating them into standard 'classical' IC devices, such that their properties can be accessed when required rather than constructing a standalone quantum computer [68].

The end goal is the accurate and reliable placement of individual atoms with nanometre precision within nanoelectronic devices,in a manner that can be integrated with standard silicon electronics and be upscaled for mass production [69].

2.2.4 Potential qubit species

A prominent material system candidate for quantum computing is the use of isolated half spin ^{31}P phosphorus atoms in an isotopically purified matrix of single crystal zero spin ^{28}Si [12]. This removes the potential interactions with the half spin minority isotope (~ 4 at.%)

of ^{29}Si present in silicon with natural isotopic abundancies [67]. Such a system holds the record for the current record for retaining quantum information for the longest time at both cryogenic and room temperatures [13]. Phosphorus is a standard n-type silicon dopant and is already extensively used throughout the semiconductor industry, thus existing doping methods can to be adapted for these new applications [16].

2.2.5 Bottom up and top down fabrication methods

The two main approaches for fabricating single atom electronics are known as 'bottom-up' and 'top-down'. For 'bottom-up' techniques, single atoms are introduced in the initial fabrication stages of a device and the device is built around them. For 'top-down' techniques, single atoms are introduced into active regions of completed or almost completed devices [70]. STM has the ability to manipulate and move single atoms with near atomic precision and has been shown to be a viable method of fabricating quantum devices [71].

Through adsorbing a layer of hydrogen onto a prepared silicon surface, desorbing a single/small cluster of hydrogen atoms between two pre-fabricated nanoscale contacts and then exposing the surface to phosphine gas, small numbers of phosphorus atoms can be incorporated into a nanoelectronic device with near atomic precision (Figure 2.5). However STM based fabrication of this type is extremely time consuming and expensive and so it is unlikely that it can be used for industrial scale applications [67].

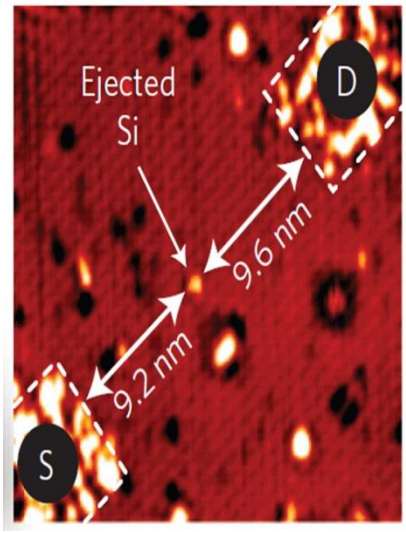


Figure 2.5 - STM image of a single ejected silicon atom in a nanoscale region between the source (S) and drain (D) contacts of a nanoelectronic device [14].

STM is also not a typical processing tool in semiconductor IC fabrication and so would be difficult to integrate into a standard process flow. As a result, methods that are easier to integrate must be considered.

Ion implantation has been explored as a technique for top down fabrication as it is already widely used in semiconductor processing and has the potential for upscaling to industrial levels using modifications to existing process flows [16]. In order to fabricate qubits using ion implantation, existing techniques need to precisely place a single atom with nanoscale accuracy in a pre-fabricated device structure. This requires both a reliable method of ensuring only a single ion is permitted to reach the active region and the end location of the ion to be within the nanoscale spatial requirements of the device [16]. Ion beams that can produce single ions are not unknown [72] [73] but the challenge is placing a single ion with the required nanoscale lateral and depth precision into position in an array of similar ions within a prefabricated device structure.

A range of physical apertures are typically used to control the beam current and spot size of ion beams. Due to the smallest standard apertures giving a much greater current than is required for quantum implantation applications, nanoscale apertures are required to be placed in front of standard apertures to further attenuate the beam. Nanoscale apertures milled into a silicon Atomic Force Microscope (AFM) [74] tip using a Focused Ion Beam (FIB) have been used to attenuate a low current ion beam over the implantation target regions. In order to ensure that only a specific region of the device is exposed to this attenuated ion beam, the AFM tip aperture is positioned over open regions within nanoscale lithographic masks [63]. In order to ensure that only a single atom has been implanted within each device, active substrates, which can detect the transient current generated by a single incident ion, have been constructed from commercial photodiodes [75]. Using this combination of nanoscale apertures and masking on a movable stage, implantation of single phosphorus ions into arrays of devices can be achieved (Figure 2.6).

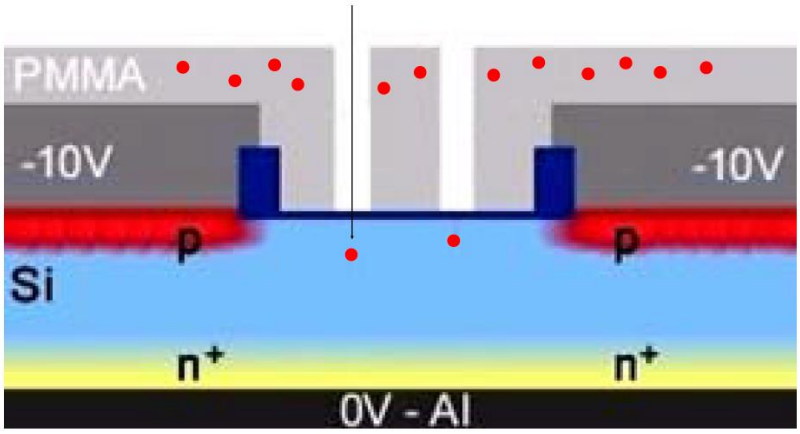


Figure 2.6 - Active substrate using nanolithographic masking to control positioning of 14 kV phosphorus ions [70] *© 2006 IEEE.*

Transient electrical currents caused by the generation of electron/hole pairs from the interaction between the incident implanted ion and the substrate can be detected. The lowest energy phosphorus ion that can currently be detected by these active substrates are

those that have been accelerated to 14 kV in the form of P^+ [76]. Currents generated by ions accelerated using lower voltages are currently too low to be detected with existing devices, although more sensitive detectors are being researched [76]. Lower energy implantations will reduce the lateral and depth straggle (furthest distance from the implantation concentration peak that an ion is predicted to travel during implantation as calculated by Monte Carlo simulations), increasing the accuracy of prediction for their final location and so increase the likelihood that they will be within the spatial requirements of the device [16]. The oxide layer used in the transistor gate region cannot be grown after the implantation as the high temperature thermal processing required to form it is known to cause the phosphorus ions to strongly segregate to the surface [58] [59].

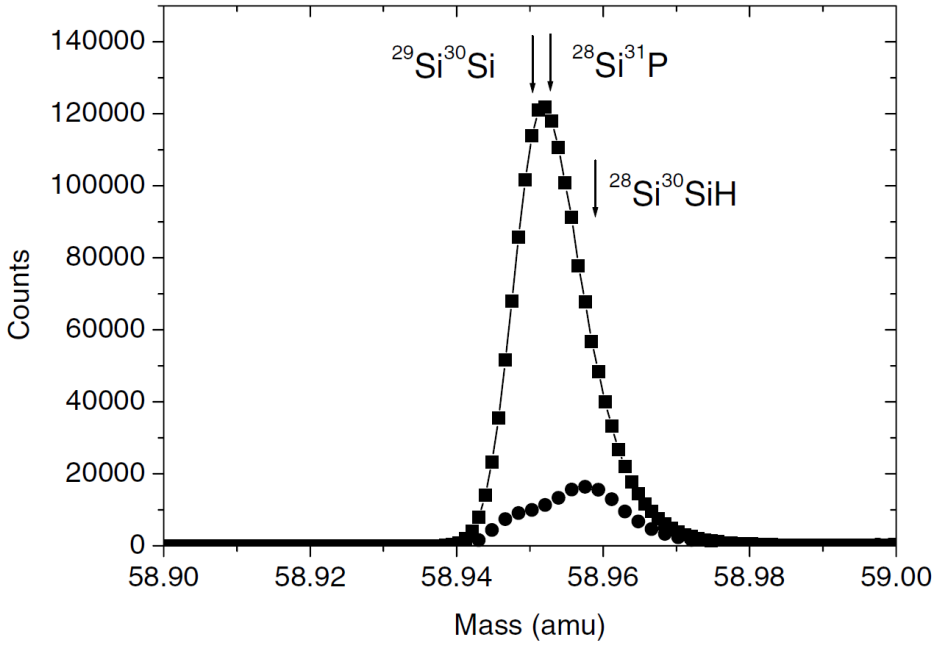
2.2.6 Ion implantation for quantum computing device fabrication

Implantation of 14 kV $^{31}P^+$ and 20 kV $(^{31}P_2)^+$ [13] ions have been shown to produce viable quantum devices when combined with nanoscale aperture masking in close proximity to a single electron transistor structure. However, these devices do not have real time detection capabilities to determine if single phosphorus atoms have been correctly implanted and so have a low yield compared to those using active substrates [75]. Research is being currently carried out on adapted photodiode avalanche detectors that are predicted to allow the detection of the implantation of lower energy phosphorus ions, down to 7 kV, due to their greater sensitivity to transient currents [76]. The greatly reduced straggle from these lower energy ions will increase the likelihood that the end location of the ions is within the spatial requirements of the device. In order to increase the chance of groups of ions being within coherence length during implantation, increased use of dimer P_2 implantation has been proposed [79].

2.2.7 Characterisation of low concentration implants

Secondary Ion Mass Spectrometry (SIMS) can be used to measure low concentration, near surface phosphorus implantation profiles in silicon but there are quantification issues due to the mass spectra overlaps between silicon-silicon complex ion species in the bulk and silicon hydride species [17].

The majority of phosphorus ions detected through SIMS are at ~ 59 amu in the form of the $(^{28}Si^{31}P)^{+}$ complex ion, whose mass spectra peak overlaps almost completely with the $(^{29}Si^{30}Si)^{+}$ complex ion (Figure 2.7).



F*igure 2.7 – SIMS mass spectra overlaps between silicon-phosphorus and silicon-hydrogen* complex *ions. Squares - Phosphorus implanted silicon. Circles - Unimplanted silicon* [80].

The $(^{28}Si^{31}P)^{+}$ ion has the highest yield detected with SIMS, as shown in Figure 2.8, and shows a signal even in pure natural abundance silicon, indicating a lower limit of sensitivity for phosphorus using SIMS in the bulk.

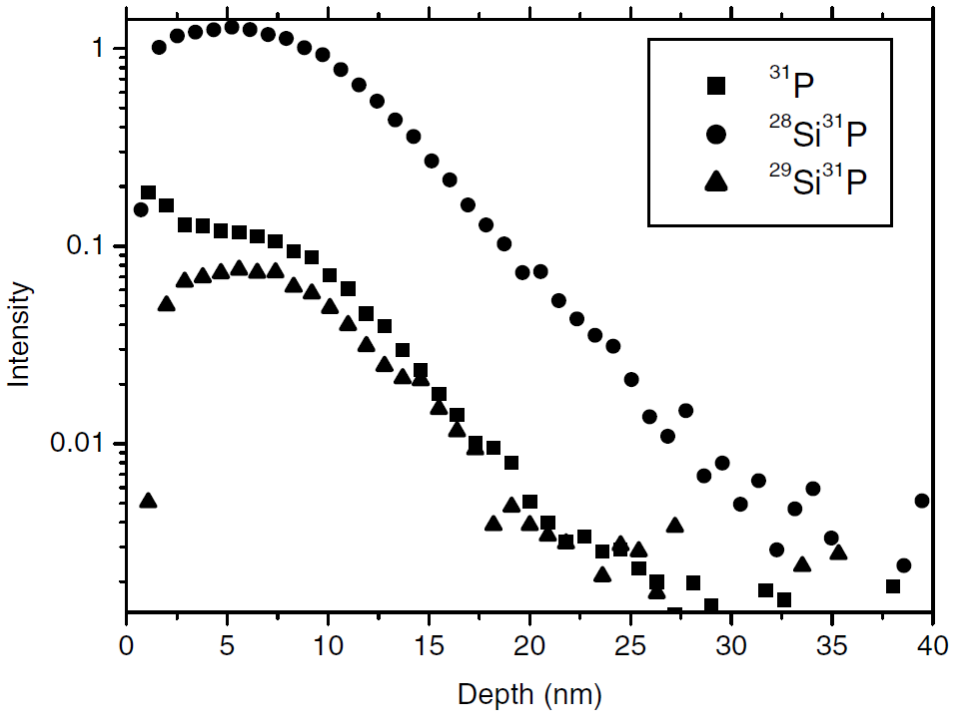


Figure 2.8 – Relative intensity ratios of phosphorus containing species detected during SIMS analysis of low concentration phosphorus implantation in silicon [80].

Non trivial amounts of the single $^{31}P^{+}$ ion are also detected at ~ 31 amu (Figure 2.9) but this has an additional overlap with the silicon hydride $(^{30}Si^{1}H)^{+}$ ion, mainly in the surface regions within the first 200 s of sputtering. Nuclear Reaction Analysis (NRA) has greater chemical sensitivity than SIMS but has lower spatial resolution. It can be used to quantify the amount of phosphorus with relatively large bin sizes compared to SIMS but cannot readily give the precise depth profile information required [80].

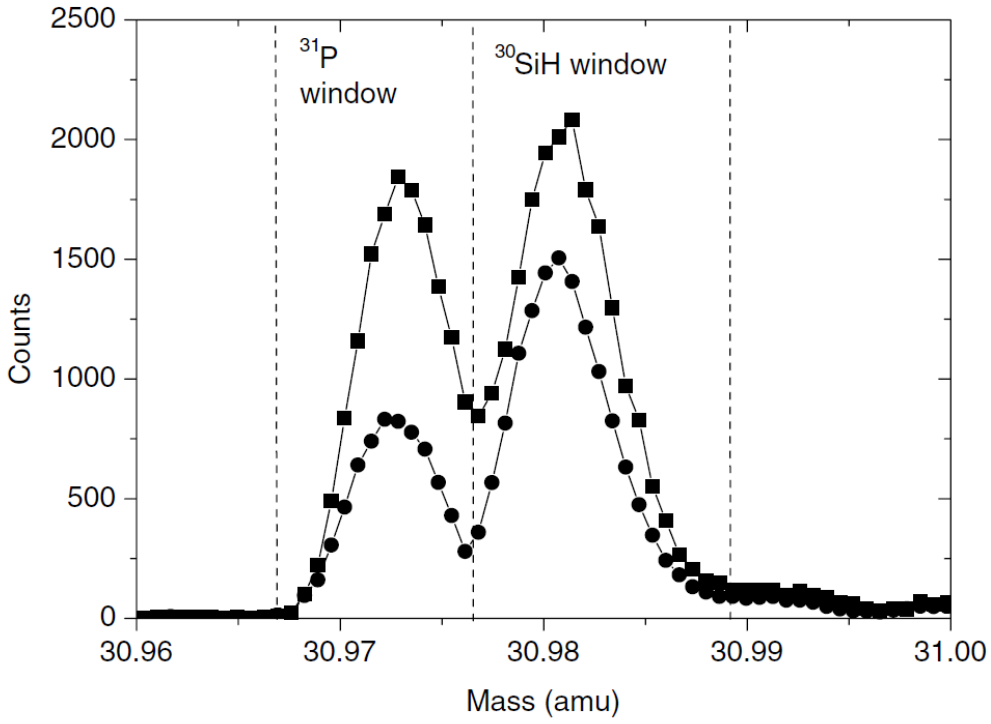


Figure 2.9 - Mass spectra overlaps between silicon and silicon hydride species. Square dotted line accumulated during first 200 s of sputtering of silicon surface. Circle dotted line accumulated in second 200 s of sputtering [80].

In order to reduce the effects of mass spectra overlaps on phosphorus quantification, implantations can be carried out into isotopically purified Si^{28} (greater than 99.9 %) epi-layers [17]. This purified material is used for actual quantum devices and is both expensive and difficult to obtain [81].

An example of a 60 kV phosphorus implantation profile (dose of 4 x 10^{11} cm^{-2}) into such an epilayer as measured by SIMS can be seen in Figure 2.10. Post implantation annealing was carried out in N_2 at 1000°C for 10 seconds in the presence of a 10 – 20 nm silicon oxide layer.

The as-implanted profile can only be clearly seen after approximately 30 nm and, although the measurement is of low concentration (~ 10^{16} at/cm^3), the profiles are noisy and it is not easy to determine their precise shape and the full extent of the phosphorus segregation to the interface after annealing.

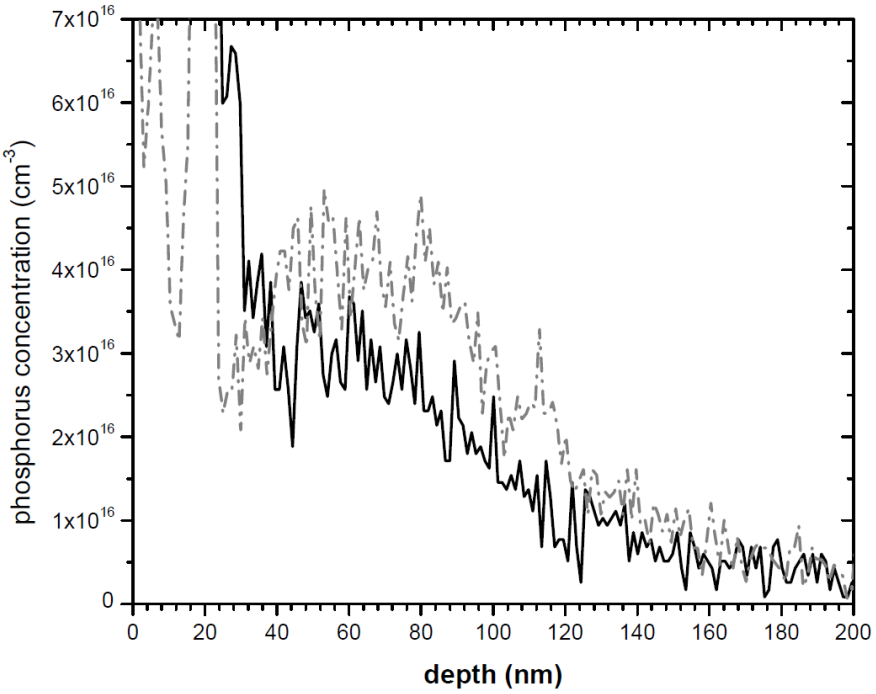


Figure 2.10 - 60 kV P implant through 10 nm SiO_2 layer. Dashed line - Implanted. Solid – After annealing. [17].

Despite the reduction in mass spectra overlaps from isotopically purified substrates, SIMS analyses of phosphorus in silicon are currently unable to give the compositional and spatial information required for fully characterising phosphorus implantation conditions suitable for qubit fabrication [17]. Simulations used to guide implantation parameters [82] are informed by materials characterisation of implanted profiles and there are potential issues with current models, including scattering effects from implantation through surface oxide layers [83].

2.3 Diffusion doping

Diffusion is a standard process of selectively doping regions of silicon substrates uniformly and cheaply [84] [85]. It is typically carried out on the industrial scale using gas phase dopants in high temperature furnaces, although liquid phase dopants are also used to reduce costs in processing. Diffusion is often carried out through open regions defined through photolithographic masking [8]. The diffusion process is often used in early stage large scale doping of surface regions, where precise control of the diffusion region is less important. The thermal processing alongside the exposure to the dopant species is extremely important and, when combined with control of surface concentration, can give a variety of diffusion profiles from the exposed region (Figure 2.11) [22].

.

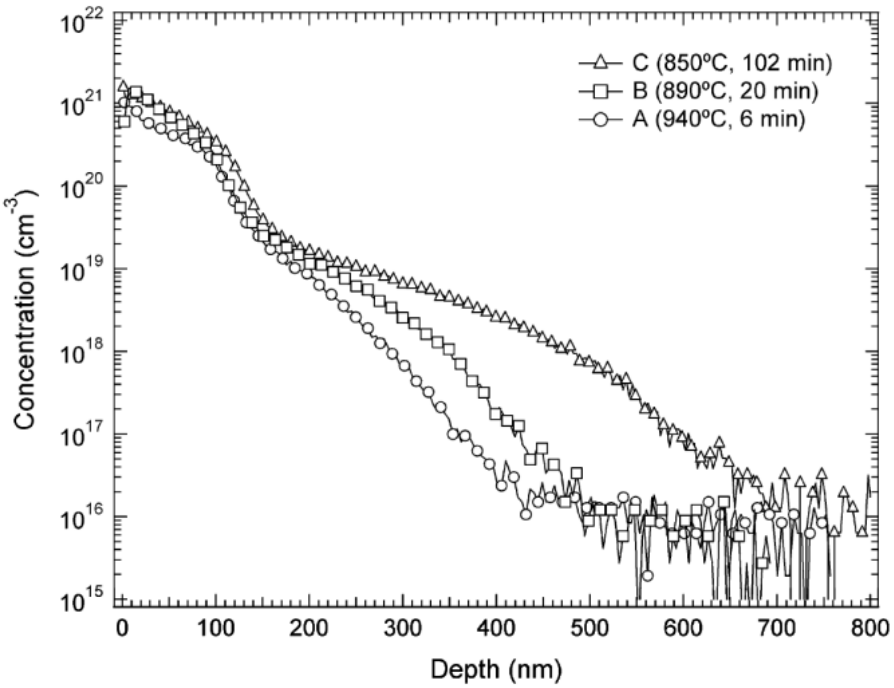


Figure 2.11 - Variation in extent and profile of phosphorus profile in silicon from a spin on dopant as a function of time and temperature [22].

The furnace diffusion process is relatively cheap per wafer as it is only restricted to the capacity of the furnace, the time taken for processing and the reagents used. However, there are still high start up and running costs, therefore reducing processing times when possible can further reduce the end cost per device. Diffusion profiles decrease in concentration away from the surface region and so it can be difficult to engineer a specific peak concentration at any depth, apart from the surface. It is also difficult to dope to a specific depth without also doping the intervening volume and so it is not generally suitable for situations requiring an isolated doped volume [8].

However, the diffusion process requires the dopant to have direct physical contact with the substrate surface and intervening layers of certain materials can slow down or completely stop diffusion. For this reason, other methods, such as ion implantation, are used for the selective doping of specific volumes with specific concentrations below the surface, especially through intervening layers impermeable to diffusion.

2.3.1 Silicon solar cells

Photovoltaic and solar energy now accounts for a large, and steadily growing, amount of renewable energy generation in the modern world. It has increased dramatically since the start of the 21st century (Figure 2.12) and is expected to increase further over the next few decades [86]. The majority (93%) of photovoltaics produced in 2015 in Europe were silicon wafer based, with 68% of them using MC silicon [20].

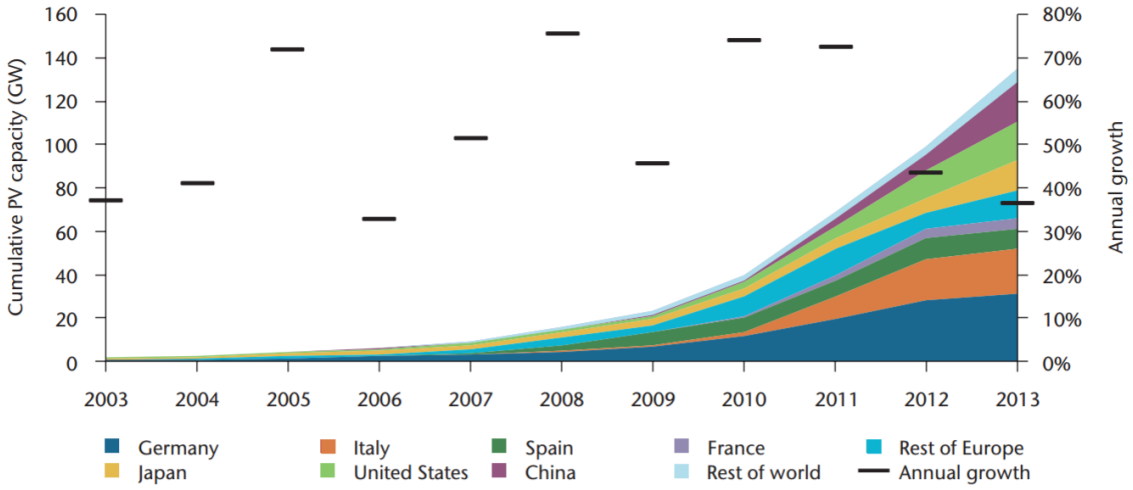


Figure 2.12 – Rise in photovoltaic capacity worldwide from 2003-2013 [86].

MC silicon has been widely used for fabricating silicon solar cells due to the reduced cost of material and the reduction in limitations in cell shapes and sizes. However, as MC silicon does not have the purity or single crystalline nature of Czochralski silicon, the efficiencies of solar cells made from MC silicon are, on average, lower [33]. Transition metal species contamination is a major source of efficiency loss in MC silicon solar cells. Even extremely low concentrations of transition metals can have large effects on device performance [87] [21].

Silicon solar cell efficiency can be optimised to a great degree through limiting the concentration, and controlling the dispersion and segregation of transition metals within the device [88]. Transition metals will often segregate to nanoscale regions, such as dislocations, within these cell materials and so require correspondingly high resolution characterisation in order to more fully understand and predict their behaviour.

2.3.2 Effect of iron in silicon photovoltaics

Iron contamination is a serious issue in MC silicon photovoltaics due to its large impact on efficiency for a relatively low concentration (Figure 2.13) [38]. The effect of iron on efficiency is also greater than that other transition metals of similar concentrations [89] and so is considered to be one of the major efficiency killing impurities in silicon photovoltaics [90].

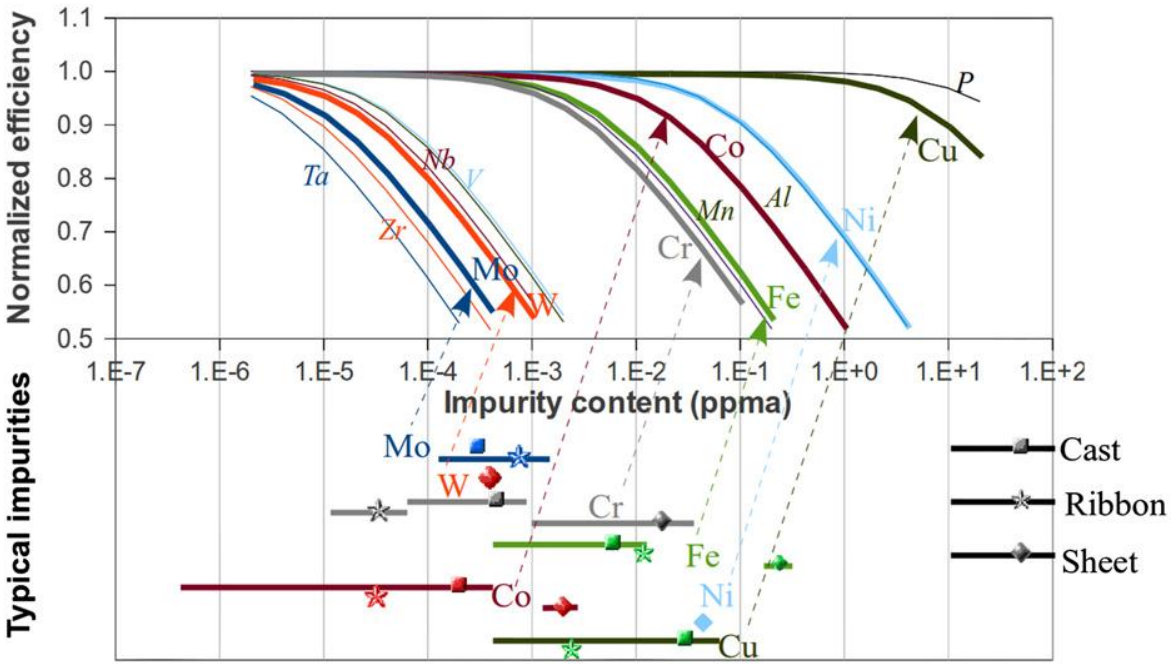


Figure 2.13 - Effects on efficiency from transition metal contamination in multicrystalline silicon [38]. *Data from* [91]. *Impurities measured by spark source mass spectrometry and neutron activation analysis.*

During the MC silicon casting process, mobile impurities, such as iron, diffuse in from the crucible walls into the melt [31]. Impurities that were present in the feedstock are also able to diffuse freely. Due to the in-diffusion of impurities from the crucible, the bottom and edges of the ingot generally result in low efficiency material with high efficiency material in the centre. In cast ingots, the top regions solidify last and are rich in dislocations [42]

and impurities. This results in regions with lower charger carrier lifetimes and eventual lower efficiencies [92].

These high impurity containing regions or ‘red zones’ are typically removed and discarded during the wafering process, resulting in a loss of 10% - 30% of material [93], as it is uneconomical for them to undergo further processing.

These regions are often referred to as ‘red zones’ due to their appearance in colour coded lifetime maps where red is an indication of low carrier lifetimes [94]. The majority of iron contamination in MC silicon is found in the form of iron precipitates [89] at grain boundaries and dislocations [95]. This combination of features can lead to these regions having low carrier lifetimes and result in lower efficiency devices [96]. Recombination due to iron precipitates is dependent on their surface area and so a smaller number of large precipitates have a reduced effect on efficiency compared to a larger number of small precipitates [97].

A small proportion of iron atoms (~ 0.5% [89]) in interstitial form are dispersed throughout the bulk [98]. Due to their wide dispersion and high recombination activity per atom compared to the highly localised precipitates [98], these interstitial atoms can have a significant impact on recombination [99]. As these interstitial atoms can more readily diffuse during thermal processes, they can be gettered at temperatures low enough to allow diffusion but without redissolving existing precipitates [92]. Electronic grade silicon has higher purity and lower levels of transition metals than is required for solar cell fabrication and so lower purity solar grade single crystal silicon is often used to reduce costs.

Solar grade single crystal silicon has a reduced concentration of transitional metals compared to MC silicon but still suffers from related efficiency losses [19]. Therefore in order to further improve efficiency in single crystal solar grade silicon and MC silicon, as

well as reduce the volume of rejected material, further processing is required to limit the effect of impurities. Further purification of the raw silicon feedstock or of the finished wafers may not always be cost effective [38]. Instead of removing them entirely, impurities can instead be redistributed to reduce their impact [92].

Gettering is the term used for the process of moving impurities away from device critical regions, where they can cause recombination and efficiency loss, towards regions with less impact [18]. In order to optimise the gettering processes, changes in specific impurity concentration and distributions need to be linked to changes in efficiency as a function of the parameters used. This requires material characterisation of these impurities on the various length scales at which they are found.

2.3.3 Gettering

Gettering consists of segregating diffuse, unwanted impurities away from the bulk regions into more concentrated, highly localised volumes away from active regions, which will remain there after subsequent processing [40]. Future thermal treatments need to be carefully managed to ensure that these segregated impurities do not redissolve and diffuse back into the bulk, undoing the original gettering process [100].

The regions to which impurities are gettered can be structural in nature, ranging from the nanoscale, in the form of dislocations and grain boundaries, to the bulk scale, in the form of gross saw damage resulting from the wafering process [18]. Changes in chemistry can be used to produce a gettering effect where solubility variations of impurities within adjacent regions of varying dopant levels can allow segregation [101]. Although the most accurate way of determining the gettering efficiency, and thus improvement in overall device efficiency, would be through fabricating a functioning device with the gettered material, this is time consuming and expensive.

Additionally, the observed gettering ability of a single processing stage can be obscured by subsequent processing stages that also improve or reduce efficiency. Whilst the effect on efficiency on the entire process flow is extremely important, in order to test the gettering efficiency of individual stages, test pieces are used and various metrics, such as carrier lifetime measurements, are used which are known to be representative of device efficiency [102]. In order to confirm that efficiency limiting impurities have been successfully gettered, there are a number of characterisation methods can measure key properties that can link to future yield [103].

Charge carrier lifetime can be taken to be an indication of the likelihood of a charge carrier recombining with a defect or impurity within a given time and thus can be a measure of the concentration and nature of the defects that can cause loss of efficiency. These lifetimes can be measured in the bulk in samples greater than 1 cm in size using techniques such as Quasi Steady State Photoconductance [104]. Similarly, carrier lifetime mapping on the centimetre and millimetre scale can be carried out using techniques such as spatially resolved microwave-detected photoconductance decay lifetime measurements - as shown in Figure 2.14 [105]. However, these techniques do not allow the direct measurement of the cause of these carrier lifetime changes and loss in efficiency. This makes it difficult to directly determine how changes in lifetime occur during processing and if there are specific crystallographic defects or impurity species that can be linked to low lifetimes. In order to directly correlate changes in lifetime with the spatial distribution and concentration of impurities, high spatial resolution microscopy (with elemental sensitivity) is required [98] [106].

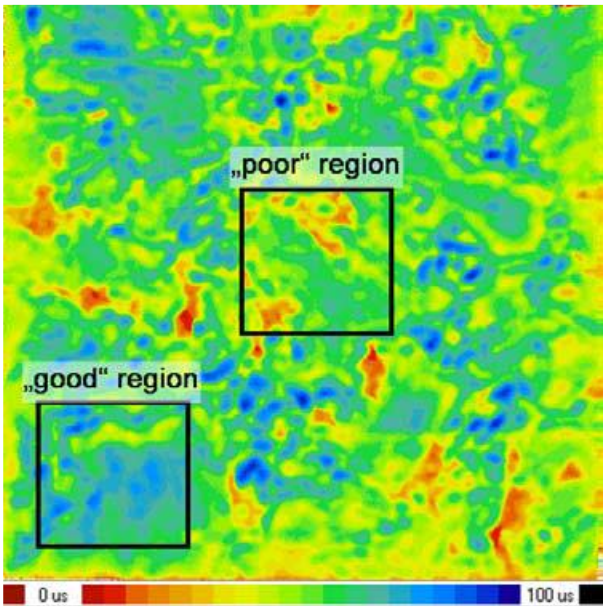


Figure 2.14 – Charge carrier lifetime map of a MC silicon wafer. Measured via spatially resolved microwave-detected photoconductance decay lifetime measurements. Surface passivated with SiN. 10 cm^2 map [105].

Bulk testing for interstitial iron in boron doped silicon can be performed with high precision down to extremely low concentrations, with Murphy et al. measuring ~ 10^{10} at/cm^3 at the limit of their detection ability [107]. Positively charged Fe^+ ions are mobile at room temperature in silicon and preferentially bind to B^- ions, forming immobile FeB pairs [108]. Depending on carried injection level [109], interstitial iron can be a more efficient recombination centre than FeB pairs. Therefore the concentration of interstitial iron can be calculated from changes in minority carrier diffusion length after dissociating FeB pairs through thermal annealing or optical activation [110].

As only interstitial iron is measured using this technique, the amount of iron segregated away from the bulk to substitutional or precipitate forms can be determined. As it is interstitial iron that is predicted to be the main cause of iron related efficiency loss [111], these changes in interstitial iron concentrations can be then linked to carrier lifetime changes and thus predicted device efficiency as a function of the gettering process.

2.3.4 Gettering of iron in silicon photovoltatics

Transition metals, including iron, are known to segregate towards, and precipitate at crystallographic defects such as grain boundaries and dislocations [112]. In the case of materials with large numbers of crystallographic defects, these can be used beneficially to act as gettering regions through the use of extended thermal treatments [113].

There are a number of types of iron gettering that are currently used in the processing of silicon photovoltatic materials. Boron [101], aluminium [114] and phosphorus diffusion [115] are all typically used in the industry as gettering processes. Of these, the optimisation and understanding the mechanisms of phosphorus diffusion gettering is of significant interest due to the fact that a phosphorus diffusion stage is the usual method to form the n doped emitter region of a standard silicon solar cell [22].

2.3.5 Phosphorus diffusion gettering

Phosphorus diffusion gettering (PDG) is carried out through exposing silicon wafers to a high concentration phosphorus source in the form of a gas or liquid source in a high temperature furnace. This forms a phosphorus silicate glass (PSG) on the surface of the silicon (the predeposition phase), which then diffuses into the bulk (emitter forming phase) [116]. Iron species have been shown to segregate heavily to this phosphorus rich region during this process, substantially reducing the amount of iron in the bulk and thus improving carrier lifetimes overall [22]. $POCl_3$ gas in tube furnaces is often used for industrial applications due to the high level of control over temperature and surface phosphorus concentration in the glass. Liquid dopants are also applied using spin-on and screen printing techniques prior to furnace treatment for smaller scale uses, including research, for ease and reduction in costs [117]. Phosphorus diffusion profiles in silicon

show a distinctive ‘kink and tail’ concentration profile as a function of depth [118], with the high concentration ‘kink’ at the very surface and the lower concentration ‘tail’ region extending into the bulk (Figure 15) . This same profile is also found in ion implanted and annealed samples [119]. The phosphorus diffusion is modelled as two separate diffusion regimes depending on the local concentration [120], where the initial high concentration ‘kink’ region diffusion is driven by double negatively charged vacancies and the tail region dominated by interstitial diffusion. In the ‘kink’ region the phosphorus concentration is above the solubility limit in silicon and forms silicon phosphide precipitates [22]. These precipitates have been shown to increase sheet resistance as they are electrically inactive [121]. Only unprecipitated phosphorus is electrically active [122], as shown from comparing SIMS compositional measurements with Electrochemical Capacitance-Voltage (ECV) measurements (Figure 2.15) as the latter remains relatively flat during the ‘kink’ region.

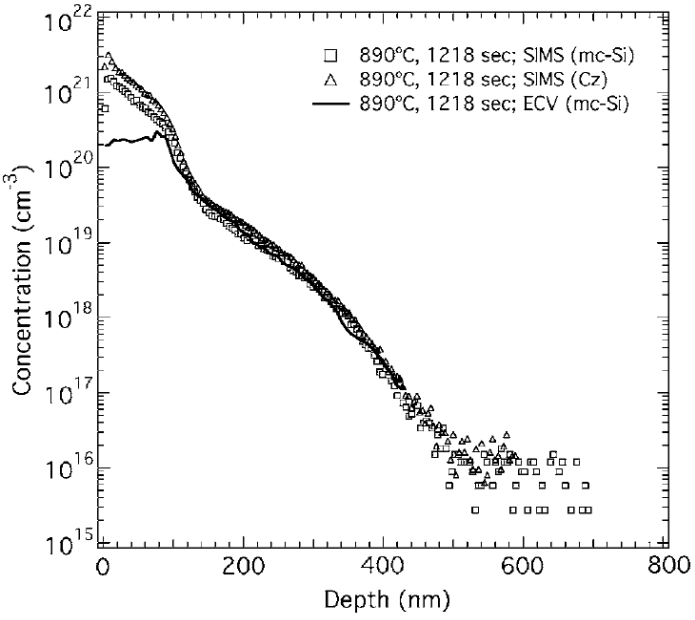


Figure 2.15 – Phosphorus diffusion profiles from single crystal and MC silicon as measured by SIMS and ECV [122].

These precipitates can be in the form of orthorhombic/cubic structures [123] (Figure 2.16). which are present in the first few nanometres below the silicon surface, or spherical (~ 2 nm) precipitates [124] at the PSG/silicon interface, which extend for some tens of nm below the surface and have been observed through Transmission Electron Microscopy (TEM). They have been shown to be formed during the predeposition phase of the phosphorus diffusion process [125], when the PSG is first formed on the silicon surface.

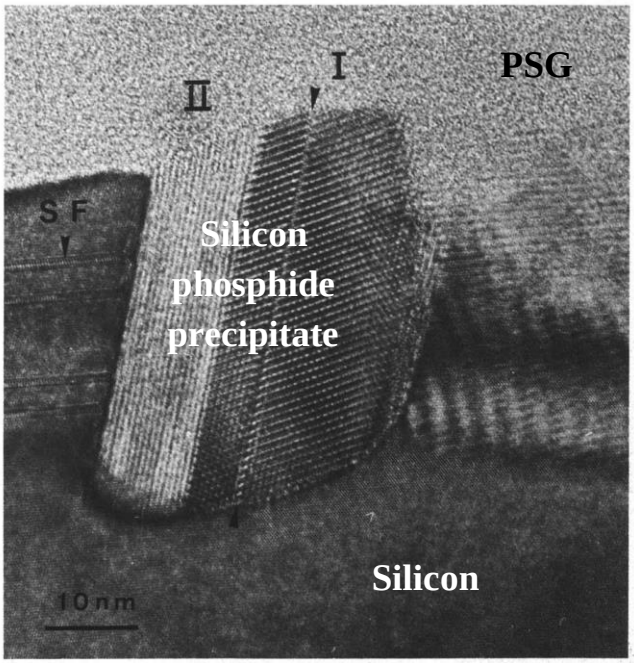


Figure 2.16 - TEM micrograph of a silicon phosphide precipitate at the silicon/PSG after phosphorus diffusion [126]. *Two crystal orientations are clearly visible within the precipitate (I and II).*

Silicon phosphide precipitates in phosphorus diffused silicon have been shown to act as centres for impurity segregation of transition metals such as platinum [127], gold [128], nickel and cobalt [26]. It has been proposed that the generation of interstitials caused by the formation of these silicon phosphide precipitates is linked with the gettering

mechanisms of these metal species [26]. Some of these metals have been observed to precipitate out of the matrix into silicide particles. Nickel silicide precipitates have also been shown to segregate close to silicon phosphide precipitates [129]. All these elements prefer to lie on substitutional lattice sites whilst iron prefers to remain interstitial so the gettering mechanism for iron may not be identical [26].

TEM Electron Dispersive X-Ray Analysis (EDX) analysis has also shown iron signals within a few hundred nm of the silicon phosphide precipitates (Figure 2.17) [26]. These were found in proximity to a particle (labelled F in Figure 2.17), which, although it could not be conclusively identified, was proposed to be composed of some combination of silicon, phosphorus, iron and oxygen.

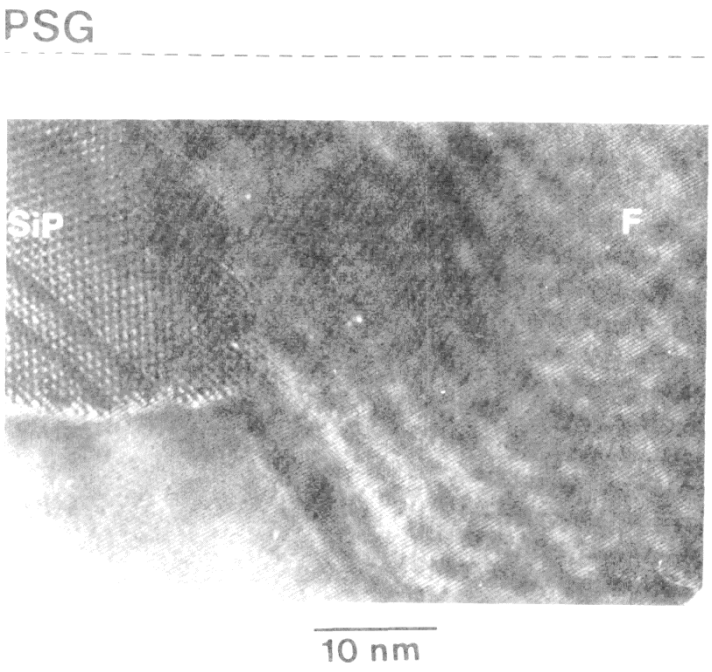


Figure 2.17 – TEM micrograph of a possible Fe containing particle, labelled F, in close proximity to a silicon phosphide particle [26] *and the PSG layer.*

There are a number of models for phosphorus diffusion in silicon that fit the measured data [130] and are considered to be well explained [122], however the models for iron gettering

during phosphorus diffusion are not completely understood. Depth profiles of iron contaminated (bulk Fe concentration of 4.4 x 10^{12} at/cm^3 before gettering) phosphorus diffused (900˚C for 90 minutes) single crystal silicon have been measured using SIMS by Shabani et al. [115]. These profiles were then compared with simulations by Schubert et al. [131]**.** The segregation of Fe, with a peak concentration of ~ 10^{17} at/cm^3 (~ 10 ppm), to the top 0.5 µm with the greatest concentration of phosphorus was correctly predicted but the shape of the Fe profile within that region was found to differ (Figure 2.18) [131]. The model for iron segregation in Figure 2.18 considers a combination of iron precipitating to oxide particles formed from the internal oxygen content of the silicon [132] and the formation of Fe-P pairs [133] from negatively charged substitutional iron with positive phosphorus ions [130].

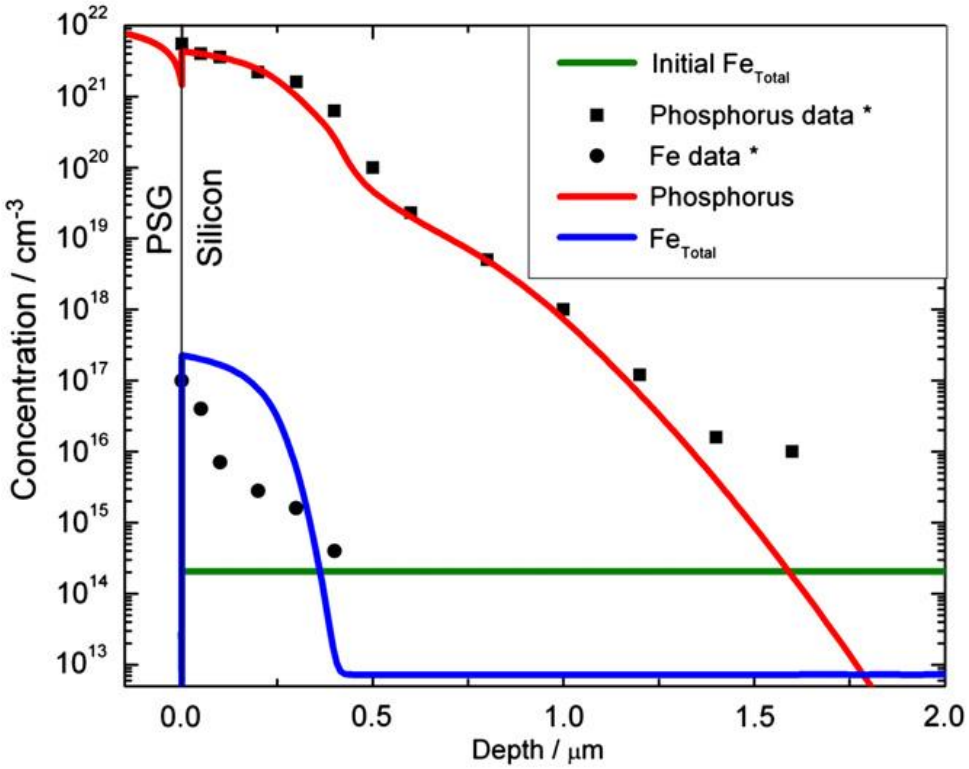


Figure 2.18 – SIMS measured concentrations of phosphorus (squares) and iron (circles) as a function of depth from the surface compared with simulation (red and blue solid lines respectively) and initial iron concentration (green solid line) [131].

Simulations have shown that phosphorus vacancy (V) clusters in the form of P_4V become the dominant phosphorus species above phosphorus concentrations of ~ 10^{20} at/cm^3 and that the metal (M) M-P_4V complex is the most energetically favourable. Through addition of this complex as a potential candidate for the location of iron to existing phosphorus diffusion models [122], simulations show better agreement when comparing between simulated iron concentrations with the measured SIMS profiles [23] (Figure 2.19). This indicates that vacancy concentration within the phosphorus rich region is strongly related to the gettering of iron.

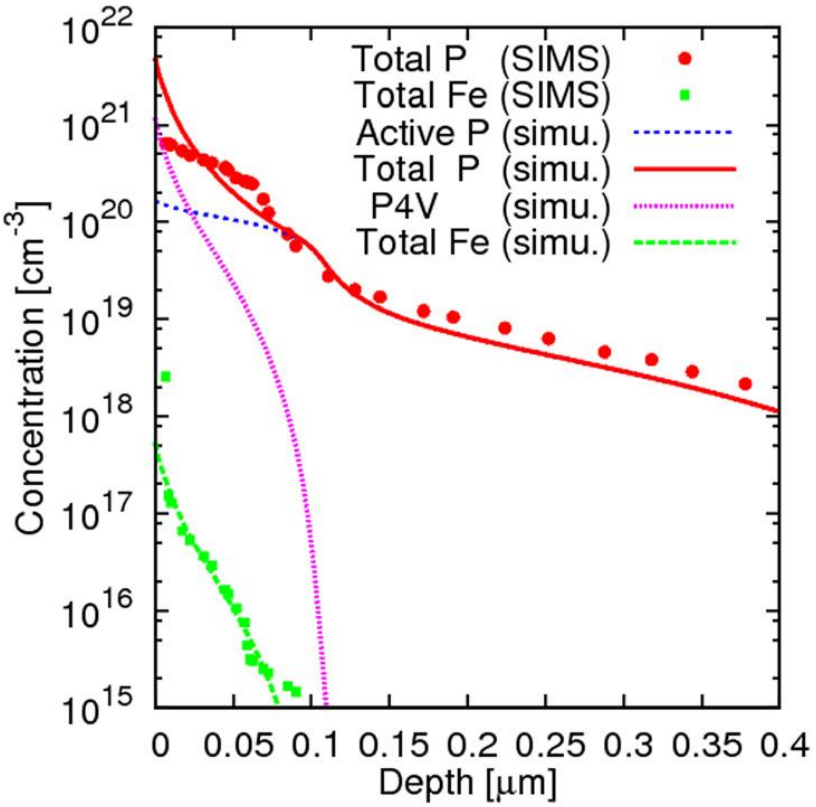


Figure 2.19 – Phosphorus and iron concentrations as measured by SIMS as a function of depth from the surface compared with simulations of phosphorus vacancy clusters [23].

2.3.6 Oxygen and iron co-clustering

It also been proposed that the increased concentration of vacancies due to the phosphorus diffusion allows oxygen to segregate to the vacancies and form oxide particles [24]. This

then creates a number of low energy sites to which iron can preferentially diffuse during PDG. Iron has shown to increase the rate of oxygen precipitation [134] and thus create more sites for further iron segregation. This proposal is supported by the spatial overlap between oxygen and iron profiles measured by SIMS in iron contaminated, phosphorus diffused silicon and is shown in Figure 2.20 [24] .

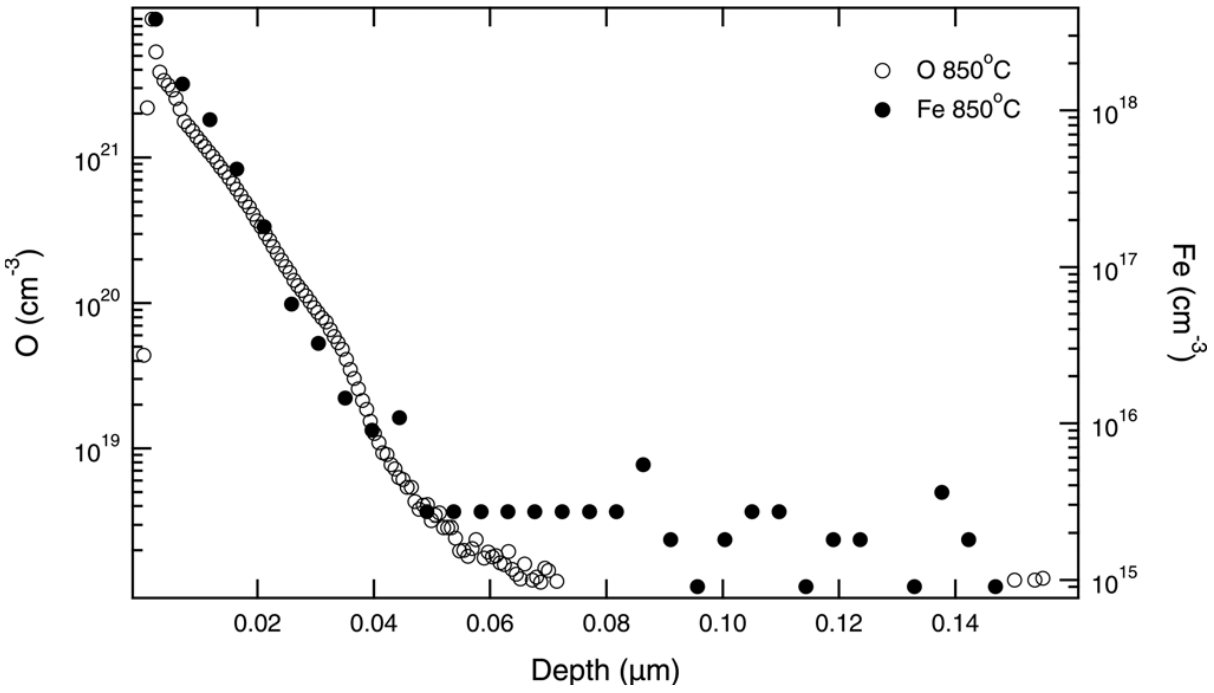


Figure 2.20 - SIMS measured depth profiles of oxygen and iron in phosphorus gettered silicon [24].

Silicon phosphide precipitates have been proposed to be related to the iron gettering process [26] through the emission of silicon interstitials during their formation. Oxygen precipitates have also been observed to form on silicon phosphide precipitates. Furthermore, EDX spectra show that these oxygen precipitates contain phosphorus [25]. This indicates that silicon phosphide precipitates may also have a role in the gettering of iron, either by themselves or through their interaction with oxygen and oxygen precipitates.

In order to determine the exact mechanism of the gettering process, the local chemistry in the top tens of nanometres of the sample surface of phosphorus gettered silicon needs to be investigated with high spatial resolution in order to demonstrate the nature, if any, of any phosphorus, oxygen and iron co-segregation.

SIMS has sufficient depth profiling resolution in order to show the spatial overlap between oxygen and iron profiles but does not have sufficient lateral resolution to unambiguously demonstrate that there is local nanoscale, heterogeneous, co-segregation of phosphorus, iron and oxygen [24]. TEM can provide excellent structural information regarding potential co-segregation and precipitation but compositional analyses via associated spectrographic methods such as EDX can have quantitative issues, especially at low concentrations in dispersed features that are not the full thickness of a TEM sample. The precipitates also will not readily be visible in TEM unless there is a distinct change in structure or strain surrounding them [135].

2.4 Characterisation techniques

The number and role of characterisation techniques applicable to semiconducting materials and devices, specifically those that are silicon based, is extensive. Many modern materials characterisation tools have been directly developed to support the requirements of the silicon IC industry, with a continuing push towards miniaturisation [8] [136]. The history list of characterisation techniques used on silicon materials and devices has been extensively covered in the literature and is outside the scope of this review. Here, emphasis is given to techniques that are specifically aimed at nanoscale characterisation for surfaces and relevant to the materials systems of interest to this thesis.

2.4.1 Scanning Electron Microscopy

Scanning Electron Microscopy (SEM) is a characterisation technique that has been used extensively throughout semiconductor fabrication and research [8]. It uses a focused beam of electrons to interact with surfaces to be imaged, with contrast being given through detection of the secondary electrons ejected due to the incident beam [8]. SEM can give structural information (and compositional information to some extent) on devices and test materials beyond the resolution limit of optical microscopy. The technique has an effective resolution limit in the tens of nanometres in the lateral plane. This is a result of the interaction volume of the electron beam penetrating hundreds of nm to microns beneath the surface of the sample. When combined with other analytical electron microscopy tools, a great deal of chemical and structural information on surfaces can be obtained at the millimetre scale down to the hundreds of nm scale. It is often used in order to guide and give context to higher resolution techniques.

2.4.2 Scanning Electron Microscopy Energy Dispersive X-ray Spectroscopy

Chemical analysis using SEM can be carried out via techniques such as SEM EDX [137], which allows a semi-quantitative chemical mapping that can be used to show distributions of various elements with a similar resolution to SEM. The interaction of the electron beam with the material causes the generation of characteristic X-rays with energies specific to each element. This is generally a qualitative technique and cannot give precise chemical compositions but can be used to spatially map elemental distributions to specific micron and nanoscale regions.

The technique is limited with regards to lighter elements, such as oxygen, due to the low energy X-rays emitted by these species, which can be easily attenuated when travelling through the bulk. Nanoscale surface analysis can suffer from significant contributions from the bulk due to the interaction volume of the electron beam.

2.4.3 Focused Ion Beam

Focused Ion Beam (FIB) uses a beam of highly focused ions, typically from a liquid metal source such as gallium, to both image and sputter material from surfaces [138]. It has similar resolution and mode of operation to SEM, in that images are generated from detection of secondary electrons caused by the incident beam. Ion imaging can be used to determine changes in crystallographic orientation of micron and nanoscale regions due to ion channelling contrast [139].

FIB is often used in order to allow cross sectioning and isolation of various sections of materials and devices in order to see structural changes and facilitate their further analysis [140]. A major use of FIB is in the preparation of site specific samples for further analysis using Transmission Electron Microscopy (TEM).

2.4.4 Transmission Electron Microscopy and Scanning Transmission Electron Microscopy

Transmission Electron Microscopy (TEM) and Scanning Transmission Electron Microscopy (STEM) are the high resolution tools of choice for atomic scale resolution of semiconductor surfaces and devices [140]. A high energy beam of electrons (typically

80 kV to 200 kV) are projected through an extremely thin (tens of nm) lamella and the manner in which the beam is diffracted through different incident angles can be used to obtain crystallographic information [141]. TEM is able to resolve atomic scale variations in structural features and can give information on local crystallography using diffraction based analysis. This allows the crystallinity of specific regions to be determined and identified, which can be used to give information on damage to materials through ion implantation or allow the identification of phases and precipitates through the crystal structure. STEM allows scanning of the highly focused electron beam spot across atomic scale specific regions of the sample and can give higher resolution images than TEM. (S)TEM cross sectional analysis gives extremely high resolution images, up to the atomic scale, when samples are correctly prepared and thinned. This technique is used as a method of confirming interface thicknesses and device structural integrity [140].

2.4.5 Transmission Electron Microscopy Energy Dispersive X-ray Spectroscopy

Transmission Electron Microscopy Energy Dispersive X-ray Spectroscopy (TEM EDX) chemical analysis can be carried out in a similar manner to that of SEM EDX. In contrast, it uses the signal from a much smaller and thinner sample, enabling a much higher resolution measurement of the spatial distribution of elements with reduced bulk contributions.

2.4.6 (Scanning) Transmission Electron Microscopy Elastic Electron Loss Spectroscopy

(Scanning) Transmission Electron Microscopy Elastic Electron Loss Spectroscopy ((S)TEM EELS) is a technique that measures the changes to the electron beam projected through the TEM sample as a function of electron energy. Small losses can be linked to specific characteristic interactions and thus chemical information can be obtained from nanoscale regions (Figure 2.21). An advantage of EELS over EDX in this case is that EELS has a greater ability distinguish to signals from the presence of light species such as oxygen [142].

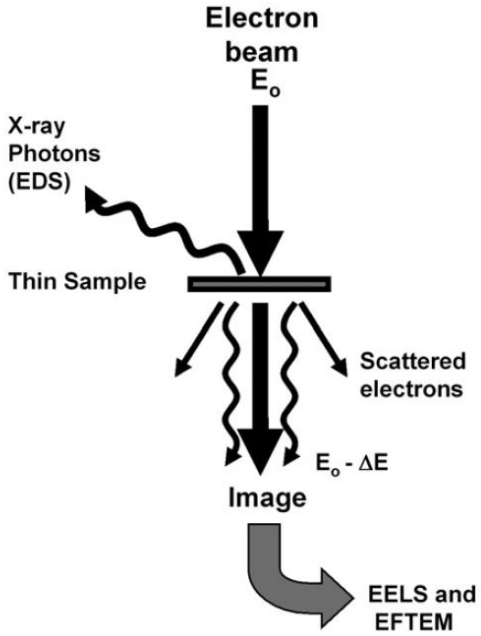


Figure 2.21 – Schematic of TEM, TEM EDX and TEM EELS [52]

Using EDX and EELS, semi-qualitative chemical analysis can be carried out with nanoscale resolution. This can give information on dopant distributions within devices and can link them with failure modes such as gate leakage or segregation to device walls. Through a combination of SEM and FIB, a specific nanoscale region or device can be

identified, then made ready for (S)TEM and associated chemical analysis. Due to this level of precision in sample preparation, and the nano and atomic scale resolution of the analysis available, S(TEM) is a major analysis tool used in modern semiconductor device research and throughout industrial processing [52].

2.4.7 Secondary Ion Mass Spectrometry

Secondary Ion Mass Spectrometry (SIMS) is a characterisation technique that uses a stream of incident ions to sputter away the surface layers of a material and collect ions that are ejected from the surface [8]. These collected ions are then identified using a magnetic sector, or quadrupole mass spectrometer in the case of dynamic SIMS used for depth profiling (Figure 2.22). These detectors only allow the analysis of a certain number of pre-selected ions so not all species are detected equally at the same time. Time of flight (ToF) SIMS is used for surface analysis where a wider range of species are required to be analysed simultaneously from a single monolayer. SIMS can provide extremely high spatial resolution on the order of a few atomic layers when using low energy ions for depth profiling analysis but the sputter crater is often tens of microns in diameter, limiting lateral spatial resolution [143]. The lateral resolution is determined by the spot size of the ion beam, with large spot sizes (typically in the tens of microns) allowing improved compositional accuracy through increased numbers of collected ions [8]. Smaller spot sizes can be used to improve lateral resolution (with a current limit of ~ 50 nm) although it does so at the expense of compositional accuracy. This is therefore usually used for elemental mapping rather than accurate depth profiling [144]. SIMS can provide chemical sensitivity up to the parts per billion, depending on the amount of material analysed and the specific type of SIMS analysis.

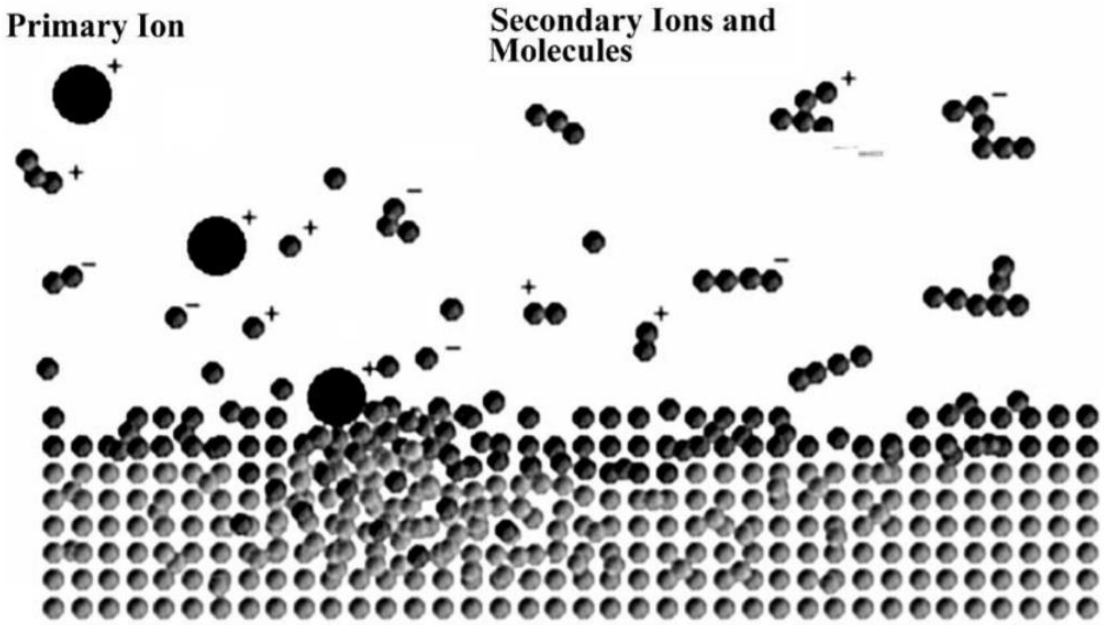


Figure 2.22 – Schematic of Dynamic SIMS sputtering mechanism [145].

Dynamic SIMS systems allow depth profiles of tens to hundreds of microns to be analysed relatively quickly. Higher energy ions increase the sputtering rate but also increase the level of intermixing between layers and so are not suitable for nanoscale depth profiling [146]. Static ToF SIMS is often used for analysis of materials which has already been sputtered to a specific depth through higher energy Dynamic SIMS sputtering. Lower beam energies and fluences constrain secondary ion ejection to surface monolayers, giving improved compositional information from the exposed surface without including bulk contributions. However, this technique is slow and is generally used where surface composition information is required. In dual-beam systems, depth is controlled by sputtering from one ion beam normal to the surface, whilst the analysis being carried out by a lower energy, angled ion beam such as to give higher accuracy, compositional measurements. This provides the best of both techniques, especially in the first few nm of analysis [146].

SIMS is the semiconductor industry standard technique for the analysis of diffusion and implantation profiles. This is due to extreme accuracy in depth profiling and high chemical sensitivity in the ppm-ppb range. It is also the technique of choice for measuring diffusion and implantation depth profiles for comparison with simulation models.

SIMS can only give an average of those features with dimensions smaller than the sputtered crater size and so the analysis of specific and individual nanoscale regions and devices is not feasible using this technique. The quantification of concentrations as measured by SIMS requires the use of known standards in order to take into account relative sputter yields of different species. The matrix effect is known to cause issues where species of different sputtering yields are present during bulk analysis [147]. As with all forms of time-of-flight mass spectrometry, there is potential for increased ambiguity in quantifying mass spectra when there are overlapping mass spectra peaks [80].

The calibration of depth measurements from SIMS can be based on a number of methods. The most common is to sputter away a crater of material, then subsequently measure its size and depth using a stylus, Atomic Force Microscope tip [148] or laser based technique. By calibrating the number of ions detected with the known volume of the crater, ratios of detected ions to total number of ions can be calculated and quantification of chemistry carried out. It takes a certain amount of time for the sputtering caused by SIMS to achieve an equilibrium sputtering crater shape [149]. This is particularly an issue in the early stages of sputtering, which corresponds to the first few nm of analysis, therefore surface and near-surface analysis using SIMS can have a number of challenges. This effect can be reduced by covering the surface to be analysed with a capping layer of material that sputters at the same rate so that equilibrium sputtering can be obtained prior to reaching the region of interest [150].

2.4.8 Nanoscale characterisation of surface regions

TEM and STEM are industry standard characterisation techniques that enable nano and atomic scale spatial characterisation on samples that are tens to hundreds of nanometres thick [52]. When combined with EDX and EELS techniques and site specific FIB lift out, impurity distributions and concentrations in specific nanoscale regions of semiconductor materials and devices can be analysed. Nanoscale variations in composition can be measured qualitatively, however quantification is difficult and bulk contributions can still obscure local nanoscale features [151]. SIMS can offer extremely high chemical sensitivity and depth resolution but has issues characterising the first few nanometres of subsurface analysis [152] and nanoscale features due to the utilisation of a micron scale spot size.

There remains a gap in the capabilities of standard characterisation techniques that are used in the semiconductor industry for quantitative atomic scale characterisation of impurities in nanoscale volumes. Atom Probe Tomography (APT) is a materials characterisation technique which combines nanoscale chemical and spatial information in 3D and is showing great promise in being able to fill this gap. As the main focus of this thesis will be based upon the application of APT to the analysis of impurity segregation to the surfaces of semiconducting materials, it is therefore fitting to give a short overview to the technique and its history.

2.5 Atom probe

2.5.1 Field Ion Microscopy

Field ion microscopy (FIM), a predecessor of modern atom probe tomography, is a surface analysis technique that was the first ever to image individual atoms [153].

It uses the process of field evaporation whereby surface atoms are evaporated from an extremely sharp tip through the application of a high electrostatic field in the V/nm range [1]. This field is generated through the application of a high potential difference and can be described by the following equation.

$$F = V / kR \quad (1)$$

Where F is the electrostatic field experienced by the tip, V is the applied potential difference, R is the radius of the tip and k is a 'field factor'. For an ideal spherical emitter, this k factor is 1 and it is used to describe deviation from ideality in the shape of the emitter and its local environment [154]. In FIM, imaging gas atoms that have been adsorbed onto the protruding crystal terraces of a very sharp, needle-shaped tip (with a tip diameter of less than ~100 nm and often less than ~ 50 nm) are field ionised through the application of a high standing electric field [155]. Using an adsorbed gas, rather than evaporating the matrix material, allows a constant stream of ions to be detected that originated from the same location (Figure 2.23). This increases the signal to noise ratio which was of great importance when using phosphor detectors available during the first applications of FIM. In order for single ion impacts to be detected, an increase in the sensitivity of the detector was required and this was through the use of micro-channel plates (MCP), which act as charge multipliers for incident ions [1].

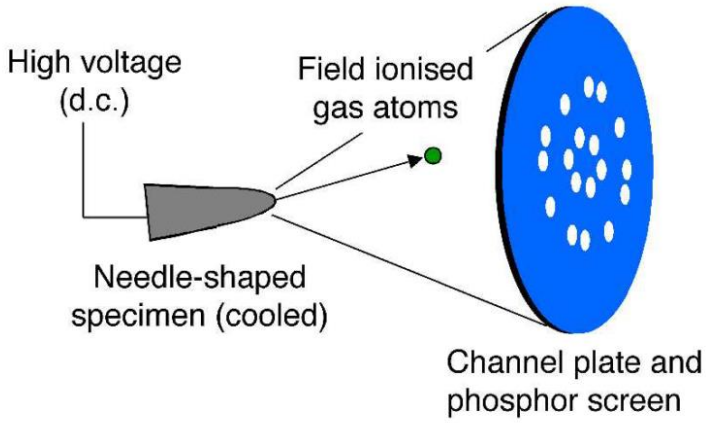


Figure 2.23 – Schematic of Field Ion Microscope [156]

The imaging gas ions are then projected by the highly divergent electric field onto a MCP and phosphor screen, providing an extremely magnified 2D projection of the atomic arrangement at the tip surface (Figure 2.24). The specimen is held at cryogenic temperatures (20 K to 80 K) to reduce surface migration of atoms during analysis, which would have the effect of blurring the spatial resolution [157] [158].

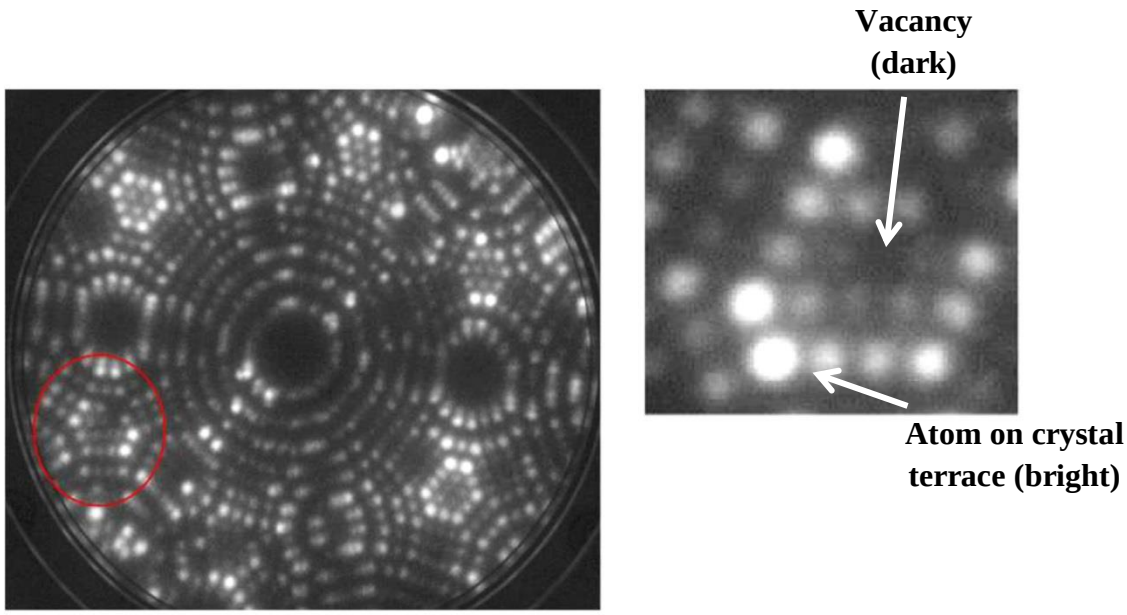


Figure 2.24 – Left - Field Ion Microscope image of a tungsten surface showing crystallographic pole structure. Bright dots are atoms at atomic terraces. Right – Vacancies showed through low contrast regions [159].

Constituent atoms can be field evaporated by increasing the electric field, consequently nanoscale regions of material can be removed in order to allow FIM images to be obtained from a limited depth profile. Field ion microscopy gives spatial information about the surface of the specimen, however, chemical information can only be inferred through variations in contrast and evaporation sequence [159] .

In order to gain more precise chemical information of regions that have been identified via FIM, time-of-flight spectrometry of field evaporated atoms emitted from the material was added to the technique. The development was known as atom probe field ion microscopy (APFIM) [160].

In order to carry out atom probe on a FIM selected region of a sample tip, a pinhole aperture is aligned to that region and the imaging gas is removed from the analysis chamber. Superposition of a pulsed field onto the standing field enables correlation of the time of detection of each ion with the application of a specific pulse that triggered the evaporation of that ion and hence allows the time-of-flight between the surface and the detector to be calculated. This evaporation of substrate atoms is in the form of detectable ions with a specific time of flight, allowing the mass to charge ratio of that ion to be calculated (Figure 2.25) [2]. Early APFIM instruments had an extremely limited field of view, since the aperture would only allow the measurement of a 1D depth concentration profile through the sample with some thousands of ions being collected as a dataset [160] [161].

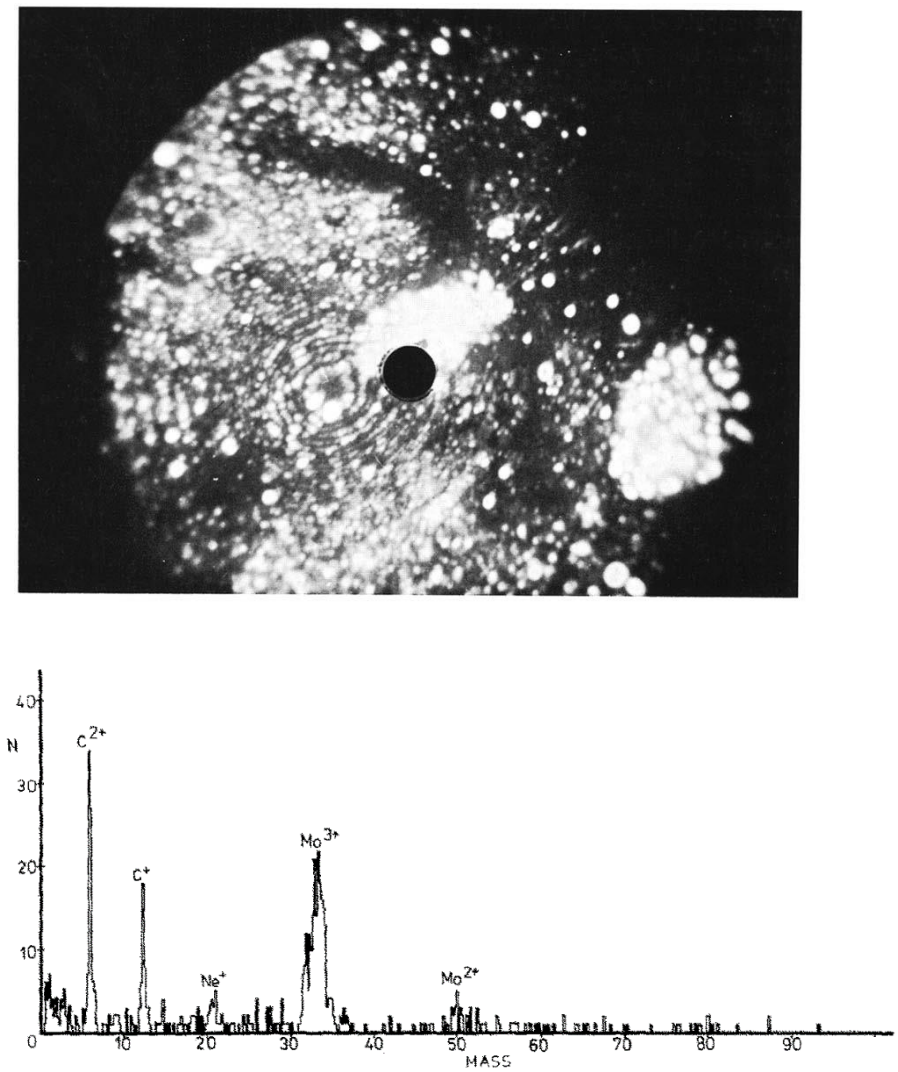


Figure 2.25 – Top - Field ion microscopy image of steel containing Mo_2C precipitates, black pinhole in centre for atom probe analysis over a precipitate. Bottom – Time of flight mass spectra of ions collected from region over pinhole showing carbon and molybdenum species [2]. *Vertical axis is the number (N) of ions detected, horizontal axis is the mass to charge ratio of the detected ions.*

Wider field of views become possible through improvements in atom probe digital detector design, enabling the collection of 2D spatial information [162]. This can then be used over time to generate a 3D reconstruction of the tip by back projecting the observed ions, leading to Atom Probe Tomography (APT) [163]. The data collected is in the form of

a 3D map consisting of every detected ion that has been linked to a known ionic mass/charge ratio. This combines spatial and compositional information on the nanoscale in an easily visualised manner. By linking regions through iso-concentration surfaces, nanoscale regions of local concentration increases can be readily observed [1]. An example is presented in Figure 2.26, where nanoscale precipitation of phases, of different composition, within a nickel superalloy are clearly visible [164].

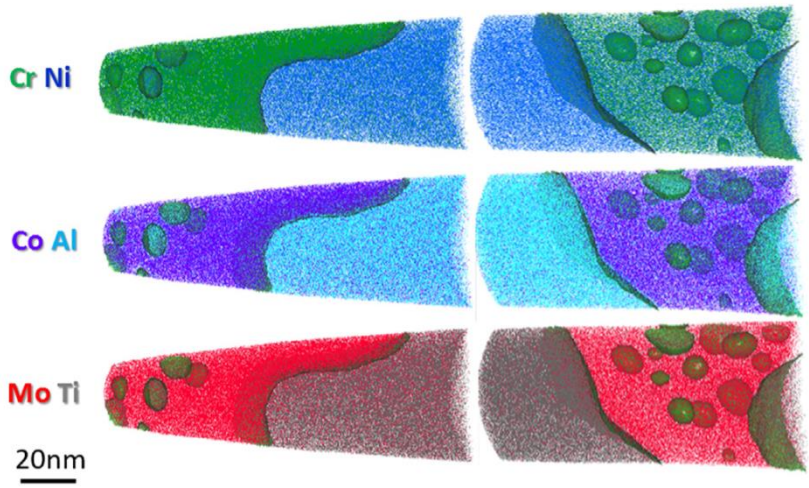


Figure 2.26 – Partitioning of different elements to nanoscale phases in RR1000 nickel superalloy. Break in centre of data set due to experiment split between two analyses on same sample [164].

As material is evaporated from the sample tip, the tip diameter will increase and so an increased field is required to continue evaporation. This sets a limit on the diameter of the samples that can be analysed for a given applied voltage limit and, given that the majority of samples will not be perfectly straight, it also sets a limit of the depth of material that can be evaporated.

In order to further increase the field experienced by the sample during atom probe analysis for a give applied voltage and to improve the data collection throughput, Nishikawa proposed the replacement of the distant electrode with a local electrode [165].

2.5.2 Atom probe tomography

Atom probe tomography is a materials characterisation technique that allows high chemical sensitivity (in the ppm range for large datasets) and extremely high spatial resolution (up to 0.2 nm in the analysis direction). There are extensive, detailed descriptions of the current applications technique [1] [7] and its history in the literature [166]. Hence, only a basic overview of the operating principles of the technique will be provided here, with special attention paid to those aspects which are relevant to the materials systems described in previous sections. All atom probe analysis carried out in this thesis used Local Electrode Atom Probes (LEAP) [167] systems and discussion will be based around these. The standard 3D reconstruction of atom probe data is based upon geometric projection of ions from the surface of the atom probe sample and models the tip as a sphere on a cone [168]. Ions are assumed to travel in a straight line from their origin, through the local electrode and onto the 2D sensitive detector plate. Figure 2.27 shows a basic schematic for atom probe analysis using a local electrode.

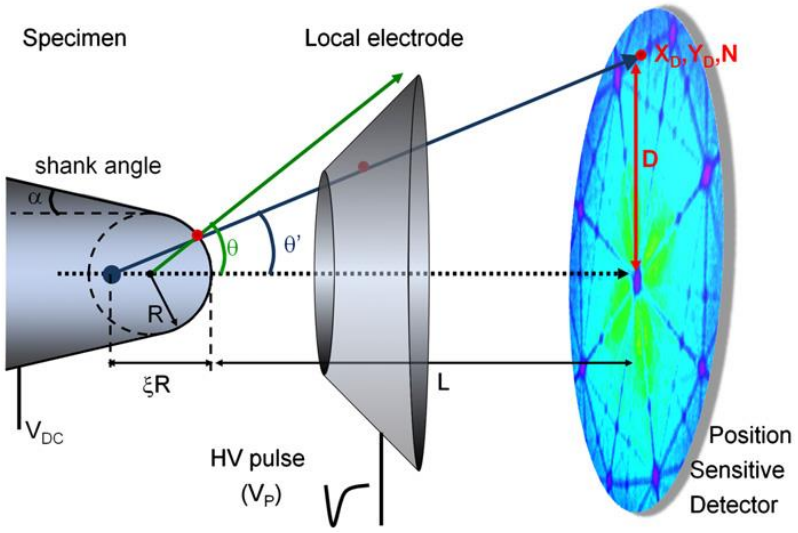


Figure 2.27 - Schematic of Local Electrode Atom Probe [169]**.**

The radius of the sphere is R, the tangential angle of ion emission is θ, the corrected radius of the sphere is ξR and the corrected angle of ion emission is θ'. These ions travel a distance of L to the detector where X-Y information is detected. The shank angle α gives a measure of how the sample tip radius will grow as the sample becomes blunter during analysis. The sample is kept at a standing voltage of V_{DC} and, in the shown example of voltage pulsing, a pulse of V_P initiates field evaporation. There is a degree of ion focussing due to the high electrostatic field from the electrode and this is taken into account in the model through an offset in the form of the Image Compression Factor (ICF - ξ) [170]. This alters the depth of the centre of the sphere used in the above model in order to match that which would be required for a true geometric projection.

In order to obtain a 3D reconstruction from the 2D information obtained from the position sensitive detector, the sequence of ions impacting on the same detector element is used. Each successive impact on a detector element is assumed to have come from the same origin point on the sample and thus the order in which they are detected gives depth formation [171].

The reconstruction is then calibrated using the theoretical evaporation field requirements for the majority species in the sample to give a measure of the diameter as a function of the voltage. This can then be further refined through altering reconstruction parameters to match known crystallographic plane spacing or interfaces known to have a specific topography [172].

Voltage pulsing was the first analysis method for time of flight mass spectrometry in atom probe and its applications were initially limited to those of highly conductive metallic elements and alloys [173].

Atom probe analysis of semiconductor materials, such as silicon, using voltage pulsing has been shown to be viable but is mainly confined to highly doped samples due to issues with conductivity [174]. Undoped silicon requires extended voltage pulse widths in order to field evaporate [175]; this leads to reduced mass resolving power in the mass spectra [176].

2.5.3 Laser pulsed atom probe tomography

Laser pulsing was introduced to atom probe in order to expand the range of analysable materials to those that were not suitable for voltage pulsing due to low electrical conductivity [177]. Laser pulsing analysis of silicon has been shown to give greater mass resolving power compared to voltage pulsing (Figure 2.28) [178].

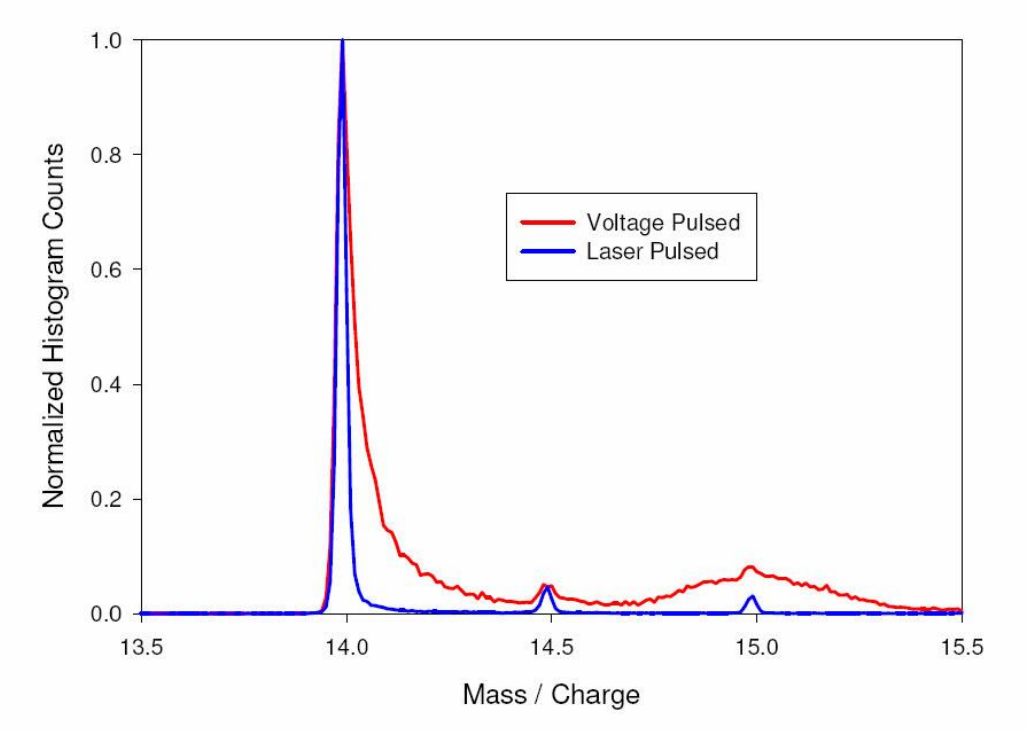


Figure 2.28 - Comparison in mass resolving power of voltage pulsing and laser pulsing of silicon [178].

The laser induced evaporation mechanism has been debated extensively in the literature and, although there are still some phenomena that have to be fully explained regarding the laser/tip interaction physics, the consensus is that the laser induced evaporation is primarily a thermal effect [179].

Due to this, the thermal conductivity of the sample to be analysed is important, in addition to the electrical conductivity. Delayed evaporation artefacts, in the form of 'thermal tails' that decay away from the initial peak, have been shown to be present in thermally insulating samples or when using high laser energies. This is due to the sample remaining at the required temperature for evaporation for an extended period, so those atoms that evaporate after a small delay appear to have an extended time of flight and thus a slightly greater mass-to-charge-state ratio [180].

Different wavelengths of laser light will each exhibit a distinct interaction behaviour with the nanoscale tips used in atom probe, giving variation in the absorbance characteristics [181]. Generally, lower wavelength lasers lead to more surface absorbance (Figure 2.29) and provide improved mass resolving power than higher wavelength lasers [182].

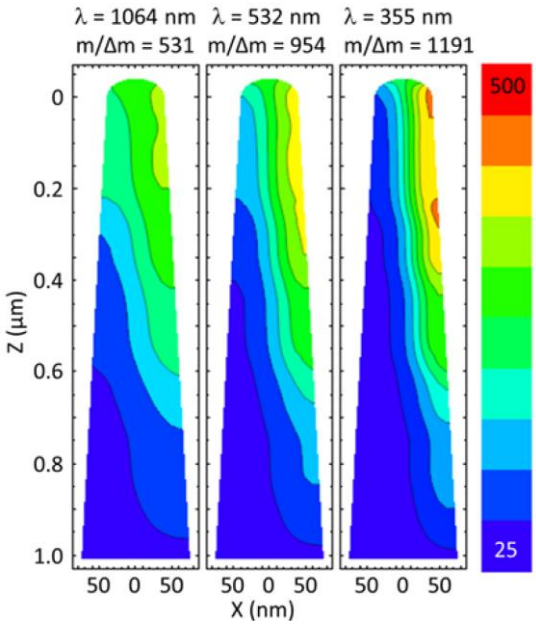


Figure 2.29 - Changes in mass resolving power and laser absorbance with variation in laser wavelength [182]..

Atom probe analysis of relatively low thermal conductivity materials using lower wavelength lasers has demonstrated improved mass resolving power and reduced thermal tails [3] (Figure 2.30). This is due to the reduced excess heating of the sample material away from the tip, which is due to the reduced spot size and increased surface absorbance.

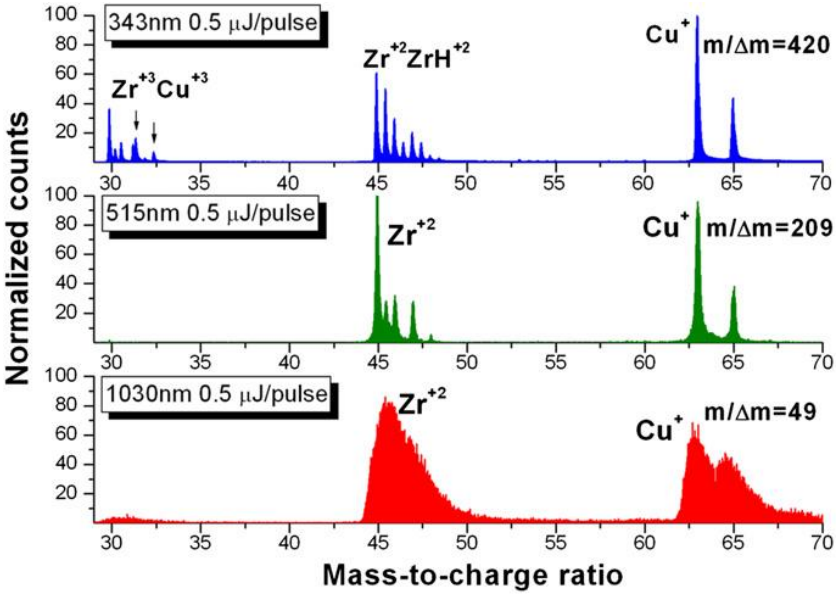


Figure 2.*30 - Comparison of effect of laser wavelength on extent of delayed evaporation, in the form of 'thermal tails'* [3].

Atom probe samples made with larger radii and larger shank angles (therefore a greater amount of material in proximity to the tip to act as a heat sink) have also been shown to have reduced thermal tails when compared to thinner samples [180].

Non uniform laser absorbance and heating can lead to the formation of non-uniform steady state specimen end forms, often causing preferential evaporation from the laser incident side. This can lead to changes in field across the sample surface, with the laser incident side experiencing a lower local field due to the increased local heating and broadening of the tip in that region [183].

The change in field can lead to mass-to-charge-state state ratio changes as a function of radius and of distance from the laser incident side, with increased numbers of singly ionised species and complex ions in that region [184]. These non-uniform end forms, which diverge from the assumptions that are used with the standard reconstruction models can lead to lead to artefacts in the reconstructed volumes [183].

2.5.4 Focused ion beam based sample preparation

Atom probe samples have extremely strict size and shape restrictions. Specimens are required to be in the form of a very sharp needle with a radius less than 100 nm [185]. Electropolishing is the standard method of producing samples suitable for atom probe from bulk material (typically metals) and consists of electrochemically etching a wire/matchstick blank to form the required tip shape [186]. Bulk silicon materials can be etched using hydrofluoric acid solutions [187], and multi-layer semiconductor materials via preferential etchants [188]. Instead of etching a bulk material, it is often easier to grow semiconductor 'whiskers' or nanowires of the geometry required for atom probe analysis onto support structures [189] or attach them to conductive metal supports [190]. In place of electrochemical etching, ion beam milling can be used to remove material from the surface of a sample in order to thin and shape it to the required geometry for atom probe analysis. Initial studies using broad ion beams and argon milling combined with physical rotation of the sample was shown to be a viable method of sharpening once the initial tip shape had been formed via other methods [191].

Initial FIB systems consisted of a single column which could be used to sharpen samples through end on milling. As viewing the sample using the FIB beam would damage the sample tip, optimisation of milling conditions was carried out emperically through comparison with TEM images [192]. When SEM was combined with FIB in dual beam FIB-SEM systems, it allowed the imaging and selection of specific micro and nano scale regions and then extraction via site specific liftout techniques (Figure 2.31) adapted from TEM sample preparation [138]. The lifted out material is then attached to a support structure such as an electropolished needle or silicon post and sharpened using a FIB to the required geometry.

The introduction of FIB milling for the routine preparation of atom probe specimens has enabled the analysis of many new types of materials that were not suitable for electropolishing. It has enabled site-specific analysis of targeted microstructural features that were previously extremely difficult to isolate within an atom probe sample [193].

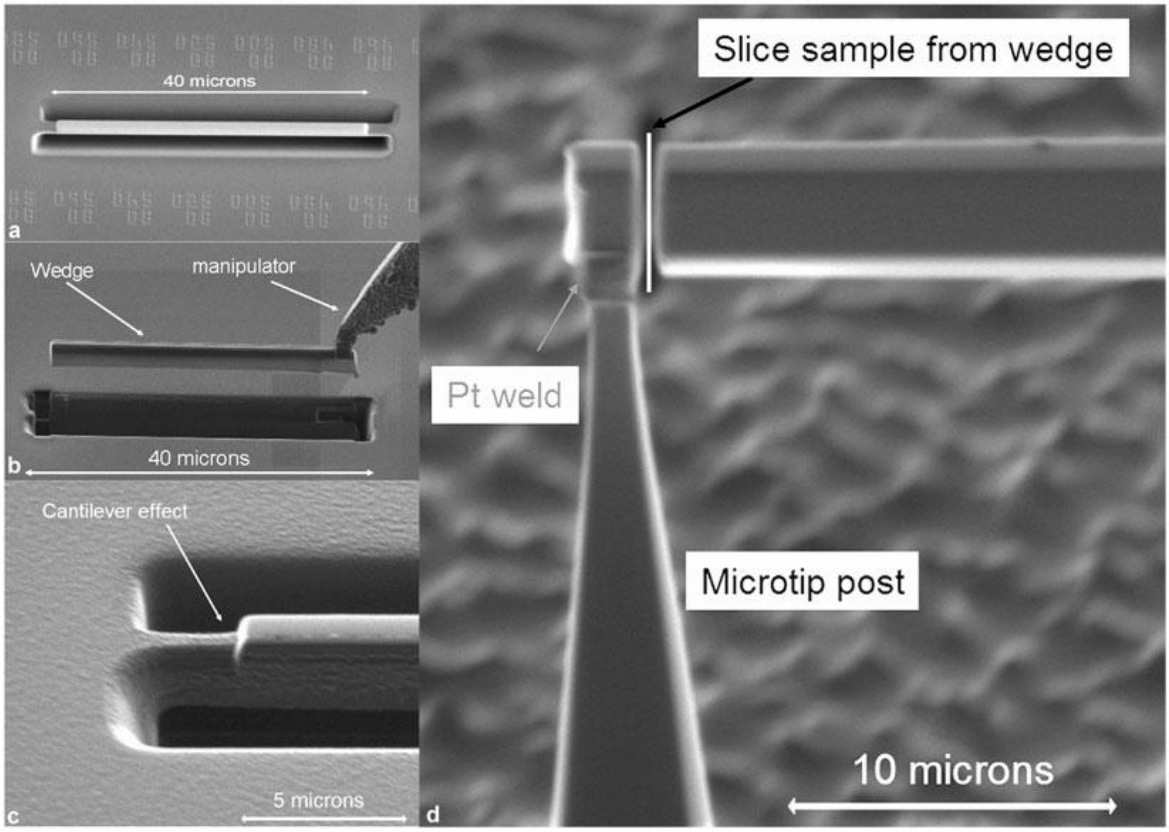


Figure 31 – FIB lift out process, including trenching, removal of wedge with micro manipulator and attachment to silicon micro post [194] [6].

The FIB liftout process (Figure 2.31) also often uses the deposition of protective material, via a highly spatially defined electron beam or FIB decomposition of an organometallic gas via a Gas Injection System (GIS) [195] in order to protect the surface of the sample during high energy FIB milling [196] [6]. These GIS deposited layers have been shown to be non-uniform in structure and composition, with Pt granules being observed by APT in FIB deposited Pt layers [197]. Through the addition of ex-situ

deposition of capping or encapsulation layers prior to FIB based sample preparation [193], the APT analysis of surface and near surface regions of materials has been made possible. These capping layers are used to preserve and delineate the surface during FIB based sample preparation [198]. Unlike those materials deposited via GIS, a small amount of capping layer is left on the finished sample and the analysis volume contains the interface between capping layer and substrate (Figure 2.32) in order to delineate the surface [6]. All gallium damage from the FIB milling process is confined to the capping layer and the transition between capping layer and substrate can be clearly seen.

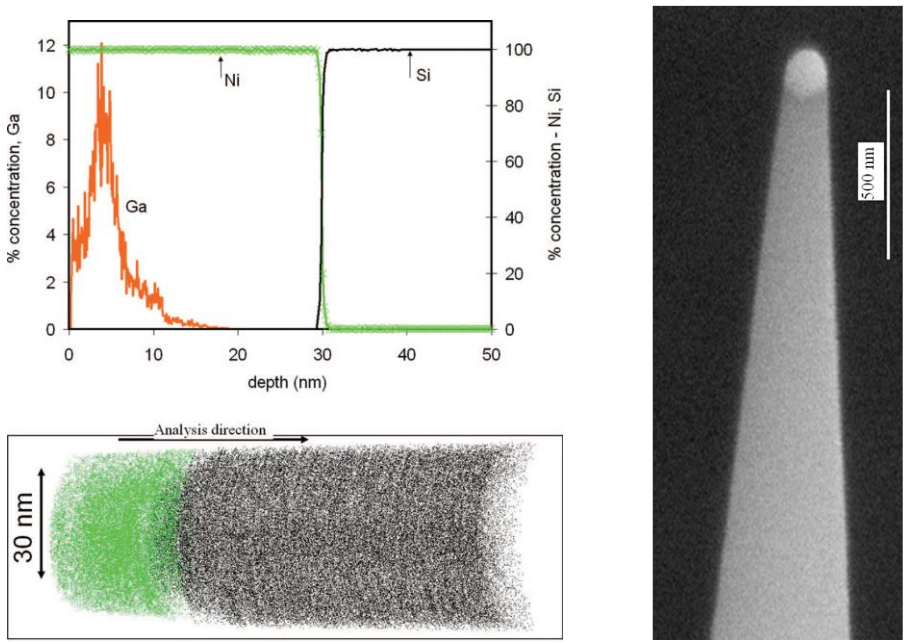


Figure 2.32 – Top left – Atom probe concentration profiles of gallium, nickel and silicon in a nickel capped, FIB milled silicon sample. Bottom left – Atom map of atom probe sample with nickel capping layer (green) and silicon (black). Right – SEM micrograph of silicon atom probe tip (grey) with intact nickel capping layer (white) [199].

The selection criteria for these capping layers are material specific but generally, good adhesion to the substrate [200], a similar evaporation field to the substrate [201] and

sufficient SEM contrast [202] are required to facilitate the retention of a small amount of capping layer in the finished atom probe sample.

Analysis through these capping layers can lead to evaporation and reconstruction artefacts due to the different evaporation field requirements of the materials from each layer [203]. At the transition point between the two layers, the species from the top layer will cease to be detected and the species from the bottom layer will start to be detected in a ring at the outer edges of the detector map. This ring will slowly expand inwards until it covers the entire detector and equilibrium evaporation is regained (Figure 2.33).

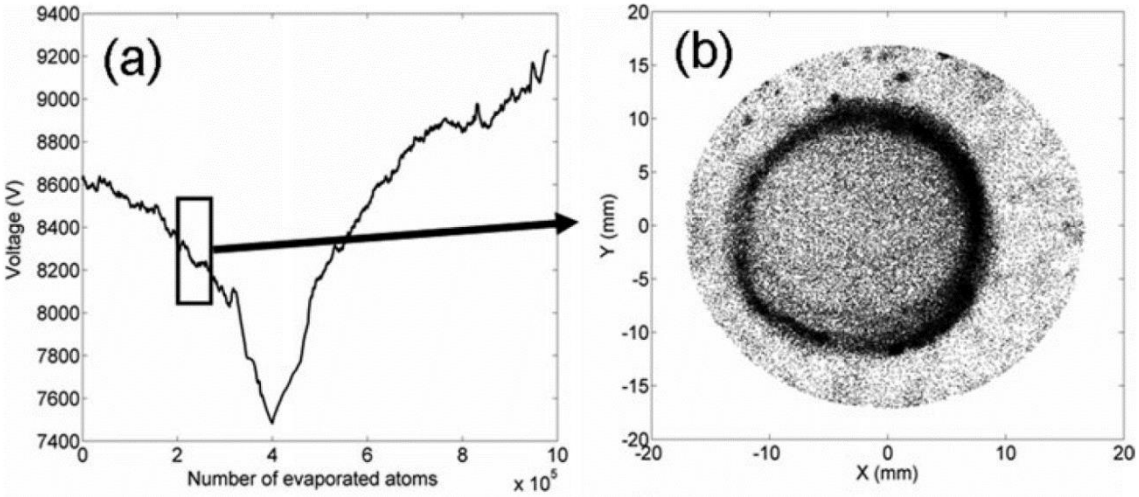


Figure 2.33 – Left –Number of atoms detected whilst analysing through an interface. Right – Detector hit map pattern before equilibrium evaporation is regained [203].

2.5.6 Atom probe analysis of semiconductor materials

Due to advances in FIB based sample preparation [6] and the increased availability of commercial laser pulsed atom probe systems, APT of electronic materials and devices has greatly increased over the last decade [204] [205]. A large proportion of these analyses have been carried out on silicon materials and devices due to the interest from the

semiconductor industry [4]. FIB based site specific sample preparation for atom probe is becoming a more routine procedure for semiconductor materials and devices [206]. With improvements in the field of view available in modern atom probes [167], individual nanoelectronic devices can be analysed within a single sample volume [5] [207] (Figure 2.34).

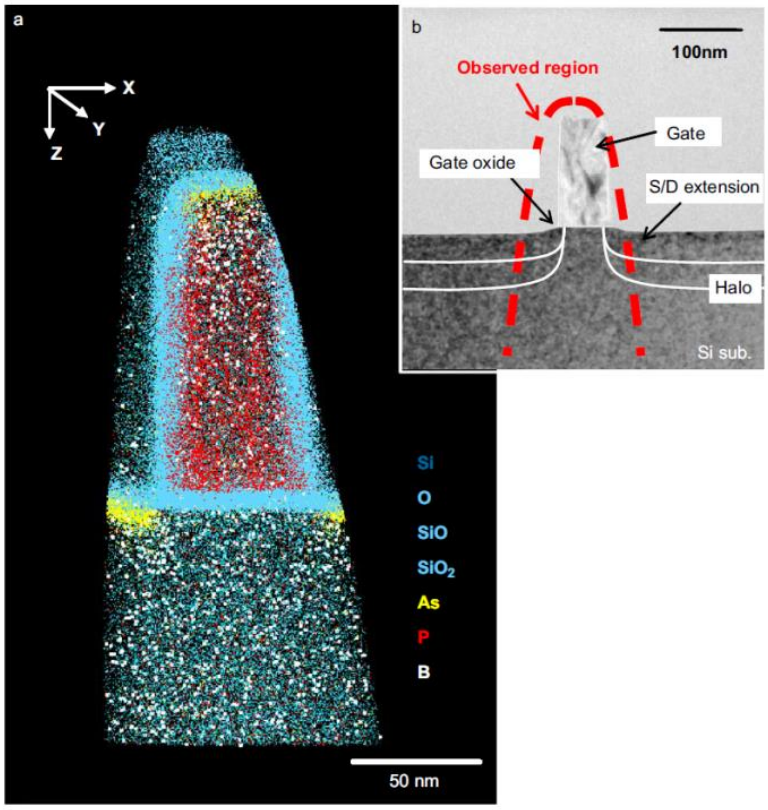


Figure 2.34 – Dopant distributions within an n-type Metal Oxide Semiconductor Field Effect Transistor device. Inset – TEM micrograph of same structure [5].

Analyses have been carried out on MC silicon in order to determine the extent of transition metal segregation to grain boundaries in order to optimise methods of improving efficiency in silicon photovoltaics [106]. Nanoscale segregation of iron species to grain boundaries in solar grade MC silicon has been directly observed [208]. Atom probe analyses have also been carried out on non silicon semiconductor materials such as GaN

[209] , germanium [210] and related structures such as quantum wells [211], quantum dots [212] and nanowires [213]. Atom probe analyses of implanted arsenic profiles (Figure 2.35) with peak concentrations of 10^{20} at/cm^3 at ~ 80 nm compare well with the industry standard technique of SIMS [214].

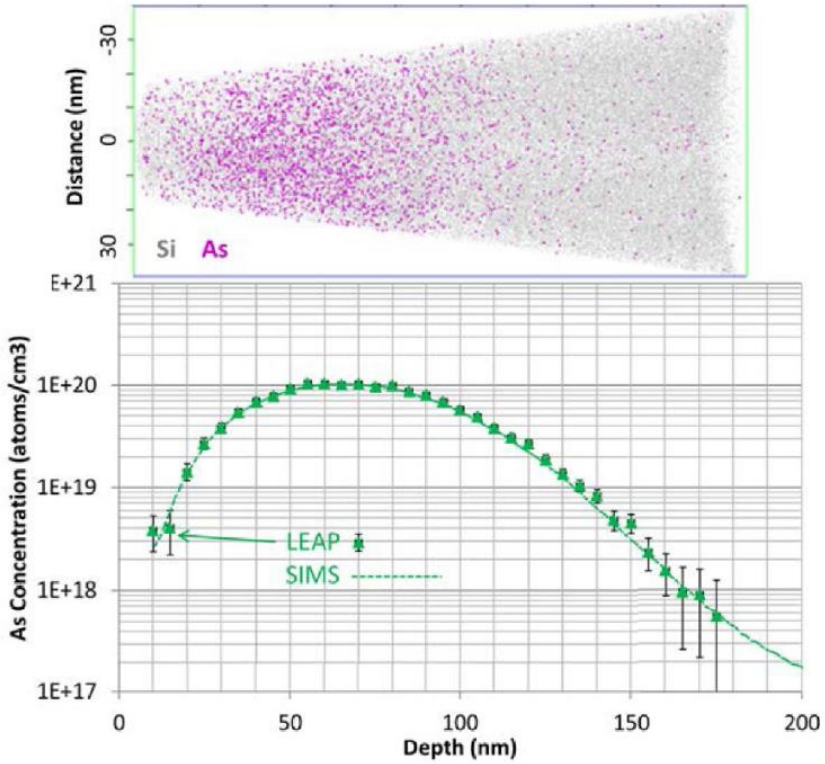


Figure 2.35 - Comparison of SIMS and atom probe profiles of arsenic ion implant in silicon [214].

APT analyses of 200 eV boron ions implanted into a pre-amorphised substrate were shown to have sharper interfaces than SIMS analyses, with peak concentrations of ~ 10^{21} at/cm^3 within tens of nm of the surface [215]. Due to the much smaller volumes of material that are analysed using APT, it is not be able to achieve the level of concentration sensitivity possible using SIMS, nor can it or be able to extend to the same depth in bulk analysis. However, modern APT can give 3D characterisation on specific nanoscale volumes with an unparalleled combination of spatial and chemical resolution [163] and superior depth resolution to SIMS in the surface regions [216].

3. Surface sensitive FIB sample preparation and APT analysis

3.1. Standard approach to Focused Ion Beam sample preparation

A standard approach to Focused Ion Beam (FIB) based atom probe sample preparation both from “bulk” regions and site specific regions [6], has been developed and widely adopted by the field. This has been shown to be viable for application to the vast majority of material systems, but there are still significant improvements that can be made, particularly when analysing low concentration species within regions that are at, or are within tens of nm from, the surface.

Detailed atom probe analyses will often be carried out on sub-volumes of the collected data rather than using the entirety of it [217]. The data collected from the surface regions often suffer from artefacts that make the data quality less than optimum and therefore these regions are often discarded from detailed analysis [194]. Some of these artefacts are a function of the atom probe technique and the material system being analysed, while others can be linked to choices in the experimental setup in terms of sample geometry [180] and analysis parameters [218]. Sample preparation choices will impact the range of viable analysis parameters and therefore need to be optimised in an iterative manner.

3.1.1 Known artefacts affecting APT surface analysis

1) Hydrogen [219] and other adsorbed gas species are present in high quantities in the surface regions.

Desorbed hydrogen can form complex ions with species from the sample matrix to give mass spectra overlaps in the form of silicon hydride $(^{30}Si^{1}H)^{+}$ and phosphorus $^{31}P^{+}$ at 31 Da. This has been linked with FIB based surface damage from the final low energy 'polishing stage', and potentially from retained material that was damaged from the initial high energy milling [6] that has not been removed by the final polishing stage [196].

2) Large variation in required standing voltage due to large changes in tip size during initial stages of analysis [1].

Levels of signal background, due to uncorrelated field evaporation, and charge-state ratios, due to increased fields, will change with increases in standing voltage. As the initial stages of analysis will have the greatest change in tip diameter over the shortest time, these effects are most prominent in the surface regions.

3) Analysis through the region of interest prior to optimum local electrode alignment, laser alignment and equilibrium evaporation.

If the region of interest is extremely close to the surface of the finished atom probe tip, then it is possible that those ions can be evaporated prior to optimum local electrode (and laser) alignment. It is standard practise to only include data in the reconstruction after all physical motion and laser alignment has completed in order to prevent this from affecting data quality. Non-equilibrium evaporation across the surface of the specimen before it has formed a steady-state shape prior to the analysis of the region of interest can also alter the final reconstruction [203].

4) Removal of region of interest through FIB milling

If the region of interest does not have a significant difference in contrast in SEM during the final stages of the FIB milling then either excess material must be left in order to ensure that is retained or it may be accidentally removed [220].

3.1.2 Current state of atom probe FIB based sample preparation

The current state of FIB based atom probe sample preparation is based around the 'lift-out' technique that was adapted from FIB based Transmission Electron Microscopy (TEM) lamella preparation [138]. Whilst the now standard lift-out procedure has been covered extensively in the literature [6] [194] [139], it is still useful to outline the stages in full in order to demonstrate the reasoning behind each of the stages and the parts of each that may need to be altered in order to optimise them toward the analysis of surface species. The stages are:

1) Find the location of a feature of interest on the surface via SEM. This can simply be a clear area free from debris or a more specific feature such as a grain boundary [221].

2) Deposition of a protective layer of low milling rate material from a gas injection system (GIS) and decomposed by electron beam or FIB onto the specific region required [222]. The choice of material [222], type of deposition and amount of material deposited [6] is dependent on the material system to be analysed and the milling conditions used in the subsequent stages. For this stage, the main requirement is that the material mills at a lower rate than the initial material in order for it to protect the sample during subsequent trench milling stages. The types

of materials used are usually low milling rate, conductive layers of tungsten or platinum containing compounds [222].

3) Trenches are milled underneath the region delineated and protected by the layer deposited in stage 2. Higher beam currents result in faster milling and reduced spatial precision whilst lower currents allow higher precision at the cost of decreased milling rates. Higher milling currents will also have correspondingly larger beam spots [223], the edges of which can potentially impede upon the protected strip and thus potentially remove it prior to the trenches being completed.

4) Lift-out from the surface using an in-situ micromanipulator [6].

5) Attaching the lift-out bar onto a support structure using further GIS deposited material and detaching a section or 'wedge' to be left behind on the support. This deposited material must also be suitable for subsequent atom probe sample analysis in terms of adhesion, thermal and electrical conductivity [200].

6) Ring milling or annular milling to shape the lift-out wedge into the required shape and size for APT. This is usually carried out using high voltage ions (30 kV) and high currents in order to decrease milling times.

7) Removal of any remaining protective deposited layer through low energy(5 kv – 2 kV) FIB milling (this stage is often referred to as 'polishing') and removal of any subsequent material that may have been damaged through the initial milling stages [196].

The main aspects of this process that inhibit analysis of surface regions are those involving the GIS based deposition of protective layers and their subsequent removal prior to atom probe analysis. In order to protect the surface regions, modifications need to be made to the standard procedure to protect the surface during FIB milling, whilst also enabling the surface to be delineated in the reconstructed atom probe volume [199]. This can be carried out through the deposition of a layer of material which is not completely removed during the final tip polishing stage and is designed to be part of the analysed volume.

The term ‘capping layer’ will be used to denote this retained and undamaged material designed to delineate and preserve the surface as opposed to ‘protective layer’, which will be used to denote material which is used to protect the capping layer/substrate interface and is removed prior to APT analysis. This choice of the capping layer material is application specific and requires good adhesion, similar evaporation field requirements to the substrate and SEM contrast to facilitate sample preparation. High purity nickel was used as a capping layer material for some of the samples used in this thesis as it has a similar evaporation field requirement to silicon and has been used in the literature as a capping layer in silicon [199]. High purity cobalt (which has a single, stable isotope in the form of ^{59}Co as compared to the multiple stable isotopes of nickel), also has a similar evaporation field requirements to silicon [1] and was used in order to reduce potential mass spectra overlap issues between the capping layer and substrate.

3.1.3 Optimisation of FIB for surface sensitive applications

The use of tailored capping layers deposited in-situ or ex-situ to the FIB milling process has previously been investigated with regards to atom probe analysis and has been discussed throughout the literature [198] [200]. However, such deposited materials are often not used for systems where the regions of interest are in direct contact with the capping layer and are within tens of nanometres of the surface. Capping layers do not prevent the accurate detection of surface species unless there are mass spectra overlaps between the two but capping layer materials without overlaps may not always be feasible. For the surface and near surface analysis of materials via atom probe an optimisation procedure is required, both during pre-FIB sample preparation and during FIB-based preparation. This must incorporate the following:

- Selection of substrate to maximise visibility of regions of interest/species of interest.
- Selection of capping layers.
- Selection of capping layer deposition method.
- Selection of surface region to be used for atom probe analysis.
- Selection of protective layer deposition parameters via electron beam and FIB decomposition of GIS material.
- Selection of FIB milling and tip shaping parameters.
- Selection of low kV FIB polishing parameters such that the optimal amount of undamaged capping layer material remains in a viable APT sample.

The end result will be an atom probe tip that has the following characteristics:

1) A final shape that is suitable for atom probe analysis with a tip diameter less than 100 nm.

2) A capping layer sufficiently thick to give enough time for tip alignment with laser/local electrode and allowing equilibrium evaporation before transitioning to the sample surface.

3) A capping layer which is thin enough to allow a transition to the substrate at a voltage suitable for observing all the species of interest in the surface regions of the substrate.

4) All FIB damage constrained to the capping layer with no/little measurable gallium damage at the interface or surface regions.

3.1.4 Atom probe analysis of surface regions

During atom probe analysis, the following characteristics should be used as indicators to the quality of the data obtained and the likelihood that the interface region has been successfully analysed through without specimen failure or other damage:

- A smooth voltage curve over the region of the capping layer/surface interface, ideally combined with a visual confirmation of a smooth transition from one material to another on the detector map. This transition is often observed through a sudden drop in evaporation combined with a change in standing voltage and the

appearance of a ring of the new material at the edge of the detector map. This will slowly spread towards the centre of the detector map and then regain equilibrium evaporation [203].

- Uniform evaporation detected across the entire 2D detector map.
- Uniform analysis conditions when analysing through the interface region in order to try and minimise the change in data quality, impact of variation in electrostatic field experienced and potential equilibrium evaporation change [224]
- The transition from capping layer to sample surface to occur at a voltage sufficient to allow visibility of the mass-to-charge-state ratios of the species of interest, including higher mass-to-charge-state ratio complex ions.
- Standing voltage at the transition between capping layer low enough such that the background contributions can be minimised.

Both material systems under analysis in this work share a large number of requirements, therefore a number of optimisation stages need to be explored. Lift outs from both planar silicon substrates and FIB sharpened pre-fabricated silicon micro posts were used in this thesis.

In order to improve the viability of atom probe analysis of implantation profiles of phosphorus into single crystal silicon which is shown in Chapter 4, it was decided to use higher conductivity natural isotopic abundance silicon substrates. This is particularly an issue when considering atom probe analysis using high wavelength lasers such as the 532 nm green laser used in the LEAP 3000X HR system available in the Oxford Atom Probe Group at the beginning of this project, as laser pulsing with a green laser has shown to give thermal artefacts on insulating substrates [225].

Additionally, it was decided to investigate if sample preparation can be facilitated through direct implantation into pre-fabricated supports and how this compared to the standard planar atom probe analysis. These planar substrates are in the form of commercial 3 mm x 7 mm single crystal silicon micro post arrays available from Cameca. They are doped with antimony to < 0.1 Ohm-cm resistivity and are available in two configurations, flat top posts with an end diameter of approximately two microns that are used as supports for atom probe lift-out samples, and pre-sharpened micro posts with an end diameter of ~ 50 nm for local electrode alignment calibrations [226]. All samples for the investigation into phosphorus, oxygen and iron co-segregation in single crystal silicon in Chapter 5 required planar lift outs.

Sample preparation optimisation stages were first carried out on planar substrates and then applied to the micro posts to determine if they were suitable for these high aspect ratio structures. 36 micro post arrays also contain three larger posts which present to act as fiducials during local electrode alignment (Figure 3.1). A single flat top micro post is shown in Figure 3.2.

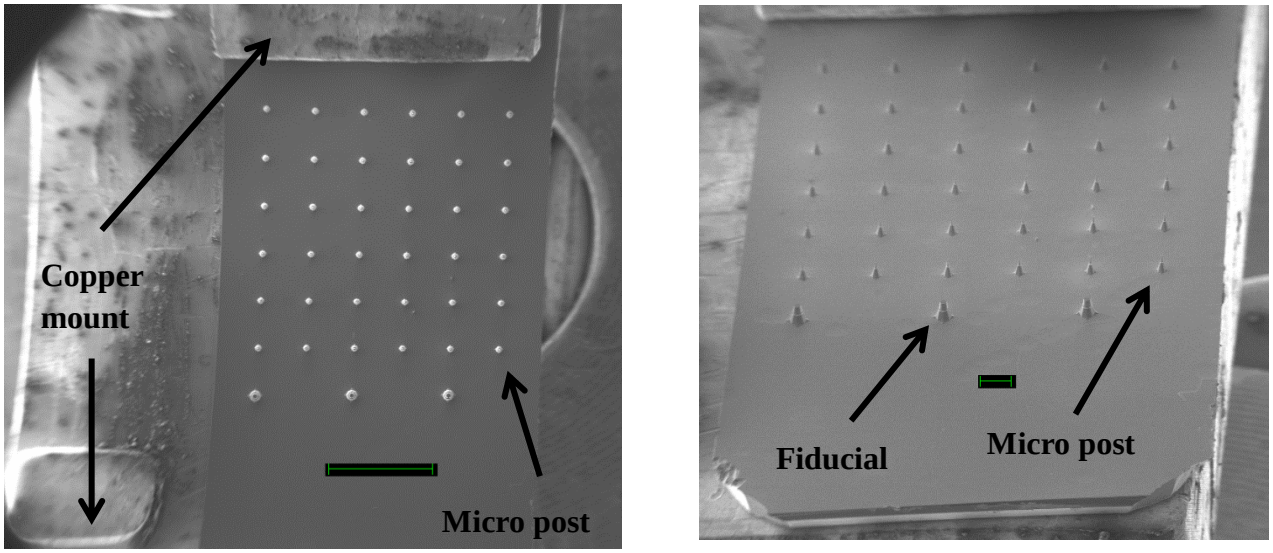


Figure 3.1 – Left – SEM micrograph of silicon micro post array placed onto an atom probe suitable mount. Scale bar 1 mm. Right – SEM micrograph of silicon micro post array with visible flat top posts and fiducials. Scale bar 200 µm.

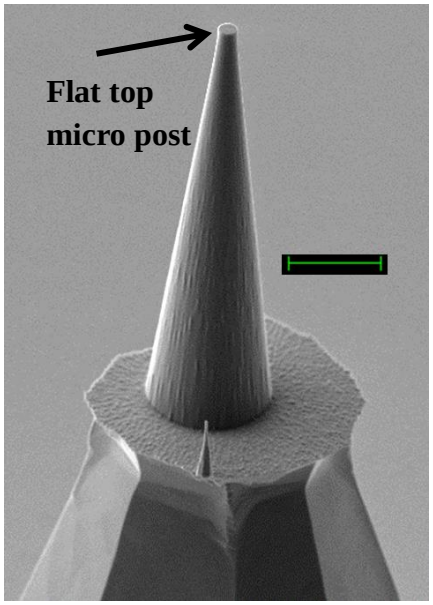


Figure 3.2 – Single silicon flat top post. Scale bar 10 µm.

The order of optimisation was as follows:

1) Optimisation of available capping layer materials and deposition methods.
2) Optimisation of FIB based sample preparation.
3) Optimisation of LEAP based analysis parameters.

3.2 Surface preservation and delineation

3.2.1 Thermal evaporation of nickel and cobalt capping layers

Thermal evaporation is a Physical Vapour Deposition (PVD) thin film coating process that uses high temperatures to deposit uniform, thin layers in the nm range from a pure source onto a surface [8]. This is carried out in high vacuum environments to increase the mean free path of the evaporated material and to prevent contaminants affecting the deposition. The pure metal sources are placed into vessels or 'boats' before being heated to the required temperature for evaporation through resistive heating. Molybdenum evaporation boats with an alumina coated centre (Testbourne, part number ME9-A0-Mo) as shown in Figure 3.3, were used in order to stop the nickel and cobalt from alloying with the tungsten boat at the high temperatures required for thermal evaporation and causing it to melt due to the resultant reduction in melting point of the new alloy. The thermal evaporator used for coating samples shown in this thesis was custom made and consisted of a glovebox containing a vacuum bell jar with samples being loaded through a nitrogen purged load lock. This bell jar was pumped down with a rotary pump and backed with an oil pump.

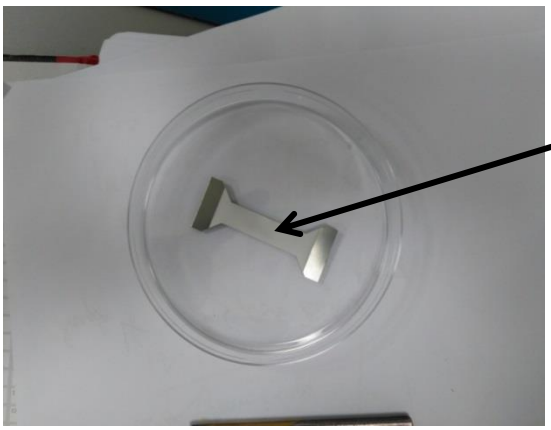


Figure 3.3 – Molybdenum evaporation boat with white alumina centre in petri dish. Total boat length is 1 7/8 inches (~ 47 mm) with a 1 inch reservoir for source metals.

Despite the coating, evaporation boats melting at high currents before sufficient deposition had occurred was the main limiting factor in the thickness of material that could be deposited. The available equipment was able to hold three such boats at any one time and it was found that, in order to ensure the thickness required (100 - 200 nm) was deposited, all three boats would be required consecutively. These boats were placed into the thermal evaporator and connected between high current terminals, a metal source was then placed into the centre of the boat in the form of high purity wire (99.99% purity). The silicon samples were stuck to glass slides using a polyimide tape (Kapton) with the areas to be coated with metal left exposed. This glass slide was then stuck to a metal support, as demonstrated in Figure 3.4, and placed inverted some tens of centimetres above the evaporation boats.

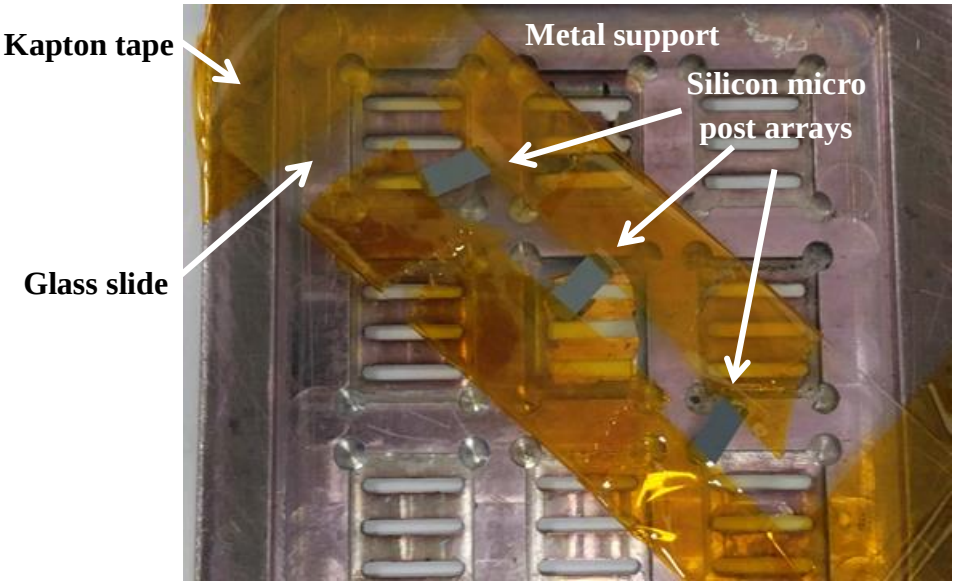


Figure 3.4 – Silicon micro post arrays prior to thermal evaporation, on a standard 75 mm x 25 mm glass slide stuck down using Kapton tape. Metal backing used purely for support.

A glass bell jar was then lowered over the evaporation apparatus with a physical shield in between the boats and the samples to be coated. The system was evacuated to 10^{-6} torr over the period of approximately 12 hours using an oil diffusion pump backed by a rotary pump.

Once at the required pressure, evaporation of the metal was carried out by slowly raising the current passing through the evaporation boats. The following stages were observed:

1) An initial reduction in the vacuum due to evaporation of surface contaminants from the boat and the source metal. The vacuum was then allowed to recover to the previous level. The shield was in place during this stage in order to prevent the deposition of contaminants,
2) Detection of material on the in-situ quartz crystal microbalance. This indicates that evaporation of the metal was taking place.

3) The physical shield was then moved away from in-between the evaporation boats and sample.
4) The current was raised until the desired deposition rate was measured on the thickness monitor; this was aimed at 0.1 nm/s in order to promote a uniform deposited layer.
5) The current was continuously raised to maintain this deposition rate until no further deposition could be detected with increased current or the connection was lost due to failure of the evaporation boat due to it melting.

This procedure was repeated for each of the boats. After evaporation was completed, the samples, metal support and glass slide were removed from the thermal evaporator. The Kapton tape, now also coated with metal, was carefully peeled back from edges of the silicon samples, and the samples were removed from the slide, as shown in Figure 3.5. The samples were then mounted either onto SEM sample stubs or atom probe suitable copper clips. The physical transfer involved in sticking down and removing of the fragile atom probe arrays was a source of yield loss through damage to the posts

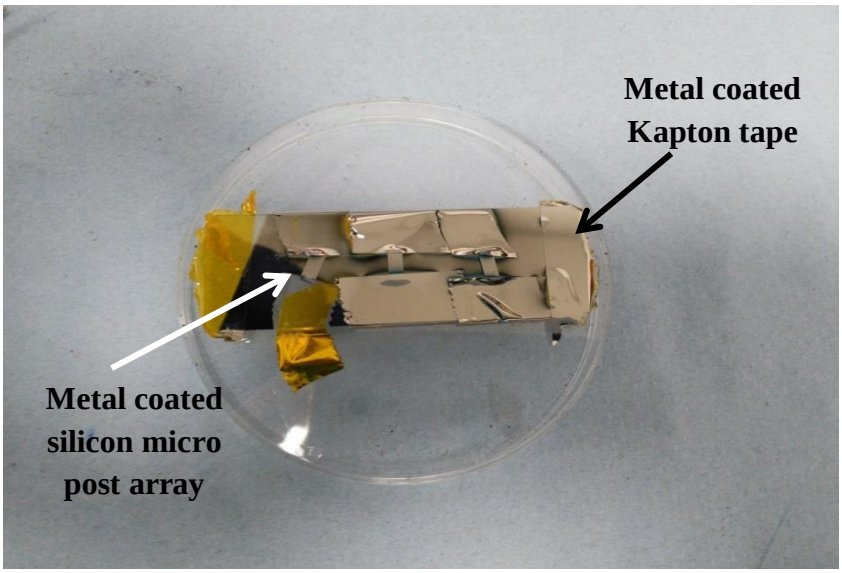


Figure 3.5 – Silicon micro post arrays on 75 mm x 25 mm glass slide from Figure 3.4, now coated with thermally evaporated cobalt.

SEM micrographs from cross sections made via FIB milling shows the uniformity and thickness of the deposited layers on the planar substrates (Figure 3.6).

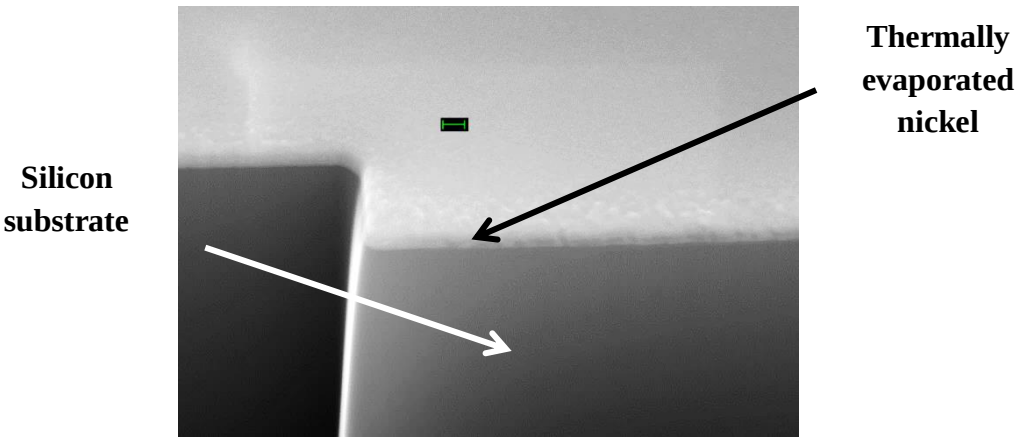


Figure 3.6– SEM micrograph of single crystal silicon substrate coated with ~ 200 nm thick thermally evaporated nickel. Tilt corrected at 36°. Scale bar 200 nm.

Since many images were taken with the sample tilted, a correction was made to the image to take this into account when giving length measurements and is noted in the figure caption when appropriate. Without this, the reported thicknesses of layers measured by SEM will not be accurate. It was found that the thickness reported by the in-situ quartz crystal microbalance were approximately one half to one third of the thicknesses measured by SEM. This was likely due to the difference in distance and orientation of the sensor within the evaporation chamber compared to the substrate, meaning that at least 50 nm of deposited material as measured by the in-situ quartz microbalance was required for the ~ 100 - 200 nm thickness required for the samples.

3.2.2 Electron beam and FIB deposition of protective layers via Gas Injection System

Electron beam deposition of tungsten was carried out on the thermally evaporated metal layer prior to FIB deposition of tungsten. This was to deposit an initial layer of tungsten through the non-damaging electron beam mechanism prior to FIB deposition of tungsten, as the latter has been shown to sputter the surface regions during deposition [222]. A typical silicon surface covered with thermally evaporated nickel can be seen in figure 3.7.

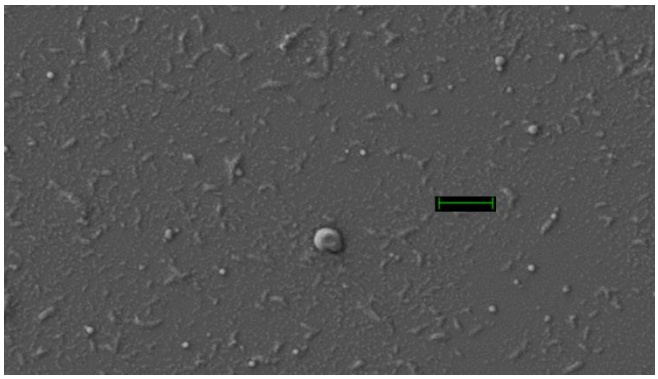


Figure 3.7 – SEM micrograph of single crystal silicon coated with thermally evaporated nickel before any GIS based deposition. Tilt correction at 36°. Scale bar 2 μm.

A reduced raster box was drawn in the SEM view to the dimensions required for the lift-out bar (25 µm x 5 µm) and exposed to a GIS stream of tungsten precursor gas for 20 minutes at a working distance of 5 mm (scan speed 8, line scan N=10) using a 5 kV electron beam at 0° tilt (normal to the SEM beam). The electron beam deposited material can be seen in Figure 3.8.

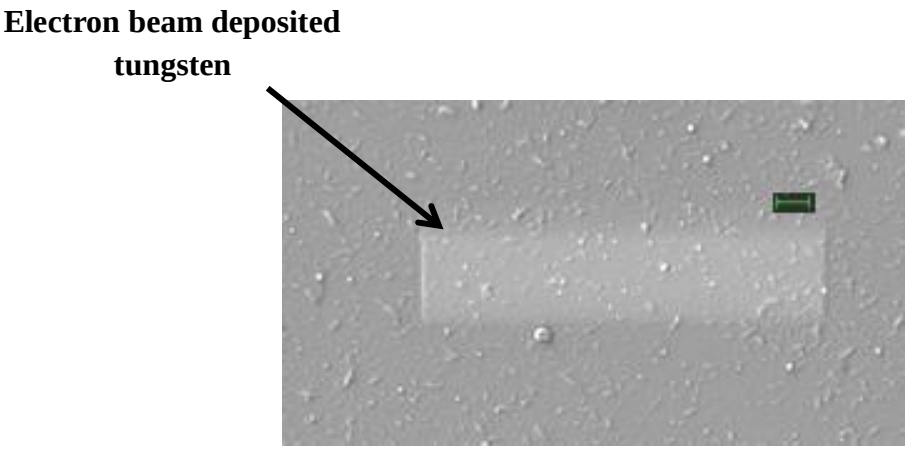


Figure 3.8 – SEM micrograph of single crystal silicon coated with thermally evaporated nickel after 20 minutes of electron beam GIS based deposition of tungsten. Scale bar 2 µm.

FIB-based deposition of tungsten was then carried out on the same region using a 30 kV beam at 150 pA current at 54° tilt (normal to the FIB beam) with a Pixel Fill Factor of 70% and a dwell time of 0.2 µs. The FIB deposited material can be seen in Figure 3.9.

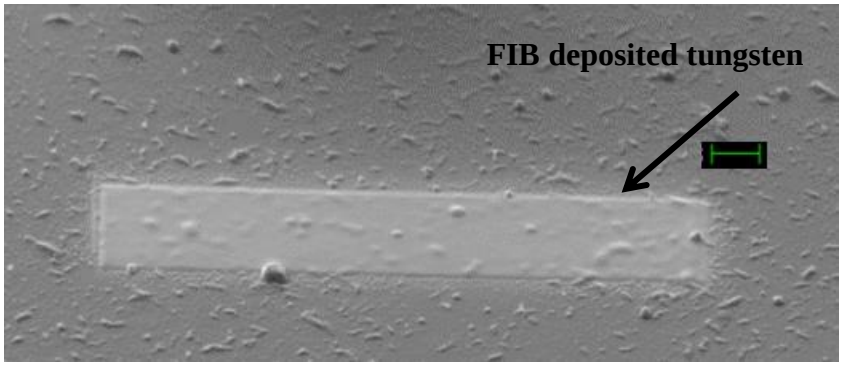


Figure 3.9 – Single crystal silicon coated with thermally evaporated nickel after 20 minutes of electron beam GIS based deposition of tungsten and ten minutes of FIB deposited tungsten. Scale bar 2 µm.

Damage to or removal of the ex-situ deposited layer of nickel would result in the underlying substrate potentially becoming unusable due to gallium damage. This approach of using both electron beam and FIB deposition can ensure the protection of the capping layer/sample interface throughout all stages of the sample preparation up to the final tip sharpening step.

For thicker ex-situ films, subsequent electron beam deposition of tungsten was unlikely to be as important in order to protect the capping layer/substrate interface, but, due to the variations in thickness of the layers deposited by the available thermal evaporation equipment, it was deemed a sensible precaution in all cases.

Additionally, the thickness of the thermally evaporated films was not easily controllable as the in-situ thickness monitor required extensive calibration; this was not possible due to time constraints. It was also not always possible to deposit from three boats due to the metal sources becoming dislodged or failing during melting.

Opening the vacuum chamber to replace sources or boats was not a possibility, as it would have produced a layer of oxidised material at the interface of the deposited layers. Therefore it was deemed prudent to develop a post FIB process deposition which would allow thin (~ 20 nm thick layers) and thick (~ 200 nm) layers to be deposited in order for the samples to survive through to the final stages of preparation. The FIB trenching parameters can be found in Appendix G. The final lift out bars can be seen in Figure 3.10 and 3.11.

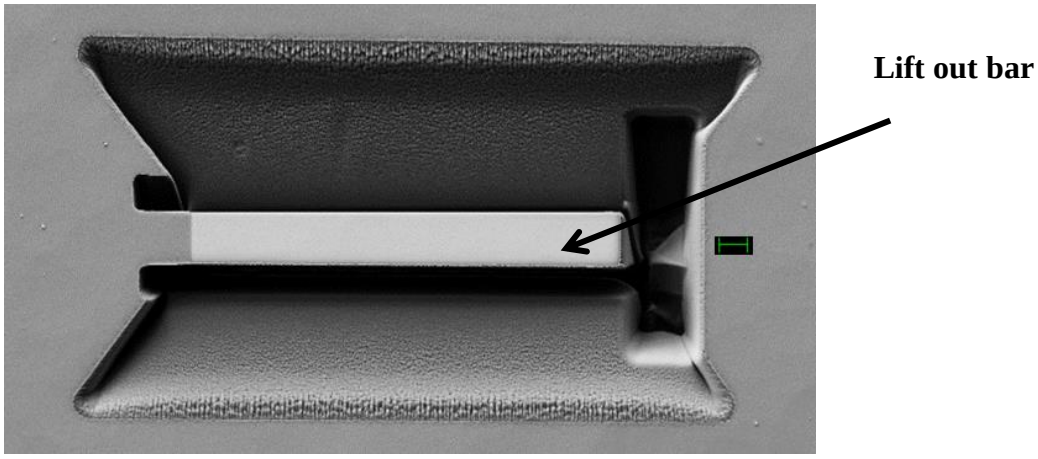


Figure 3.10 – Single crystal silicon substrate with ~ 200 nm of thermally deposited cobalt. Lift-out bar protected by ten minutes of electron beam tungsten deposition and 20 minutes FIB tungsten deposition. Scale bar 2 µm.

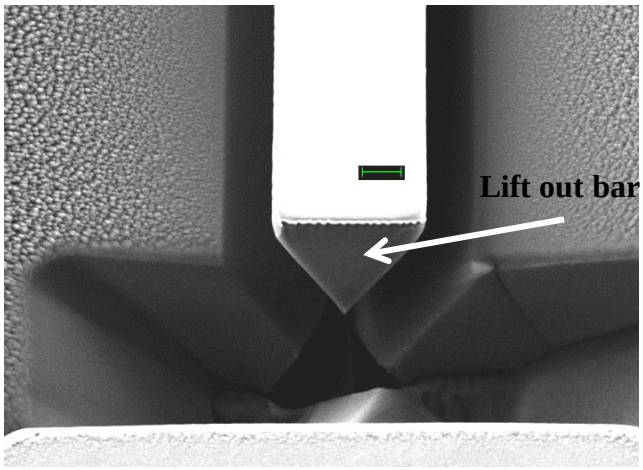


Figure 3.11 – Lift-out bar from figure 3.10 shown to be free of debris and ready to lift-out. Scale bar 2 µm.

3.2.3 Surface sensitive FIB milling of lift out samples

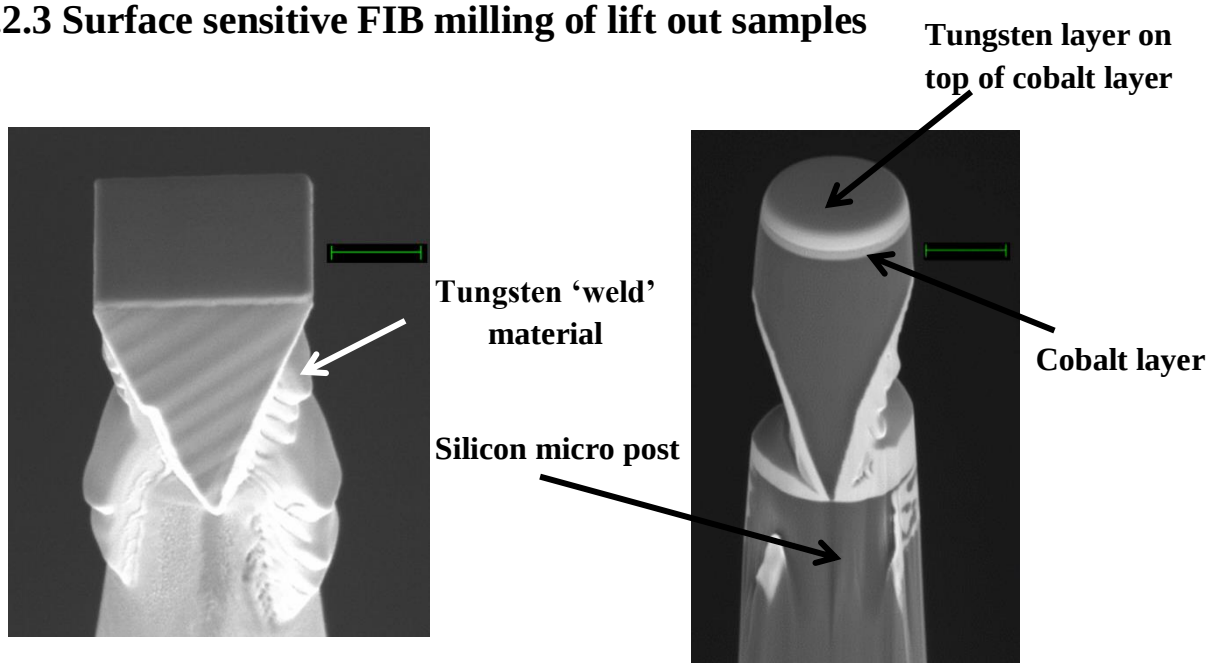


Figure 3.12 –Left - SEM micrograph of a completed lift-out sample on silicon micro post, scale bar 1µm. Right – SEM micrograph completed lift-out sample on silicon micro post after first stage of annular milling. Scale bar 1µm.

The corners of the lift out wedge were then removed through annular milling with an outer diameter of 5 µm and an inner diameter of 2 µm using a 30 kV 300 pA beam. This was carried out until the lift out wedge and the silicon post were of the same diameter (Figure 3.12). Further annular milling was then carried out to shape the tip, using an outer diameter of 5 µm and an inner diameter of 500 nm using a 30 kV 300 pA beam.

This milling was carried out until the diameter of the post at the capping layer /silicon interface is between 200 and 300 nm in diameter (Figure 3.13 – Left). The top of the post was then imaged using a 2 kV 250 pA beam to remove all but a small section of the cobalt capping layer [196], and to reduce the diameter of the tip to below 100 nm (Figure 3.13 – Right).

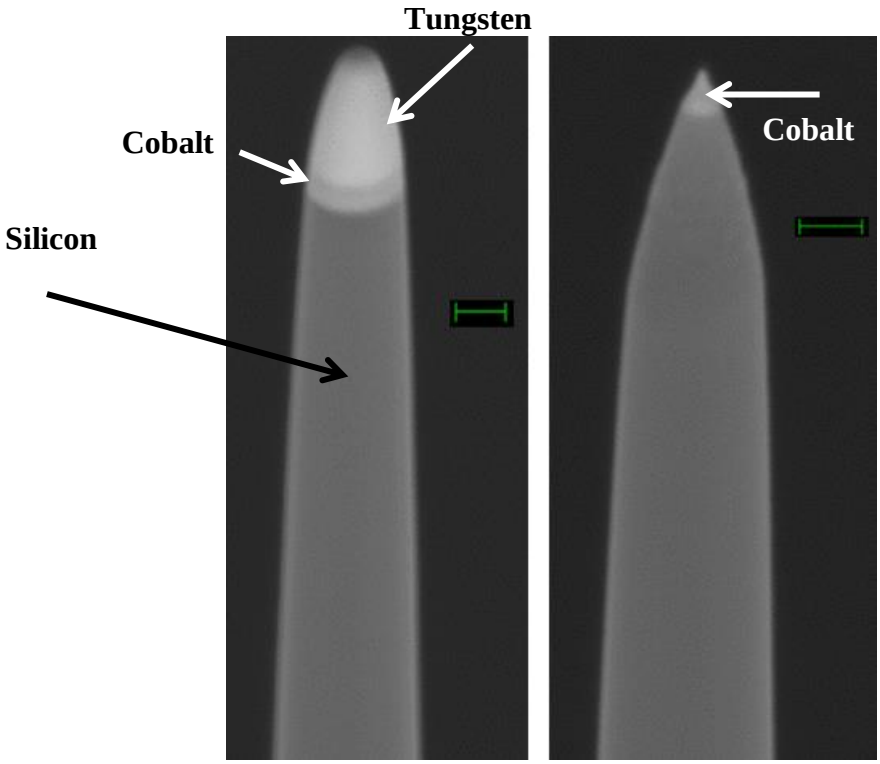


Figure 3.13 – Left – SEM micrograph of single crystal silicon post before low kV polishing stage. FIB and electron beam deposited tungsten and cobalt capping layer clearly visible. Scale bar 200 nm. Right - SEM micrograph of single crystal silicon post after low kV polishing stage. Tungsten layer removed but with cobalt capping layer remaining on thicker tip. Scale bar 200 nm.

At this length scale, the exact thickness of the capping layer is difficult to determine using SEM and so a small amount of variability is expected, however it was possible to optimise a capping layer thickness that can be linked to less than 500,000 detected ions of metal in the atom probe analysis (Figure 3.13 – Right)

3.2.4 FIB Sample preparation of flat top silicon micro posts

FIB based surface sensitive specimen preparation of the pre-fabricated flat top micro post was adapted from the surface sensitive lift-out procedure. The main change, as there was no requirement for trenching, lifting out and mounting samples, the entire process that must be completed was greatly reduced in time and required resources. The remaining stages are those of deposition of protective layers using GIS decomposed material and sharpening to a suitable size and shape for atom probe analysis.

The initial electron beam deposition of tungsten compound on the top of the micro post uses the same conditions as that used in Figure 3.8. Due to the greatly reduced area to be deposited on, a shorter deposition time was required. Two to three minutes of deposition was found to be sufficient in a box 2 µm x 2 µm based around the centre of the micro post (Figure 3.14)

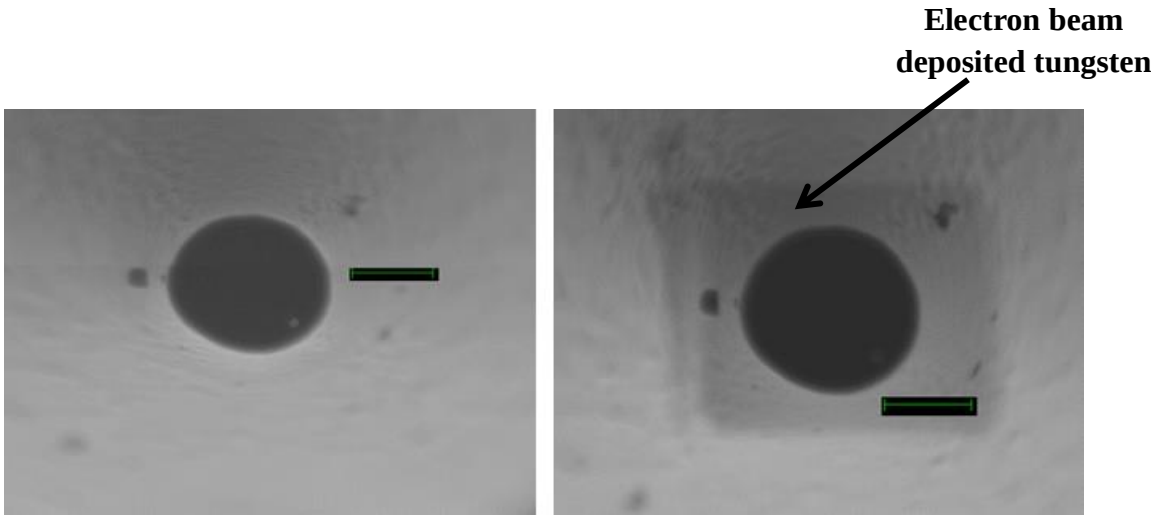


Figure 3.14 – Left - Top down SEM micrograph of silicon micro post capped with cobalt. Scale bar 1 µm. Right - Top down SEM micrograph of silicon micro post capped with cobalt, after 3 minutes of tungsten electron beam deposition. Scale bar 1 µm.

After electron beam deposition, FIB deposition was carried out on the same area with the stage tilted normal to the FIB beam (54º) for 2-3 minutes using the same conditions as used in Figure 3.11. The deposited material is clearly visible in a thick layer directly on top of the post and deposition can also be seen on the shank starting approximately 500 nm below the tip in Figure 3.15.

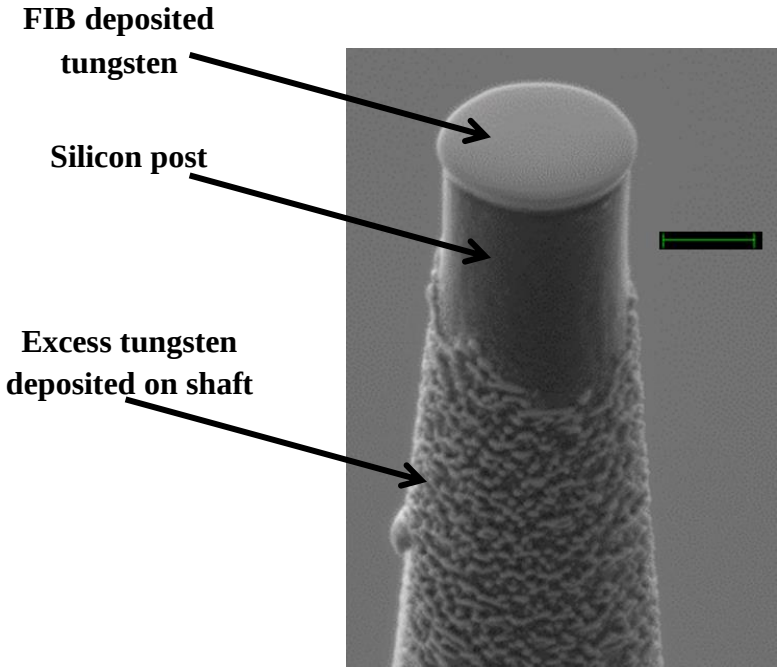


Figure 3.15 – SEM micro graph of single crystal silicon post capped with cobalt, after 3 minutes of tungsten FIB deposition. Scale bar 1 µm.

The milling conditions for the micro post sample were the same as that for the lift out sample but only required the second stage to form the tip. Annular milling was carried out on the micro post using an outer diameter of 5 µm and an inner of 500 nm using a 30 kV

300 pA beam. This milling was carried out until the diameter of the post at the thermally evaporated metal capping layer interface with the silicon was between 200 and 300 nm (Figure 3.16 – Left).

Low kV polishing was then carried out using an imaging mill until all the tungsten had been removed from the tip. Only a small amount of thermally evaporated capping layer was found to be visible and the tip diameter was less than 100 nm (Figure 3.16 – Right). These can be seen to be very similar in size and shape to those made from lift out samples (Figure 3.13) and indicates that this approach is suitable for sample preparation from silicon micro posts.

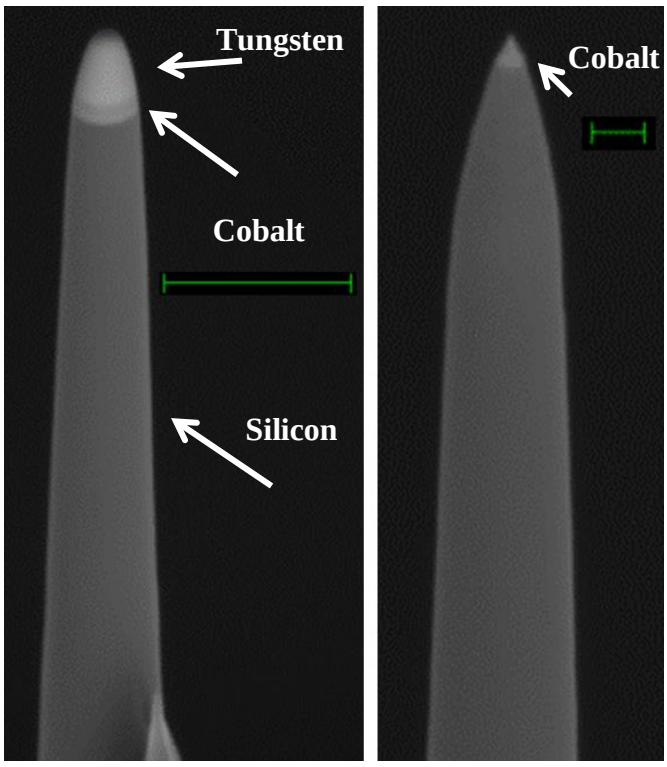


Figure 3.16 – Left – SEM micro graph of single crystal silicon post capped with cobalt, 2 minutes electron beam tungsten deposition and 3 minutes FIB tungsten deposition. Scale bar 1 µm. Right – SEM micro graph of Single crystal silicon post with small amount of cobalt capping layer remaining after 2 kV FIB polish. Scale bar 200 nm.

It was found that thermal deposition of thin films (~ 200 nm) of pure nickel or cobalt onto silicon surfaces, followed by electron beam/FIB deposited tungsten and optimised FIB liftout and milling using the parameters explained in the above sections gave repeatable and undamaged analysis of the capping layer/silicon interface. Further adaption of this process to flat top silicon micro-posts was also found to be viable.

3.3 Optimisation of atom probe analysis parameters

3.3.1 Parameters for yield

Once the sample preparation was been carried out in the manner appropriate for surface sensitive materials as described above, there are a number of considerations for selecting the initial parameters for atom probe analysis in order to ensure surface delineation, surface preservation and optimal data collection. There must be no gallium damage in the interface region between the capping layer and substrate, or in the region of the substrate below the capping layer. There must be equilibrium evaporation of the capping layer prior to the analysis of the interface region. The transition between capping layer and substrate should, ideally, be a gradual process as opposed to a single instantaneous event. This is to prevent micro fractures, which can be sometimes observed at such a transition event along with a sudden change in composition and increase in required voltage, from being interpreted as a real transition through the interface.

Two main priorities of atom probe analysis are yield and data quality. Atom probe yield is often considered to be mainly through reducing likelihood of sample fracture and maximising the amount of collected data. However when analysing systems that only have a small volume of interest, yield can be redefined to include the parameter of requiring that

volume to be present [7]. For analysis of a multilayer system using atom probe, there may be separate optimal analysis conditions for each layer, in order to maximise data quality and yield. These are typically due to the difference in evaporation field requirements for the different layers which can lead to poor quality data or sample fractures if analysis parameters are not changed to compensate [203]. If too many parameters are simultaneously changed then it can be difficult to directly compare between the different layers, therefore the variations are minimised where possible.

3.3.2 Optimisation of detection rate

The detection rate is defined as a percentage of how often a pulse event (voltage or laser) is linked to a detection event. For high frequency pulsing at 200 kHz, a detection rate of 0.5% indicates that of the 200,000 pulses per second only 0.5% resulted in a detected event [7]. Maintaining a constant detection rate is often considered to be important to obtaining comparable data from different regions and is used as an inline control metric through varying the standing voltage. This allows gradual, automatic increases in standing voltage to maintain a set evaporation rate as a function of increasing tip diameter and also allows the standing voltage to be raised and lowered automatically whilst analysing through different layers. However, as voltage induced stress is known to be a factor in sample fracture, this can lead to decreased yield when attempting to analyse materials with high evaporation field requirements [1].

3.3.3. Optimisation of laser energy

In the case of using a capping layer with a similar, but not identical, evaporation field requirement to the substrate, the laser energy can be altered to allow evaporation of the often higher field capping layer whilst preventing the standing voltage from reaching too high a level [200]. Usually this approach is used to remove residual high field GIS deposited material from the surface using high laser energies before the laser energy is reduced to optimal levels for the analysis of the substrate. During this process, there will be an interface region where the higher laser energy will be used to evaporate material of interest and after the laser energy has been reduced, there will also be a region where the equilibrium evaporation shape of the specimen will be altered [203].

In those cases where there is a region of interest extremely close to the surface, such that they can spatially overlap with the above interface region, this variation in laser energy can cause changes in observed ions and their location. Therefore attempts should be made to minimise this as a function of variation in laser energy through these regions. One method is to keep the laser energy used for analysing through an interface constant. This requires the selection of parameters that can allow the analysis of both the capping layer material and the substrate with minimal changes in the mass spectra.

Variation in laser energy can also cause changes in mass spectra such as the mass-to-charge state ratio relative abundances and the proportion of species detected as complex molecular ions, with higher laser energies increasing the likelihood of singly charged ions and complex ions, especially in the regions close to the laser incident side of the specimen [227]. Depending on the species of interest, this can be used to increase the visibility of low concentration peaks with potential for mass spectra overlaps through shifting the charge state ratios into a mass-to-charge-state that is less obscured by majority species. An

example of this would be to increase the visibility of iron mass spectra peaks in a silicon matrix by increasing the laser energy such that the $^{56}Fe^{+}$ ion was preferentially evaporated over $^{56}Fe^{2+}$, which has a major overlap at 28 Da with the majority matrix species of $^{28}Si^{+}$.

3.3.4 Optimisation of pulse frequency

As a general approach, the pulse frequency used in atom probe analysis should be as high as possible to increase data collection rates and reduce the increased effect of field evaporated noise and hydrides, but low enough to reduce excess multiple detection events and allowing the visibility of high mass/charge ratio species [7]. Pulse frequencies will also have an effect on measured hydride species that are produced from hydrogen within the analysis chamber. As the rate of hydrogen adsorption is constant during analysis, increased pulse frequency will reduce the amount of hydrogen species detected per pulse [219].

3.3.5 Optimisation of base temperature

Atom probe analysis sample temperatures should be kept as low as possible to improve spatial resolution whilst not impacting yield [224]. Decreased base sample temperatures will reduce thermally induced surface migration of atoms and thereby increase the lateral resolution. However, reduction in temperature can also increase the samples brittleness and reduce yield. This is especially important in those materials that are already brittle or damaged through irradiation or ion implantation.

3.4.6 Analysis limiting artefacts

The two material systems to be analysed in this work are based on single crystal silicon but have different chemical species of interest. If it is assumed that the optimised sample preparation is carried out and the capping layer/substrate interface is intact during analysis, the system will have the following (but not exhaustive list) list of potential analysis-limiting artefacts that can arise as a function of the material system and of the experimental analysis parameters.

Ion implantation of phosphorus into single crystal silicon:

- Mass spectra overlaps between silicon hydride $(^{30}Si^{1}H)^{+}$ and phosphorus $^{31}P^{+}$ at the 31 Da peak.
- Mass spectra overlaps between silicon thermal tails and phosphorus between both $^{31}P^{+}$ and $^{31}P^{2+}$ charge states at 31 Da and 15.5 Da respectively.
- Mass spectra overlaps between phosphorus and the species in the metal capping layers used in both single ions and complex ions.
- Background noise preventing identification of low signal phosphorus peaks.

Surface segregation of iron after phosphorus diffusion in iron contaminated single crystal silicon:

- Mass spectra overlaps between silicon $^{28}Si^{+}$ and iron $^{56}Fe^{2+}$ majority species at 28 Da.
- Mass spectra overlaps between complex silicon ions $^{28}Si_2^{+}$ and iron $^{56}Fe^{+}$ at 56 Da.
- Mass spectra overlaps between silicon oxide species $(^{28}Si_2{}^{16}O)^{+}$ and$(^{56}Fe^{16}O)^{+}$iron oxide species at 36 Da.
- Background noise preventing identification of low signal iron peaks.

4. Atom probe analysis of low concentration, near surface ion implantation of phosphorus in single crystal silicon

This chapter presents a number of representative atom probe analyses of implanted micro posts and lift outs that were analysed using LEAP 3000X HR and LEAP 5000 XR atom probe systems supplied by Cameca. The LEAP 3000X HR has a detection efficiency of 37% and uses a green laser with a wavelength of 532 nm. The LEAP 5000 XR has a detection efficiency of 52% and uses a ultra-violet laser with a wavelength of 355 nm.

APT analyses of semiconducting materials using UV wavelength laser pulsing as used in the LEAP 5000 XR system have been shown to give improved mass resolving power compared to that of green laser pulsing [3]. The improved detector efficiency will also improve the signal to noise ratio of lower concentration species within the reduced volumes predicted by the implantation conditions used here.

The mass spectra and measured implantation profiles are shown for each sample are discussed and compared as function of a variety of changes in processing and analysis parameters. Comparisons with simulations via Stopping and Range of Ions In Matter (SRIM) [82] profiles are also made.

4.1 Description of analysis approach

There are two main questions asked in this chapter. Firstly, is atom probe tomography (APT) a viable analysis method for the characterisation of depth profiles of low

concentration, low energy phosphorus ion implantation into single crystal silicon? Secondly, can these implants be made into pre-fabricated silicon micro posts instead of standard planar substrates to reduce sample preparation time and what effects does this have on the measured profiles?

There is sufficient open space between and around these posts to allow standard, planar APT sample preparation via Focused Ion Beam (FIB) lift out techniques [6] to be carried out for comparison purposes. The doses used in these samples are all above the limit at which transient enhanced diffusion is expected, which approximately corresponds to a peak concentration of 0.05 at.% [228]. The extent of this diffusion is influenced by the dose implanted, with higher doses leading to greater interstitial formation and an increase in transient enhanced diffusion [229]. In order to determine the effect of Rapid Thermal Anneal (RTA) processing, comparisons of phosphorus profiles before and after RTA are given where available.

SRIM simulations of 14 kV phosphorus implantation into single crystal silicon have given an average predicted range (the depth of highest concentration) of ~ 22 nm and a depth straggle (defined in SRIM as the square root of the variance of the distribution of the profile) of ~ 10 nm [82]. The predicted lateral straggle is orders of magnitude lower than the diameter of the flat top micro post [16] and so the 2 µm diameter of the surface of the flat top micro post can be considered to respond to the implantation in the same manner as a large, planar substrate. This indicates that for the as-implanted samples the full implantation profile will be contained with ~ 40 nm of the surface and will have a maximum peak concentration of ~ 0.2 at.%. This gives a predicted volume of interest of ~ 50 nm x 50 nm x 40 nm given typical atom probe sample sizes and a capping layer thickness of a few nm [1].

A range of phosphorus doses predicted to give peak concentrations of 0.2 at.%, 0.1 at.% and 0.01 at.% were used in order to determine the detection limits of APT for phosphorus for the length scales given above. These concentrations (~10^{19} at/cm^3 – 10^{20} at/cm^3) are many orders of magnitude higher than are used in actual implantation for quantum devices and are also significantly higher than those that can be measured by Secondary Ion Mass Spectrometry (SIMS) (~10^{16} at/cm^3 [17]). SIMS analyses contain far greater volumes of material compared to APT and thus have a much lower concentration limit [214]. These implantation concentrations, whilst close to the detection limit of APT, were deemed likely to be detectable in APT. For the RTA processed samples, a minimal shift in depth and concentration peak of the phosphorus profile is predicted as there is likely to be some segregation to the surface [78] [230].

A collaborator, Dr Brett Johnson at the University of Melbourne, predicted a drop by 10 at.% in peak concentration and a shift of the implantation peak ~ 2 nm towards the surface as a result of the annealing. This calculation was carried out using phosphorus diffusion constant values as calculated by Bracht et al. [231] via the FLorida Object Orientated Process Software package [232]. The increase in diffusivity with concentration above the transient enhanced threshold was not included in the calculations and as the phosphorus is above the limit at which transient enhanced diffusion is known to occur [233], this prediction is likely to underestimate the shift in the profile due to the RTA.

This surface segregation will cause additional issues with quantification due to mass spectra overlaps. Due to low sample yield due to the fragility of the implanted samples, it was not always possible to make full comparisons between pre-fabricated supports and planar substrates or between RTA and non RTA processed samples.

Full SRIM, implantation and RTA parameters can be found in Appendix B.

The analyses shown in this chapter have been selected as the most representative of those available to show how variation between the above conditions can change the measured phosphorus distribution. Whilst a range of analysis conditions (laser powers, base temperatures, pulse frequencies and detection rates) were attempted across a number of samples of both micro posts and lift outs for the implanted materials in this work, not all sample datasets were found suitable for reporting after rigorous analysis of the reconstructions. These unusable datasets often showed evidence of a too thin/missing capping layer, micro fracture events which removed the surface implanted region or excess gallium damage to the implanted region. Any of the above issues rendered the data unusable for quantifying the phosphorus concentration and distribution.

Where possible, comparisons are made between the following:

- Phosphorus implantation profiles from as-implanted micro posts and lift outs.
- Phosphorus implantation profiles from annealed micro posts and lift out.
- Changes in mass spectra and phosphorus profiles as a result of capping layer selection.
- Changes in phosphorus implantation profiles from single and complex ion implantation.
- Changes in phosphorus implantation profile from varying implantation dose.
- Changes in mass spectra due to analysis on different atom probe systems.

Reconstruction was carried out using the Integrated Visualisation and Analysis Software (IVAS) 3.6.12 package and used a standard voltage based approach to determine the initial tip diameter prior to refining the reconstruction [7]. The initial radius and Image Compression Factor (ICF) were altered to match the plane spacing of the silicon [100]

plane as closely as possible and to maximise the flatness of the capping layer surface [214] [234]. The region used to generate the Spatial Desorption Map [235] that showed the plane spacing was generated from a 2 nm cylinder centred around the region of lowest ion count in the detector hit map, this region of low intensity is linked to the evaporation behaviour of the 100 pole [7].

It was found that the analysing through a thickness of capping layer material corresponding to an average of ~ 250,000 ions was strongly linked to increased chance of fracture at the capping layer/silicon interface [198]. This is likely to be related to the standing voltage at which the analysis reaches this interface, with thicker capping layers having an increased voltage requirement and thus increasing the stress on the sample at the weak point of the interface. The majority of successful analyses of the capping layer/silicon interface were carried out with less than ~ 250,000 capping layer ions, this was enough to provide a uniform layer in the reconstruction yet not so thick that it increased the chance of fracture. It was found that a voltage of ~ 3 – 3.5 kV was optimal for analysing through the interface without fracturing.

For those samples that were found to survive the controlled evaporation of interface without fracturing, it was often found that uniform evaporation of the capping layer material would cease and silicon ions would be detected at the outermost ring of the detector. This behaviour in multi-layer systems is linked the change in preferential evaporation from the capping layer to the substrate (combined with capping layer retention at the centre of the tip) and has been reported in the literature previously [203]. This can be considered to be a reasonable indication that the interface was analysed without any micro fracture events but this process also can lead to density variations and reconstruction artefacts at the interface.

No samples implanted to give 0.01 at.% peak concentrations were found to be viable during atom probe analysis and so the results shown in this chapter are based around implanted to give 0.2 at.% peak concentrations.

4.2 Analysis using LEAP 3000X HR

4.2.1 Analysis of implanted micro post with nickel capping layer. Predicted peak phosphorus concentration 0.2 at.%.

Analysis conditions: LEAP 3000X HR, 55 K, 200 kHz pulse frequency, 0.2 nJ laser energy throughout analysis, 0.2% detection rate in capping layer and 0.4% after the capping layer.

The following stages are presented in detail in order to demonstrate the optimisation process of the analysis of a phosphorus implantation profile in a silicon substrate using a nickel capping layer. All further nickel capped samples were analysed in a similar manner.

A low laser energy was used in this sample in order to reduce the effects of thermal tails where possible and decrease the potential for complex ions and laser induced artefacts [224].

The atom map shown in Figure 4.1 is of the phosphorus species at 15.5 Da and 31 Da in purple, with a 15 at.% iso-concentration surface of Ni^+ used to initially delineate the surface between the nickel capping layer and the silicon substrate. This concentration was selected as it was the lowest concentration of nickel which still gave a coherent surface sufficiently far away from the capping layer/silicon interface to allow the species on either side around it to be visible when constructing a depth profile. Coherency of the layer was

assessed by whether a smooth and unbroken iso-concentration surface could be generated. The species was chosen to prevent mass spectra overlaps between $^{58}Ni^{2+}/^{29}Si^{+}$and $^{60}Ni^{2+}/^{30}Si^{+}$ species at 29 Da and 30 Da respectively from causing artefacts in the uniformity and location of the nickel iso-concentration surface.

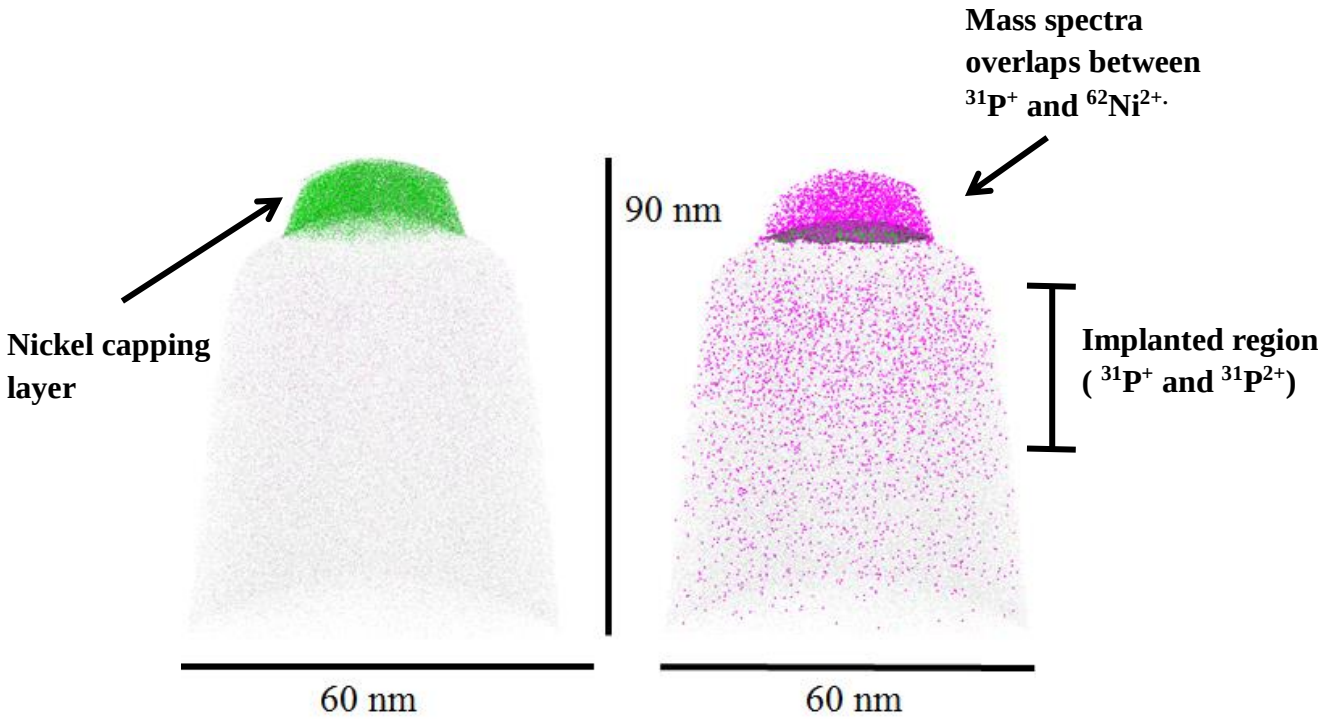


Figure 4.1 – Atom map of implanted micro post (0.2 at.% predicted peak concentration of phosphorus) with nickel capping layer.

Left – Nickel (green), silicon (grey) and phosphorus (purple) species are shown. Right – Silicon (grey) and phosphorus (purple and enlarged three times the size for clarity) ions are shown. A Ni^{+} (15 at.%) iso-concentration surface can be seen in green between the capping layer and substrate.

In this sample, the greater concentration of phosphorus species can be readily seen in the atom map in the ~ 30 nm region below the Ni^{+} iso-concentration surface. The majority of silicon ions in all atom maps shown have been removed for clarity whilst all of the phosphorus ions are shown.

Nickel has natural isotopic abundancies of ^{58}Ni (68.08%), ^{60}Ni (26.22%), ^{61}Ni (1.14%), ^{62}Ni (3.63%), ^{64}Ni (0.93%) and silicon has ^{28}Si (92.23%), ^{29}Si (4.67%) and ^{30}Si (3.1%). The apparent high concentration of phosphorus above this surface is due to the overlap between $^{62}Ni^{2+}$ and the single isotope of phosphorus in the form of $^{31}P^{+}$ at 31 Da.

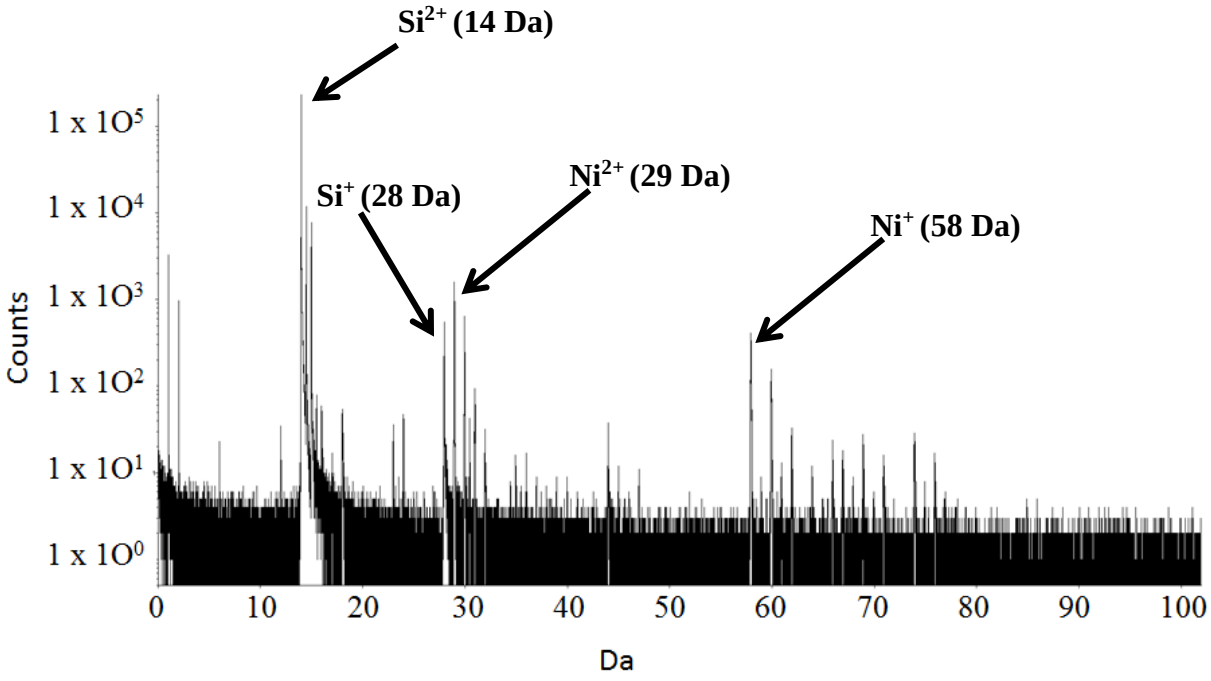


Figure 4.2 – Mass spectra of full dataset shown in Figure 4.1. Majority species of silicon are found as Si^{2+} at 14 Da but also as Si^{+} at 28 Da. Nickel capping layers species are observed as $^{58}Ni^{2+}$ at 29 Da and $^{58}Ni^{+}$ at 58 Da.

The full mass spectrum for the full dataset can be seen in Figure 4.2. As is the standard for displaying atom probe data, the x-axis is shown in the mass-to-charge ratio unit of the Dalton (Da) [1]. The species with mass-to-charge-ratios greater than 62 Da belong to nickel oxides and gallium species and so will not be of direct relevance unless they are at the interface. Additionally, due to the evaporation field requirement differences between the capping layer and the substrate materials there can be a significant difference between the standing voltage required for each region for a given detection rate. During atom probe

data reconstruction, the recorded time of flights of each detected ion are processed through a correction step to take into account the variation in standing voltage through the analysis (voltage correction) and that the ion is projected from a 3D object onto a 2D detector (bowl correction). As these corrections are generally carried out on the dataset as a whole to give sufficient signal to calibrate the correction, it uses the total numbers of ions and the average time of flight for each peak. It also adds an offset in time of flight to allow the shifting of the peaks to match known mass-to-charge ratios. This can be an issue when dealing with overlapping peaks that can be one species within the capping layer and another below it. In this case such a peak would be at 31 Da, as within the capping layer it would be considered to be $^{62}Ni^{2+}$ and below the capping layer it would be considered to be $(^{30}Si^{1}H)^{+}$ or $^{31}P^{+}$.

With small changes in voltage, this can lead to a widening or changing of the shape of the peak on either side of the interface and so a global ranging approach can lead to ranging peaks that are correct for the entire dataset but are subtly incorrect for both sides of the interface. As the ranging is often carried out on the peak as a whole, it is the small peaks of low concentration species that will be affected the most and can have their measured abundance increased the most (through addition of noise or other species ranged incorrectly) or decreased (through the peak only being partially ranged or completely unranged). To counteract the effects of variation in standing voltage as a function of passing through the capping layer interface, a local ranging approach was used. The initial global ranging carried out in the initial reconstruction was used to delineate the rough locations of the interface and then used to position a cylindrical Region of Interest (ROI) volume after the interface as shown in Figure 4.3. The mass spectra from this region can then be extracted and used to more accurately range the species of interest.

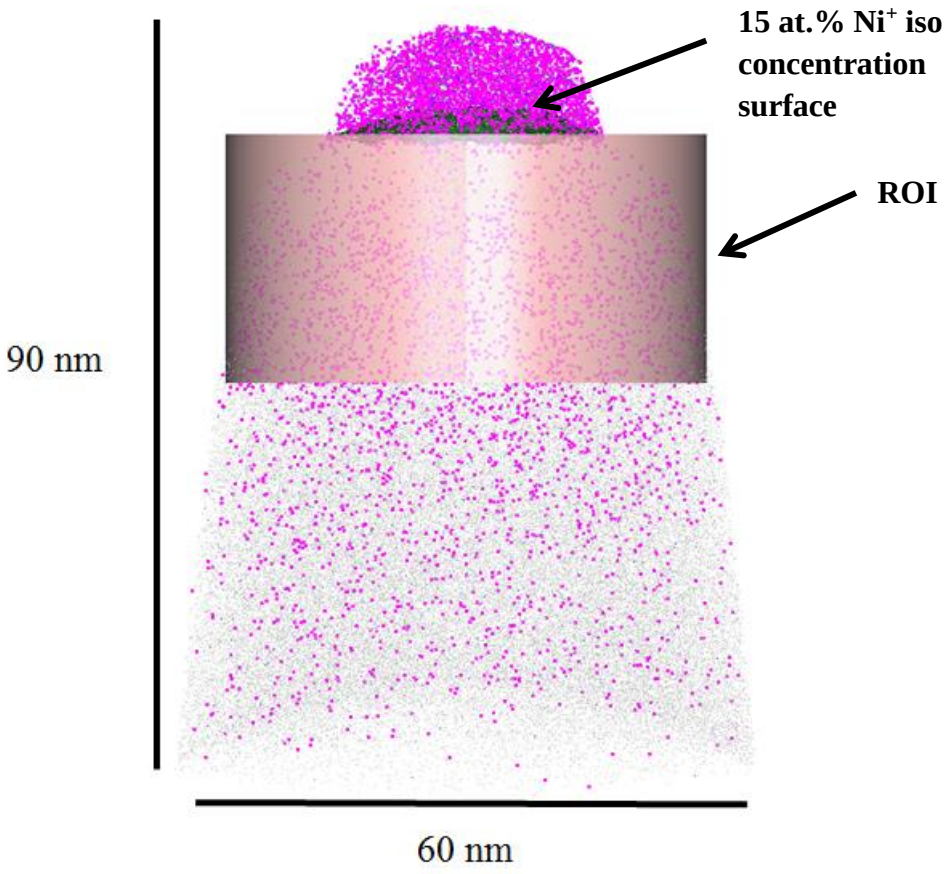


Figure 4.3 – Atom map showing placement of ROI in the implanted region immediately below the 15 at.% Ni^+ iso-concentration surface to aid in mass spectra ranging.

Nickel species in the 1^+ charge state can be found at 58 Da ($^{58}Ni^+$), 60 Da ($^{60}Ni^+$), 61 Da ($^{61}Ni^+$), 62 Da ($^{62}Ni^+$) and 64 Da ($^{64}Ni^+$) and are shown in Figure 4.4.

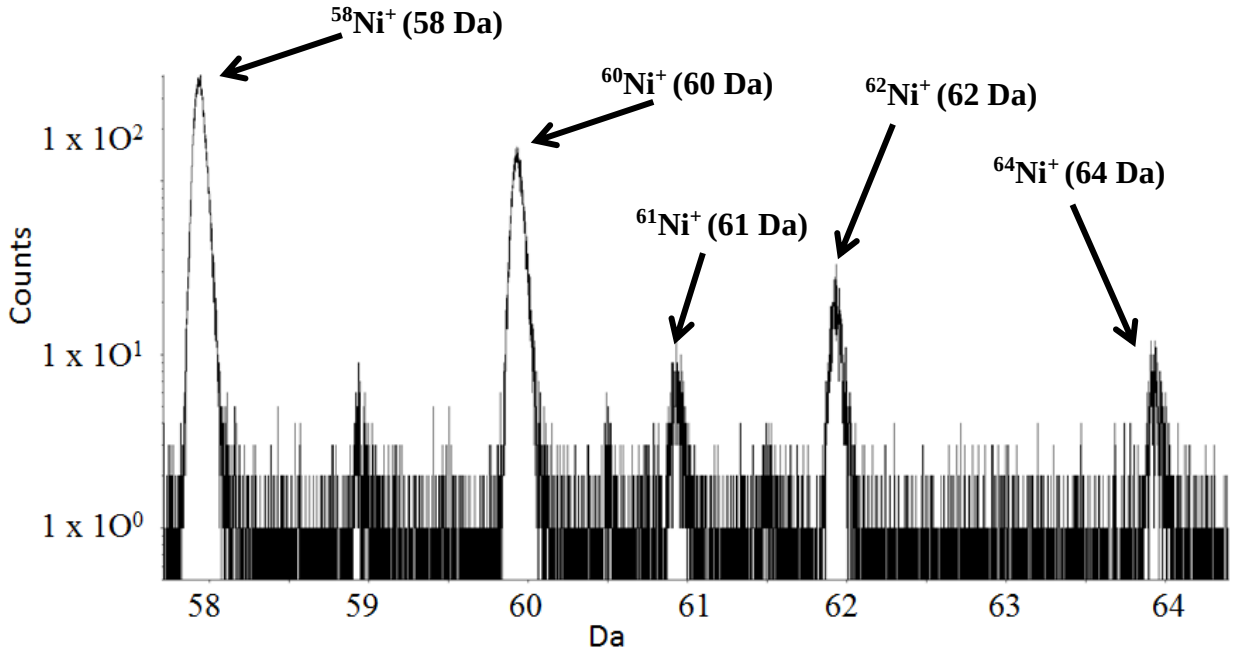


Figure 4.4 – Mass spectra of full dataset in Figure 4.1 in the 58 - 64 Da range. Nickel species in Ni^+ charge state are visible.

Mass spectra overlaps between complex ion phosphorus species $(^{31}P_2)^+$ and nickel species $(^{62}Ni^+)$ at 62 Da in this section of the mass spectrum may contribute to the difficulties in quantification of phosphorus at and near the nickel/silicon interface. The mass spectrum from the ions contained within the ROI are shown in Figure 4.5, showing a reduced contribution from the Ni^+ ions.

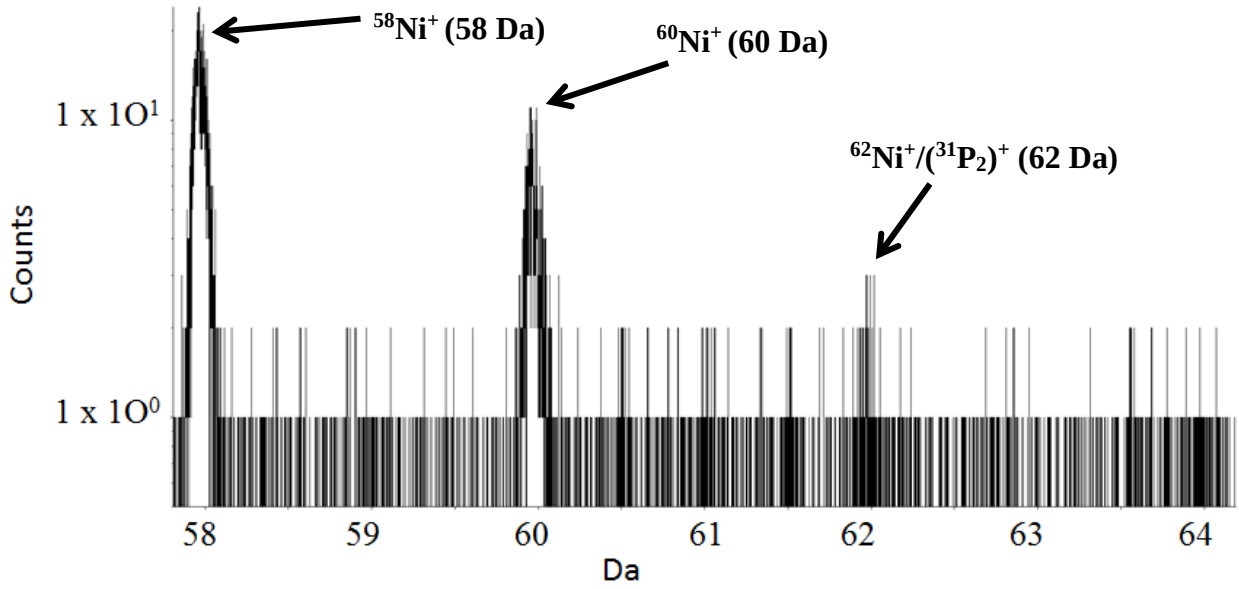


Figure 4.5 – Mass spectra from ROI in Figure 4.3 in 58 - 64 Da range. Only majority nickel isotopes of $^{58}Ni^{+}$ (58) Da and $^{60}Ni^{+}$(60 Da) are clearly visible.

Only the major isotopes of nickel at $^{58}Ni^{+}$ and $^{60}Ni^{+}$ at 58 Da and 60 Da can be readily seen in the mass spectrum generated from the ROI. There is also a potential peak at 62 Da which may be $^{62}Ni^{+}$. This is due to both the reduced concentration of nickel in the region below the 15 % Ni^{+} iso-concentration surface and also due to the changing field effects at the nickel/silicon interface.

Silicon species in the Si^{+} charge state can be found in Figure 4.6 at 28 Da ($^{28}Si^{+}$), 29 Da ($^{29}Si^{+}$) and 30 Da ($^{30}Si^{+}$) along with nickel species in the Ni^{2+} charge state at 29 Da ($^{58}Ni^{2+}$), 30 Da ($^{60}Ni^{2+}$), 30.5 Da ($^{61}Ni^{2+}$), 31 Da ($^{62}Ni^{2+}$) and 32 Da ($^{64}Ni^{2+}$). Phosphorus species can be found at 31 Da ($^{31}P^{+}$) as can silicon hydride from the ^{30}Si isotope ($^{30}Si^{1}H^{+}$)$^{+}$.

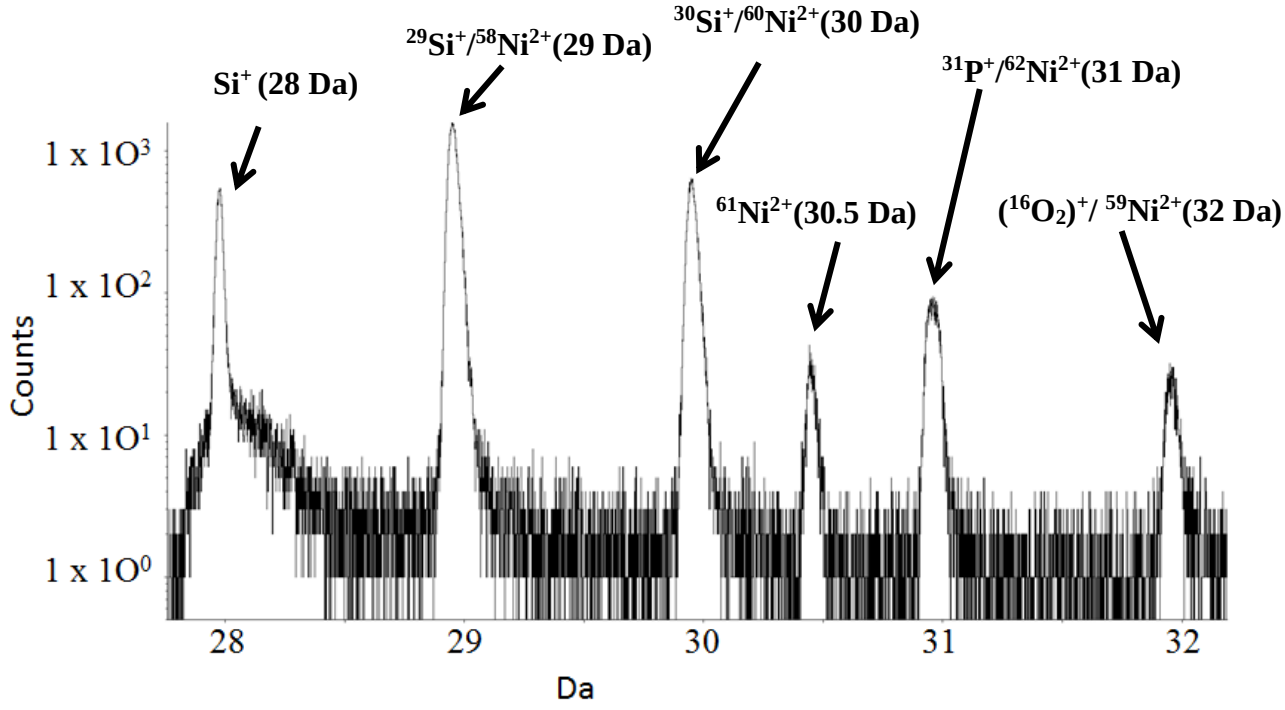


Figure 4.6 – Mass spectra of full dataset from Figure 4.1 in the 28 Da to 32 Da range. Multiple overlaps between silicon, nickel and phosphorus are observed.

Mass spectra overlaps at 31 Da between phosphorus species ($^{31}P^+$), nickel species ($^{62}Ni^{2+}$) and silicon hydride $(^{30}Si^{1}H)^+$ are a factor in preventing quantification of phosphorus concentrations at and near the nickel/silicon interface. There is also a potential overlap between the single ion $^{31}P^+$ and the complex ion $(^{31}P_2)^{2+}$ at 31 Da which cannot be deconvoluted and so there is the potential for undercounting phosphorus contributions by ranging the latter as the former. Through inspecting the mass spectrum obtained from the ROI in the same region (Figure 4.7), the ratio of the silicon Si^{2+} species can be seen to have returned to values closer to their natural abundancies (^{28}Si (92.23%), ^{29}Si (4.67%) and ^{30}Si (3.1%)) and have minimal contributions from nickel.

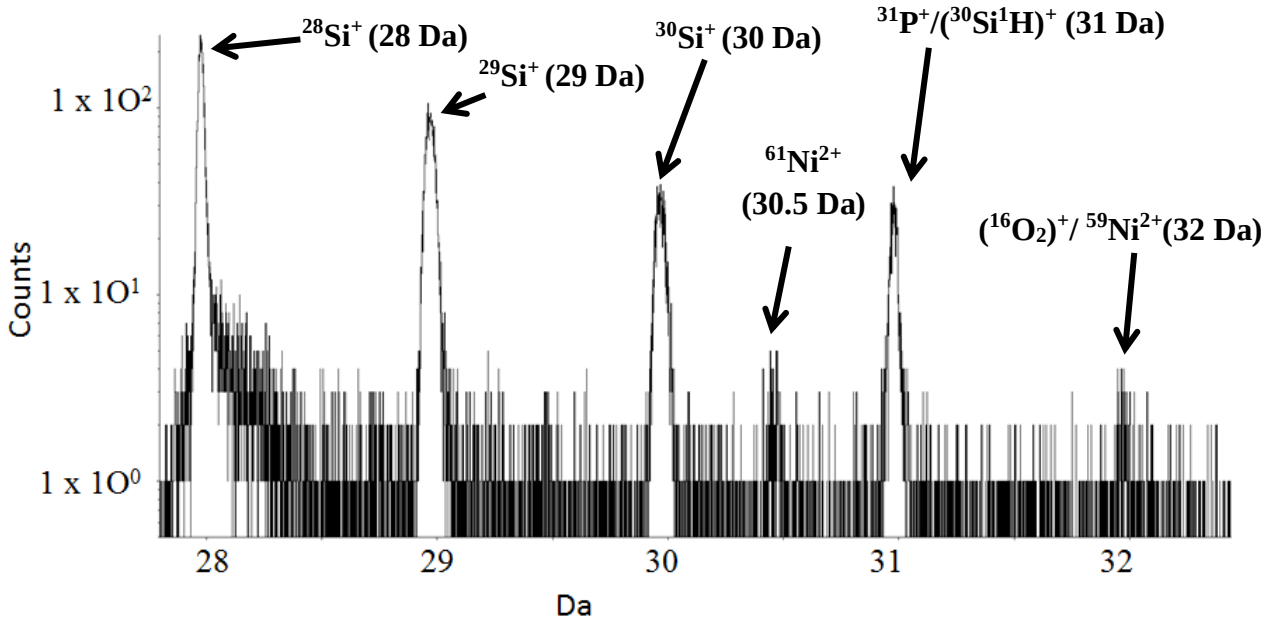


Figure 4.7 – Mass spectra from ROI in Figure 4.3 in the 28 Da to 32 Da range. Reduced contributions from Ni^{2+} species are observed.

These peaks, and the one at 31 Da, will still have some contributions from nickel species as there is still a small but visible peak at 30.5 Da from the $^{61}Ni^{2+}$ species. This indicates that the majority of the peak at 31 Da does not consist of nickel and instead will be mainly phosphorus or silicon hydride.

The majority of silicon ions in this sample were observed in the Si^{2+} species at $^{28}Si^{2+}$, $^{29}Si^{2+}$ and $^{30}Si^{2+}$ at 14 Da, 14.5 Da and 15 Da respectively, and so the effects of thermal tails from delayed evaporation from these species are increased proportionally compared to the Si^{+} species. The phosphorus $^{31}P^{2+}$ species is also present at 15.5 Da and so, although it does not have a direct overlap with another species, the thermal tails from Si^{2+} species can be seen to overlap with this peak (Figure 4.8).

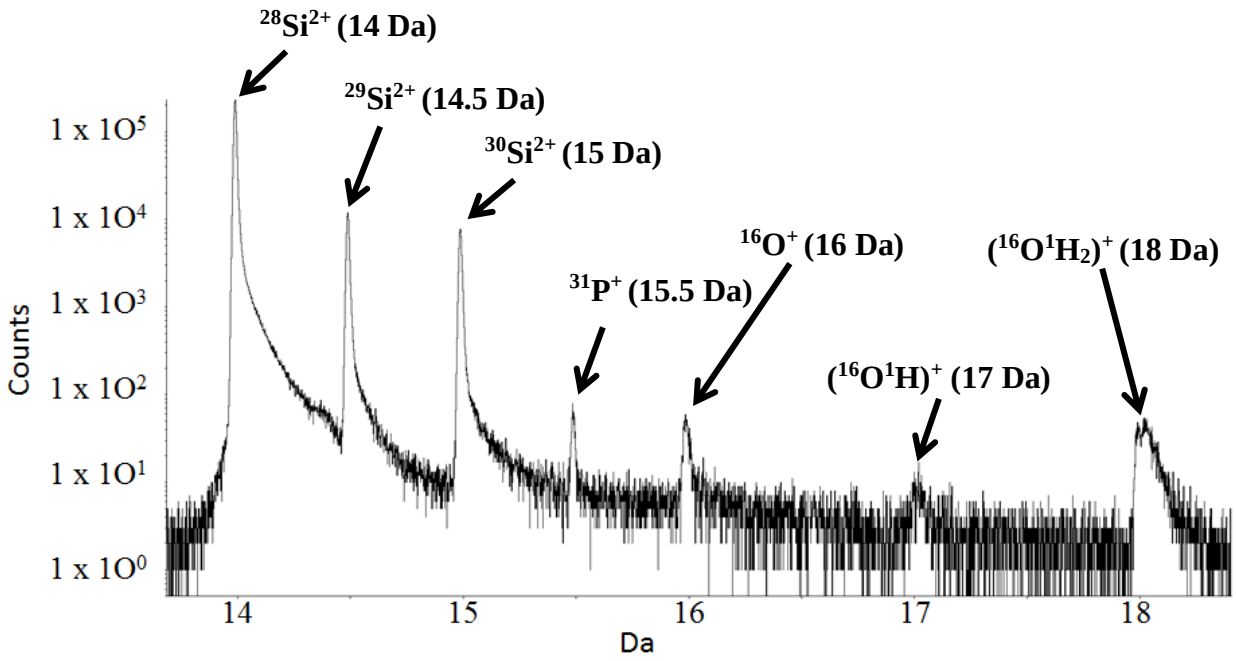


Figure 4.8 – Mass spectra of full dataset in Figure 4.1 in the 14 Da to 18 Da range. Thermal tail contributions from silicon species can be seen overlapping with the phosphorus peak at 15.5 Da.

Phosphorus species can be seen at 15.5 Da (P^{2+}) and oxygen species at 16 Da ($^{16}O^{+}$), 17 Da ($^{16}O^{1}H)^{+}$ and 18 Da ($^{16}O^{1}H_2)^{+}$. The thermal tail contributions from all three silicon species can be seen to contribute to the phosphorus peak and can prevent precise quantification of the phosphorus concentration and also reduce the spatial resolution. The mass spectrum from the ROI, shown in Figure 4.9, shows that the phosphorus peak at 15.5 Da retains some contribution from the thermal tails from the silicon species but to a lesser extent due to the reduced ratio of silicon ions to phosphorus ions within the implanted region.

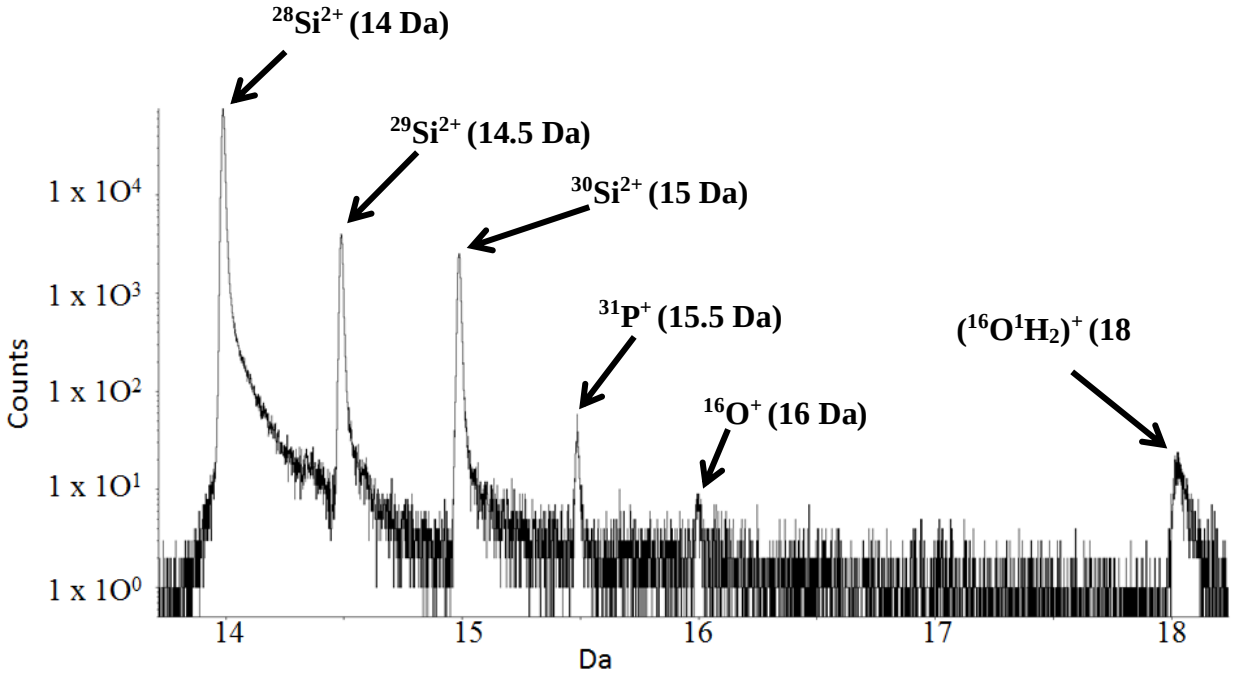


Figure 4.9 – Mass spectra from ROI in Figure 4.3 in in the 14 Da to 18 Da range. Reduction in thermal contributions from silicon species to phosphorus peak at 15.5 Da.

The Ni^{+} 15 at.% iso-concentration surface was used in these samples to give a coherent and uniform layer that can be used to give a rough determination of the location of the nickel /silicon interface for the placement of the ROI for local ranging. It also allows the generation of proximity histograms that will take into account any curvature in this interface [7]. Without taking interface curvature into account, the concentration profile generated from it would have sections compressed or stretched due to the local curvature of the interface and so would not be a true measure of the concentration as a function of depth. A proximity histogram was therefore made using an interface from the Ni^{+} 15 at.% iso-concentration surface.

All depth profiles generated by proximity histograms shown in this chapter used a binning size of 1 nm. This is due to the small numbers of ions expected as part of the implanted profiles and to allow the smoothing of the profiles for easier visual comparison between each other and with simulated profiles. A standard IVAS background correction was carried out on all the data shown in this chapter. This calculates background from the

entire dataset used and removes a uniform number of ion counts in time of flight space [7]. This can be considered to remove a standard offset of ion counts proportional to the width of each ranged species but does not take into account any variation from this that can be due to thermal tail or other effects.

When using atom probe analysis of silicon samples, the native oxide surface layer can be used as a delineation point for the start of concentration profiles, but in this case there was not sufficient oxygen or silicon oxide species to be able to use these as an iso-concentration surface [214]. As this sample had been dipped in HF prior to deposition of the capping layer in order to promote adhesion of the capping layer, the original silicon oxide layer which had been implanted through will have been removed and the subsequent silicon oxide will have regrown from the implanted material. As such a regrowth will be approximately 2 nm in thickness; this will potentially shift the location of the measured profile closer to the surface by the same amount. The reduced amount of silicon oxide measured and the lack of a uniform layer of the small amount that was detected in this sample may be due to a small micro-fracture event during evaporation of the interface.

The concentration profile of silicon oxide is shown in Figure 4.10. The profile from the 32 Da peak is displayed in order to give an indication of the contribution of the overlaps from the $^{64}Ni^{2+}$ species, and thus an indication of where the phosphorus profile from the 31 peak can be considered to be free from overlaps from the $^{62}Ni^{2+}$ species. As the contributions from the $^{64}Ni^{2+}$ species to the 32 Da peak will be approximately 1/3 of the contribution of $^{62}Ni^{2+}$ species to the 31 Da peak due to their relative isotopic abundancies, once the 32 Da peak has reached background levels then it can be reasonably assumed that any contribution from the $^{62}Ni^{2+}$ species to the 31 Da peak will also have be reduced to below background levels.

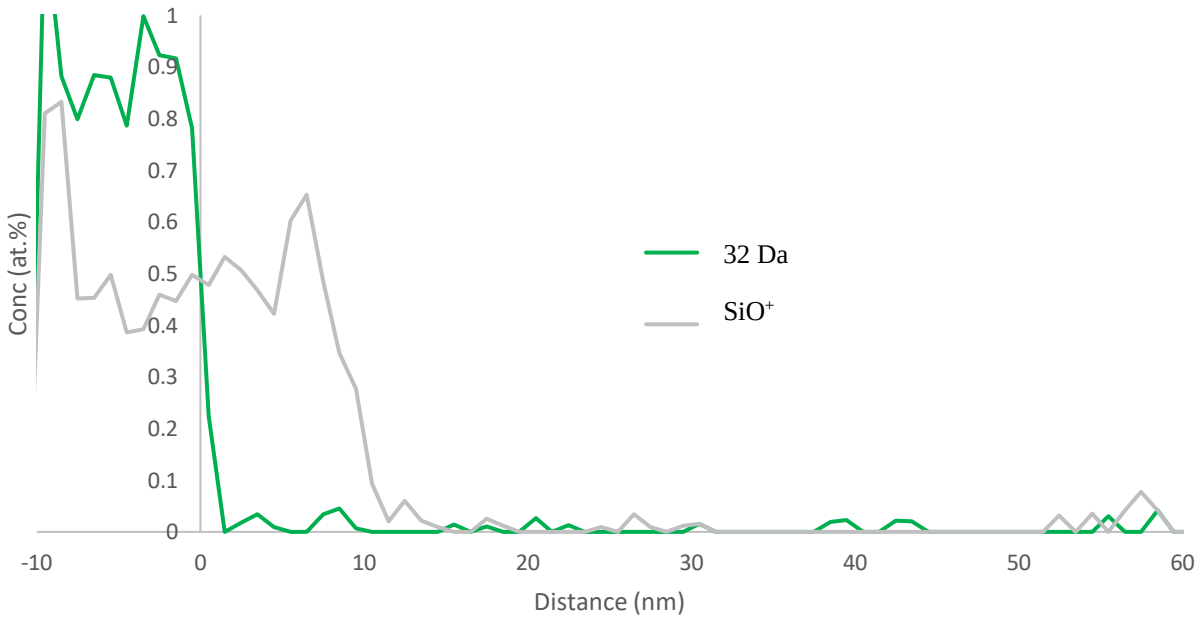


Figure 4.10 – Proximity histogram concentration profiles of silicon oxide and species at 32 Da generated from a 15 at.% Ni^+ iso-concentration surface.

The 30.5 Da peak from the $^{61}Ni^{2+}$ could also been used to delineate the surface as it as a similar ratio to that of the $^{62}Ni^{2+}$ species, but it also has the greater risk of thermal tail overlaps from the silicon species and so it was decided to use the 32 Da peak for delineation in this case. The 32 Da peak also has an overlap with the complex $^{16}O_2^+$ ion and so there is potential for contributions from that but, as silicon oxide and other oxygen species are not present in high enough quantities, it is unlikely they will be an issue. It can be seen in Figure 4.10 that the 32 Da species profile gives a much sharper interface than the silicon oxide profile and visual inspect of the atom map surface showed a non-uniform layer in the centre of sample which protruded into the region below the end of the 32 Da profile. This suggests that if a micro fracture did occur and only a small amount of silicon oxide was left, this was preferentially retained during the evaporation process due to its insulating nature and appears deeper than expected [203].

The lack of a distinct silicon oxide layer makes it difficult to determine an exact start position to draw the implantation profile but the first point where the 32 Da species reaches a local minimum can be a reasonable assumption. In this case, this is at 1.5 nm deeper than the original iso-concentration surface generated from the 15 at.% Ni^+ species.

Concentration profiles of the two main phosphorus containing species (P^+ and P^{2+}) were plotted alongside the silicon oxide and 32 Da species in Figure 4.11. The complex ion $^{31}P_2^+$ at 62 Da was not found in any amount above background levels in this region, and so is not included in it.

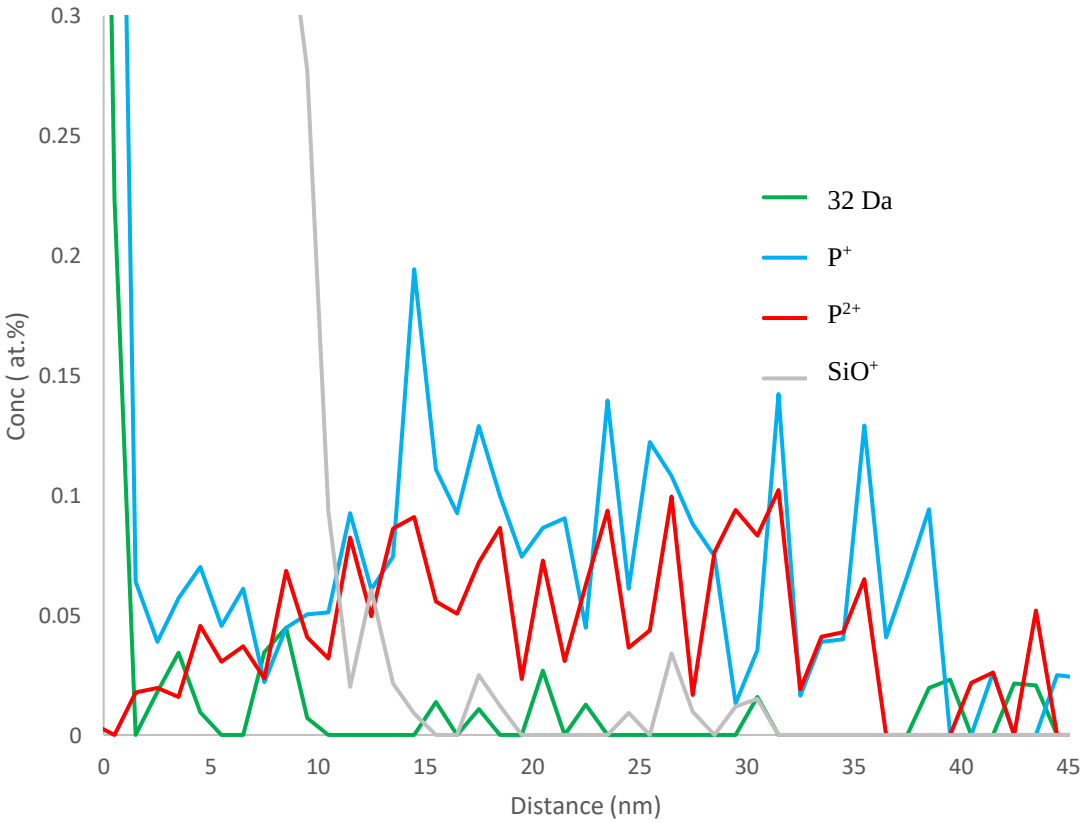


Figure 4.11 – Proximity histogram concentration profiles of phosphorus containing species (P^+ and P^{2+}) overlaid on the silicon oxide and species at 32 Da profiles.

It can be seen that the two phosphorus species contribute approximately equal amounts to the profile, but that the overlaps caused by nickel and silicon hydride contributions to the

31 Da P^+ profile blur the starting point of that species in the first ~ 1.5 nm below the capping layer.

The P^{2+} peak can be seen to also begin approximately at the same point as the first local minima of the 32 Da species and does not show the same blurring at the surface. This tentatively suggests that the P^{2+} species could be used to give a more reliable starting location of the concentration profile but due to the changing evaporation field conditions at the interface, it cannot be guaranteed that the appearance of a species at a certain point is not just the result of changing surface field conditions making that charge state preferential [183]. However as the P^{2+}species is more likely to be obscured by thermal tail contributions in this sample, an increased proportion of phosphorus in this state may end up blurring the spatial resolution of the profile due to increased local noise and may require a more local background noise correction [236].

The P^+ and P^{2+} species were summed and overlaid with the silicon oxide and 32 Da species profiles in Figure 4.12. It can also be seen that, although the main body of the profile is now raised in concentration and is much clearer, the starting point of the profile is now blurred due to the mass spectra overlaps that occurred with the 31 Da peak.

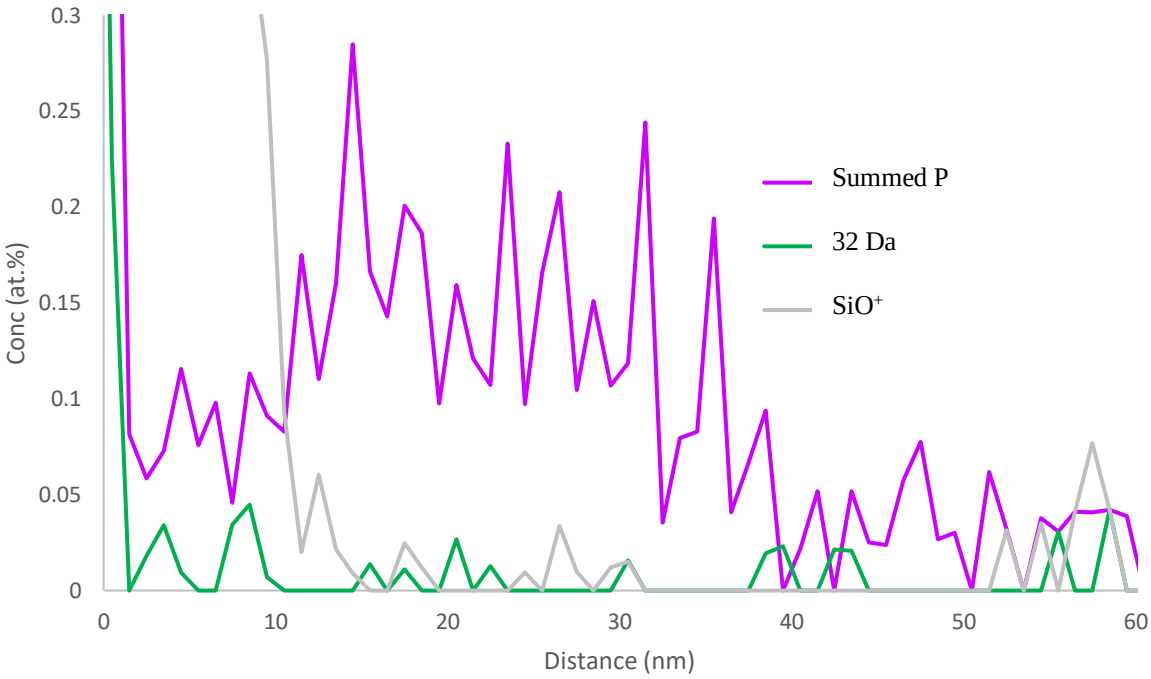


Figure 4.12 – Proximity histogram concentration profiles of summed phosphorus, silicon oxide and species at 32 Da profiles.

This summed phosphorus concentration distribution shows a distinct implantation profile form and, in order to compare it with simulation, a range of SRIM profiles of 14 kV P^+ implantation profiles with peak concentrations of 0.2 at.% and 0.16 at.% were overlapped onto the summed phosphorus profile in Figure 4.13. The overlapped regions at the surface have been removed to make ease visual comparison between measured profiles and simulation.

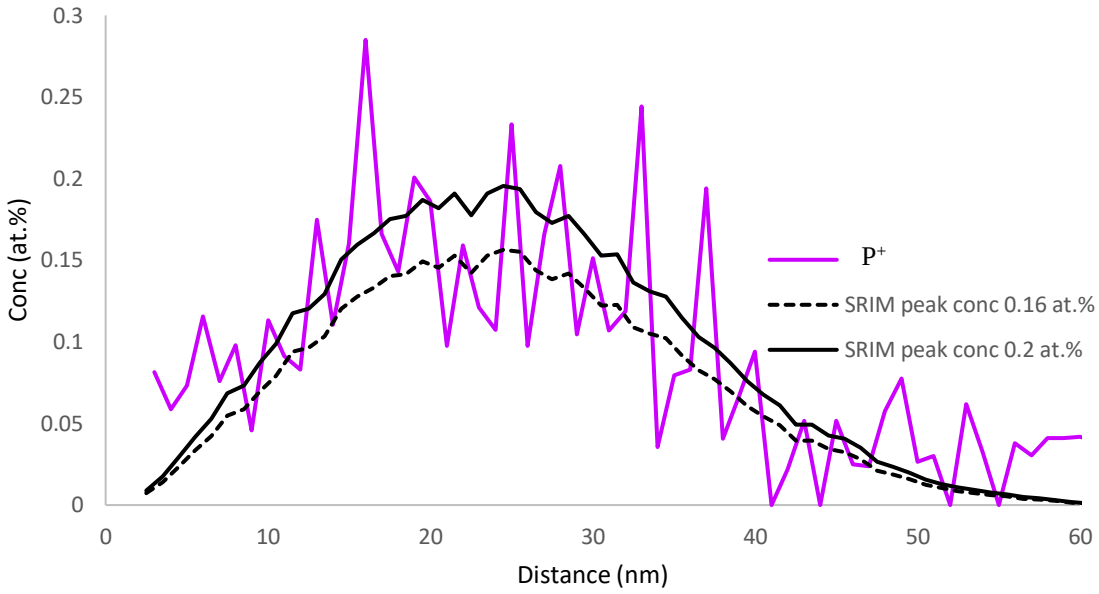


Figure 4.13 – SRIM profiles of 14 kV phosphorus with peak concentrations of 0.2 at.% and 0.16 at.% overlaid on the summed phosphorus profile.

The nickel/phosphorus overlap region at the start of the profile has been removed and the SRIM profiles have been offset by 1.5 nm, using the first local minima of the 32 Da species (corresponding to the end of the nickel capping layer) to define the starting point. The 0.2 at.% SRIM profile predicts a slightly higher concentration than was measured while the 0.16 at.% SRIM profile appears to fit more closely to the profile. Both profiles underestimate the extent of the tail region and, as the implantation was carried out without any tilt or twist parameters to prevent ion channelling expected in single crystal silicon [8], this extended tail region can be attributed partly to this.

There is also a reasonable degree of noise in the measured profile compared to the profile calculated via SRIM. Despite the relatively large bin size of 1 nm, the numbers of phosphorus ions within each bin are still very low (Figure 4.14). Small local variations in phosphorus ions between adjacent bins can therefore lead to large changes in apparent

concentration. Increasing the number of detected phosphorus ions to smooth out the curve without increasing the implant dose could be carried out through increasing the detector efficiency of the atom probe used.

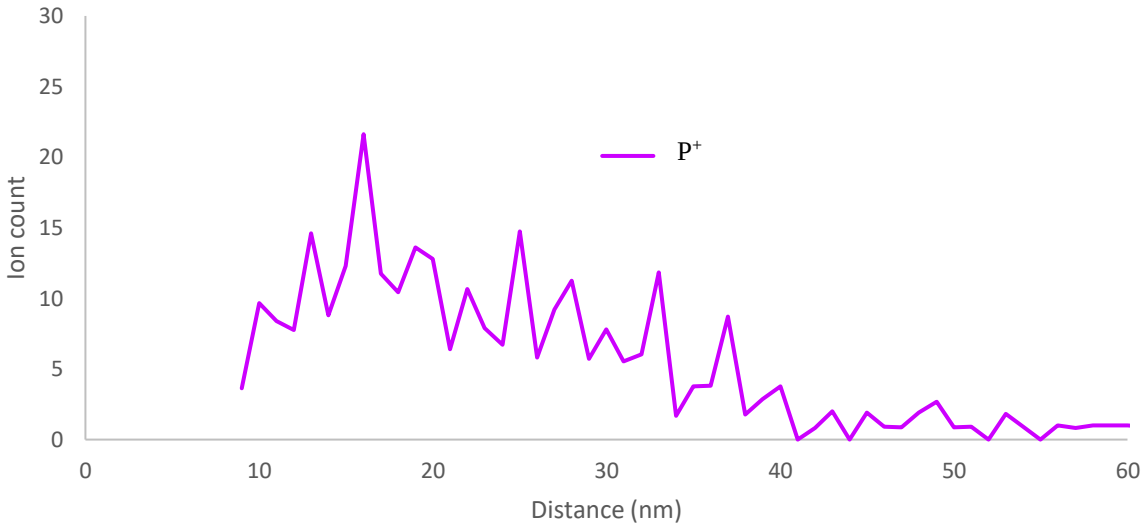


Figure 4.14 – The summed phosphorus profile from Figure 4.13 expressed in ion count. The overlapped regions at the start of the profile have been removed for clarity.

In order to more directly allow for comparison with other datasets and observe variation between implantation and annealing conditions, the implanted region measured must be as close as possible in size and volume between datasets. In this case, a 30 nm x 30 nm x 100 nm cylindrical ROI was created such that it passed perpendicularly through the Ni^+ 15 % iso-concentration surface and all ions within that ROI were extracted for further analysis seen in Figure 4.15.

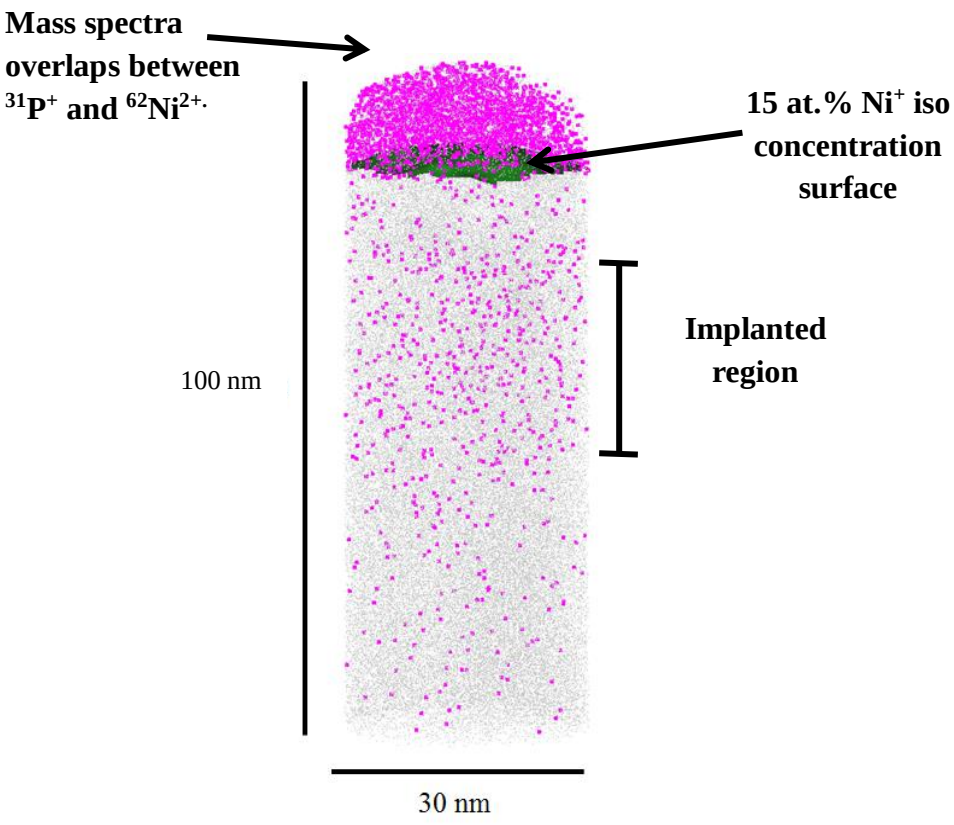


Figure 4.15 – 30 nm x 30 nm x 100 nm ROI projected through the centre of the full dataset. Silicon (grey) and phosphorus (pink and enlarged for clarity) ions are shown. A 15 at.% Ni^{+} iso-concentration surface can be seen in green between the capping layer and substrate.

An iso-concentration surface of 15 at.% Ni^{+} species was generated and an ROI of the region directly below this iso-concentration surface was used to confirm the position and accurate ranging of the mass spectra peaks of phosphorus. Minimal changes to the mass spectra and ranging were observed compared to those obtained from mass spectra from the entire sample over the same depth range, this indicates that there was no significant difference in the mass spectra due to laser effects from the centre of the sample compared to the edges

A proximity histogram was generated from the Ni^{+} 15 at.% iso-concentration surface and the summed phosphorus profile from the P^{+} and P^{2+} charge states was plotted and SRIM profiles of 0.16 at.% and 0.2 at.% peak phosphorus concentration were overlaid (Figure 4.16). It can be seen that although the peak concentration seems to reach the predicted 0.2 at.%, the profile, the signal becomes extremely noisy after ~ 25 nm.

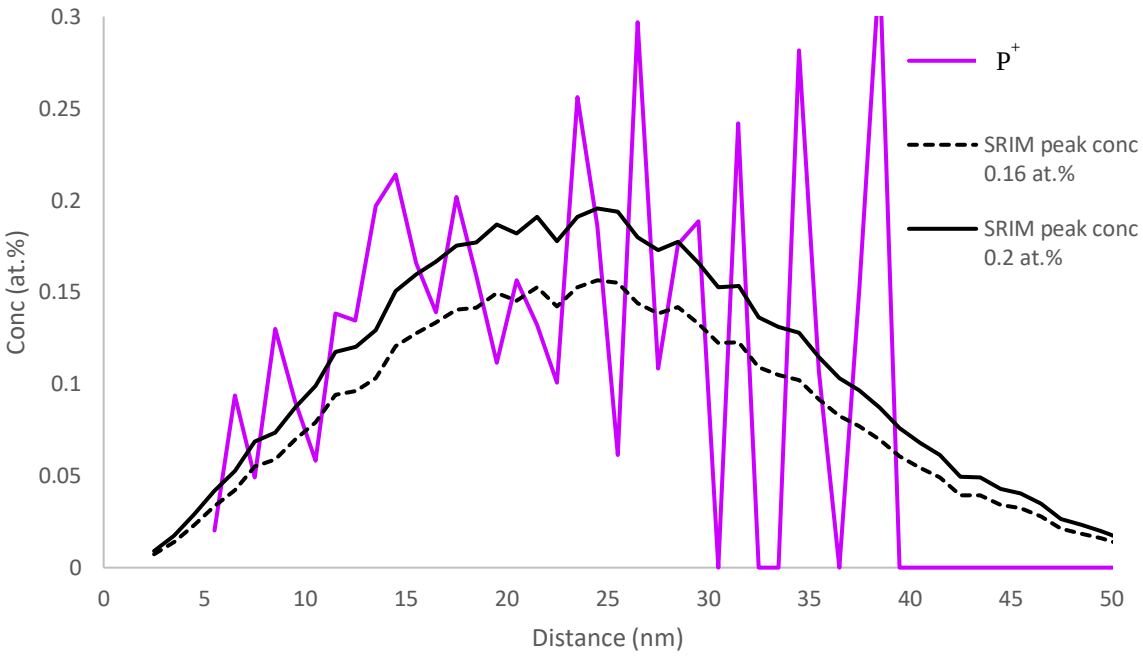


Figure 4.16 - SRIM profiles of 14 kV phosphorus with peak concentrations of 0.2 at.% and 0.16 at.% overlaid on the measured phosphorus profile from the 30 nm x 30 nm x 100 nm ROI.

Through plotting the depth profile of phosphorus ion count (Figure 4.17), it is shown to decrease to background levels in the 25 nm – 30 nm region, indicating that only the main section of the implanted profile will be visible with reasonable signal within this reduced volume. When comparing similar samples to each other using this reduced volume, it will

mean that the lower limit of concentration that is directly comparable in terms of ion count will be reduced.

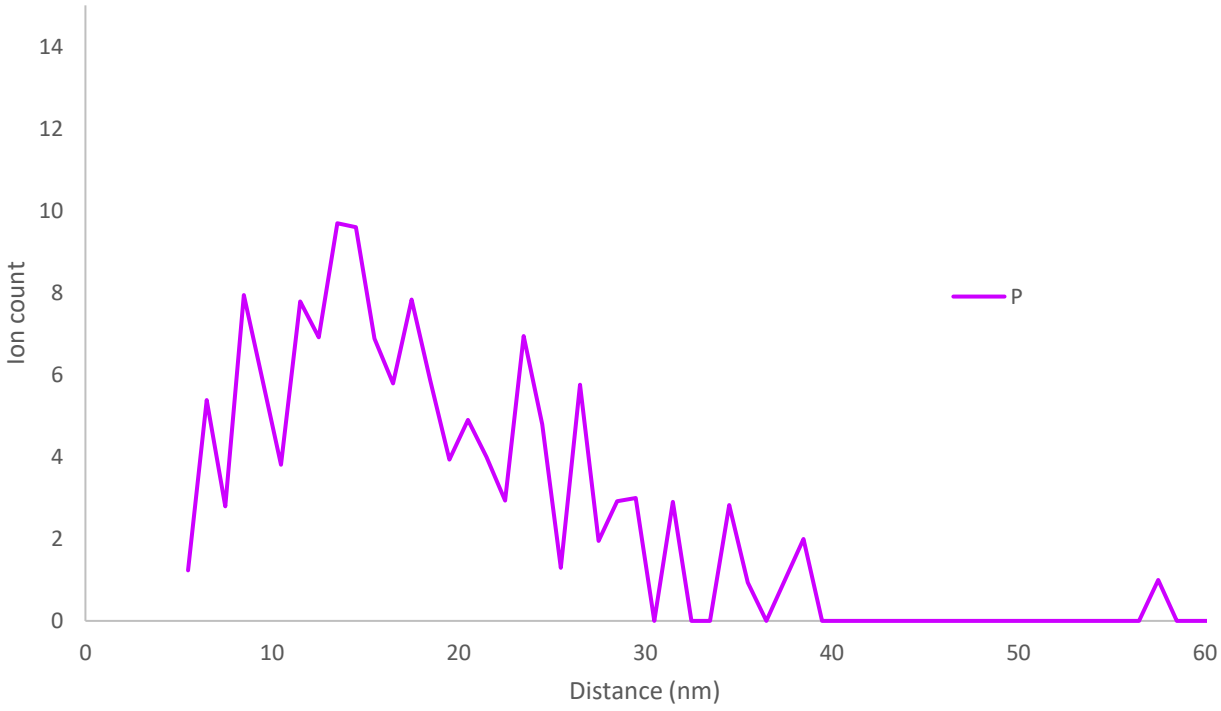


Figure 4.17 – The phosphorus profile in terms of ion count for the implanted profile after the first local minima of phosphorus concentration for the 30 nm x 30 nm x 100 nm ROI.

4.2.2 Analysis of lift out sample with nickel capping layer. Predicted peak phosphorus concentration 0.2 at.%.

Analysis conditions: LEAP 3000X HR, 40 K, 200 kHz pulse frequency, 0.32 nJ laser energy throughout, 0.4% detection rate in capping layer and 0.5% after capping layer.

In an attempt was made to reduce the effect of thermal tails from the majority silicon species obscuring the phosphorus mass spectra peaks, a reduced base temperature of 40 K was used in the analysis of the sample shown in Figure 4.18. A higher laser energy was used than was used for the micro post sample in order to reduce voltage induced stresses during the interface region and it was kept constant in an effect to attempt to reduce changes in mass spectra throughout the interface region.

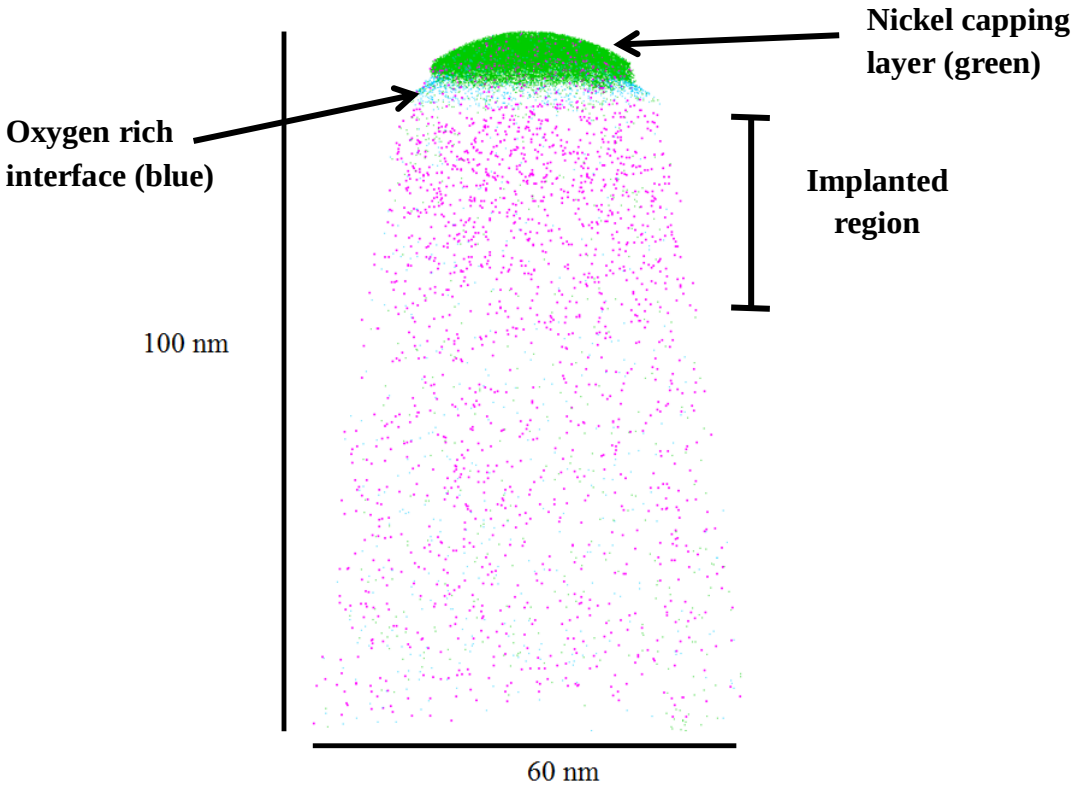


Figure 4.18 – Atom map with nickel (green), oxygen (blue) and P^{+} and P^{2+} species (purple).

A 15 at.% Ni^+ iso-concentration surface was used to initially delineate the capping layer/substrate interface and an ROI was used to determine the local mass spectra beneath this. Phosphorus peaks at 31 Da (Figure 4.19) and 15.5 Da (Figure 4.20) are clearly visible below the iso-concentration surface. No peak at 62 Da was found in the region below the iso-concentration surface, indicating that $(^{31}P_2)^+$ complex ions are not present.

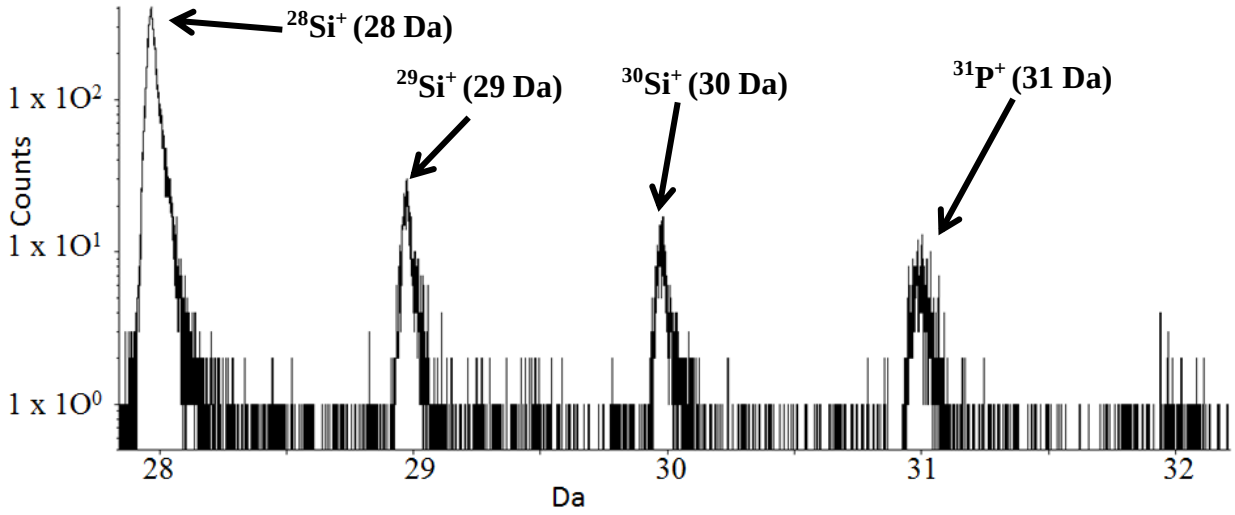


Figure 4.19 – Mass spectrum from ROI in the 28 Da – 32 Da range.

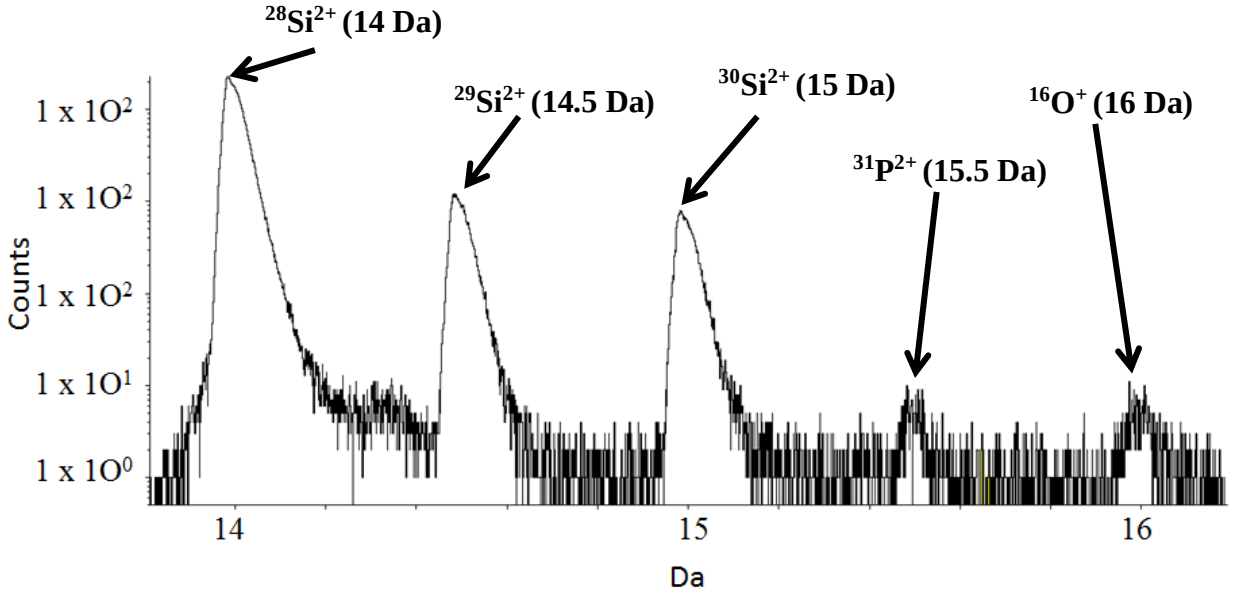


Figure 4.20 – Mass spectrum from ROI in the 14 Da – 16 Da range.

A coherent, as assessed by a smooth and unbroken iso-concentration surface, silicon oxide layer was found at the surface of the sample (Figure 4.21) and was found to start at - 5 nm but had its main concentration region starting at -1.5 nm. The 15 at.% Ni^+ iso-concentration surface was again used to generate a proximity histogram due to the increased flatness and uniformity compared to that of the silicon oxide.

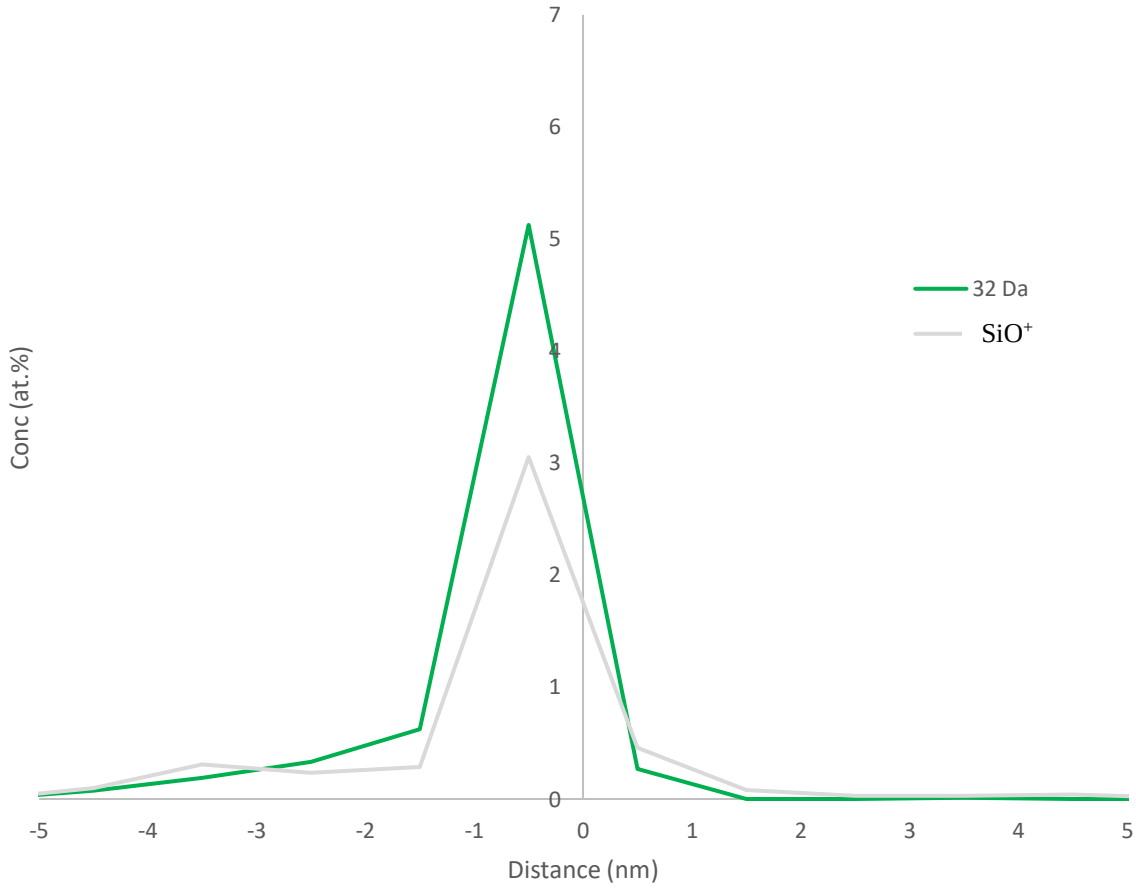


Figure 4.21 – Profiles of silicon oxide and species at 32 Da generated from the 15 % Ni^+ iso-concentration surface.

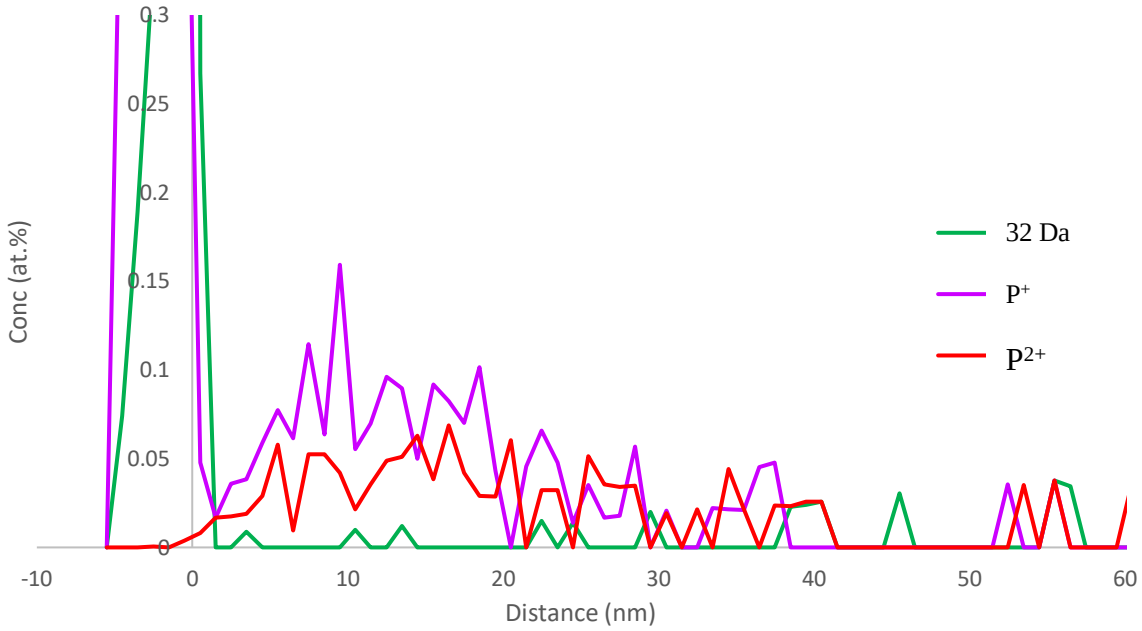


Figure 4.22 – P^+ and P^{2+} species concentration profiles and species at 32 Da generated from 15 at.% Ni^+ iso-concentration surface.

The P^+ and P^{2+} species concentration profiles can be seen to overlap over the same depth profile in Figure 4.22, with P^+ species contributing more than the P^{2+} species. The summed phosphorus profile in Figure 4.23 appears to peak prior to the predicted depth of ~ 23 nm and instead peak at ~ 15 nm.

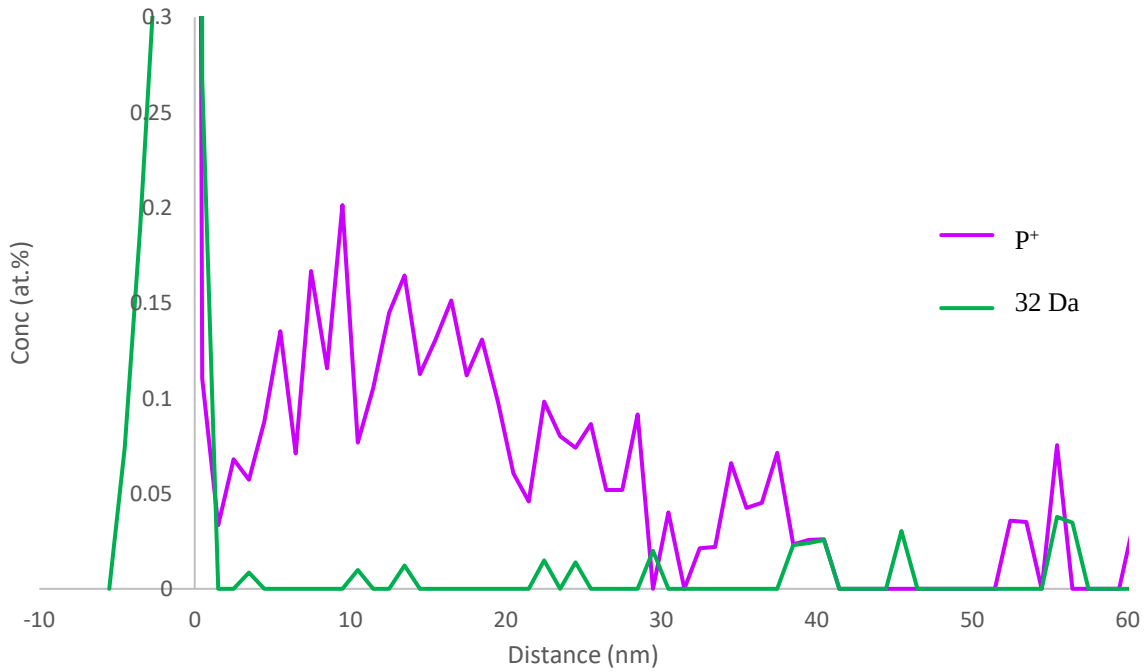


Figure 4.23 – Summed phosphorus concentration profile and species at 32 Da generated from 15 at.% Ni^+ iso-concentration surface.

Due to the lack of the silicon oxide layer in the micro post sample, the phosphorus profile had been deemed to start at the first local minima of the species at 32 Da which would relate to the end of the nickel capping layer. Despite this being the most suitable method for the limited information available, this will likely have some inaccuracies in starting due to the observed offsets between the start of the silicon oxide layer and the first local minima of the species at 32 Da in the lift out sample in Figure 4.21. It was found that the comparison of the concentration profiles of the micro post and the lift out showed good agreement with the latter being offset by 5 nm from the initial 15 at.% Ni^+ capping layer (Figure 4.24). SRIM profiles of predicted peak phosphorus concentrations of 0.2 at.% were found to overestimate the peak concentration. A better fit was found using 0.16 at.% predicted peak phosphorus concentration. The profile shape for both was found to be a good fit although in order to obtain greater depth agreement with the measured profiles, a

greater offset than 5 nm may be needed. However, this may not be a justifiable decision due to the lack of information about the exact starting point of the silicon oxide layer.

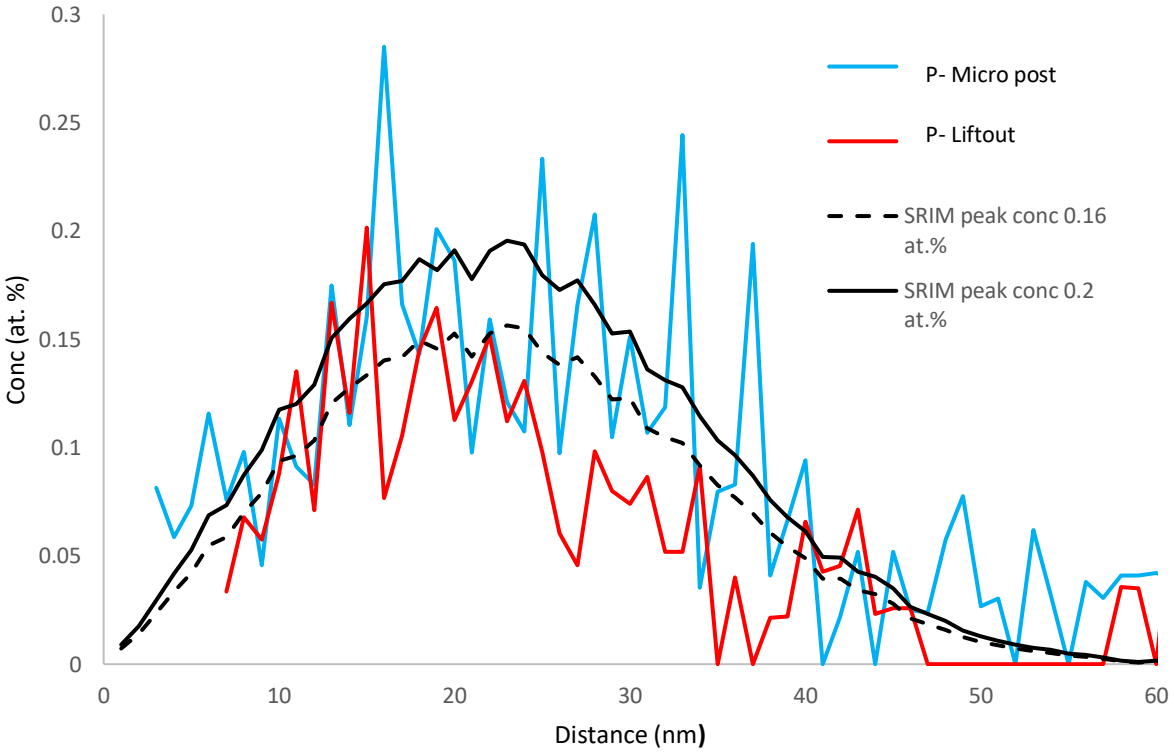


Figure 4.24 –Comparison between phosphorus concentration profiles from implanted micro post and lift out. SRIM profiles for 0.2 at.% and 0.16 at.% are overlaid.

This indicates that although the expected ~ 2 nm silicon oxide is almost certainly present at the surface of these samples, the apparent thickness as measured by APT is much thicker. Due to evaporation artefacts at the nickel/silicon oxide/silicon interface, this thicker oxide layer is correspondingly less dense [203]. This shows that, in order to correctly determine the location of the starting point of the implantation profile, the depth at which silicon oxide is first detected needs to be used rather than the first rise to a local maxima.

The ion counts from 30 nm x 30 nm x 100 nm ROIs from each sample were extracted and normalised in the same manner as the concentration profiles and are presented in Figure 4.25. There were small differences in depth in each sample at which mass spectra overlaps from the capping layer ended, and so the profiles were truncated where they both reached a local minimum in ion count.

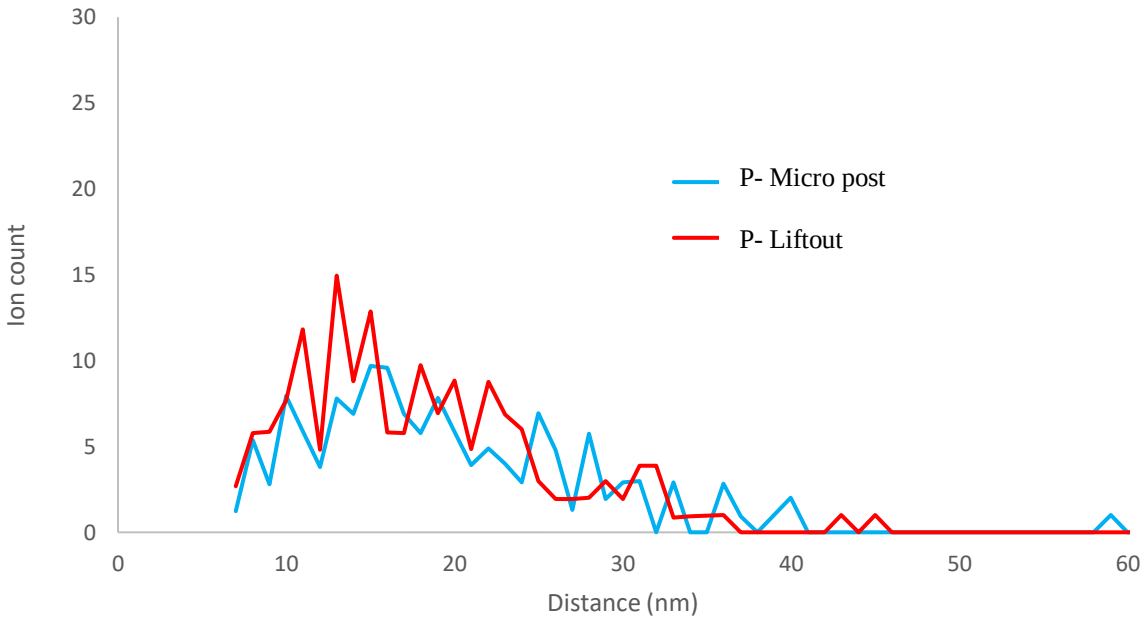


Figure 4.25 – Comparison between summed phosphorus ion counts between implanted micro post and lift out samples for 30 nm x 30 nm x 100 nm ROI.

The phosphorus ion count profiles from the micro post and lift out sample show good agreement. The total number of phosphorus ions in a comparable volume (30 nm x 30 nm x 60 nm) for the micro post was 140 and the lift out contained 170. These values are slightly offset but, as this only a comparison between two single samples, repeats would be required to determine how statistically significant this offset is. The analysis parameters were also not completely identical and repeat measurements need to be taken from both

micro post and lift out samples with identical analysis parameters. The difference between these two summations is small enough that small variations in ranging and background could readily account for these and a more rigorous automated ranging approach could improve the confidence of these measurements.

A single lift out sample that was implanted with the 0.1 at.% predicted peak concentration was successfully analysed, although the analysis conditions were substantially different from the samples shown here such that they would not be readily comparable. However, the measured profiles do match reasonably well with those shown here and indicate that the peak concentration of 0.1 at.% is reaching the limit of detection of these implants. This comparison can be found in Appendix C using the single viable dataset from those samples implanted with 0.1 at.% peak concentration phosphorus.

4.2 Analysis using LEAP 5000 XR

4.2.1. Analysis of implanted micro post with cobalt capping layer. Predicted peak phosphorus concentration 0.2 at.%. Laser energy 50 pJ

Analysis conditions: 200 kHz, 50 K, 50 pJ, 0.5% detection rate all the way through analysis.

This sample was not dipped in HF prior to the deposition of a cobalt capping layer. The choice not to remove the implanted oxide layer prior to deposition was made due to the availability of the LEAP 5000 XR system and the UV laser system therein. The atom probe analysis of fragile materials and multilayer systems which contain both conductive and insulating layers has been shown to be more viable using these lower wavelength lasers. Therefore, it was deemed that even though the potentially thicker, damaged oxide layer may reduce yield, it was an acceptable risk in order to potentially improve quantification of the phosphorus in the interface regions.

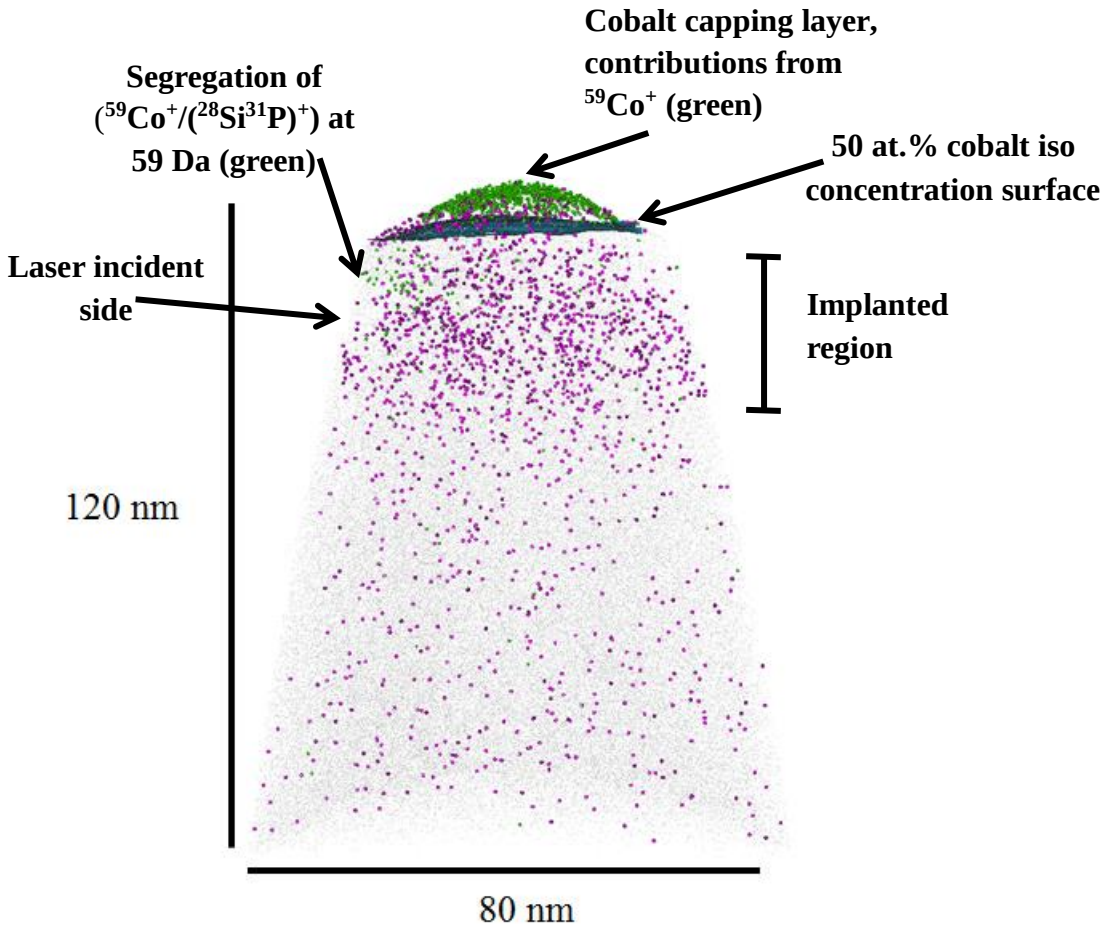


Figure 4.26 – Atom map showing distribution of $^{31}P^{+}$ and $(^{31}P_2)^{+}$ species(purple) with 59 Da ($^{59}Co^{+}$/($^{28}Si^{31}P)^{+}$) species (green) and silicon (grey). Iso-concentration surface of 15% cobalt species (blue).

A visual segregation of the species at 59 Da to the laser incident side can be observed in the atom map in Figure 4.26. Known phosphorus containing species ($^{31}P^{2+}$,$^{31}P^{+}$and $(^{31}P_2)^{+}$ at 15.5 Da, 31 Da and 62 Da respectively) are also seen at the depth predicted to contain the majority of the implant and the segregated species at 59 Da are approximately at the start of that implant region.

This segregation was not found in analyses of similar materials using the LEAP 3000X HR system and can be linked to the increased surface absorbance and reduced spot size of the UV laser used in the LEAP 5000 XR system [3].

The atom map shown in Figure 4.27 is a top down view of Figure 4.26 that has also been clipped in the z direction to isolate the implanted region. The species at 59 Da species (shown in green) can be clearly seen segregating to the laser incident side in the upper left of the figure.

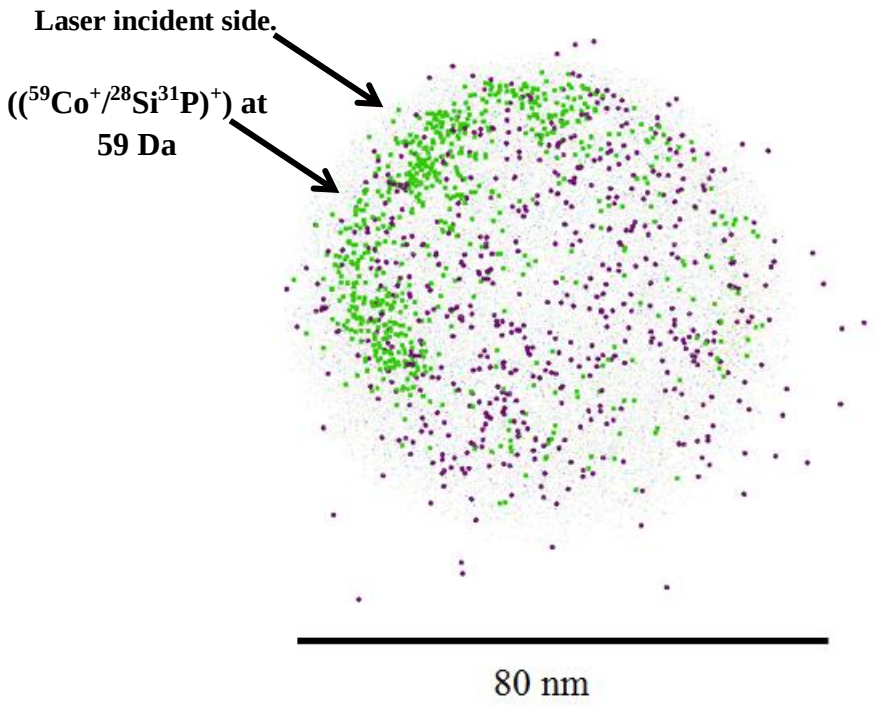


Figure 4.27 – Top down view of atom map, clipped to isolate the implanted region. P^+, P^{2+} and P_2^+ species (purple), 59 Da ($(^{59}Co^+/^{28}Si^{31}P)^+$) (green).

It is possible that this ion species is residual cobalt that has diffused from the capping layer due to the laser heating, atoms from a non-uniform capping layer from that side of the tip

or a delayed evaporation or reconstruction artefact that has shifted the apparent location of this species. However, this species is located precisely at the depth where the implanted region is predicted to be and thus should be considered to potentially be $(^{59}Co^{+}/^{28}Si^{31}P)^{+}$**.** It is not immediately apparent if this laser-induced segregation will result in a concentration change across the sample tip as a function of distance from the laser or if it is only a change in the type of phosphorus containing species. If the local concentration changes as function of location due to a laser induced effect, the extraction of a central ROI in order compare implant dose in terms of ion count may be inaccurate. As the P_2^{+} complex ions do not show this visual segregation to the laser incident side, this provides some evidence that the laser induced segregation of the SiP^{+} species is just preferential evaporation of phosphorus in that form. In order to assist in local ranging of mass spectra in the implanted region, a ROI was placed around the predicted implanted region, highlighted by the known phosphorus species and the mass spectra extracted from the ions within.

Peaks corresponding to the $(^{59}Co^{+}/^{28}Si^{31}P)^{+}$ and $(^{59}Co^{1}H)^{+}$ species at 59 and 60 Da can be seen in the mass spectra in Figure 4.28. As the capping layer is of cobalt rather than nickel, there are no mass spectra overlaps between at 62 Da and so any peak there can be considered to be $^{31}P_2^{+}$. A small peak at 15.5 Da can be seen in Figure 4.30. The Si^{2+} charge state is the majority species detected for this sample but the extent of the thermal tails can be seen to be minimal. The amount of phosphorus in the P^{2+} charge state is also minimal. There is a preference for silicon ions to be detected in the Si^{2+} species in this sample. Peaks at 29.5 Da, 31 Da and 32 Da are seen in Figure 4.29 which correspond to $(^{59}Co^{2+}/^{28}Si^{31}P)^{2+}$, $(^{31}P^{+}/^{30}Si^{1}H)^{+}$ and $^{16}O_2^{+}$ respectively.

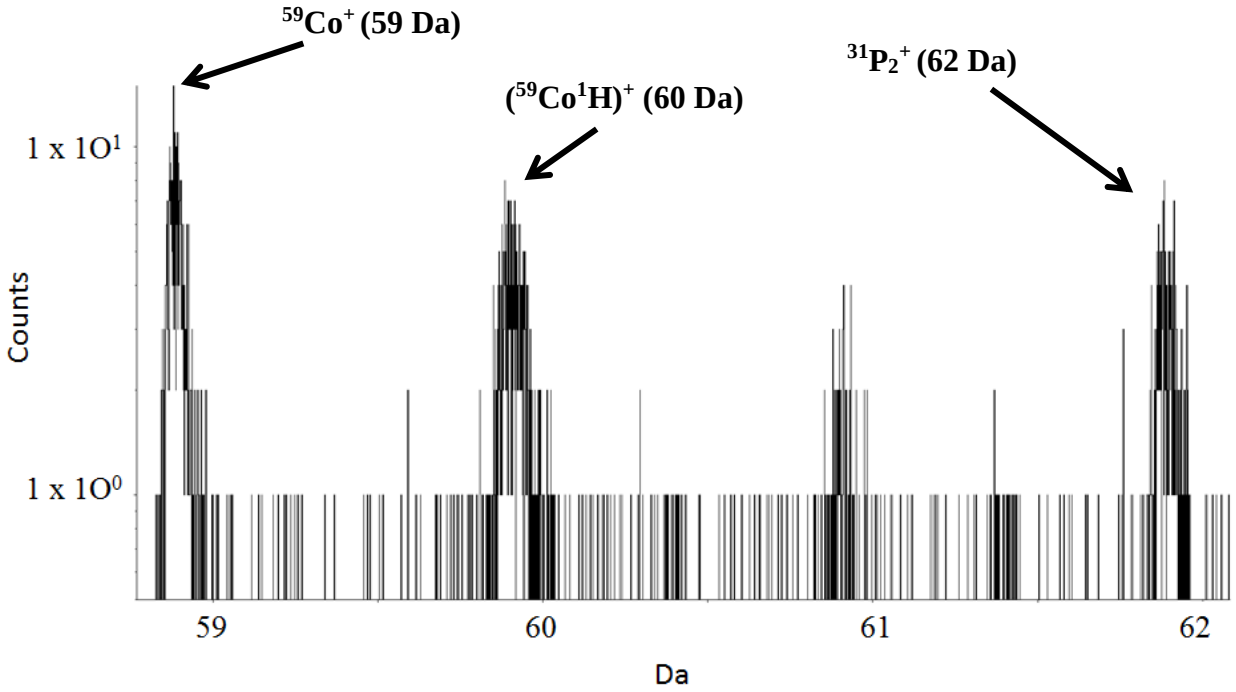


Figure 4.28 – Mass spectra of 59 Da – 62 Da range in ROI.

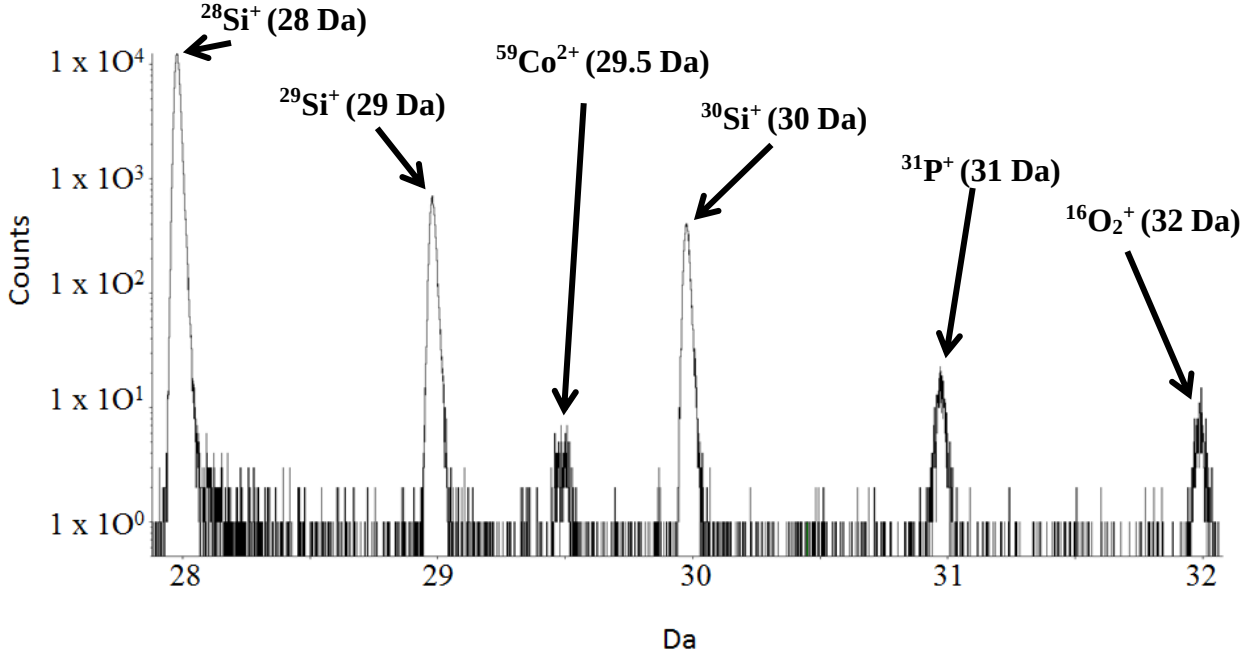


Figure 4.29 – Mass spectra of 28 Da – 32 Da range in ROI.

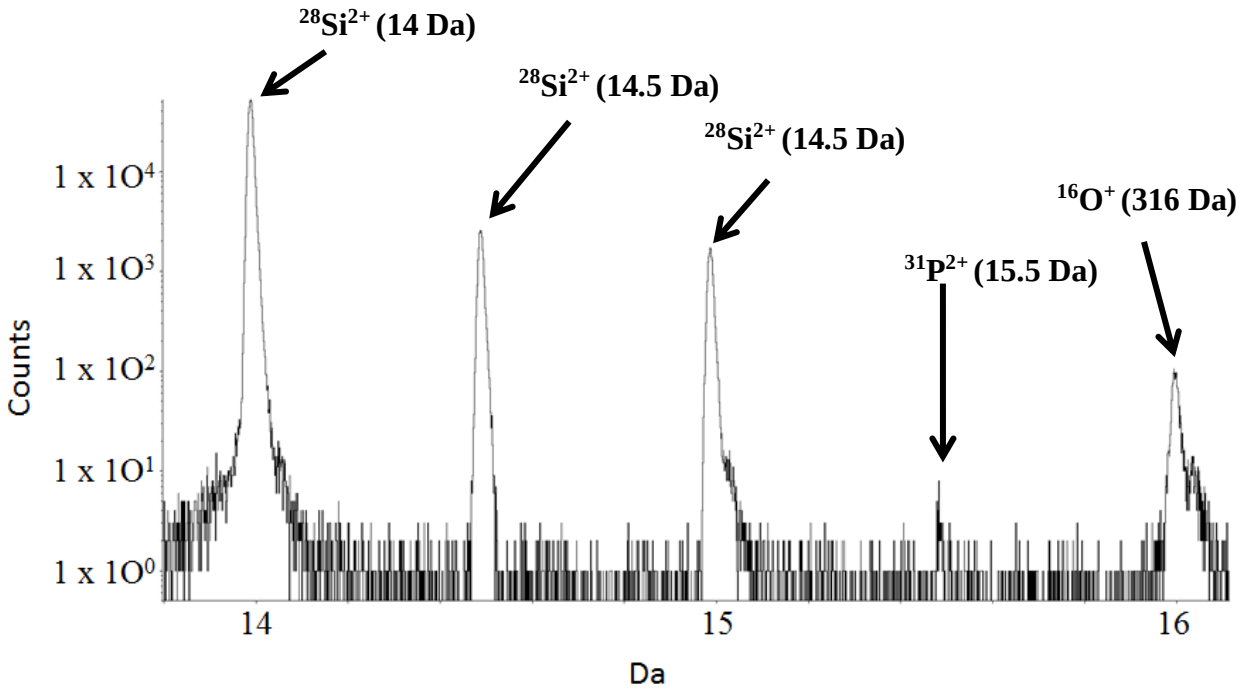


Figure 4.30 – Mass spectra of 14 Da – 16 Da range in ROI.

A 15 at.% cobalt iso-concentration surface to initially delineate the surface and the silicon oxide ($^{28}Si^{16}O)^{+}$ at 44 Da) profile around this surface is shown in a proximity histogram in Figure 4.31. It was possible to generate a smooth and unbroken 3 at.% silicon oxide iso-concentration surface, so it is likely that the oxide layer was intact prior to analysis. Due to the thinness of the capping layer it was not possible to determine the exact starting point of the silicon oxide layer.

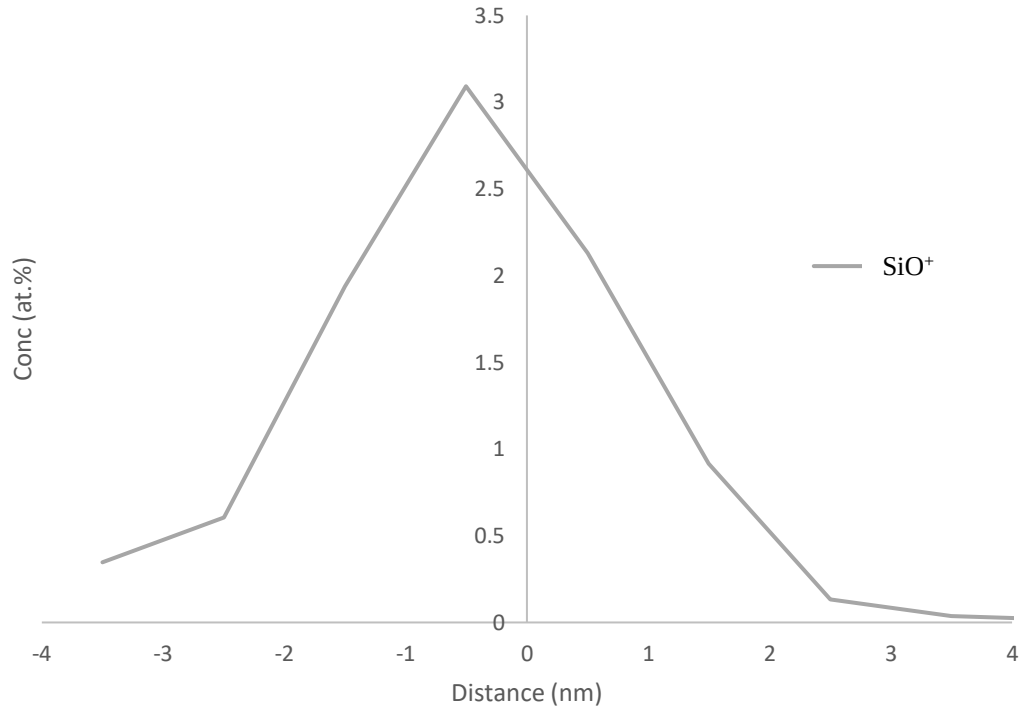


Figure 4.31 – A silicon oxide layer can be seen close to the interface generated from the 15 at.% cobalt iso-concentration surface capping layer. The start of the interface was deemed to start at ~ - 5 nm.

A starting point ~ -5 nm from the initial 15 at.% cobalt iso-concentration surface is reasonable via extrapolating from the peak shape in Figure 4.31 and from previous LEAP 3000X HR analyses of similar samples (Figure 4.21).

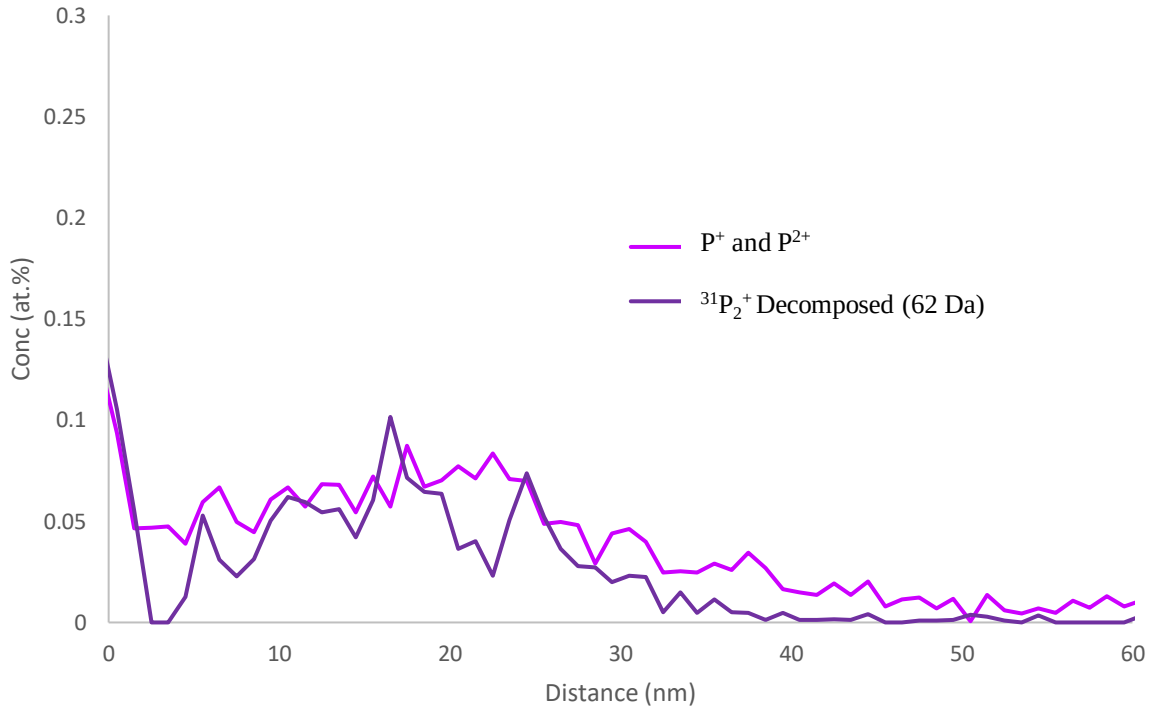


Figure 4.32 – Concentration profile of single ion phosphorus species (P^+ and P^{2+}) and the decomposed complex phosphorus ion P_2^+ generated from 15 at.% cobalt iso-concentration surface.

It can be seen in Figure 4.32 that there is a substantial contribution from the species at 62 Da, in the form of the P_2^+ complex ion, to the overall phosphorus concentration profile. The majority of the single ion phosphorus species detected were in the P^+ charge state, with the P^{2+} species only contributing a small amount to the profile. The P_2^+ profile can be seen to rise from the background at approximately 3 nm into the profile whilst the summed P^+ and P^{2+} profile can be seen to not reach background levels prior to rising in concentration into the main implant peak. This is likely due to the overlap between $^{31}P^+$ and $(^{30}Si^1H)^+$ at 31 Da, as a similar overlap does not seem to affect the P_2^+ species. Care must be taken when using the decomposed profile from the P_2^+ species. Although the

decomposition process is required to correctly report the summed phosphorus concentration, it also causes an apparent increase in concentration in the tail region when the P_2^+ ion count has reached background levels. At this point, the background contributions from the P_2^+ species are effectively double, potentially artificially increasing both the concentration and extent of the tail region.

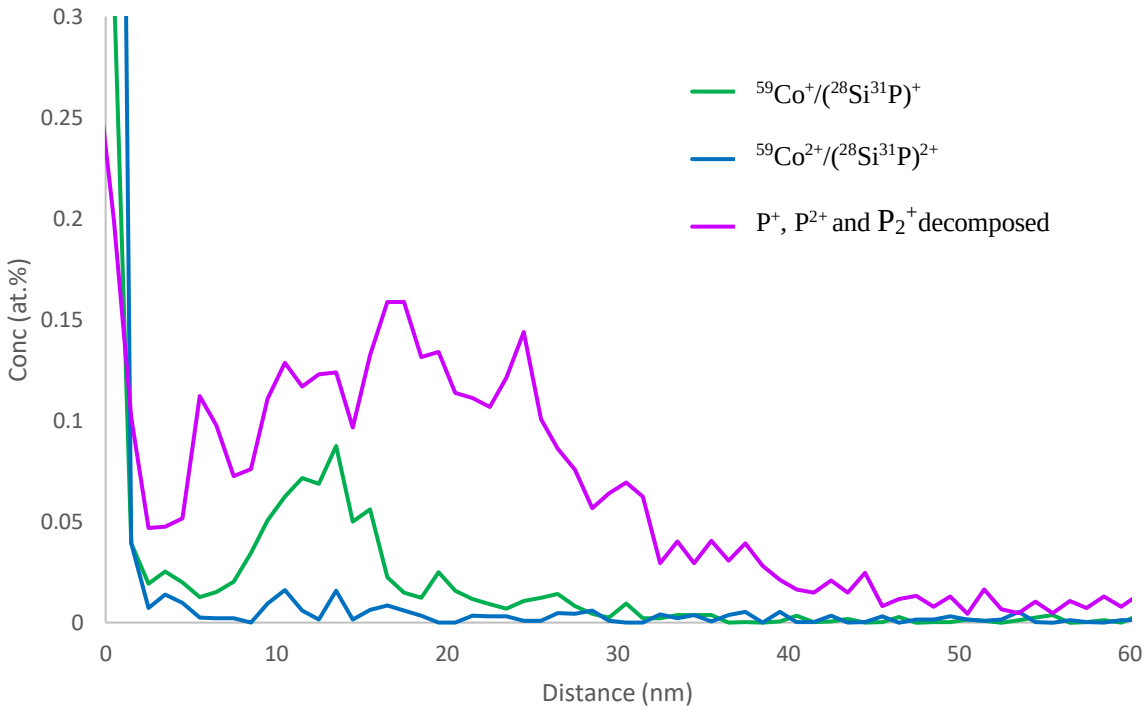


Figure 4.33 – Concentration profile of summed known phosphorus species compared with $^{59}Co^+/(^{28}Si^{31}P)^+$ species at 59 Da and $^{59}Co^{2+}/(^{28}Si^{31}P)^{2+}$ species at 29.5 Da.

By overlaying the depth profiles from known phosphorus species onto those from 59 Da and 29.5 Da (Figure 4.33), it is apparent that the increase in concentration is within the implanted region and indicates that these species are indeed $(^{28}Si^{31}P)^+$ and $(^{28}Si^{31}P)^{2+}$.

Further evidence for the identity of the $(^{28}Si^{31}P)^{+}$ and $(^{28}Si^{31}P)^{2}$ species can be seen via the drop in concentration of known phosphorus species (P^{+}, P^{2+} and P_2^{+}) over the same region as an increase in these species at 59 Da and 29.5 Da. As the overall concentration does not suggesting that the preferential form of phosphorus in this region has shifted towards $(^{28}Si^{31}P)^{+}$ and $(^{28}Si^{31}P)^{2+}$.

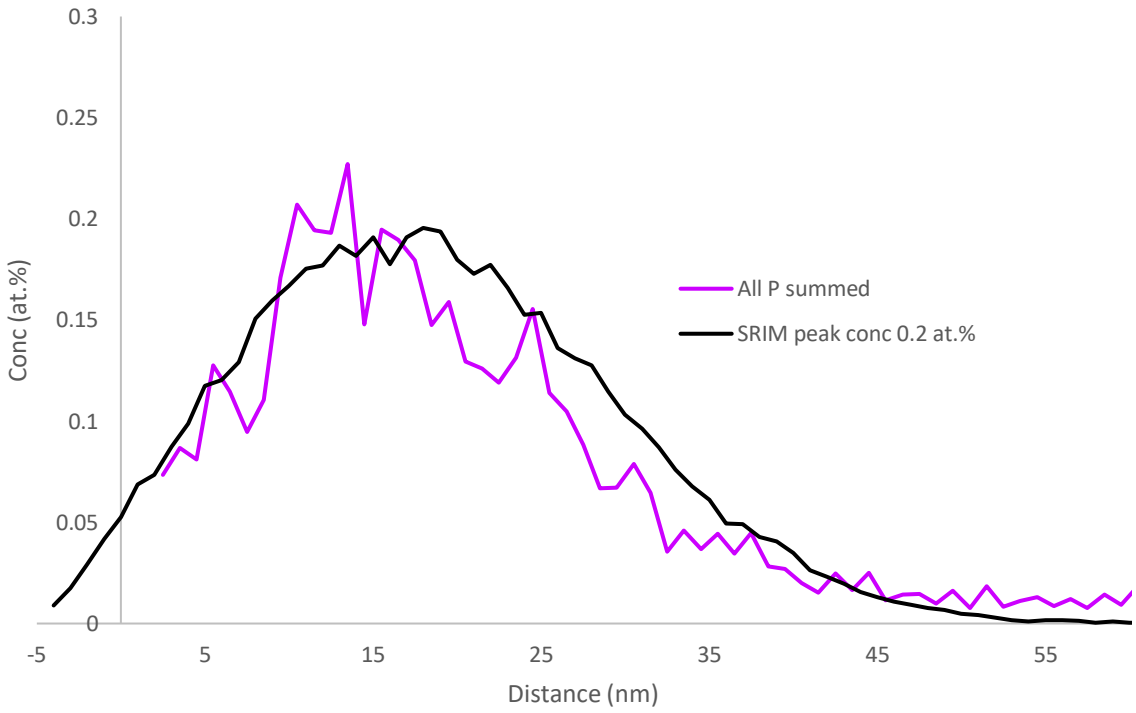


Figure 4.34 – All summed phosphorus species, including the deconvoluted $(^{28}Si^{31}P)^{+}$, $(^{28}Si^{31}P)^{2+}$ and $^{31}P_2^{+}$ species, compared with a SRIM profile of predicted peak concentration of 0.2 at.%. Profiles drawn from 15 at.% cobalt iso-concentration surface.

The concentration profile of all phosphorus species, including the $(^{28}Si^{31}P)^{+}$, $(^{28}Si^{31}P)^{2+}$ and $^{31}P_2^{+}$ species, are summed in Figure 4.34 and compared with the SRIM profile of predicted peak concentration of 0.2 at.% phosphorus. The start of the SRIM profile was offset by -5 nm from the 15 at.% cobalt iso-concentration surface in order to take into account the starting point of the silicon oxide layer.

The shape of the measured profile matches that of the SRIM profile but with small offsets in concentration and depth. As with previously seen samples (Figure 4.23), this lower peak concentration can be linked with extended tail regions and mislabelling of the 31 Da species at $^{31}P^{+}$ instead of $^{31}P_2^{+}$. This latter mislabelling artefact is more likely in this sample due to the increased contribution from the $^{31}P_2^{+}$ peak at 62 Da to the overall phosphorus concentration.

The offset in the depth of the peak can be linked to the selection of the starting point of the silicon oxide layer used, an increased offset may be required as was suggested after observing the same feature in a sample analysed using the LEAP 3000X HR (Figure 4.23). There are potential issues with SRIM predictions of implantation profiles of phosphorus in silicon [83], therefore semi arbitrarily changing the starting position of a given SRIM profile to fit the measured profile may not be appropriate.

In order to determine if the $(^{28}Si^{31}P)^{+}$ species segregation to the laser incident side also results in an increase in the overall concentration of phosphorus in that region, and consequently a reduction in the rest of the reconstruction, a 30 nm x 30 nm x 100 nm ROI was extracted from the centre of the dataset for further analysis. A clipped, top down atom map of the implanted region is given in Figure 4.35.

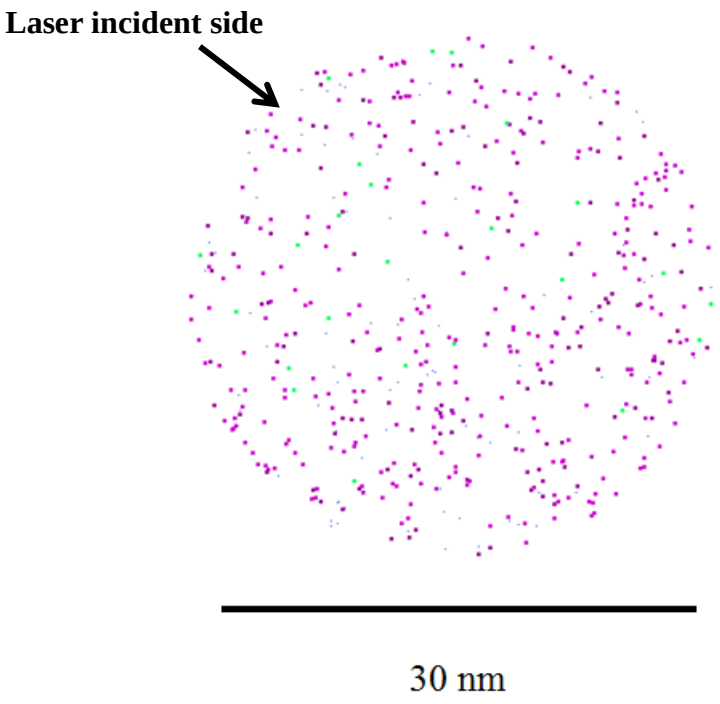


Figure 4.35 – Top down view of clipped atom map of known phosphorus species (purple) and peak at 59 Da (green) from the 30 x 30 x 100 nm ROI.

There is no apparent segregation of the species at 59 Da in the 30 nm x 30 nm x 100 nm ROI in Figure 4.35. This indicates that the segregation of the species at 59 Da,($^{59}Co^{+}$/($^{28}Si^{31}P)^{+}$) to the laser incident side (Figure 4.27 is restricted to the outer shell of the tip as expected from UV laser pulsing [179]

4.2.2 Analysis of implanted micro post with cobalt capping layer. Predicted peak phosphorus concentration 0.2 at.%. Laser energy 25 pJ

Analysis conditions: 50 K, 25 pJ, 200 kHz, 0.5 % detection rate throughout analysis.

In order to reduce the potential effect of the laser-induced segregation of phosphorus species and the reduction of field evaporation of complex ion species in general, a laser

pulse energy of 25 pJ was used in analysing this sample compared to the 50 pJ laser energy used in the previous sample (4.2.1), whilst the same detection rates were used. This had the effect of increasing the standing voltage required to maintain the same detection rate. It also dramatically reduced the yield of samples that survived analysis through the capping layer/substrate interface. Only a single sample analysed using a pulse energy of 25 pJ was successful (Figure 4.36).

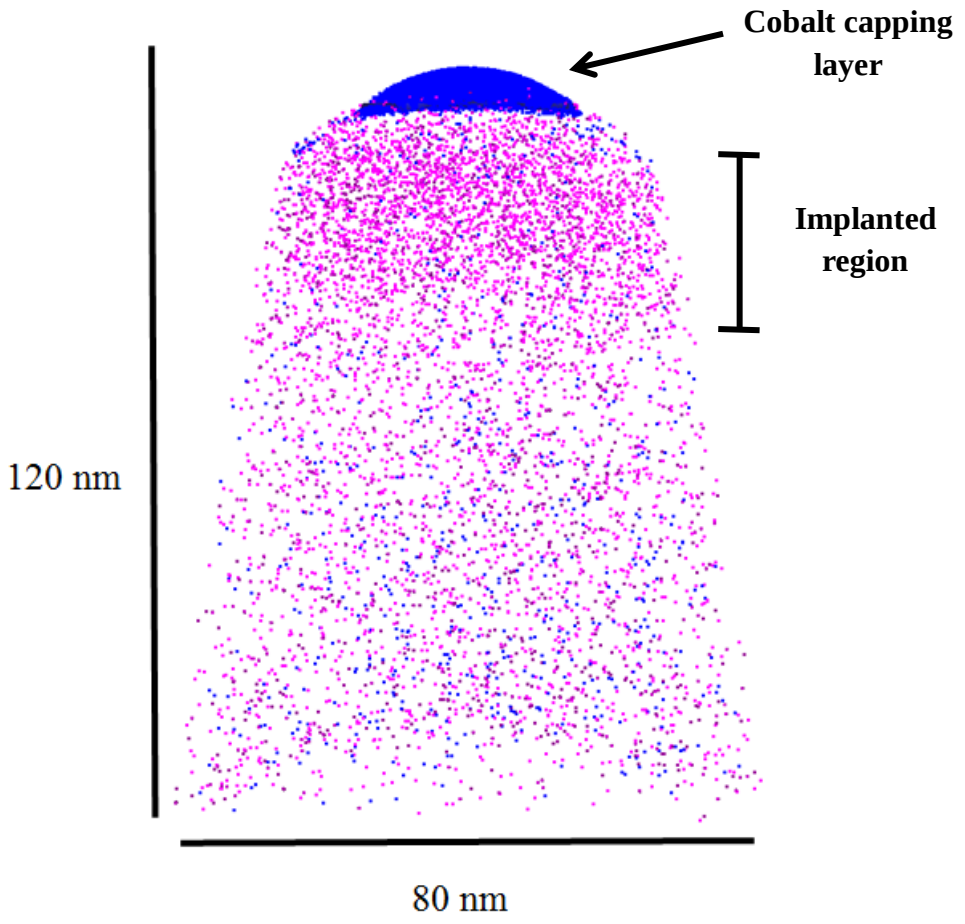


Figure 4.36 – Atom map of distribution of P^+ and P^{2+} species and cobalt capping layer species.

An atom map of the distribution P^+ and P^{2+} species can be seen in Figure 4.36, showing a distinct concentration at the predicted implantation depth. No such visible segregation

could be observed for potential phosphorus containing species such as $(^{28}Si^{31}P)^+$ or P_2^+ at 59 Da and 62 Da respectively.

A 15 at.% cobalt iso-concentration surface was generated and a ROI was placed around the implanted region to inspect the local mass spectra and assist in local ranging.

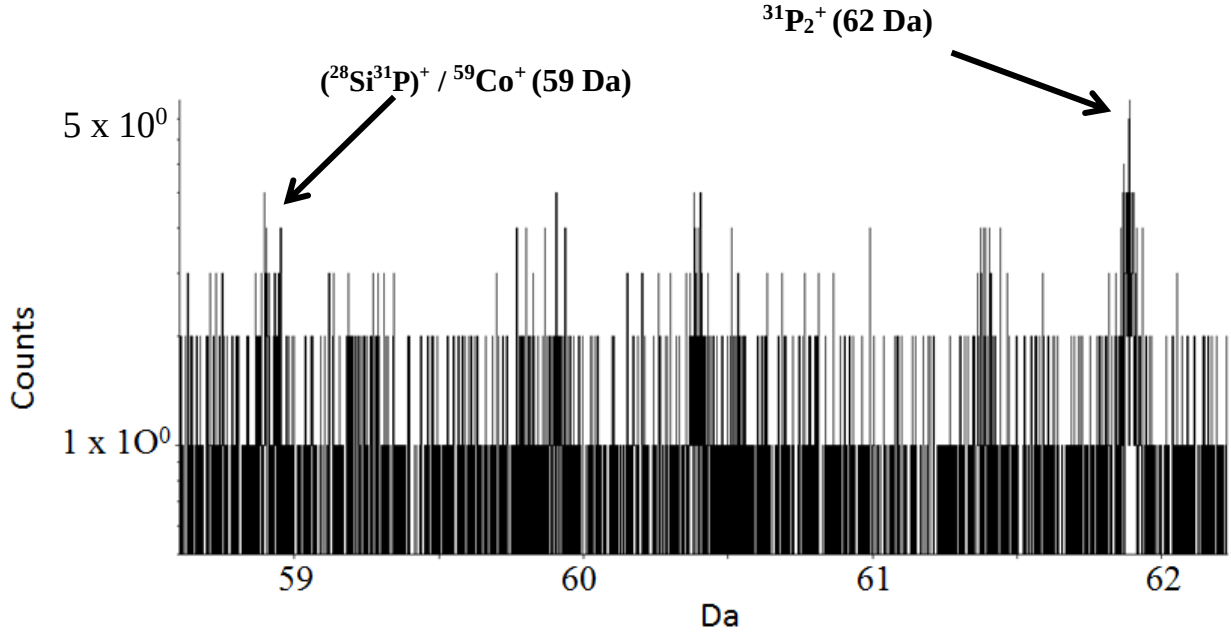


Figure 4.37 – Mass spectra in 50 Da – 62 Da region of ROI.

There is no significant peak at 59 Da and a small peak at 62 (Figure 4.37), indicating a reduced potential contribution from the $^{28}Si^{31}P^+/^{59}Co^+$ species in both the capping layer and implanted region and a small contribution from the P_2^+ species to the phosphorus profile (Figure 4.37). This reduction in complex ion species in this sample compared to that found in the sample analysed using 50 pJ laser pulses (Figure 4.28) can be linked to the increased standing field required to maintain the given detection rate whilst using a reduced laser pulse energy.

Similarly to that found for the sample analysed using 50 pJ laser pulses (Figure 4.29), there is a small peak at 29.5 Da that corresponds to the $(^{28}Si^{31}P)^+/^{59}Co^{2+}$ species and a peak at 31

Da that corresponds to $^{31}P^{+}$/ $(^{30}Si^{1}H)^{+}$. Despite a lower ion count within the ROI of this sample, there is also a noticeable increase in the noise background in Figure 4.38 compared to that in Figure 4.29.

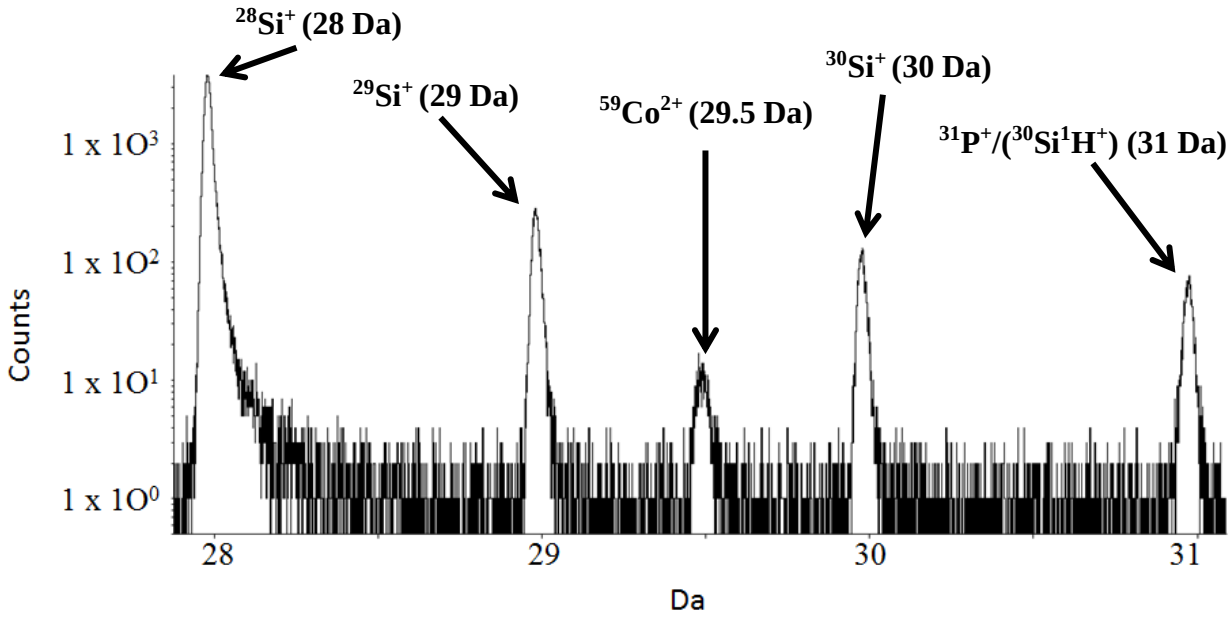


Figure 4.38 – Mass spectra in 28 Da – 31 Da region of ROI.

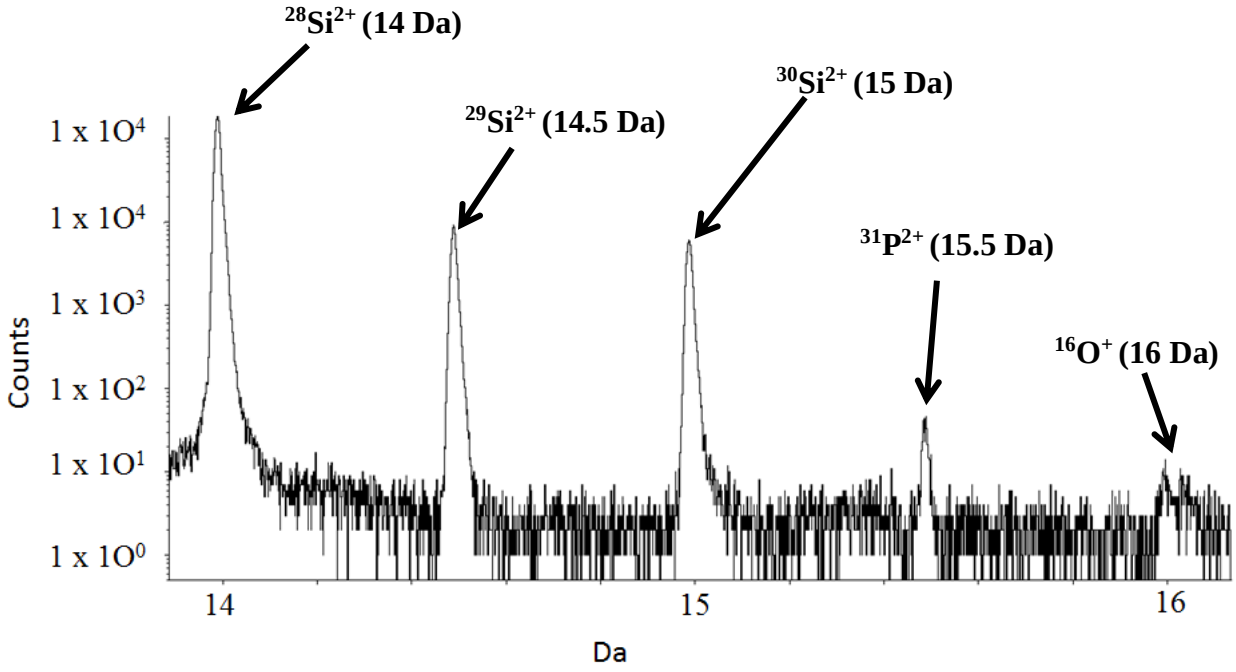


Figure 4.39 - Mass spectra in 14 Da – 16 Da region of ROI.

The P^{2+} peak at 15.5 Da is considerably larger than that found in the sample analysed using 50 pJ laser energy (Figure 4.30) and the charge state ratio Si^{2+}/ Si^{+} was also increased (Figure 4.38 and 4.39) . This, combined with the reduction in the complex $^{28}Si^{31}P^{+}$ and P_2^{+} ions, indicates that the majority of the phosphorus in this sample was found in the P^{+} and P^{2+} ionic species. The background noise level for both Si^{+} and Si^{2+} charge state regions (Figures 4.38 and 4.39) was also greater than for the samples analysed using 50 pJ (Figures 4.29 and 4.30).

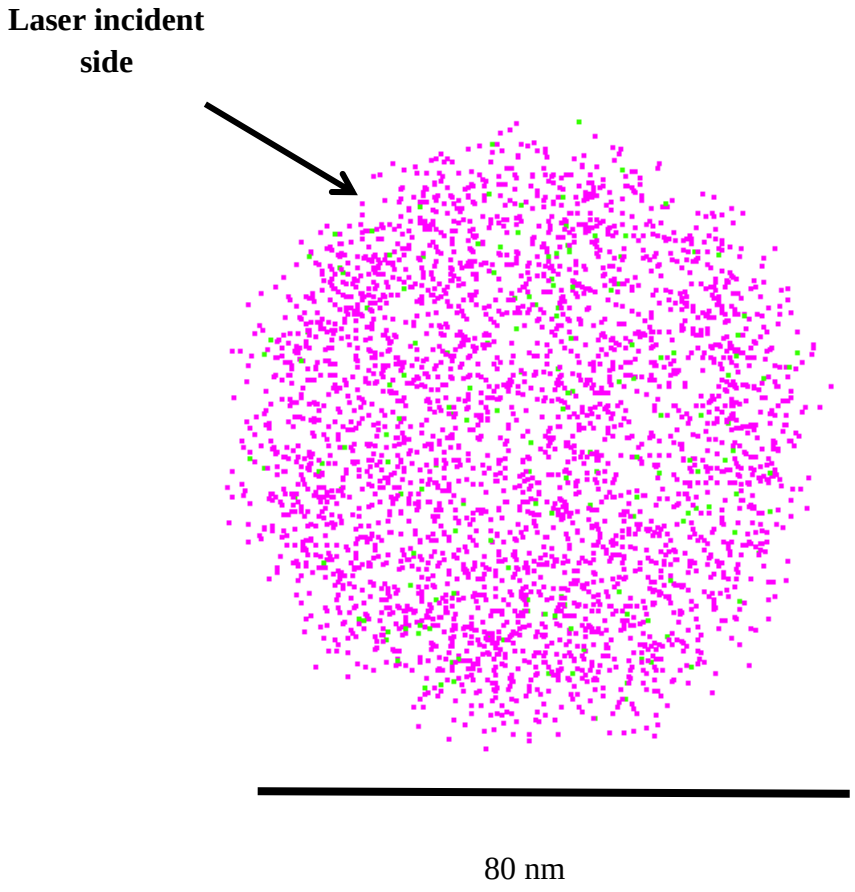


Figure 4.40 – Top down view of clipped atom map section in the implanted region with known phosphorus species (purple) and species at 59 Da (green).

No segregation of the species at 59 Da, corresponding to $(^{28}Si^{31}P)^{+}$, was found to the laser incident side in this sample (Figure 4.40). This indicates that the standing field required for evaporation was suitably high when using laser pulse energies of 25 pJ to make the formation of these complex ions less preferential. The lack of segregation of the $(^{28}Si^{31}P^{+})$ species to the laser incident side suggests that the concentration of phosphorus species is more likely to be laterally uniform and so the extraction of an ROI volume for comparison between different samples will be more representative.

This reduction in complex ion formation, especially the $^{31}P^{+}$ ion, and greater preference for singly charged ion evaporation will give increased spatial resolution in the phosphorus distribution [237] and reduce the effect of mislabelling of the $^{31}P_2^{2+}$ ion as $^{31}P^{+}$ at 31 Da.

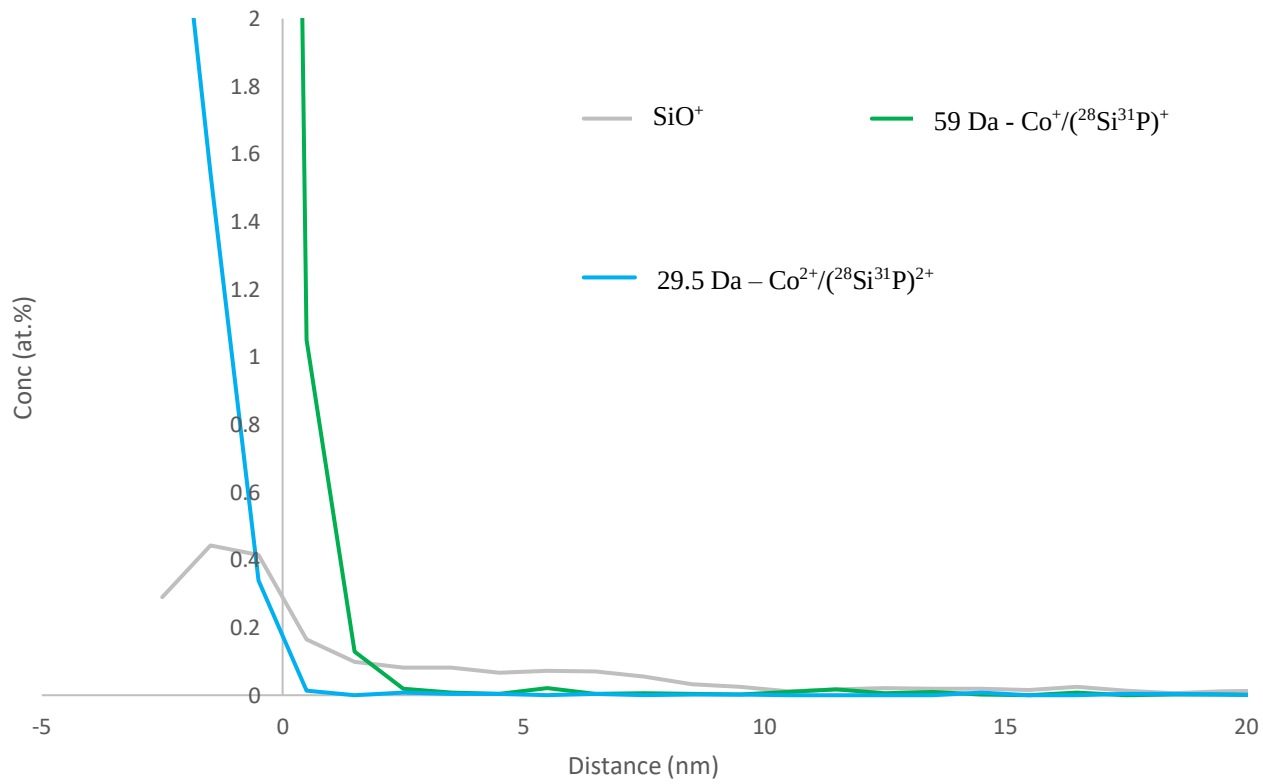


Figure 4.41 – Profiles of species at 59 Da ($^{59}Co^{+}/(^{28}Si^{31}P)^{+}$), species at 29.5 Da ($^{59}Co^{2+}/(^{28}Si^{31}P)^{2+}$) and silicon oxide from 15 at.% cobalt iso-concentration surface.

There was no visible peak in concentration of potential SiP species in the regions beyond the capping layer interface (Figure 4.41). Due to the relative thinness of the cobalt capping layer, it was not possible to determine the precise start of the silicon oxide layer that can be used to define the start of the implantation profile. The extent of the measured silicon oxide layer reaches background levels at ~ 10 nm after the interface; this is likely due to preferential retention of a small amount of oxide during analysis of the interface and is non-physical. The starting point of the silicon oxide, assuming a smooth decline from the measured peak, is at ~ - 5 nm from the interface from the 15 at.% cobalt iso-concentration

surface. This corresponds with previous apparent starting depths of silicon oxide seen in LEAP 3000X HR analysis of similar samples in Figure 4.23 and is a reasonable starting point for the implantation profile to be measured from. However, as previously seen in Figure 4.34, this estimate of the required offset for the start of phosphorus profile may be lower than required.

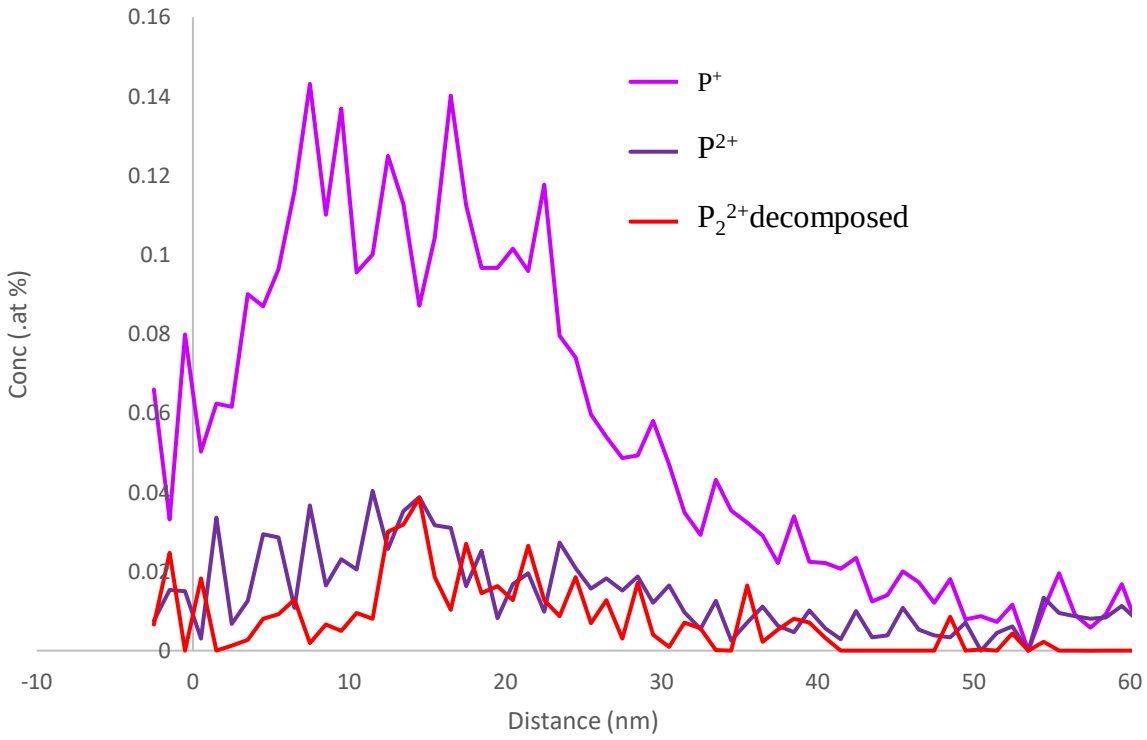


Figure 4.42 – Phosphorus concentration profile with P^+, P^{2+} and P_2^+ (decomposed).

The majority of phosphorus profile is from the P^+ species, with relatively equal amounts from the P^{2+} species and the decomposed P_2^+ complex ion (Figure 4.42). This contrasts with the ratios of phosphorus species in the sample analysed using 50 pJ laser pulses in Figure 4.32, where more phosphorus was found in the P_2^+ species and less in the P^{2+} species. This shows that in this sample, the preferential phosphorus species has shifted significantly towards the singly charged P^+ species from the P_2^+ species.

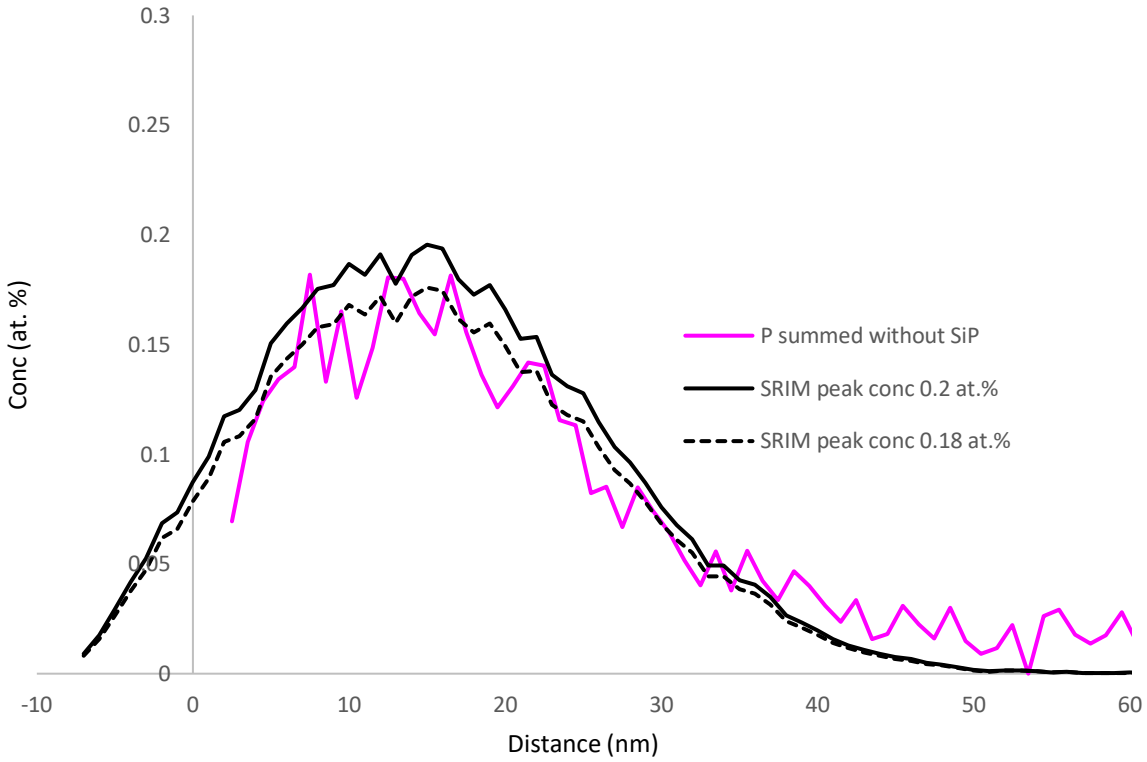


Figure 4.43 – Comparison of measured phosphorus profile with SRIM profiles of predicted peak phosphorus concentrations of 0.2 at.% and 0.18 at.%.

The starting point of the SRIM profile was set at -5 nm from the 15 at.% cobalt iso-concentration surface in order to match the estimated start of the silicon oxide signal (Figure 4.43).

The SRIM profile from the predicted peak phosphorus concentration of 0.2 at.% is shown to again over estimate the peak concentration of the measured profile, although the profile shape shows good agreement. A SRIM profile from the predicted peak phosphorus concentration of 0.18 at.% fits the measured profile better, although the measured profile also shows a small but significant tail section after ~ 40 nm which is not predicted by SRIM.

This overestimation by SRIM of the peak concentration was also found in LEAP 3000X HR analyses of similar samples (Figure 4.24). This reduction in peak concentration can be linked to phosphorus from the extended tail region but, as there is a reduced contribution from the complex P_2^+ ion, there is less likely to be any mislabelling of it as $^{31}P^+$ at 31 Da, thus reducing the apparent concentration. As the SRIM profiles match more closely to the measured profile, it is likely that this is occurring and the lower laser power has improved the accuracy of the measurement.

4.2.3 Comparison of concentration profiles from atom probe analyses using 50 pJ and 25 pJ laser pulse energies

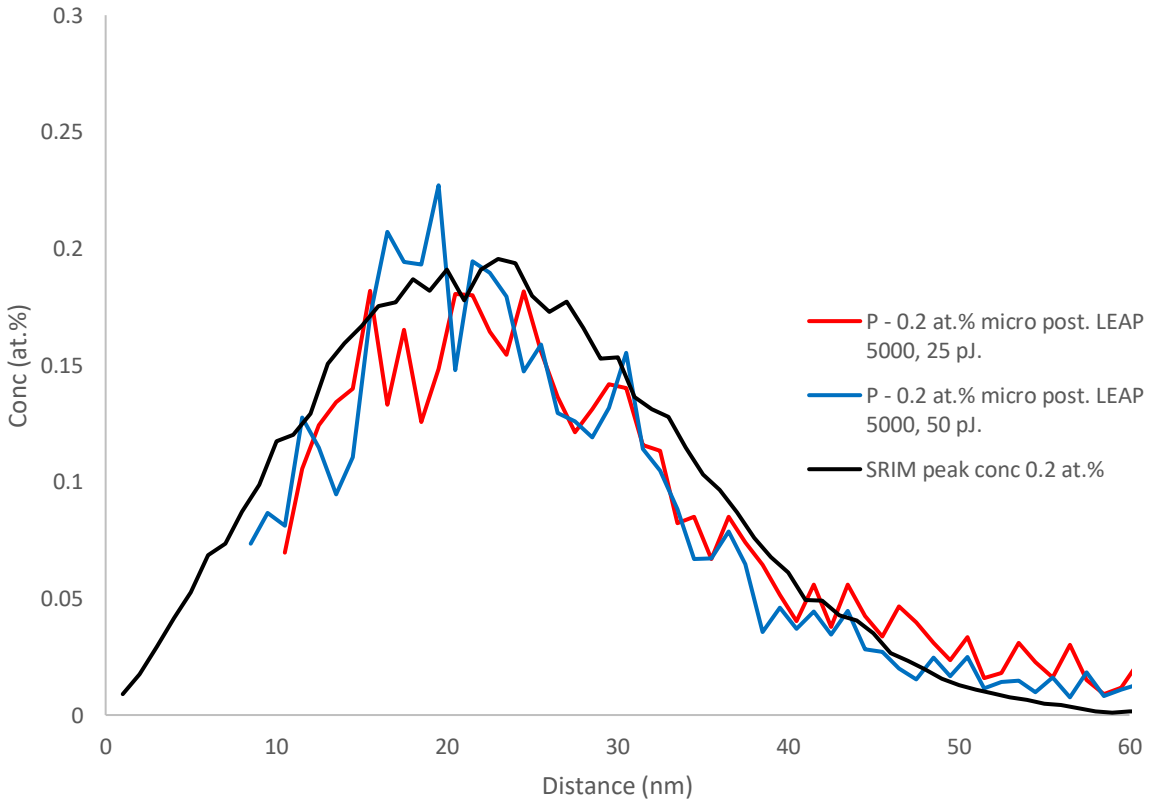


Figure 4.44 – Summed phosphorus profiles from micro posts analysed with 50 pJ and 25 pJ laser energies compared with SRIM from the predicted peak phosphorus concentration profile of 0.2 at.%.

The depth profiles of phosphorus for the two micro posts were normalised against their respective starting points with reference to their respective silicon oxide layers. There is good agreement between the measured phosphorus profiles from micro post samples analysed with 25 pJ and 50 pJ laser energies (Figure 4.44) and, in both cases, the peak concentration is less than is predicted by SRIM. Although reconstruction artefacts can alter the apparent depth profile of the implant, the peak concentration should not be affected [214]. Therefore, the drop in concentration can be attributed to physical effects prior to atom probe analysis or ranging/compositional errors of the mass which are relatively independent of the reconstruction parameters.

4.3 Comparison between analyses of LEAP 3000X HR and LEAP 5000 XR

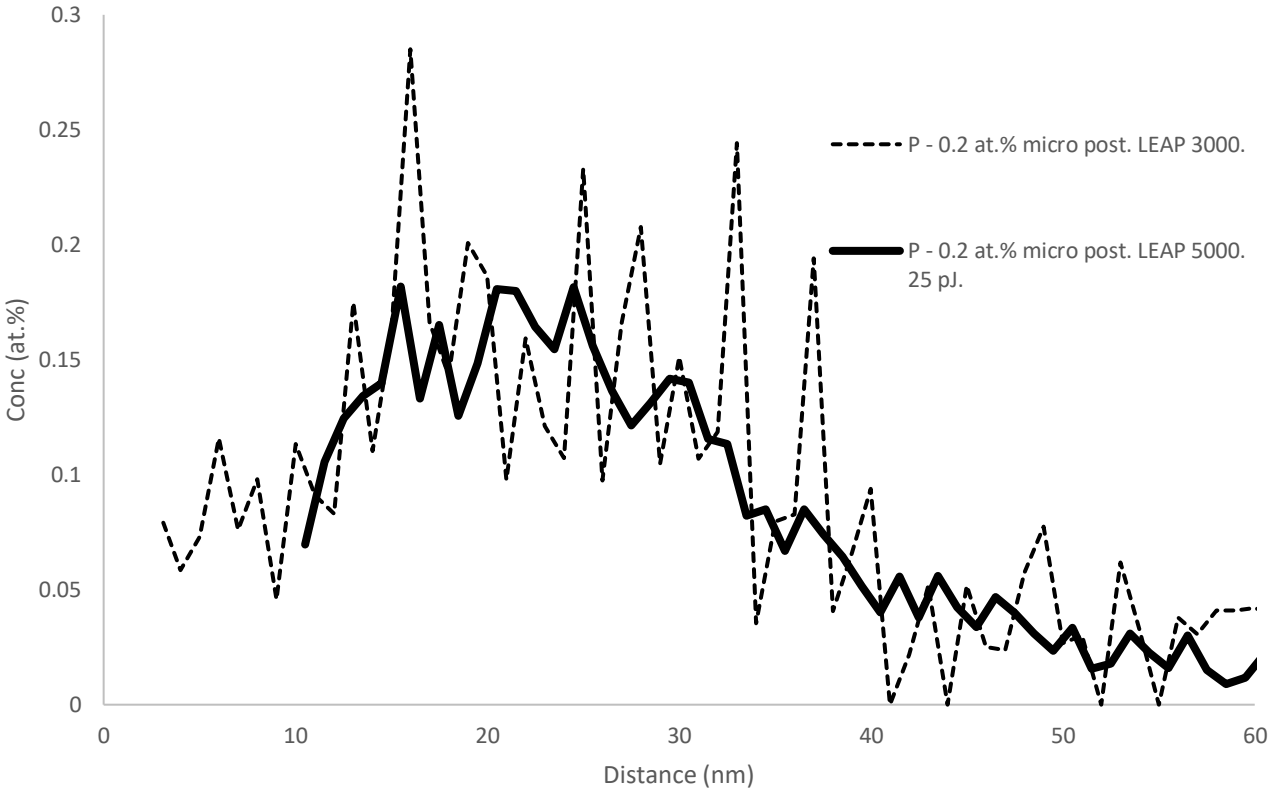


Figure 4.45 – Phosphorus profiles from generated from micro posts analysed using LEAP 3000X HR and LEAP 5000 XR systems.

The phosphorus profiles of implanted micro posts as measured on the LEAP 3000X HR and the LEAP 5000 XR with normalised depths from their respective starting points of the peak at 32 Da and the start of the silicon oxide layer are overlaid in Figure 4.45. For both of these analyses, almost all of the phosphorus species were detected as P^+ and P^{2+}, and so are the most comparable of the two. The profile from the LEAP 3000X HR analysed sample did not have a sufficient silicon oxide layer to act as a delineation layer, so instead

the end of the capping layer region was used instead. The sample analysed using the LEAP 5000 XR did have a sufficient silicon oxide layer to act a delineation layer for the start of the SRIM profiles. As shown in Figure 4.21, the locations of the start and end of the capping layer and silicon oxide layers have an offset of a number of nm, and so this will have likely affected the accuracy of the overlap of the two profiles in Figure 4.45. The peak concentrations of both compare well but there is a distinct increase in variation of phosphorus concentration between adjacent bins for the profile from the LEAP 3000X HR analysed sample compared to the LEAP 5000 XR analysed sample. This can linked to the increased detector efficiency of the LEAP 5000 XR system (52% vs 37%) which would increase the phosphorus signal to noise ratio for the ranged species.

4.4 Analysis of effect of Rapid Thermal Anneal processing

4.4.1 Analysis of implanted micro post with cobalt capping layer. Rapid thermal anneal. Predicted peak phosphorus concentration 0.2 at.%. Laser energy 50 pJ

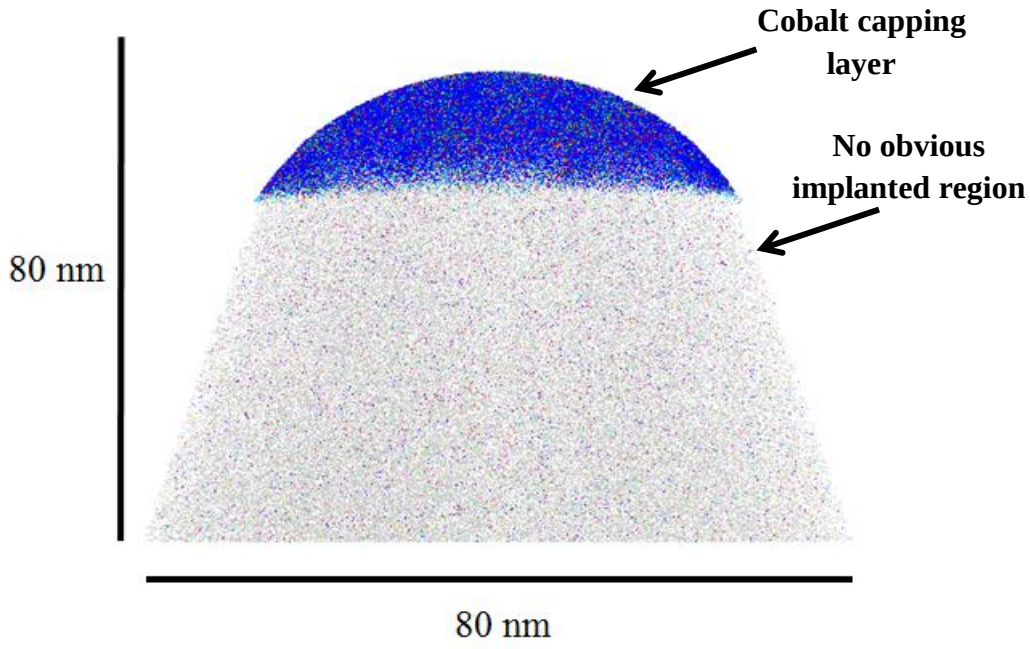


Figure 4.46 – Atom map with silicon (grey) and cobalt species (dark blue) shown.

Analysis conditions: 50 K, 50 pJ, 200 kHz, 0.5 % detection rate throughout analysis.

Analysis of RTA processed implanted micro posts was carried out to determine the extent of surface segregation of phosphorus (Figure 4.46). A 15 at.% cobalt iso-concentration surface was generated and an ROI placed in the interface region used to aid in mass spectra ranging. There was no obvious visual segregation of phosphorus to the implanted region shown in Figure 4.47. Mass spectra of this sample were extremely similar to that of the as-implanted micro post analysed using the same analysis conditions (Figures 4.28,

4.29 and 4.30) and thus are not shown again here. An initial signal of silicon oxide was detected at ~ - 5nm from the 15 % cobalt iso-concentration surface (Figure 4.47).

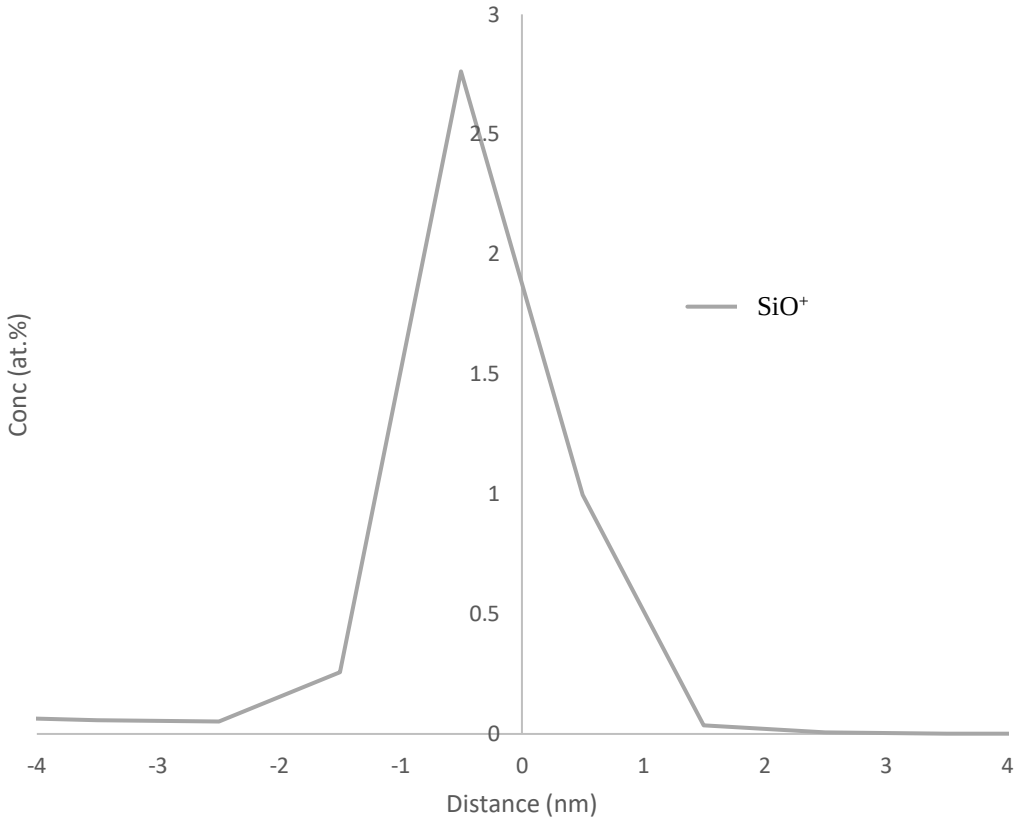


Figure 4.47 – Coherent silicon oxide layer visible in reconstruction with starting point of ~ -5 nm compared to the iso-concentration surface of 15% cobalt iso-concentration surface.

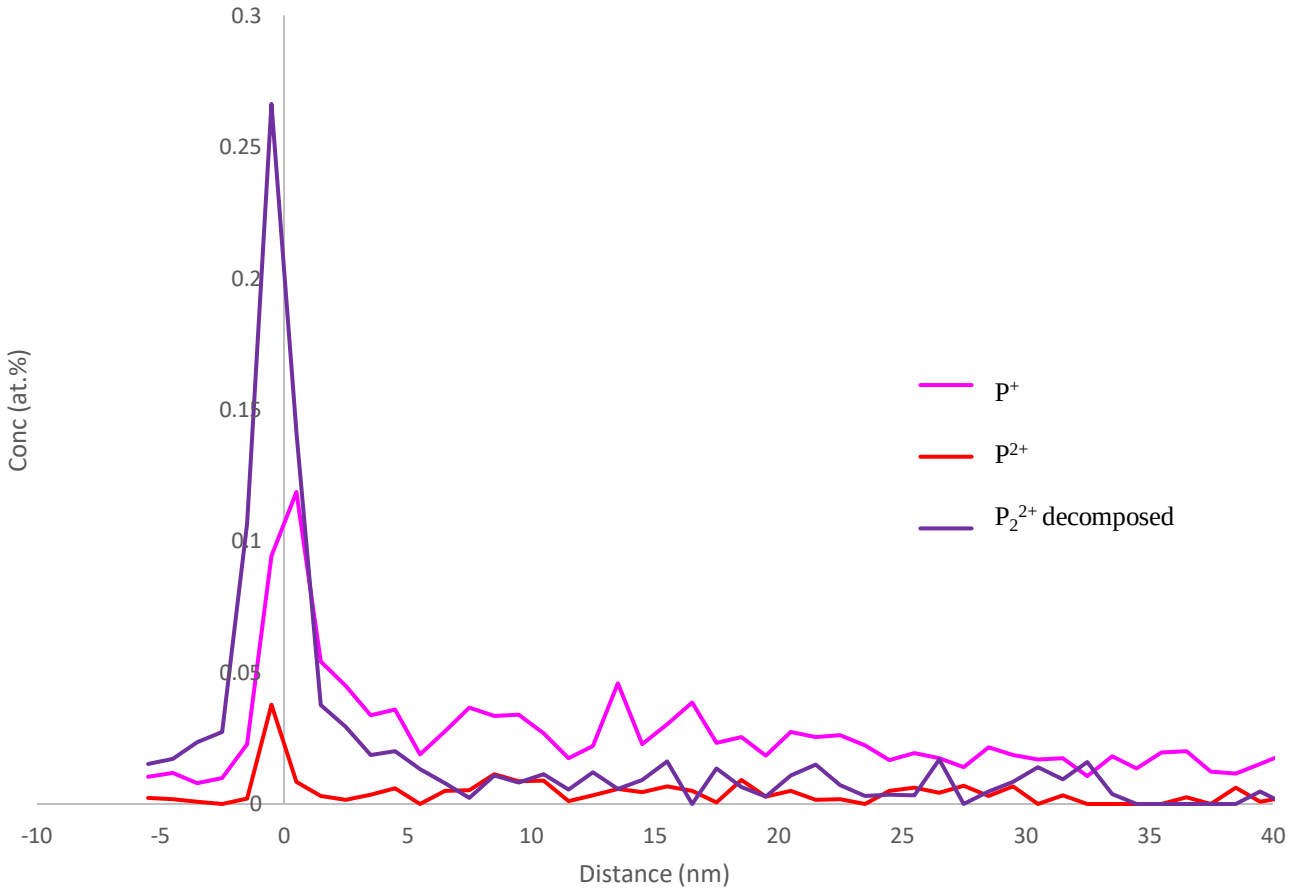


Figure 4.48 – Phosphorus species of P^+, P^{2+} and P_2^+ (decomposed) profiles from 15 at.% cobalt iso-concentration surface.

Due to the lack of mass spectra overlaps between the cobalt capping layer and the P^+, P^{2+} and P_2^+ species, the segregation of phosphorus to the interface of the 15 % cobalt iso-concentration surface can be clearly seen (Figure 4.48). The largest contribution is from the P_2^+ species, with the P^+ and P^{2+} contributing in decreasing concentration. This preferential formation of complex ions in known phosphorus species also indicates that there are likely contributions from other phosphorus complex ions in the capping layer in the form of $(^{28}Si^{31}P)^+$ and $(^{28}Si^{31}P)^{2+}$ at 59 Da and 29.5 Da respectively. There is also likely to be a contribution from the $(^{30}Si^{1}H)^+$ species at 31 Da which can potentially increase the apparent concentration of phosphorus.

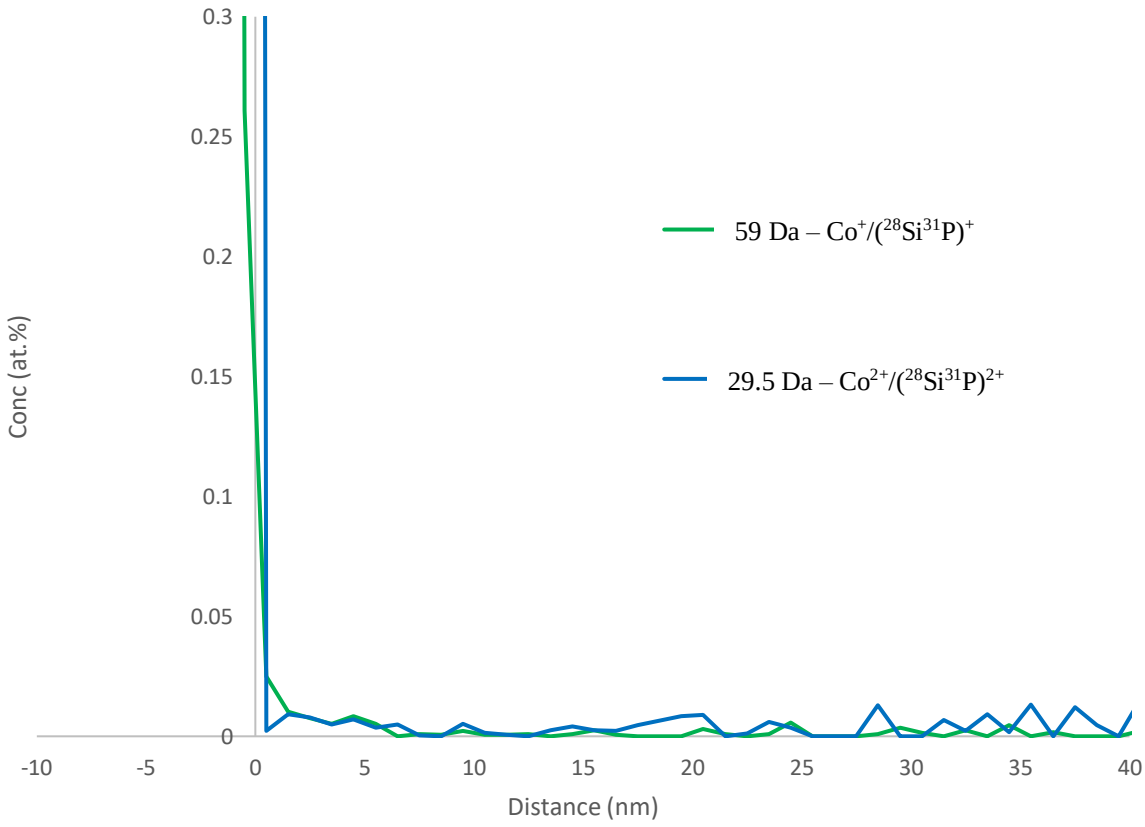


Figure 4.49 – Profiles of ($^{59}Co^{+}$/($^{28}Si^{31}P)^{+}$) and ($^{59}Co^{2+}$/($^{28}Si^{31}P)^{2+}$) at 59 Da and 29.5 generated from the 15 at.% cobalt iso-concentration surface.

There are sharp interfaces of ($^{59}Co^{+}$/($^{28}Si^{31}P)^{+}$) and ($^{59}Co^{2+}$/($^{28}Si^{31}P)^{2+}$) species at the 15 at.% cobalt iso-concentration surface; these quickly reduce to background levels within the first few nm after the interface (Figure 4.49). This indicates that although there may not be contributions from $(^{28}Si^{31}P)^{+}$ or $(^{28}Si^{31}P)^{2+}$ complex ions after the capping layer interface, there will almost certainly be contributions from these species at the interface and this will prevent a full quantification of the phosphorus at the surface. This indicates that although, cobalt capping layers have less direct mass spectra overlaps than nickel, they still prevents accurate quantification of phosphorus at the surface.

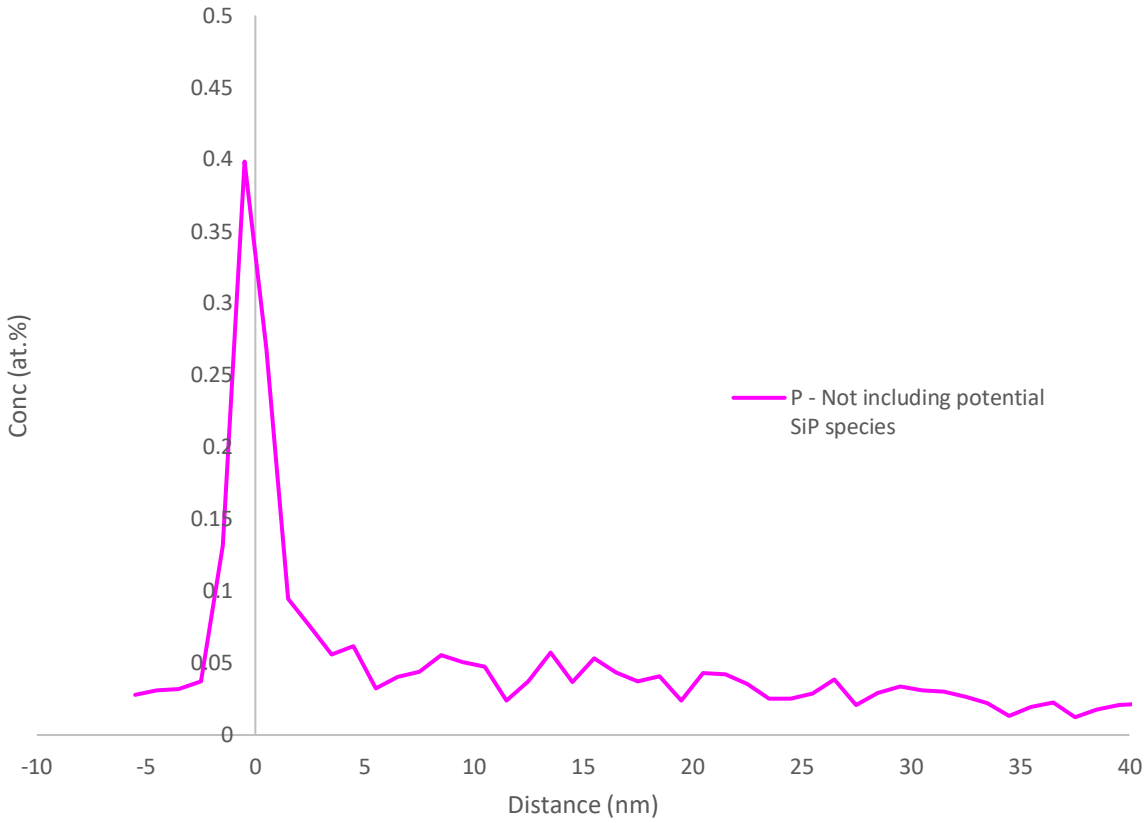


Figure 4.50 – All summed phosphorus species concentration profile without potential SiP species

The sum of phosphorus concentration from known phosphorus species, not including potential SiP species, shows a peak of approximately 0.4 at.% at the interface (Figure 4.50). This is twice the concentration that is predicted from the peak of the implantation profile and is much sharper. The concentration of phosphorus species after the initial peak is relatively low and shows a slow decrease over tens of nm.

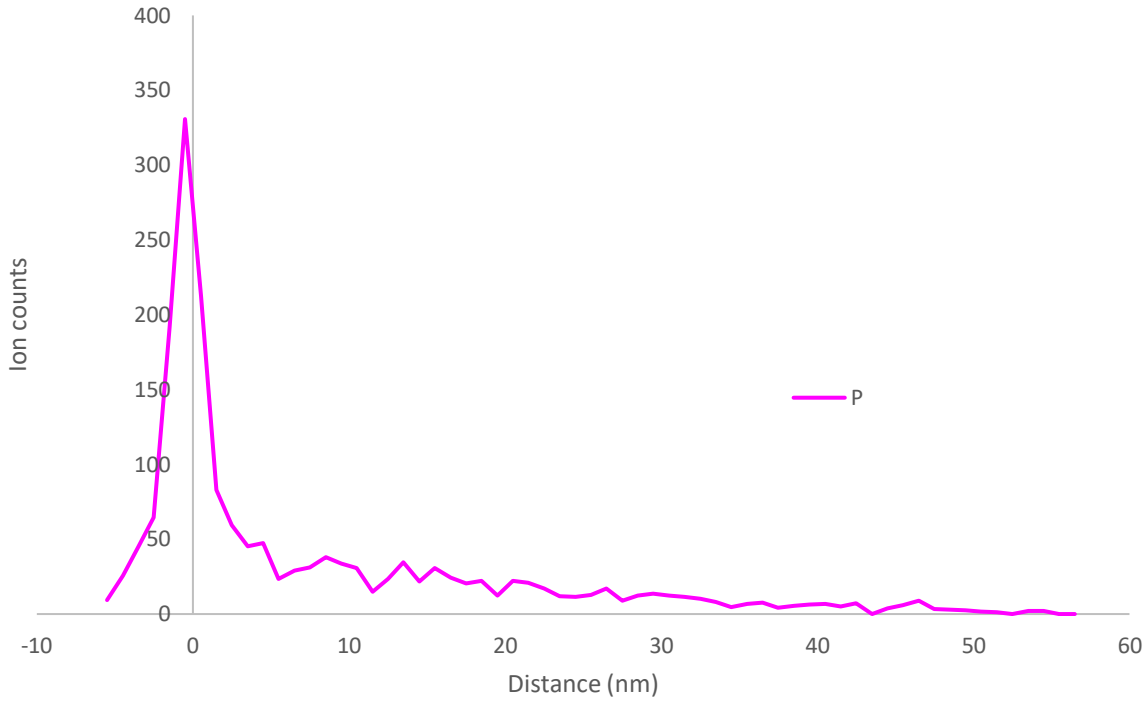


Figure 4.51 – All summed phosphorus species ion counts, not including potential SiP species.

Phosphorus ion counts show that the increase in concentration at the interface is not due to evaporation artefacts, and there is a definite increase of phosphorus species at the interface. The ion count after the peak shows a steady decrease towards background levels over the same depth as that of the phosphorus concentration profile in Figure 4.51.

4.4.2 Comparison of phosphorus profiles between as-implanted implanted micro posts and RTA micro posts

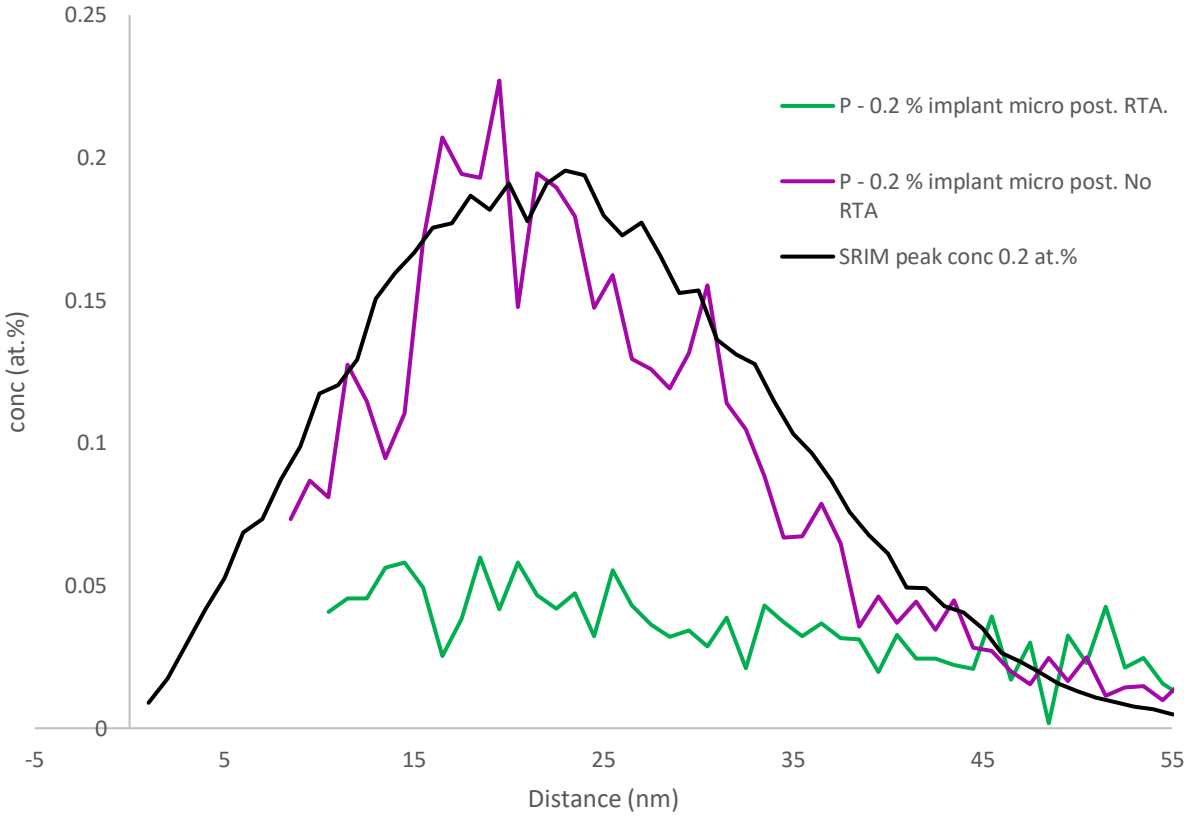


Figure 4.52 – Comparison of phosphorus profiles from the as-implanted micro post and RTA micro post as analysed using 50 pJ with SRIM profile 0.2 at.%

In order to compare the effects of the RTA on micro post sample implantation profiles, the concentration profiles from full datasets of as-implanted and RTA samples that had been analysed using the same laser pulse energy of 50 pJ were normalised for depth and overlaid in Figure 4.52. The regions that have mass spectra overlaps from the capping layer regions were removed for clarity. There is a distinct drop in phosphorus concentration in the RTA processed sample over the implanted depth, showing the level of phosphorus segregation to the surface.

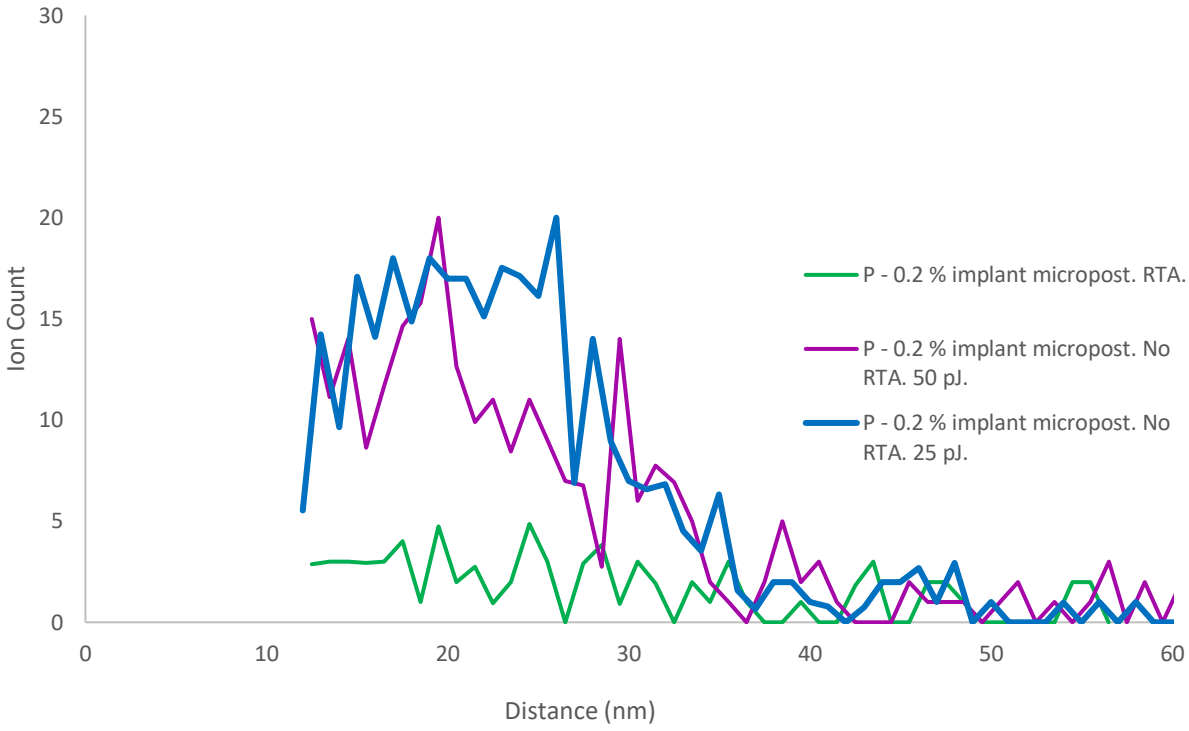


Figure 4.53 – Comparison of phosphorus ion counts in 30 nm x 30 nm x 100 nm ROIs taken from as-implanted micro posts and a RTA processed implanted micro post

The comparison between the total number of detected phosphorus ions within comparable volumes (30 nm x 30 nm x 60 nm) for two as-implanted micro posts that were analysed, using 50 pJ and 25 pJ laser energies respectively, and a RTA micro post analysed using 50 pJ is shown in Figure 4.53. It can be seen that the as-implanted sample analysed using 50 pJ has more variation in the profile compared to the sample analysed using 25 pJ and the overall number of detected phosphorus ions is lower. Phosphorus ions were summed from identical volumes (30 nm x 30 nm x 40 nm), starting at the first point of each of the profiles shown in Figure 4.34). The as-implanted micro posts analysed using 50 pJ and 25 pJ contained 253 ions and 316 ions respectively whilst the analysed RTA sample volume contained 62 ions. This is a clear indication that there has been considerable phosphorus diffusion during the annealing process resulting in surface segregation.

The sample analysed with 50 pJ laser pulses showed segregation of complex phosphorus ions in the form of $(^{28}Si^{31}P)^+$ at the laser incident side and an increased contribution from the $^{31}P_2^+$ species compared to the sample analysed with 25 pJ laser pulses. This laser induced segregation of these species to the laser incident side may have caused a reduction in phosphorus ion count in the ROI extracted from the centre of the sample. The increased contribution of $^{31}P_2^+$ species in this sample will also increase the likelihood for some ions at 31 Da due to $^{31}P_2^{2+}$ being labelled as $^{31}P^+$.

Due to the mass spectra overlaps between $^{59}Co+$ and $(^{28}Si^{31}P)^{+,}$ it was not possible to determine if laser side induced segregation of phosphorus in the form of complex SiP ions occurred during analysis of the RTA sample, potentially reducing the amount of phosphorus detected within a ROI extracted from the core of the sample. As the increased laser energy increased, the preference for the $(^{28}Si^{31}P)^+$ species in the as-implanted sample in the region with the highest concentration of phosphorus (Figure 4.9), it is reasonable to assume that a similar preference would be experienced in the high phosphorus concentration regions at the capping layer interface in the RTA processed sample. However, this would be entirely constrained to the capping layer regions where mass spectra overlaps between $^{59}Co^+$ and $^{28}Si^{31}P^+$ would entirely obscure this change in observed species. This would further prevent the accurate quantification of phosphorus at the surface of the RTA sample and restrict any quantification of phosphorus segregation to the measurement of how much phosphorus has moved away from the implanted region after RTA processing.

The RTA parameters used for annealing the micro post arrays were identical to those used for planar substrates and, as the micro posts are high aspect ratio structures, it is likely that they will not respond in exactly the same as the planar substrates in terms of heating and cooling during this high temperature processing. The RTA process, including the one used

for the samples in this thesis, uses extremely fast pulses, high intensity flash lamps to heat substrates to the temperatures required for annealing irradiation damage (~ 1000°C) and activating dopants while preventing excess dopant motion.

In particular, heat dissipation from such high aspect ratio structures into the substrate is likely to be slower than that from planar substrates and this may increase the amount of time that the implanted region of the micro post is at a sufficient temperature for diffusion of phosphorus to occur, increasing the extent of surface segregation. This has implications for the suitability of directly implanted pre-fabricated supports as analogues for implanted planar substrates when high temperature processing is involved, although this does not prevent them from being used when thermal treatments are not used. Despite repeated analyses of lift out samples from planar regions of implanted and RTA process micro post arrays, none were viable for comparison with the micro post samples in order to determine any potential change in phosphorus segregation. Complex ion implantation in the form of 28 kV P_2^+ ions was also carried out into micro post arrays in an attempt to determine if the implant profile was sharper than the 14 kV P^+ ions as theory predicts [79]. It was found that there was contamination from the implanter cathode and the implantations were not successful.

4.5 Discussion

4.5.1 Use of implanted micro posts as analogues for planar substrates

The commercial micro posts supplied by Cameca have been shown to be a reasonable analogue to planar lift outs for the atom probe analysis of 14 kV phosphorus implanted silicon, with peak concentrations between 0.1 at.% and 0.2 at.% at a depth of approximately 20 nm – 25 nm.

A major cause of concern in the use of Cameca micro post arrays for direct ion implantation with the procedure used in this work, is the requirement that the thermal evaporation of the capping layer is carried out over the entire micro post array. This means that there is a large area of metal-covered silicon surrounding the sharpened posts during analysis, which is not an issue when analysing lift out samples. Fracture events during the analysis of the sharpened micro posts, which had been coated with thermally evaporated metal capping layers, were found to be linked to large sections of metal coating delaminating from the region surrounding the analysed post. This had the effect of depositing a large amount of material onto the instrument's local electrode, rendering it unusable for further experiments, often even after standard oxygen plasma cleaning procedures.

4.5.2 Limits of detection

A main aim of this work was to determine the viability of the atom probe analysis of phosphorus implantation profiles for aiding models for single ion implantation for quantum devices. The results in this work have shown that atom probe is indeed viable for characterising phosphorus implants in the 0.1 at.% - 0.2 at.% peak concentration range. Due to the small numbers of atoms involved in these implants, it is unlikely that further reduction in implantation dose can be measured with reasonable confidence. At reduced concentrations, only the peak of the implant may be visible, and this is unlikely give sufficient information on the profile shape to properly inform simulations.

The peak concentration for an phosphorus implantation profile in silicon would need to be less than or equal to 0.05 at.% in order to not be affected by transient enhanced diffusion [233]. Below this concentration, the implantation and post implantation annealing are more closely analogous to those used for single ion implantation. Therefore, there may be limited application for the use of APT in characterising such implantation profiles, as atom probe is unlikely to be able to reliably measure them. However the approach for measuring phosphorus profiles in this manner can also be applied to higher dose, shallow implants that are used for modern nanoelectronics. As the 14 kV implantation profiles could not be measured reliably from the very start of the profile, due to mass spectra overlaps, it is likely that atom probe analysis of reduced energy implants will be limited when using metal capping layers.

It is possible to analyse these implants in the plane of implantation rather than parallel to them. This will increase the amount of implanted material analysed, and so increase the confidence in measuring lower concentrations. This would require a nanoscale capping layer/silicon interface to be placed parallel to the analysis direction and would be

extremely difficult, but not impossible, to carry out using standard FIB sample preparation. It has been shown that there is a non-trivial amount of evaporation artefacts in such vertically aligned multi-layer systems that would likely prevent the implantation depth being measured accurately when it is placed parallel to the analysis direction [238].

4.5.3 Phosphorus species

Higher laser energies (50 pJ) increased the number of types of potential phosphorus-containing ions detected in the experiment, from a minimum of one (P^{2+}) to an observed maximum of six (P^{2+}, P^{+}, P_2^{+}, P_2^{2+}, SiP^{+} and SiP^{2+}). With each additional phosphorus species observed, the total number of phosphorus ions is split into an increased number of peaks. Each of which will have its own background level of noise. As each of these peaks will, therefore, constitute a smaller ion count, as the concentration decreases they will more quickly reach the level of known statistical variation within the background. This will result in a reduction in the lower limit of concentration that can be measured, and an increase in variation within measured profiles. Therefore, to optimise the limit of detection, the detection of phosphorus should be manifest within the smallest number of peaks where possible. P^{2+} ions are preferred as they lack a mass spectra overlap from other detected species. However, this may also lead to the incorporation of increased noise from thermal tails from the neighbouring silicon peaks. Hence, there may be a lower limit of the P^{+}/P^{2+} charge state ratio that is optimal for maximising the phosphorus signal. Due to sample to sample variation, even when sample preparation and analysis is carried out using identical parameters, this is likely to also vary sample to sample and would be difficult to determine in advance. It would be possible to vary the laser energy during the APT analysis in order to obtain and maintain a specific P^{+}/P^{2+} ratio but this would also have the effect of altering the thermal tail and background contributions to each of these species, so

measuring the real change in the signal is not a trivial matter. It would also potentially change the apparent planar distribution of phosphorus due to an increase or decrease in tip temperature on the laser incident side. Removal of background and thermal contributions cannot be carried out during the analysis, as it requires a full reconstruction and thorough analysis of the mass spectra. Therefore in-line control of the specific P^+/P^{2+} ratio for optimal signal, through varying laser energy, is not currently a viable method.

4.5.4. Comparison of LEAP 3000X HR and LEAP 5000 XR systems

The improved detection efficiency of the LEAP 5000 XR system has shown to improve the smoothness of the measured phosphorus implantation profile through increasing the signal of low concentration species (Figure 4.45). Low laser energies (~ 0.2 nJ/25 pJ) in both systems were found to cause phosphorus to be detected preferentially in the P^+ and P^{2+} states, minimising the number of species containing phosphorus and thus improving the signal to noise ratio of the measured profile. However, low laser energies were found to reduce yield when using both LEAP systems.

4.5.5 Comparison with Stopping and Range of Ions in Matter simulations

When using the start of the native silicon oxide peak at the predicted start of the implantation profile, good agreement was found with SRIM simulations. However, the predicted peak concentrations were almost always overestimated compared to measured concentrations. The analyses using low laser energy on the LEAP 5000 XR gave the best agreement with the predicted SRIM profile peak concentration and also gave the smoothest profile. This is likely due to the increased signal to noise ratio of the phosphorus species as they were mainly confined to the P^+ and P^{2+} charge states rather than being split

across many contributing peaks. The silicon oxide layer was generally found not to be suitable for generating a uniform surface from which a proximity histogram can be formed.

4.5.6 Capping layer requirements

The ex-situ deposition of thermally evaporated metal capping layers of cobalt and nickel were found to be viable in terms of adhesion and field evaporation requirements. Although nickel has mass spectra overlaps with phosphorus species at 62 Da and 31 Da, the extent of these overlaps can be determined using ratio between those peaks and the nickel peak at 30.5 Da, which does not contain a direct overlap with any other species. Standard peak deconvolution using the IVAS software is carried out on a global scale where an entire dataset, or significant portion of it, is used. For situations where the intensity of these overlaps change with spatial location, as in the case of the region around a metal capping layer/silicon interface, a spatially localised peak deconvolution method would be appropriate. This has been shown to be a viable method by London et al. [239].

Cobalt has a single isotope and although this initially appears to be preferable to that of nickel as there are no direct overlaps with single phosphorus ions, there are overlaps with the silicon phosphide ions at 59 Da $(^{28}Si^{31}P)^{+}$ and 29.5 Da $(^{28}Si^{31}P)^{2+}$. These ions were detected when using the higher laser energies that were linked with increased yield and caused local segregation of phosphorus to the laser incident side, apparently due to thermally assisted surface migration during the experiment, leading to a non-uniform phosphorus concentration as a function of distance from that side.

The measured profiles when using nickel or cobalt capping layers also suffered from mass spectra overlaps from the capping layers in the first few nm of the region after the profile and so the very start of the profiles could not be quantified accurately. This is a similar

effect to that which has been seen in SIMS and requires that any comparison between profiles can only be carried out on sections below the overlapped regions [17]. It was found that the profiles could only be measured reliably approximately 10 nm after the start of the silicon oxide layer, which is an improvement on some SIMS measurements. However, as the atom probe analyses used higher implant doses, they may not be directly comparable.

It was not possible to directly quantify the phosphorus overlap with silicon hydride at the 31 Da at the capping layer/silicon interface region as a function of capping layer and analysis conditions. This was due to issues with hydrogen in the analysis contributing hydride species to the analysis in non-consistent amounts. Unimplanted and capped control samples showed a peak at 31 Da at the capping layer regardless of analysis condition. It would be possible to minimise this contribution through using high pulse frequencies and detection rates, but this would likely reduce sample yield for only a small increase in confidence in the phosphorus concentration [219]. Likewise it was not possible to directly quantify the amount of phosphorus segregated to the surface and silicon oxide layer of the implanted samples due to mass spectra overlaps. However, it was instead possible to compare the amount of phosphorus that had diffused away from the implanted region due to the RTA. Interestingly, the analyses showed there was an increase in the amount of phosphorus moving away from the implanted region in the annealed micro posts compared to the annealed planar substrates. This is likely due to the high aspect ratio micro posts not responding identically to that of the planar substrates during the anneal, due to their decreased rate of cooling and resultant increased time spent at high temperatures.

In cases of samples that had their oxide layers removed prior to deposition of the capping layers, the regrown oxide layer will have likely caused an additional offset of 2 - 3 nm on the measured profile.

4.5.7 Summary

It has been found that the concentration limits of atom probe analysis prevent it from being used for analysing phosphorus implant doses that are below the transient enhanced diffusion limit and used in implantation for quantum computing applications. Atom probe analysis is likely restricted to analysis of peak concentrations at 0.1 at.% or just below, corresponding to ~ 10^{19} at/cm^3.

Due to mass spectra overlaps with the metal capping layers used, atom probe analysis of such low concentration phosphorus cannot be readily measured within ~ 5 nm of the end of the capping layer. This will prevent the analysis of lower energy implants than 14 kV, as they will have a shallower implantation profile.

Quantification of the surface segregation of phosphorus during RTA processing using APT is not directly possible due to mass spectra overlaps with the capping layers used here. A measure of the surface segregation can be made by comparing the amount of phosphorus that has moved away from the implanted region.

4.6 Future work

The majority of the phosphorus quantification issues are due to mass spectra overlaps between phosphorus and the chosen capping layer materials of nickel and cobalt, if these could be replaced with a more suitable capping layer material which does not have these issues, then it would make analysis far more streamlined and would potentially allow analysis of surface segregated phosphorus species. These issues can be solved by both implanting phosphorus into, and then capping with, isotopically pure ^{28}Si. There would be no issues with mass spectra overlaps from the capping layer species and any SiH^+ peaks

that would be also cause overlaps would now only form at the 29 Da peak rather than the 31 Da.

The deposition of isotopically purified ^{28}Si is used extensively in phosphorus qubit test structures [67] and is typically deposited epitaxially onto a standard natural abundance silicon wafer of the required crystal orientation. It has also been shown to be readily analysable using UV laser pulsed atom probe [240]. As the phosphorus implant is near surface, a 100 nm epitaxial layer of isotopically purified ^{28}Si would allow a full profile to be obtained. A further 20 – 30 nm of the same isotopically purified ^{28}Si could then be deposited after implantation in order to fully encapsulate the implanted region. Then a capping layer of high contrast metal, such as nickel or cobalt, would be deposited and surface sensitive FIB sample preparation, used in the manner similar to that shown in this work, could be conducted such that a small amount of the metal layer is visible in the SEM in the finished sample and also in the atom probe analysis. As isotopically purified ^{28}Si is the material of choice of fabricating phosphorus based quantum devices, this approach would allow analysis of implantation profiles into a more directly comparable sample rather than having to carry out implantation into natural abundance silicon.

This approach for sample preparation could also be adapted to make samples suitable for SIMS by increasing the ^{28}Si capping layer thickness to allow equilibrium sputtering prior to analysing the implanted region and removing the metal capping layer. This approach has previously been shown to be viable in SIMS analysis of isotopically purified silicon multi-layers [241], where APT has shown give sharper interfaces than SIMS [240].The main reported issue with SIMS analysis of low concentration phosphorus profiles in silicon is due to overlaps between silicon hydride peaks at 31 Da at the very surface and a bulk overlap issue at 59 Da between $(^{28}Si^{31}P)^+$ ions and $(^{29}Si^{30}Si)^+$ complex ions, both of these issues would be reduced or eliminated entirely through the use of isotopically pure

silicon. By carrying out both techniques on similar substrates, as described above, it would be feasible to combine the superior depth resolution of atom probe with the low concentration sensitivity of SIMS.

Low temperature wafer bonding [242] could be used to join two implanted surface regions in order to increase the amount of implanted material analysed in a standard APT analysis. This could be combined with cross sectional FIB liftout and APT analysis [243] in order to reduce yield loss through analysing through a planar interface.

5. Atom probe analysis of iron contaminated, phosphorus diffused silicon

5.1 Description of analysis approach

In order to investigate the nanoscale distribution of phosphorus, oxygen and iron in the surface regions of single crystal silicon substrates subjected to phosphorus diffusion [24], atom probe analysis of iron contaminated and uncontaminated phosphorus diffused substrates was carried out.

The samples in this chapter were analysed using LEAP 3000X HR and LEAP 5000 XR atom probe systems supplied by Cameca. The LEAP 3000X HR has a detection efficiency of 37 % and uses a green laser with a wavelength of 532 nm. The LEAP 5000 XR has a detection efficiency of 52 % and uses a ultra-violet laser with a wavelength of 355 nm.

SIMS measurements of iron segregation to the surface of phosphorus diffused silicon in the literature have indicated that the average concentration of iron can be expected to peak at approximately 3×10^{18} at/cm^3 at the surface of the silicon and will reduce to a background level of 3×10^{15} at/cm^3 after approximately 50 nm [24] [115]. As pure silicon has a density of 5×10^{22} at/cm^3, this corresponds to a peak concentration of 0.006 at.% (60 ppm),

Whilst this peak concentration is within the detection limits of atom probe, given sufficiently large datasets and low variation in background noise levels [1], it is unlikely

that the number of ions collected from the analysis volume of approximately 50 nm x 50 nm x 50 nm can be expected to contain the full iron profile.

Due to the mass spectra overlaps between majority single ion species of iron $^{56}Fe^{2+}$ and silicon $^{28}Si^{+}$ at 28 Da and the overlap between complex silicon ions $(^{28}Si_2)^{+}$ and iron $^{56}Fe^{+}$ at 56 Da, it is extremely difficult to determine the contributions from low concentration iron species in silicon using atom probe at the concentrations expected from the samples analysed in this work [244]. This indicates that iron is unlikely to be able to be observed unless it is highly spatially segregated with an increased localised concentration above the detection limit of or is present in a non-overlapped species such as $(^{54}Fe^{16}O)^{+}$ at 70 Da or $(^{54}Fe^{16}O)^{2+}$ at 35 Da [245].

As it has been proposed by Syre et al. that iron will be segregated to high oxygen concentrations in the surface regions in the form of oxide particles and that iron can also accelerate oxygen precipitation [24], it is reasonable to restrict focus in attempting to locate iron species to regions close to any oxygen rich regions. Due to the low concentrations and mass spectra overlaps between iron and silicon, in order to determine if there is any iron present in the tens of nm surface regions of the iron contaminated, phosphorus diffusion silicon substrates used in this work, special attention needs to be made to the interpretation of the mass spectra. SIMS measurements of the corresponding oxygen concentration profile, which extends over the same depth as the iron profile, peaks approximately at 8 x 10^{21} at/cm^3. This corresponds to ~ 10 at.% and would so be readily detected through atom probe analysis. SIMS measurements of the corresponding phosphorus profile, which peaks at the surface above the solubility limit of phosphorus in silicon [122], indicates that phosphorus species should be detectable in the surface regions and may be in the form of silicon phosphide precipitates.

The combination of low iron concentration (even in the segregated regions at the surface) and the mass spectra overlaps between iron and silicon species indicates that it would be difficult to definitively prove the presence of iron species in these samples. However, the presence of oxygen rich regions or oxide particles could be used as an indicator of the presence of iron and give information about their role in the phosphorus diffusion gettering of iron.

5.1.1 Substrate selection, iron contamination and phosphorus diffusion

Boron doped (1 Ωcm) 100 Czochralski silicon wafer pieces were rubbed with high purity (99.99%) iron on their non-polished side in order to break through the native oxide layer and deposit iron at the silicon surface [246]. This is because iron diffusion through silicon oxide is extremely slow compared to diffusing through pure silicon. Iron was diffused into the silicon for 24 hours at 800°C to give a uniform bulk concentration calculated to be ~ $3x10^{12}$ at/cm^3 [18]. This high temperature process initially forms an iron silicide layer at the surface of the silicon from which the iron diffuses into the bulk. This iron silicide layer was subsequently removed using an acid etch prior to the diffusion of phosphorus [247].

The phosphorus diffusion was carried out at Tetreon, Surrey at 875˚C for 28 minutes in a $POCl_3$ diffusion furnace [248]. This consisted of 25 minutes under $POCl_3$ and O_2 with flow rates of 750 standard cubic centimetres per minute (SCCM) and 500 SCCM respectivel, and 3 minutes purge under N_2 at 10 standard litres per minute. These gettering parameters were within industry standard parameters for n-type doping the surface of silicon for solar cell emitter formation emitter [249]. The phosphorus silicate glass (PSG) formed in this furnace treatment was then removed through an HF dip and the samples

were then coated with a thermally evaporated capping layer of ~100 nm high purity (~ 99.99%) nickel or cobalt metal.

In order to be able to be certain that the data collected via atom probe is from the undamaged surface regions, the criteria for determining if an atom probe analysis is viable is very strict. Both a clear metal capping layer and a clear surface silicon oxide layer are required to be visible in the atom probe reconstruction for optimal data analysis [214]. Without these, it is not possible to delineate the silicon surface and to determine an objective depth measurement at which any features of interest are occurring. As the detection of oxygen rich regions within tens of nm of the surface is required, a coherent surface silicon oxide layer is required in order that prevent isolated regions of a remaining yet damaged oxide layer being mistakenly identified as discrete oxide particles.

The final stage of the phosphorus diffusion involves a high temperature anneal, so the samples are unlikely to be as fragile as the ion implanted silicon samples presented in Chapter 4. Control samples were also made through diffusing phosphorus directly into non-iron contaminated samples in the same furnace treatment. Due to the extremely low concentration of iron predicted in the bulk from the non-phosphorus diffused samples, iron contaminated silicon samples without phosphorus diffusion were not used analysed using atom probe. SEM micrographs of cross sections of various phosphorus diffused substrates were also taken and show potential surface variation in the phosphorus silicate glass layer and thus potential variation in surface concentration of phosphorus. These can be found in Appendix D.

SIMS and atom probe analyses of phosphorus diffused samples with no intentional iron contamination were also carried out in order to obtain base line experimental data with which to compare the iron contaminated samples. This also gives some independent

verification for the depth profiling capabilities of atom probe compared to the industry standard technique of SIMS. Phosphorus depth profiles showed good agreement with those from the iron contaminated samples in this thesis. These can be found in Appendix E.

5.2 Atom probe analyses using LEAP 5000 XR of iron contaminated silicon

A number of atom probe specimens from the iron contaminated, phosphorus diffused (875°C, 28 minute furnace treatment) silicon substrates were fabricated using the surface optimised FIB based sample preparation method shown in Chapter 3. All samples had their Phosphorus Silicate Glass (PSG) layer removed through a HF dip immediately prior to having a ~ 100 nm layer of thermally evaporated cobalt deposited on them. It was quickly found that these samples were able to be analysed at relatively low temperatures (~ 35 K) without noticeably losing yield. Analysis using temperatures below 35 K dramatically increased yield loss when analysing through the cobalt capping layer/silicon interface. A range of laser energies between 25 pJ and 75 pJ were used to determine the impact on the mass spectra of potential iron containing species whilst all other parameters were kept constant (pulse frequency of 200 kHz, base temperature of 35 K and 0.5% detection rate) throughout each analysis. A number of samples of iron contaminated, phosphorus diffused silicon were found to have high concentrations of phosphorus in the first tens of nm beneath the surface. These samples were found to have the most promising indications of heterogeneous oxygen distributions and potential indications of iron containing species and are presented here. Comparisons are also made with samples of iron contaminated, phosphorus diffused silicon with no phosphorus rich regions and identically phosphorus diffused control samples with no iron contamination.

5.2.1 Atom probe analysis of iron contaminated, phosphorus gettered silicon. Laser energy 50 pJ

An atom map of a cobalt capped, iron contaminated, and phosphorus diffused silicon sample is presented in Figure 5.1.

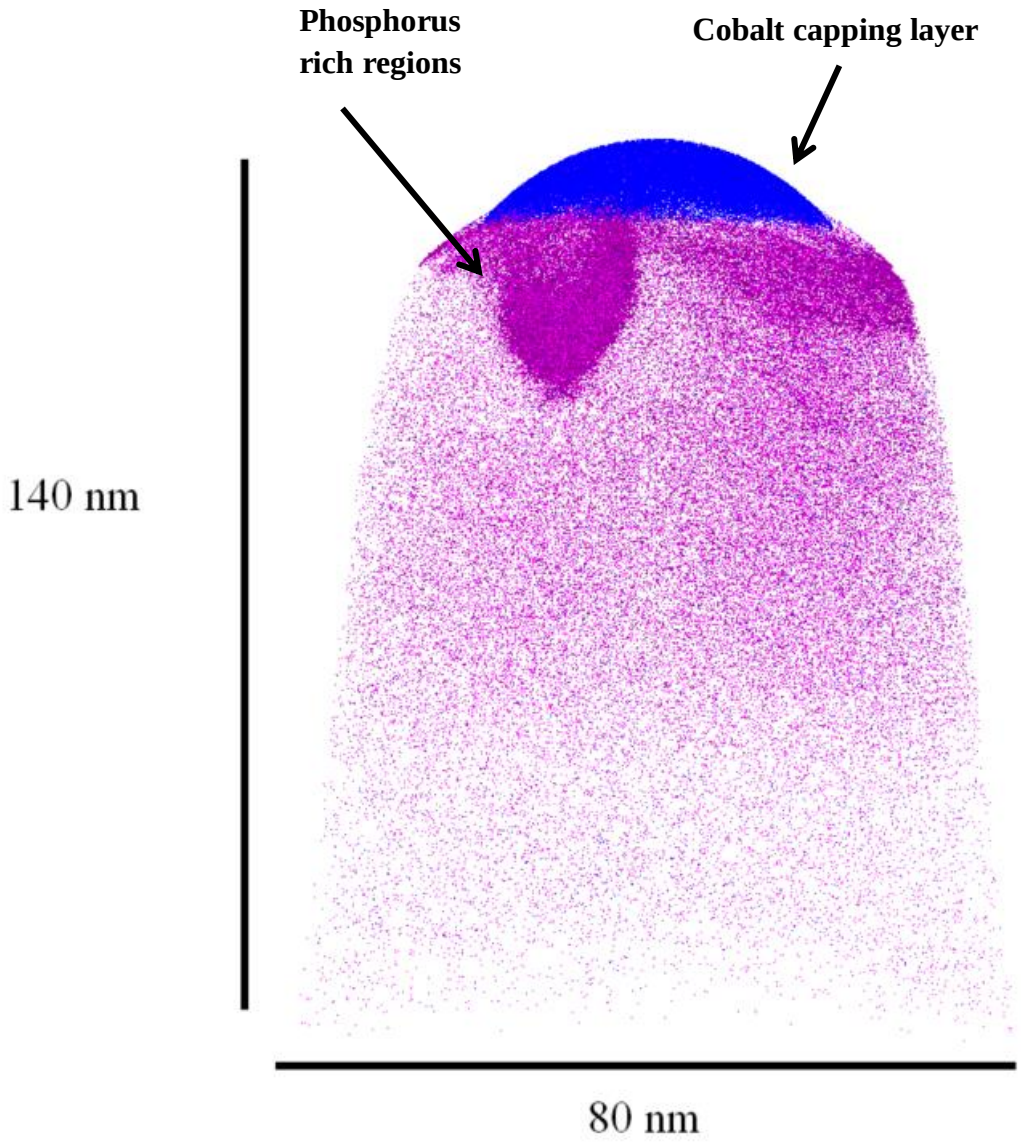


Figure 5.1 – Atom map showing all phosphorus (purple), and silicon (grey) species. Capping layer shown via cobalt species (blue).

A number of phosphorus rich regions can be clearly seen just under the cobalt capping layer; these regions contain phosphorus species in a number of states. The following species were observed: P^{2+} (15.5 Da), P^{+} (31 Da), P_2^{+} (62 Da), P_3^{+} (93 Da) and P_4^{+} (124 Da).

These phosphorus rich regions have been previously been proposed to be silicon phosphide precipitates [250] (See 2.3.5 in the literature review) and are known to preferentially lie along specific crystallographic orientations. During APT analysis, these phosphorus rich regions were found to evaporate preferentially compared to the surrounding silicon. This indicates that they have a reduced evaporation field requirement compared to silicon, causing a focussing effect in the trajectories of the constituent ions onto the detector. This results in such regions having an apparent increase in density compared to the surrounding material in the reconstruction [203]. A top down, cropped view of phosphorus rich region showed two main high concentration regions, angled at almost 90° to each other (Figure 5.2), indicating crystallographic faceting [125] [251].

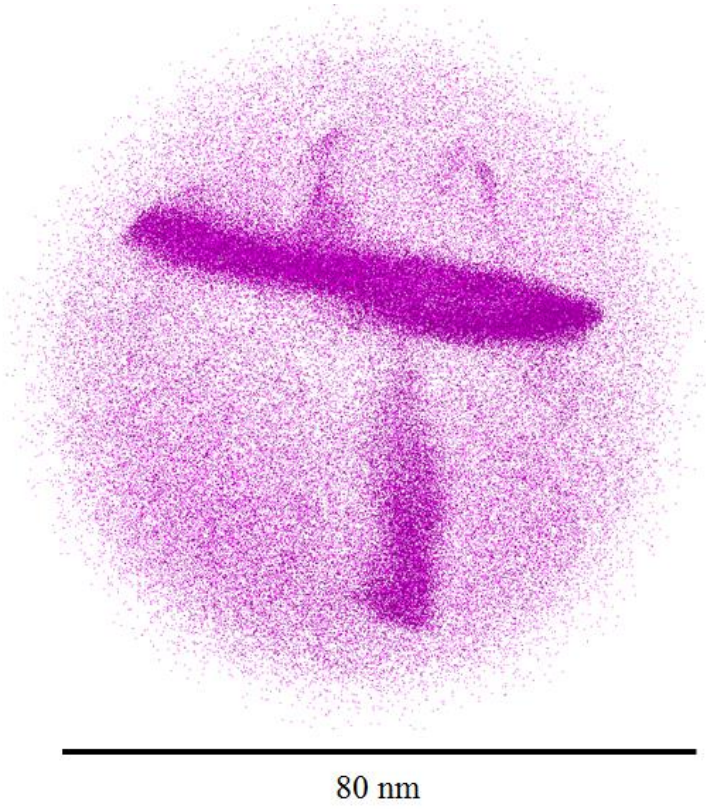


Figure 5.2 – Cropped atom map shown top down to show phosphorus rich regions.

A high concentration of cobalt species (50 at.%), was used to generate an iso-concentration surface to initially delineate the surface of the interface. This concentration was chosen as it maximised the extent of the coverage of the interface by the iso-concentration surface whilst remaining uniform and unbroken. A 3 at.% phosphorus iso-concentration surface was generated from the combined decomposed phosphorus species. This low concentration surface highlights two distinct phosphorus rich regions and a curved line of local phosphorus concentration that appears to be decorating a dislocation [252] (Figure 5.3). Dislocations have been spatially linked to the formation of silicon phosphide precipitates [253] but no segregation of species other than phosphorus was observed to this feature. It has been described as a dislocation here due to both the shape of the features and local increase of concentration of phosphorus which have been previously been used as identifiers in atom probe analysis [254].

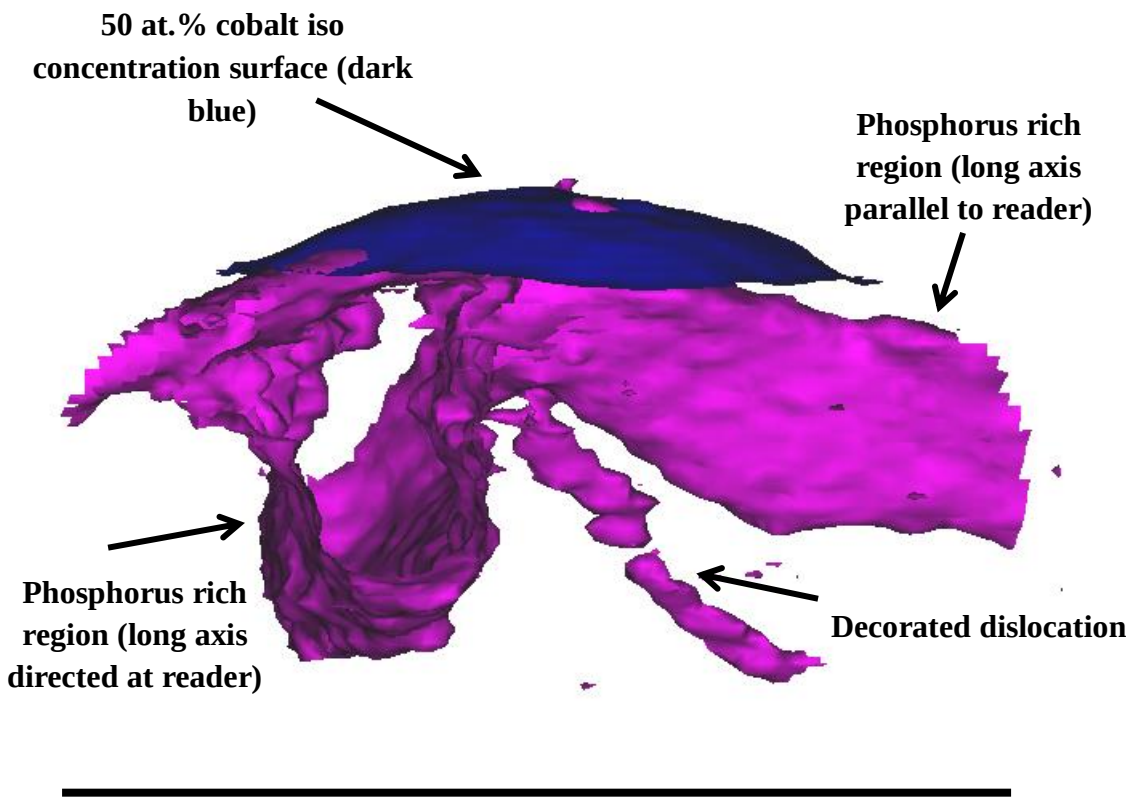


Figure 5.3 – 3 at.% phosphorus iso-concentration surface showing phosphorus rich regions and dislocation (purple). 50 at.% cobalt species iso-concentration surface also shown (blue).

A 10 at.% phosphorus iso-concentration surface shows the phosphorus rich regions more clearly in Figure 5.4 and the orientation of the reconstruction has been chosen to highlight the shape and the structure of the phosphorus rich regions.

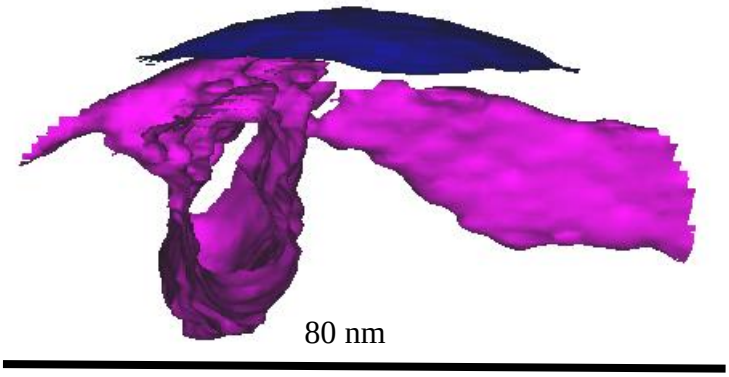


Figure 5.4 – 10 at.% phosphorus iso-concentration surface showing precipitates more clearly (purple). 15 at.% cobalt species iso-concentration surface also shown (blue).

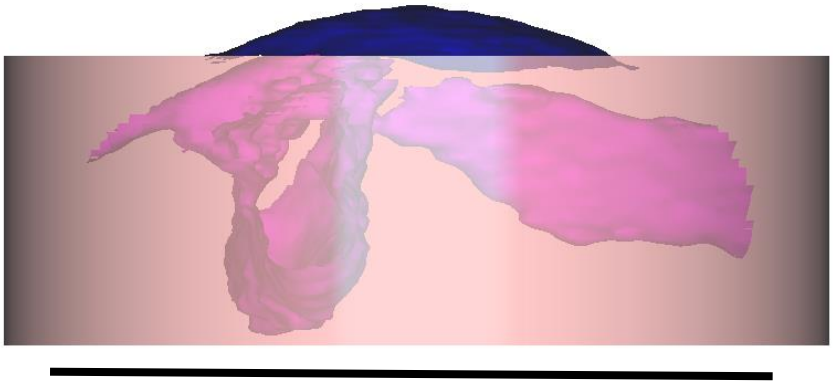


Figure 5.5 – ROI incorporating phosphorus precipitates to assist in mass spectrum analysis.

In order to more accurately range and interpret the mass spectrum from the region immediately below the cobalt capping layer, a cylindrical Region of Interest (ROI) was generated and placed around the phosphorus rich regions, as shown in Figure 5.5. The mass spectra from this can be seen in Figure 5.6.

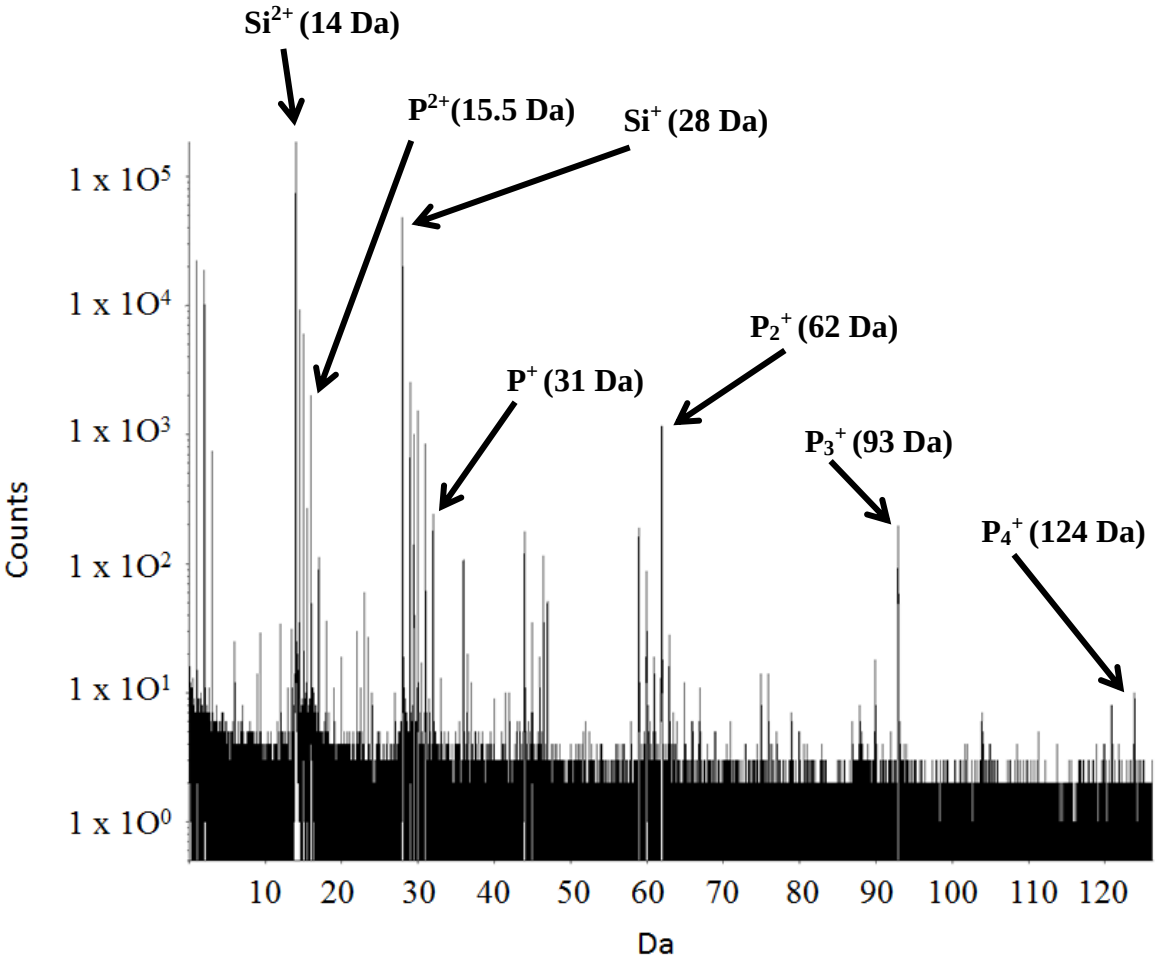


Figure 5.6 – Full mass spectra from ROI around phosphorus rich region in Figure 5.5.

As is the standard for displaying atom probe data, the x – axis is shown in the mass-to-charge ratio unit of the Dalton (Da) [1]. The majority species from this ROI is in the form silicon ions, with a preference for the Si^{2+} species at 14 Da over the Si^{+} species at 28 Da. No peaks were seen at 56 Da which would signify the presence of the Fe^{+} ion and there were no visible contributions of the Fe^{2+} species to the $^{28}Si^{+}$ peak at 28 Da. This is not surprising considering that a low contribution from the Fe^{2+} species would be easily overwhelmed by the silicon signal at 28 Da. The majority of phosphorus was found in complex ion species of P_2^{+} at 62 Da and P_3^{+} at 93 Da with contributions from P^{2+}, P^{+} and P_4^{+} at 15.5 Da, 31 Da and 124 Da respectively. Large contributions from complex ions have been previously observed in APT analysis of complex semiconductors and have been

linked to reduced lateral spatial resolution and compositional accuracy, due to decomposition of clusters in flight [237]. In order to highlight the local concentrations of various species in relation to the phosphorus rich regions shown in Figure 5.4, a number of additional iso-concentration surfaces of oxygen and silicon oxide were generated and presented in Figure 5.7.

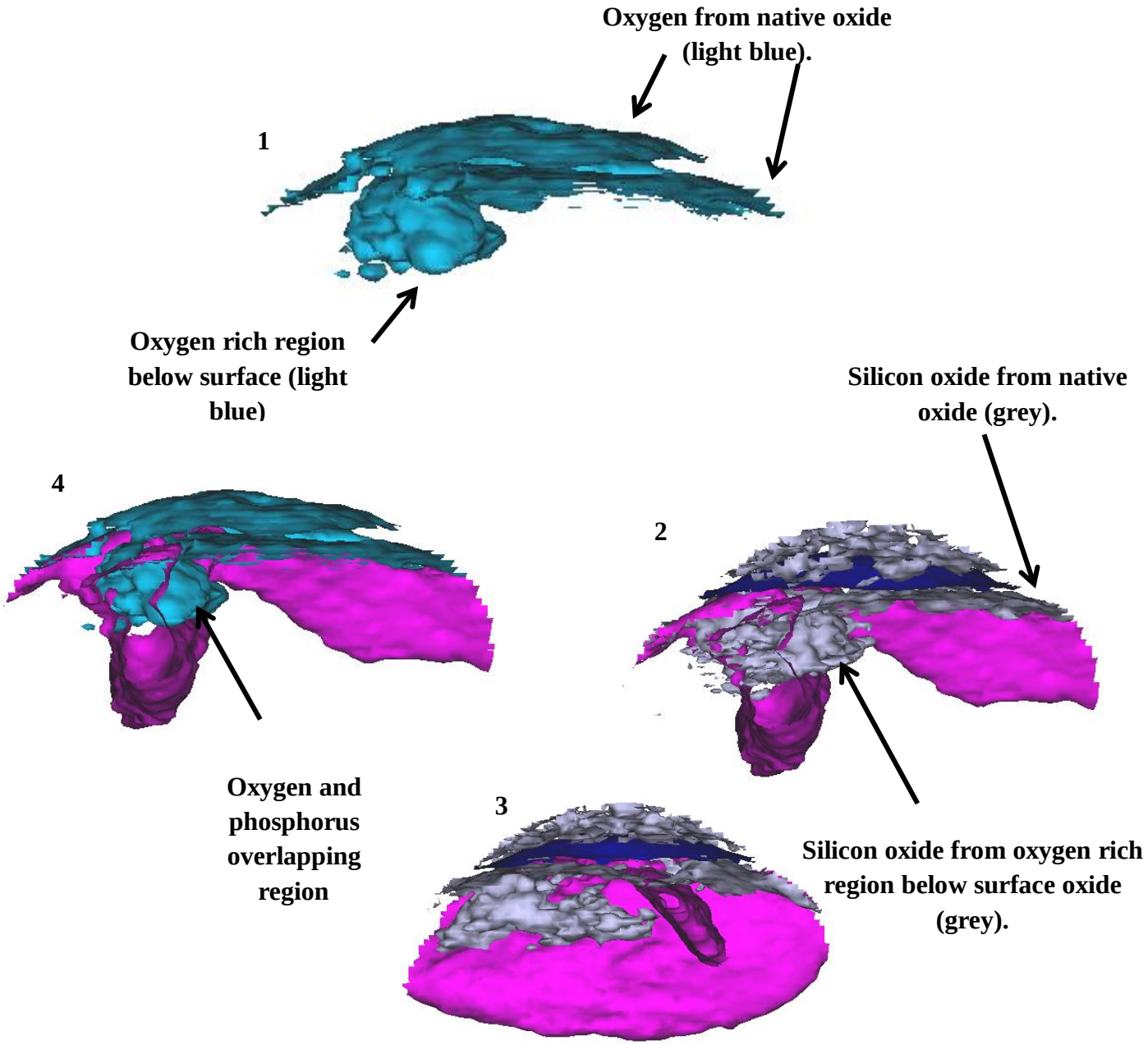


Figure 5.7 – Cobalt (dark blue), phosphorus (purple), silicon oxide (grey) and oxygen (light blue) iso-concentration surfaces. Details given overleaf.

The different images in Figure 5.7 are described in more detail below:

1) – 5 at.% decomposed oxygen iso-concentration surface. This contains contributions from 16 Da ($^{16}O^+$), 32 Da $(^{16}O_2)^+$ and 44 Da (SiO^+) species. The lower layer at the surface can be linked to the oxygen species present at the capping layer interface, the upper layer can be linked to adsorbed oxygen species. There is a large oxygen rich region that is located adjacent to the phosphorus rich region.

2) – 1 at.% silicon oxide iso-concentration surface overlaid onto the 10 at.% phosphorus iso-concentration surface. Silicon oxide rich regions can be seen at the surface within the capping layer region and below the capping layer region. This double layer of silicon oxide iso-concentration surfaces that are spatially separated has also been shown in implanted samples and can be linked to the preferential retention during the capping layer/substrate interface [203].

3) – 1 at.% silicon oxide iso-concentration surface overlaid onto the 10 at.% phosphorus iso-concentration surface. This is the same as 2) but with a 90° rotation to further define the location of the silicon oxide rich region and the shape of the phosphorus rich regions.

4) – The 5 at.% decomposed oxygen iso-concentration surface overlaid over the 10 at.% phosphorus iso-concentration surface.

In order to determine the potential segregation of potential oxygen and iron species to the surface regions, a proximity histogram [7] was generated from the iso-concentration surface of 50 at.% cobalt species (Figure 5.8). There is a distinct increase in oxygen at the surface regions (~ 20 at.%) which is in excess of that which would be expected from just contributions from the silicon oxide layer.

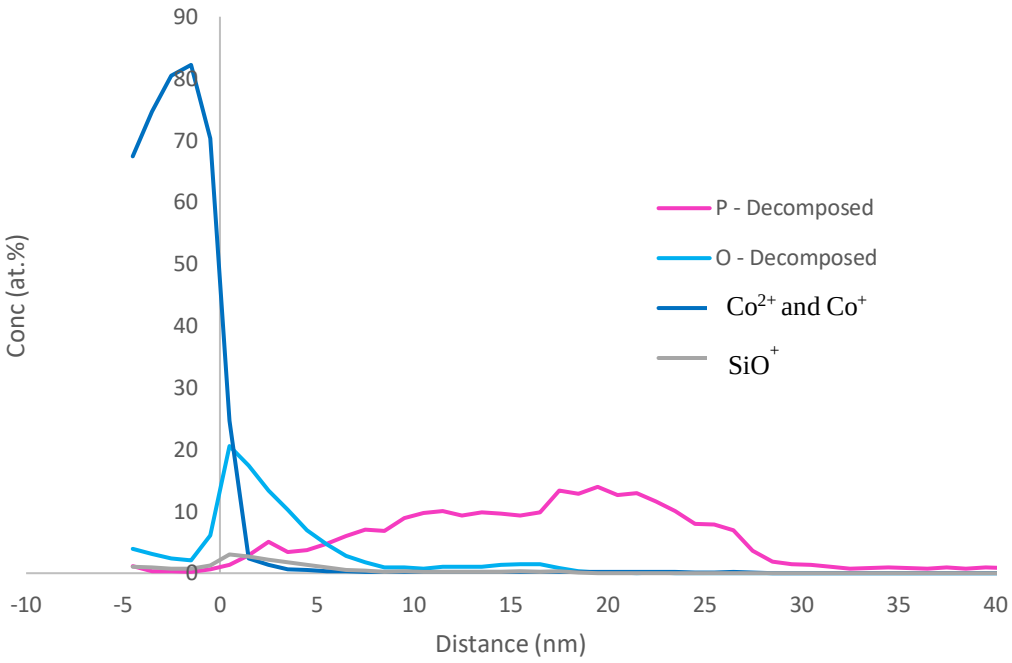


Figure 5.8 – Cobalt, oxygen, phosphorus and silicon oxide concentration profiles from a 50 at.% cobalt iso-concentration surface.

These localised concentrations of phosphorus were not found in every atom probe sample, which indicates that there is likely non-uniform diffusion. The oxygen profile of the phosphorus diffused samples extends over a noticeably longer depth that would be expected from a native silicon oxide, implying the oxygen profile is linked to the diffusion process. TEM analysis from the literature shows that orthorhombic silicon phosphide precipitates preferentially form at and are in contact with the PSG/silicon interface in phosphorus diffused samples [126] and at the silicon oxide/silicon surface in ion implanted samples [119]. The phosphorus concentration measured here does not peak at the interface as expected [255], and instead peaks approximately 20 nm below the surface, although it does remain in contact with the surface oxide. This indicates that there may be some nanoscale variation in the orientation and size of precipitates that are visible via atom probe but this may be averaged out when analysed with an analysis technique with reduced

lateral resolution such as SIMS. There are likely to be reconstruction artefacts during the analysis of these regions caused by the close proximity of the native oxide, phosphorus rich regions and second oxide region but, the general depth profile can be considered to be accurate [256]. On closer inspection of the oxygen and oxygen rich region, it can be seen that the species at 36 Da is also spatially segregated to the oxygen rich region and quickly reduces to a background level within 5 nm after it (Figure 5.9).

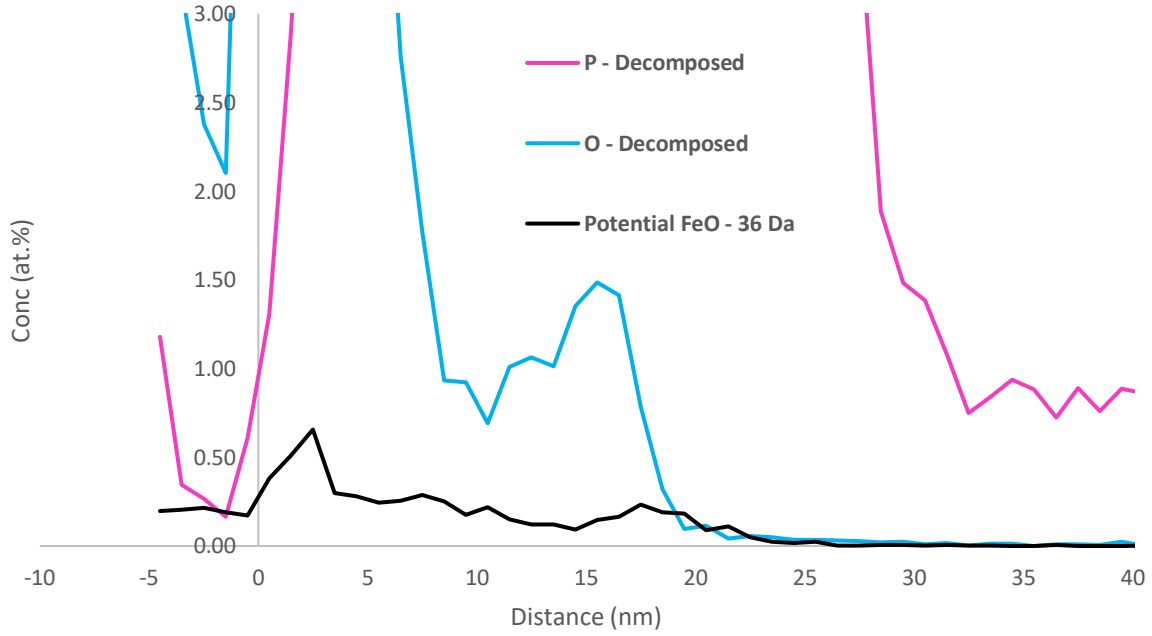


Figure 5.9 - Profiles from oxygen, phosphorus and the species at 36 Da from 50 at.% cobalt iso-concentration surface.

Although a species at 36 Da has been linked with the $(^{56}Fe^{16}O)^{2+}$ ion in iron contaminated polycrystalline silicon [245], it is not the only potential species that can contribute to this peak. One potential overlapping species at 36 Da is that of the complex C_3^+ ion. Carbon is known to be detected in multiple complex ion states in atom probe [257] . A method to determine the contribution from the C_3^+ ion to this peak is through determining the extent

of spatial segregation of other known carbon species of C^{2+}, C^{+} and C_2^{+} at 6, 12 and 24 Da respectively (Figure 5.10).

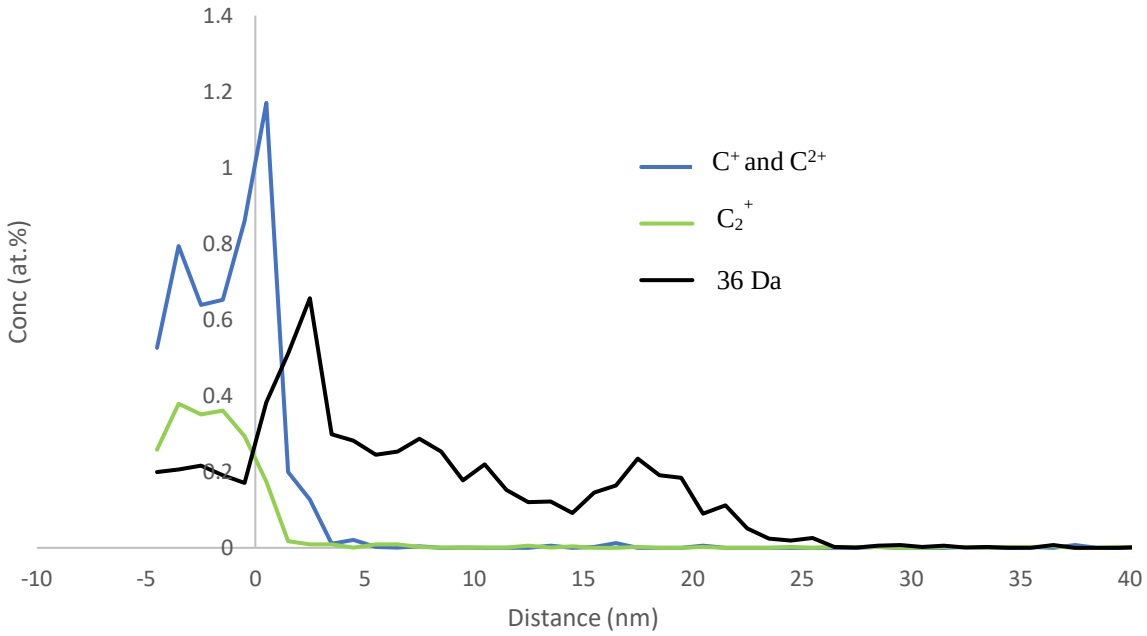


Figure 5.10 – Profiles of potential carbon species from 50 at.% cobalt iso-concentration surface.

Whilst there is some spatial overlap prior to the interface between the 36 Da ion species and the ions from known carbon-containing peaks at 6 Da, 12 Da and 24 Da, these profiles stop abruptly ~ 3 nm after the interface whilst the 36 Da species continues further into the silicon to ~ 25 nm in depth. The ratio of the carbon containing species prior to the interface shows a decrease in concentration with increased complex ion size, with C^{+} ions having the highest concentration, then C_2^{+}, with C_3^{+} ion having the lowest.

It is unlikely that an increase in the C_3^{+} ion at 36 Da would not also lead to a corresponding increase from carbon species at 24 Da and 12 Da. This indicates that carbon contribution to the 36 Da species from the C_3^{+} ion is confined to the capping layer region

and the first ~ 3 nm of the sample below the interface. In order to obtain further 3D information on the spatial segregation of the species at 36 Da, the location of the 36 Da species was overlaid over iso-concentration surfaces of cobalt, phosphorus and silicon oxide These are shown in Figure 5.11 that there is a distinct segregation of the 36 Da species towards the high phosphorus concentration at the centre of the larger phosphorus rich region.

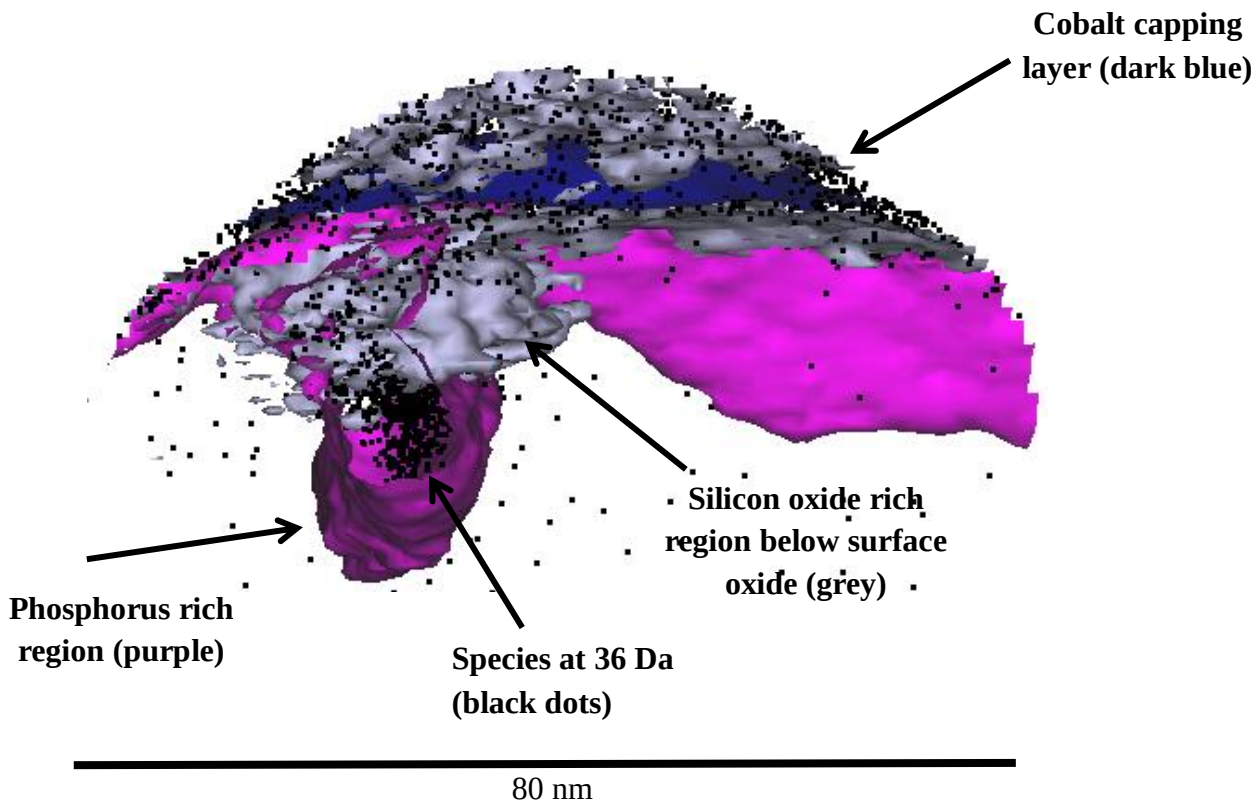


Figure 5.11 – 1 at..% silicon oxide (grey), 50 at.% cobalt (blue) and 10 at.% phosphorus (purple) iso-concentration surfaces. Species at 36 Da species shown as black dots.

There appears to be a definite spatial relationship to the oxygen rich regions, the phosphorus rich regions and the species at 36 Da. To further investigate this, the local mass spectra and spatial distribution of species around this region was extracted and

analysed in detail. Through this, it may be possible to observe smaller peaks and nanoscale segregation that may not have been previously observable.

5.2.1.1 Transmission electron microscopy of iron contaminated, phosphorus diffused silicon

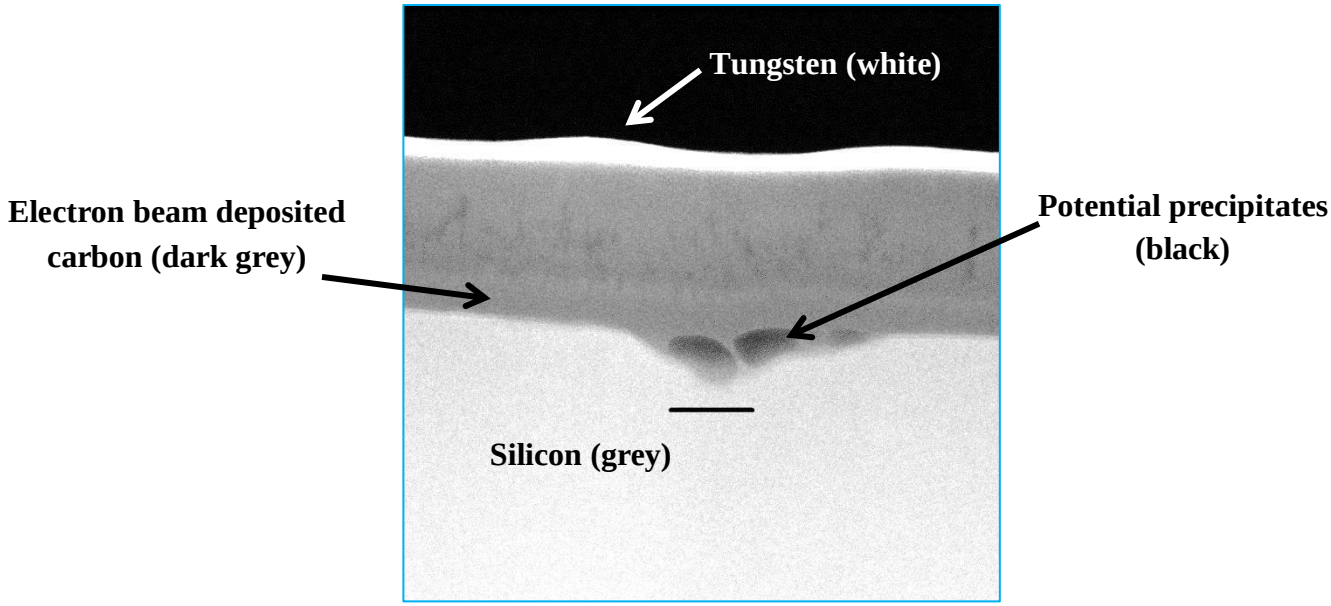


Figure 5.12 – TEM annular dark field micrograph of potential precipitates. Scale bar is 50 nm.

Prior to the more detailed APT analysis around the phosphorus rich regions, (Scanning) Transmission Electron Microscopy (S)TEM was carried out on samples from the iron contaminated, phosphorus diffused substrates with the assistance of Dr Mohsen Danaie. Dark regions were found at the silicon interface regions through annular dark field imaging shown in 5.12, these are in contrast to the surrounding silicon substrate and carbon and tungsten protective layers. Previous TEM analysis of phosphorus rich regions in similar

samples have shown that that they often will show a crystalline structure which diffraction analysis links to the SiP phase of silicon phosphide [250].

However, diffraction analysis showed them to be amorphous and Electron X ray Dispersive Spectroscopy (EDX) analysis showed no traces of phosphorus within the particles. However a trace amount of iron was detected via EDX within ~ 100 nm of their vicinity. Iron signals have been previously detected via EDX in close proximity to silicon phosphide precipitates [26] but as, these showed no phosphorus signals, their composition is unknown.

Damage during FIB based sample preparation could be the cause of their amorphous nature but does not explain the lack of phosphorus detected. Further TEM analyses would be required in order to confirm their nature.

5.2.1.2 Analysis of silicon phosphide precipitates

As STEM was unable to give suitable local compositional information on the phosphorus rich regions, the larger precipitate from Figure 5.7 was extracted from the main dataset using a cuboid ROI (Figure 5.13). The larger phosphorus rich region was selected for extraction as it was seen to have a significant amount of the 36 Da species present directly adjacent to it.

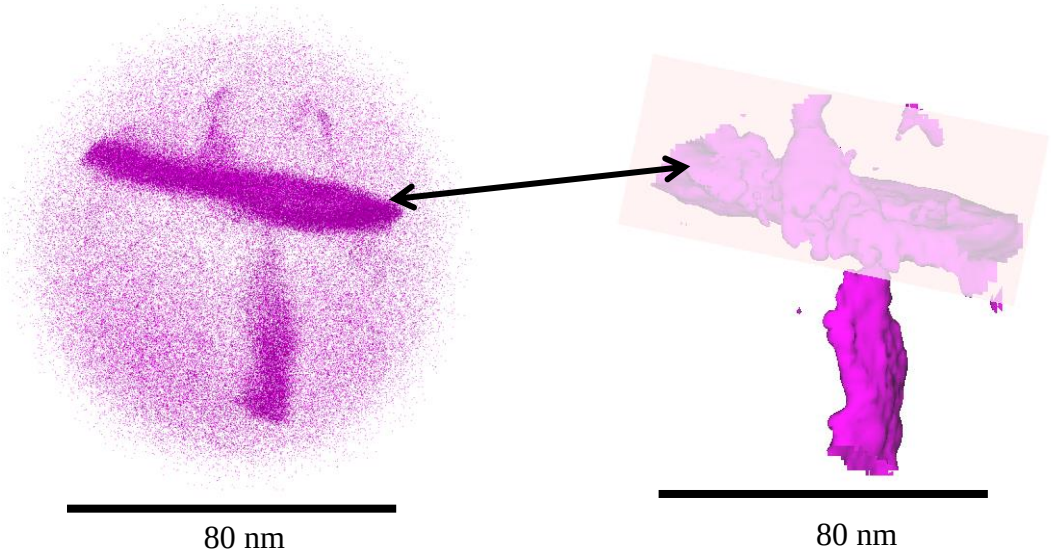


Figure 5.13 – Left - Top down view of atom map highlighting phosphorus distribution Right- ROI used to extract the larger of the two phosphorus rich regions shown as 10 at.% phosphorus iso-concentration surface.

The mass spectra from this ROI extracted in Figure 5.13 is presented in Figure 5.14 and shows a similar distribution of silicon and phosphorus species to that originally obtained from the cylindrical ROI used in Figure 5.6. There is a distinct reduction in the background contributions due to the reduced ion count for this ROI and so small concentrations of locally segregated species may be more visible. No peaks at 56 Da (that can be linked to $^{56}Fe^{+}$) can be seen in Figure 5.14 but the peak at 36 Da can be seen in Figure 5.15 and the spectra around the 36 Da peak is shown in Figure 5.16.

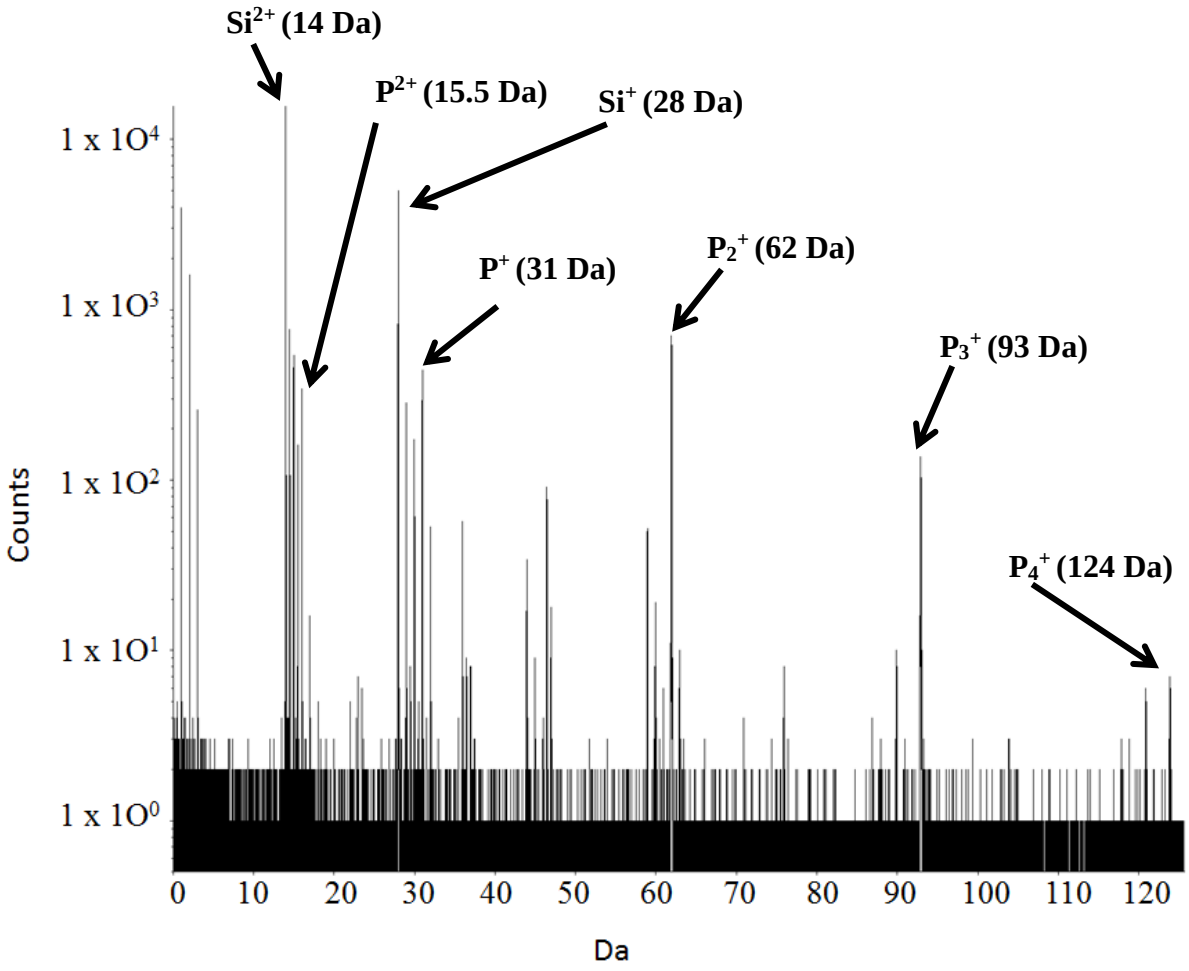


Figure 5.14 – Full mass spectrum of phosphorus rich region extracted via ROI in Figure 5.13.

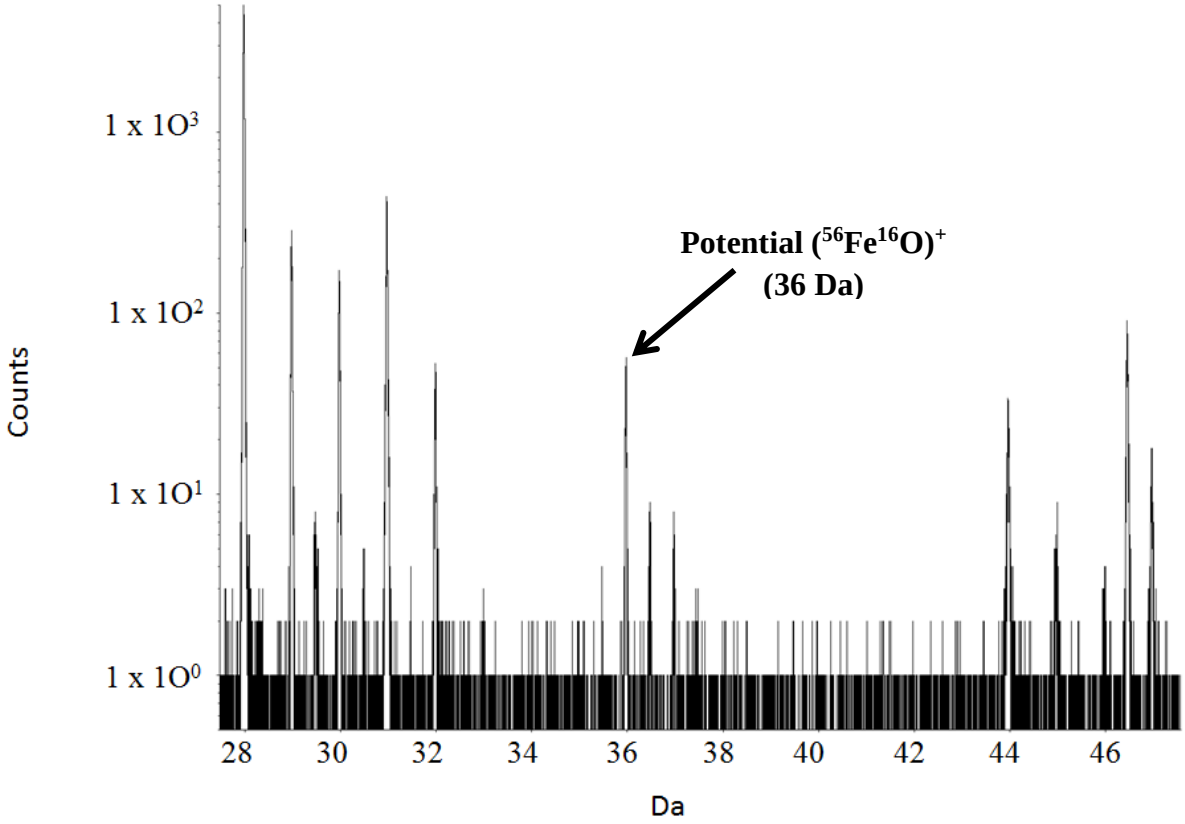


Figure 5.15 – Mass spectra from 28 Da to 48 Da range of phosphorus rich region extracted via ROI in Figure 5.13.

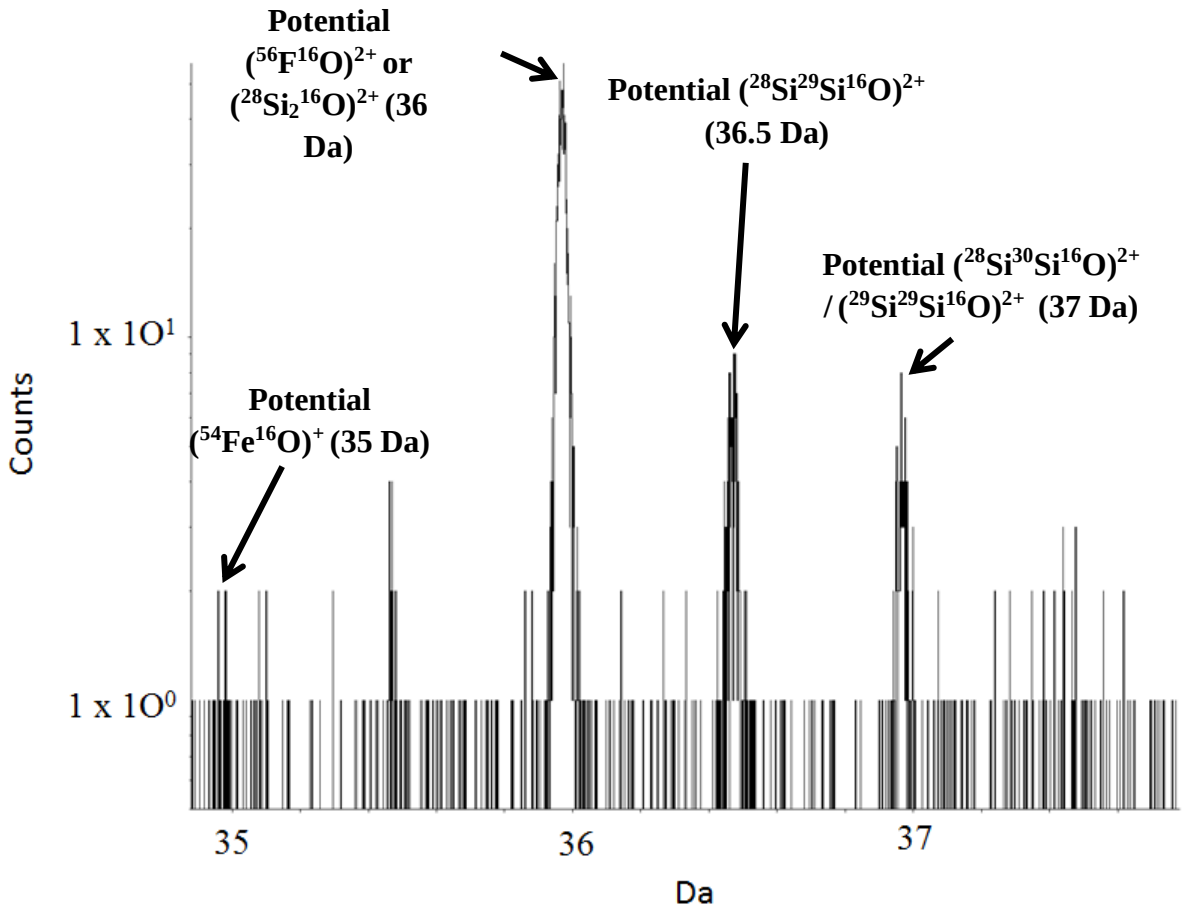


Figure 5.16 – Mass spectrum of 34 to 38 Da range from the phosphorus rich region extracted via ROI in Figure 5.13.

The peaks at 36.5 Da and 37 Da are not within the expected natural abundancies for iron oxide species and instead appear to match those of the silicon $(^{28}Si^{29}Si^{16}O)^{2+}$ and $(^{28}Si^{30}Si^{16}O)^{2+}$/ $(^{29}Si^{29}Si^{16}O)^{2+}$ respectively, if the peak at 36 Da is in fact $(^{28}Si_2{}^{16}O)^{2+}$. There is a very small peak at 35 Da which can be linked to the minority $^{54}Fe^{16}O^{2+}$ species, which does not have overlaps with silicon species, and indicates that the 36 Da peak could contain a small concentration of $^{56}Fe^{16}O^{2+}$.

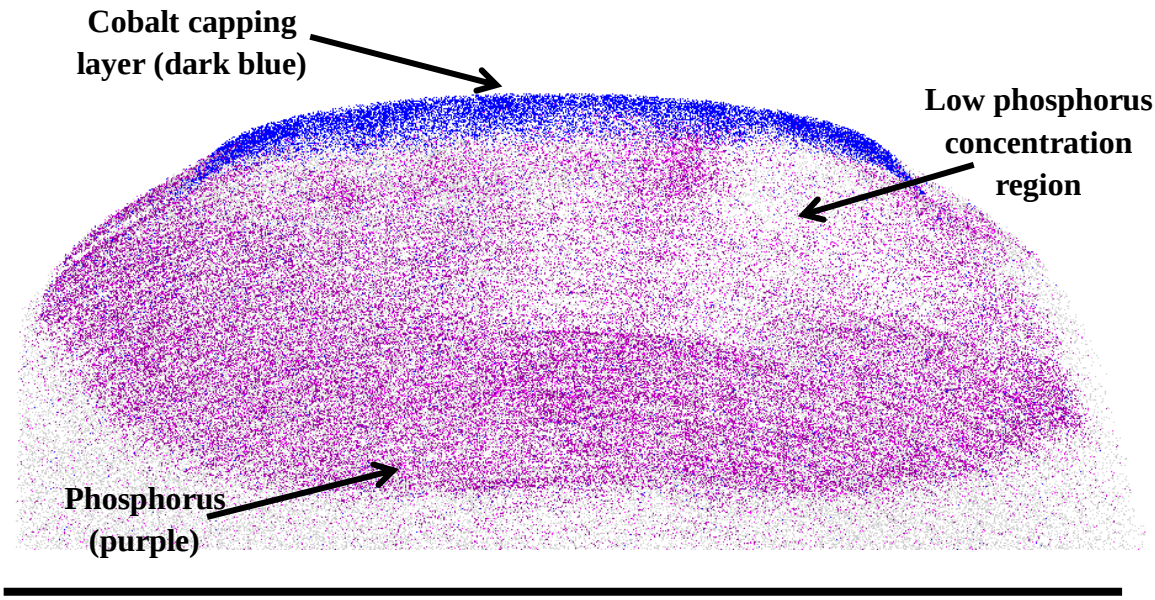


Figure 5.17 – Atom map from volume extracted by ROI showing high concentration phosphorus region with phosphorus (purple), cobalt (dark blue) and silicon (grey). Crystallographic planes are visible within the phosphorus rich region.

Through inspection of the atom map from the volume extracted by ROI in Figure 5.17, distinct crystallographic planes are visible within the phosphorus rich region. This gives weight to them being identified as silicon phosphide precipitates and henceforth they will be referred to as such. The planes within the precipitate were not observed to match directly with those of the silicon matrix however silicon phosphide precipitates have been previously observed to have different orientations to their matrix [126]. There is also a region of low phosphorus concentration that is between the main body of the precipitate and the capping layer which was also found to be rich in oxygen species (Figure 5.18).

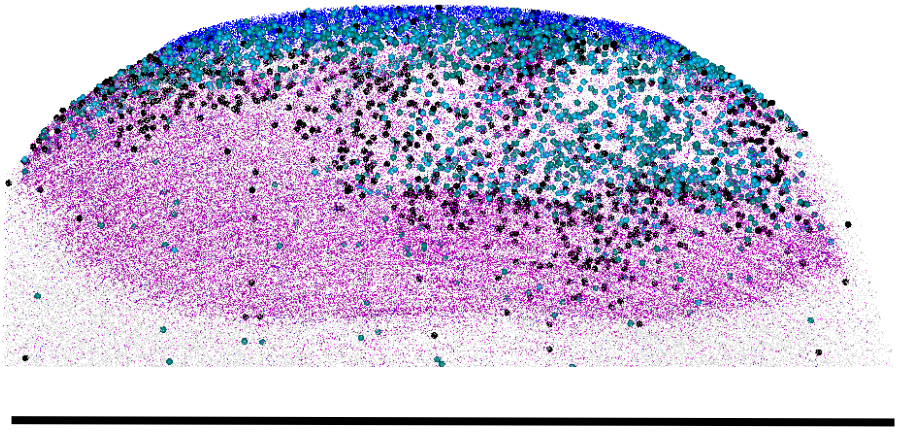
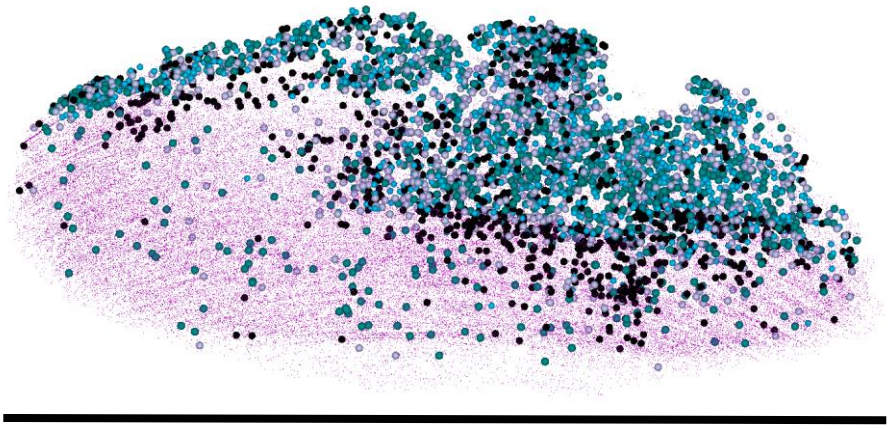


Figure 5.18 – Extracted ROI showing silicon phosphide precipitate with phosphorus (purple), cobalt (dark blue) and silicon (grey). Oxygen species at 16 and 32 Da (blue) and the species at 36 Da (black) are enlarged for clarity.

More localised analysis of the precipitate was carried out by extracting the volumes encapsulated by a 10 at.% phosphorus iso-concentration surface, it can be seen that a significant amount of oxygen species and the species at 36 Da are spatially segregated together (Figure 5.18).

There is also a distinct segregation of both of these species to both of the silicon phosphide precipitates, but this segregation is more pronounced for the larger phosphorus rich region. This could imply that there is a relationship between local oxygen enrichment with both local concentration of phosphorus and size of the precipitate

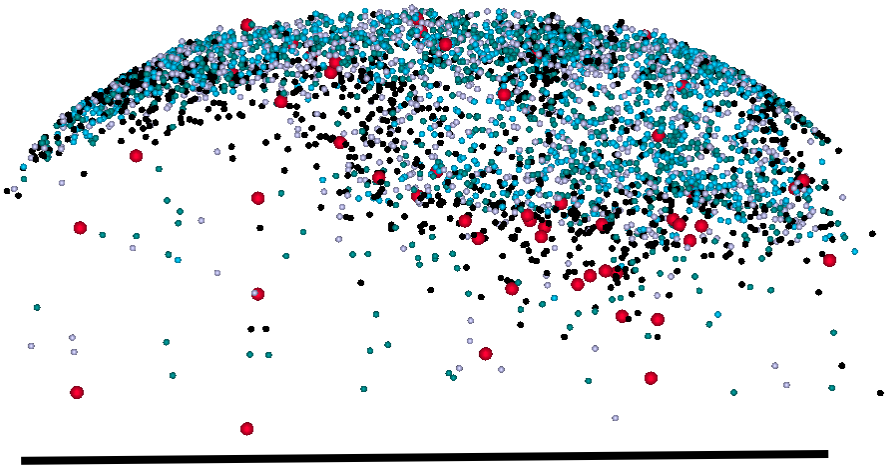
The oxygen enrichment to the larger of the two precipitates is more apparent, and to allow further detailed investigation, the larger precipitate was again extracted and can be seen in Figure 5.19.



60 nm

Figure 5.19 – Atom map of large silicon phosphide precipitate with phosphorus species (purple), oxygen species (blue) and species at 36 Da (black). All species apart from phosphorus and silicon have been enlarged for clarity.

For further clarity, the reconstruction in Figure 5.19 is shown again but with silicon and phosphorus ions removed (Figure 5.20). This makes the segregation of the species at 36 Da to the edges of the oxygen rich region more easily observed.



60 nm

Figure 5.20 – Oxygen species (blue), silicon oxide species (grey), species at 36 Da (black) and species at 35 Da (red – enlarged for clarity).

Due to the previously mentioned overlap between silicon oxide complex ions ($^{28}Si_2{}^{16}O)^{2+}$ and iron oxide species ($^{56}Fe^{16}O)^{2+}$ at 36 Da, the segregation of the species at 36 Da cannot be used as conclusive evidence of iron decoration of the oxygen rich region predicted [24]. As there is not a similar overlap between silicon oxide species and the minority iron isotope complex ion ($^{54}Fe^{16}O)^{2+}$ at 35 Da, the location of this species was also overlaid onto the atom map of Figure 5.20.

It can be seen that there is a small preferential segregation of the potential ($^{54}Fe^{16}O)^{2+}$ species at 35 Da to that of the location of the 36 Da species. However, due to the very low numbers of these species at 35 Da, changes in local background can cause an apparent increase in their concentration. The changing evaporation field conditions at the interface of the silicon phosphide precipitate and the oxygen rich region could cause such variations in background.

In order to more clearly visualise the structure of the phosphorus rich regions and oxygen rich regions, iso-concentration surfaces of 25 at.% phosphorus and 1 at.% oxygen were generated and shown in Figure 5.21.

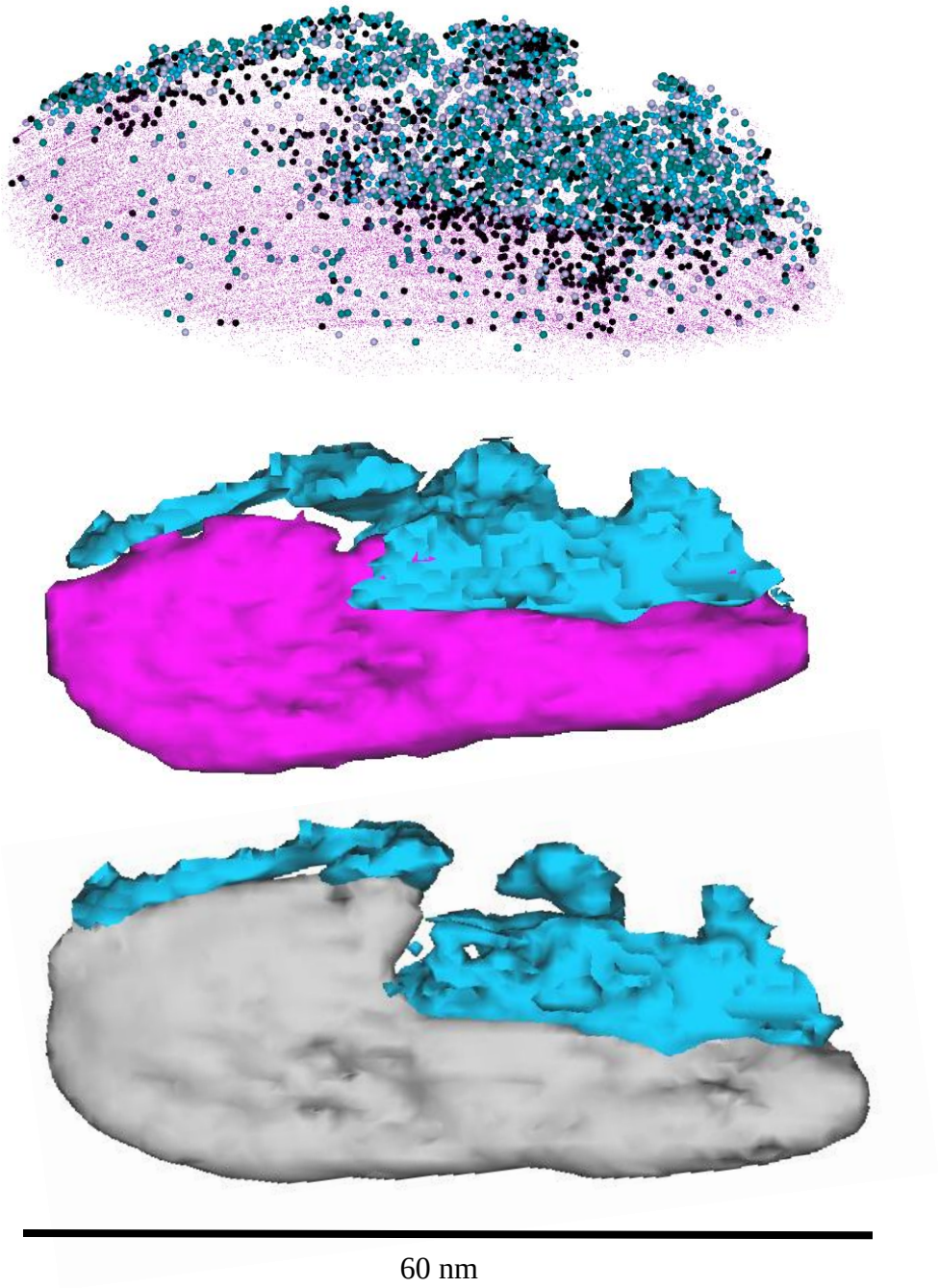


Figure 5.21 – Top - Atom map of large silicon phosphide precipitate with phosphorus species (purple), oxygen species (blue) and species at 36 Da (black). Middle - 25 at.% phosphorus iso-concentration surface and 3 at.% oxygen iso-concentration surface. Bottom - 30 at/nm^3 atomic iso-density surface (all atoms) in grey. Oxygen 1 at/nm^3 oxygen iso-density surface in blue.

These values were chosen as the minimum values giving the most coherent and uniform surfaces from both species. It is important to note the large difference in concentrations that are used to generate surfaces, with the concentration of oxygen contained within the iso-concentration surface being far lower than that used for the phosphorus. This indicates that there is a large change in density between the two regions. To further demonstrate this, two iso-density surfaces were generated and are included at the bottom of Figure 5.21. The iso-density surface in grey is from 30 at/nm^3 and comprises contributions from all ions; the iso-density surface in blue is from summed oxygen species and is at 1 at/nm^3.

In order to obtain a measurement of the concentration profile through the precipitate, a volume encapsulated by a 25 at.% phosphorus iso-concentration was selected. A cylindrical ROI with a diameter of 10 nm was projected through the flattest part of this iso-concentration surface and used to generate a 1D concentration profile of phosphorus and silicon species (Figure 5.22).

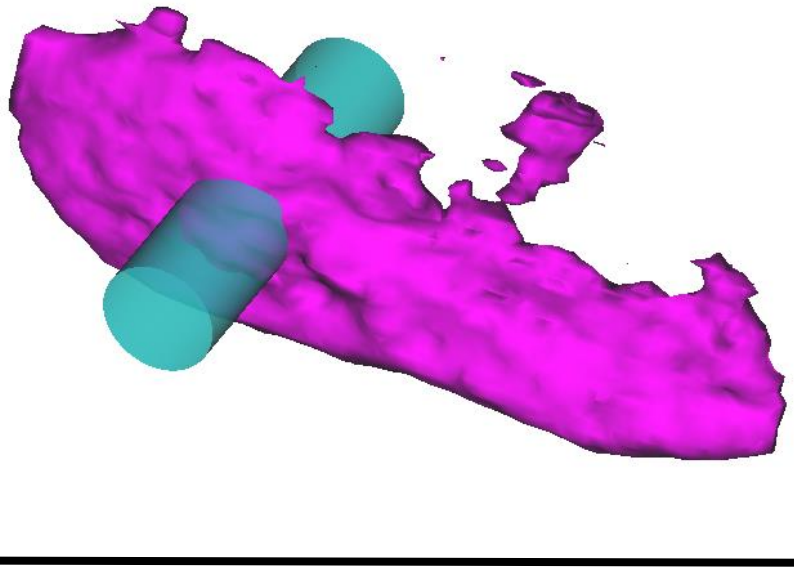


Figure 5.22 – 4 nm diameter, 13 nm long cylindrical ROI through 25 at.% phosphorus iso-concentration surface.

The bulk decomposed mass spectra extracted from the entire silicon phosphorus precipitate as delineated by a 25 at.% phosphorus iso-concentration surface was found to be 67.4 at.% silicon, 26.2 at.% phosphorus, 1.7 % at.% oxygen and 3.9 at.% hydrogen. The concentration profiles of decomposed silicon and phosphorus from this ROI can be found in Figure 5.23, where the peak concentration of phosphorus is found to be 34.7 at.%, with a corresponding silicon concentration of ~ 65.2 at.%.

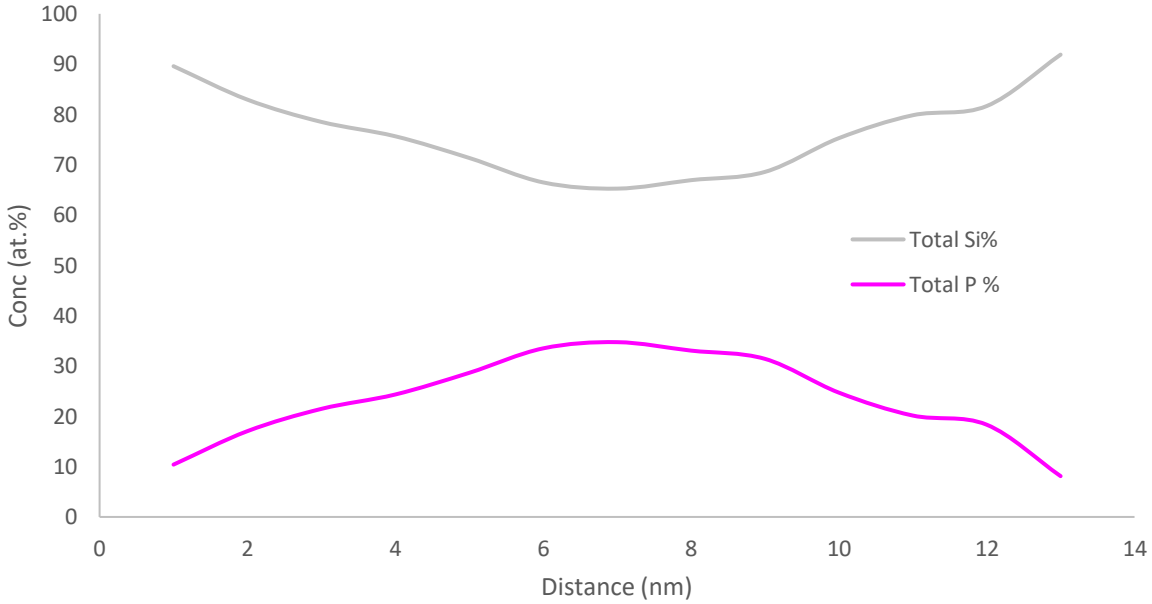


Figure 5.23 – Profiles of phosphorus and silicon species through cross section of silicon phosphide precipitate via ROI as shown in Figure 5.25.

Silicon concentrations were from the Si^{+} and Si^{2+} species and phosphorus from the P^{2+}, P^{+}, P_2^{+}, P_3^{+}, P_4^{+}, SiP^{2+} and SiP^{+} species. As the depth resolution of atom probe is greater than that of the lateral resolution and less prone to variation due to evaporation, a ROI was also placed along the short axis of the precipitate. A similar profile to that of the lateral profile with a relatively uniform peak phosphorus concentration of 30 at.% was found.

Silicon phosphide precipitates are not expected to have an internal variation in concentration and diffraction experiments indicate that they are expected to be

stoichiometric SiP [250]. The maximum phosphorus concentration through the centre of the iso-concentration surface and the total phosphorus composition are significantly lower than the 50 at.% that is expected.

The ratio of the phosphorus ions to the silicon ions was calculated from the cross sectional profile and shown in Figure 5.24 and was found to have a maximum ratio of $SiP_{0.5}$ or Si_2P. This is unlikely to be a true representation of the stoichiometry as this silicon/phosphorus ratio has not been measured by any other technique and is expected to be SiP [126].

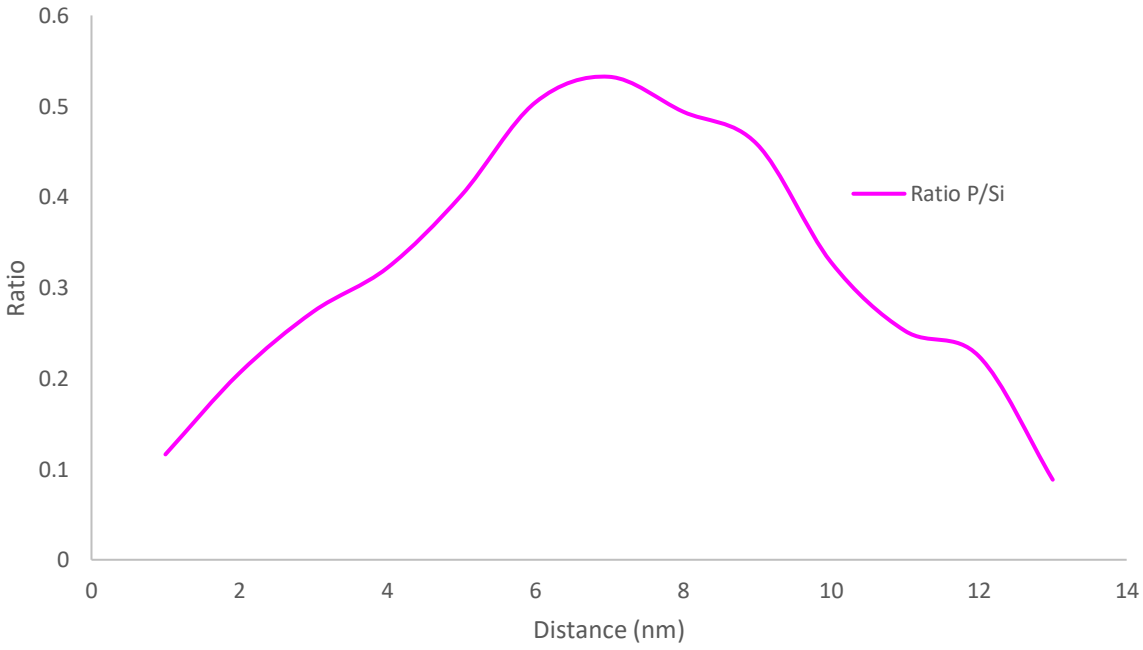


Figure 5.24– Ratio of number of phosphorus ions to silicon ions

Through observing the increase in total ion count as a function of increased phosphorus concentration through the silicon phosphide precipitate, it can be seen that there is a definite increase in apparent density with increased phosphorus concentration (Figure 5.25).

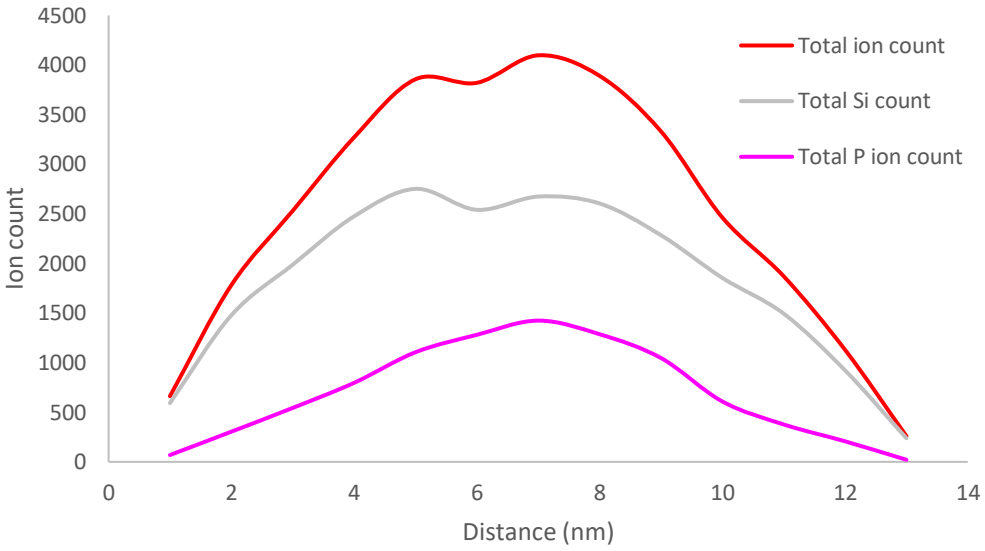


Figure 5.25 – Total ion count, total silicon ion count and total phosphorus ion count.

The increase in ion counts within the phosphorus rich regions has implications for determining the apparent segregation of low concentration species within, and around, these regions. Increased ion counts indicate an increase in measured density, so low concentration species may appear to segregate there compared to nearby regions of lower density purely based on the increased number of ions.

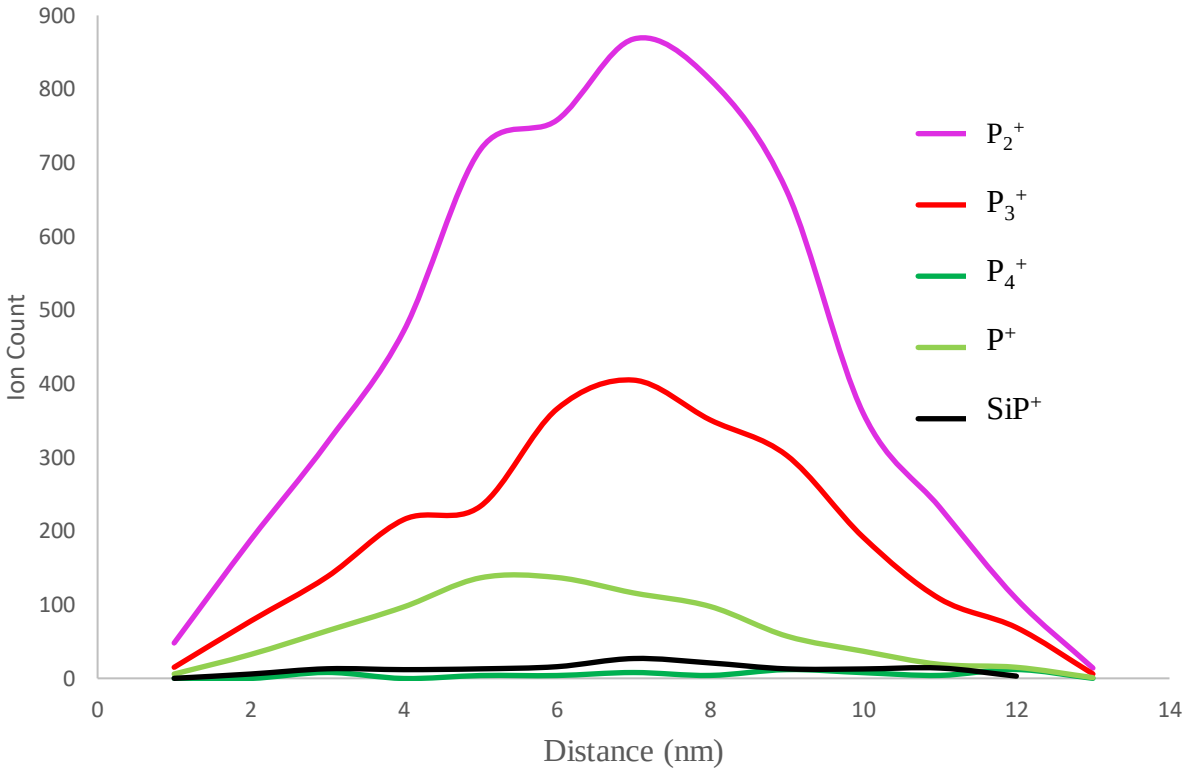


Figure 5.26 – Ion counts of single and complex ion phosphorus species through cross section of the precipitate.

The local field variation can also be seen in the change in the ratio of the complex ion species through the cross section of the precipitate. The majority of the phosphorus ions are found in complex ion species, with the being the greatest contributor. Single phosphorus ions in the P^+ species contribute less than both P_2^+ and P_3^+ complex ions (Figure 5.26). There are a number of potential reasons why the APT measured phosphorus composition of these precipitates is lower than that predicted by diffraction analysis. There is a distinct blurring of the interface between the precipitates and the silicon matrix due to the preferential evaporation of the precipitates during analysis. This prevents the interface being clearly defined by an iso-concentration surface and thus excess matrix material will be included in compositions generated using this technique.

Phosphorus has a single isotope and therefore it is not possible to distinguish between the singly charged single phosphorus ion P^+ at 31 Da and the doubly charged complex P_2^{2+} ion at 31 Da. Similar overlaps are also possible at 62 Da between the singly charged P_2^+ complex ion and the doubly charged P_4^{2+} complex ion.

This effect can lead to ions being mislabelled and thus change the apparent concentration [237]. In this case, as there seems to be an overall reduction in phosphorus concentration compared to that predicted by other techniques, some P_2^+ ions are likely being mislabelled as P^+. The ratio between the species is not uniform across the entire profile. At 5 nm, the numbers of P^+ and P_2^+ ions increase whilst those P_3^+ ions decrease. The change in ratio of P^+/P_2^+ species and thus the extent of the mislabelling is unlikely to be uniform across the precipitate due to the evaporation field changes with the general increase in phosphorus concentration. The increase in the lowest concentration complex SiP^+ ion and P_4^+ at approximately 7 nm also coincides with the peak concentration of the precipitate, so can be considered as an indication of the location of the greatest reduction in evaporation ield requirements. However, this region is also the location of highest density of all ions and therefore cannot be considered conclusive evidence of segregation as they may be visible there purely as a function of density.

5.2.2 Atom probe analysis of iron contaminated, phosphorus diffused silicon. Laser energy 75 pJ

Similar spatial overlaps were also found between oxygen and silicon phosphide precipitates in an identical sample to that shown in 5.2.1 that was analysed using 75 pJ pulses rather than 50 pJ (Figure 5.27).

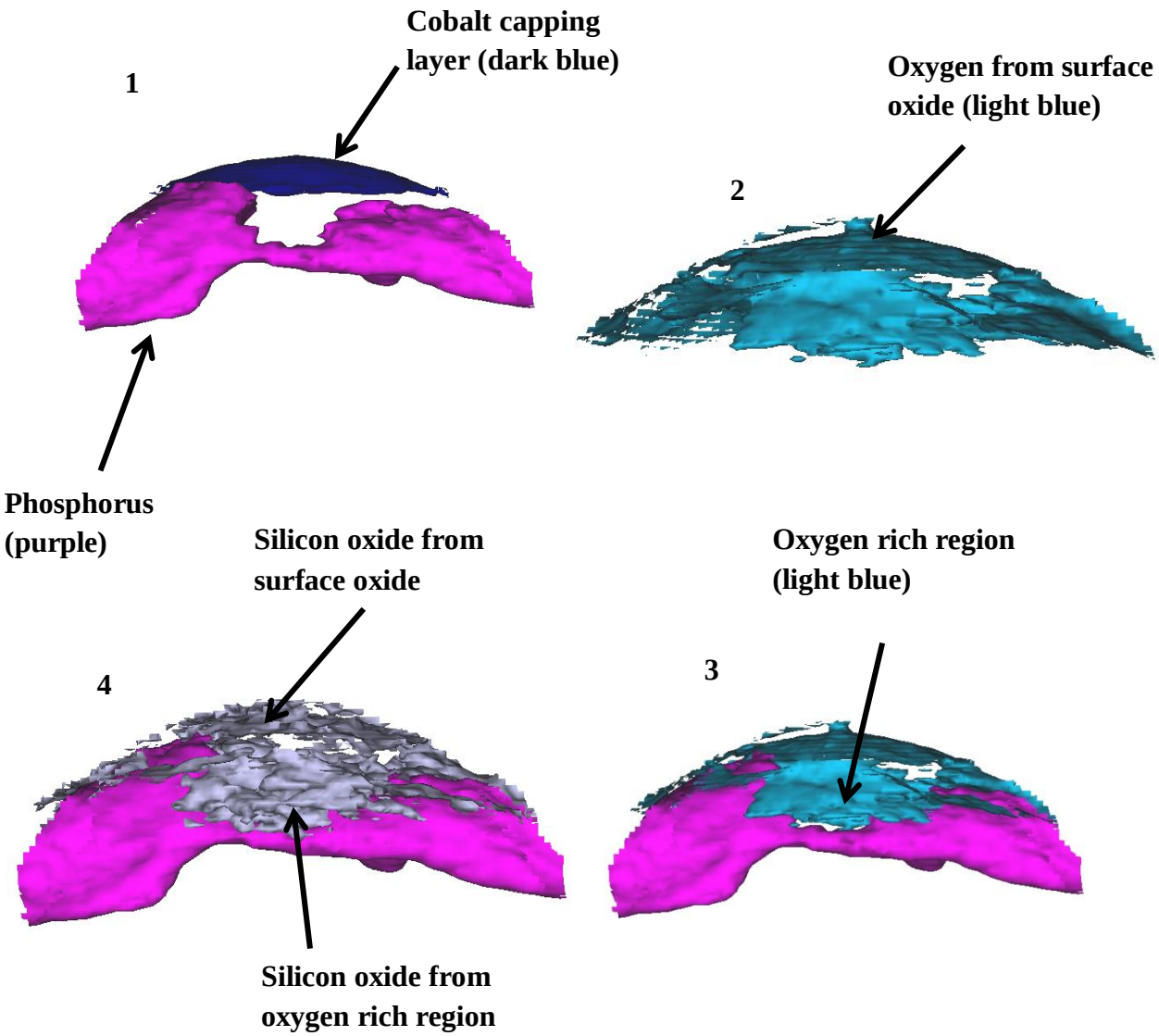


Figure 5.27 – Clockwise from top left. 1)10 at.% Phosphorus iso-concentration surface, 50 at.% cobalt iso-concentration surface. 2) 5 at.% oxygen concentration surface, 3) 5 at.% oxygen iso-concentration surface overlaid over a 10 at.% phosphorus iso-concentration surface 4) 5 at.% silicon oxide iso-concentration surface overlaid over 10 at.% phosphorus iso-concentration surface.

This increase in laser energy was chosen in order to attempt to shift the charge state ratios of iron species into the Fe^+ singly charged state, away from the overlap at 28 Da between $^{28}Si^+/^{56}Fe^{2+}$ and become more visible in the mass spectra. Species at 56 Da were observed within this sample and spatially segregated to the oxygen rich regions but it was not possible to directly determine if they were $^{28}Si_2^+$ ions or $^{56}Fe^+$ ions due to their low

numbers, preventing isotopic identification. The increase in laser energy could also increase the likelihood of complex iron ions to be formed such as $(^{56}Fe^{16}O)^{+}$ at 72 Da and $(^{56}Fe^{16}O)^{2+}$ at 36 Da. The species at 36 Da is again observed to segregate to oxygen rich regions, decorating the interface between the oxygen rich and phosphorus rich regions (Figure 5.28).

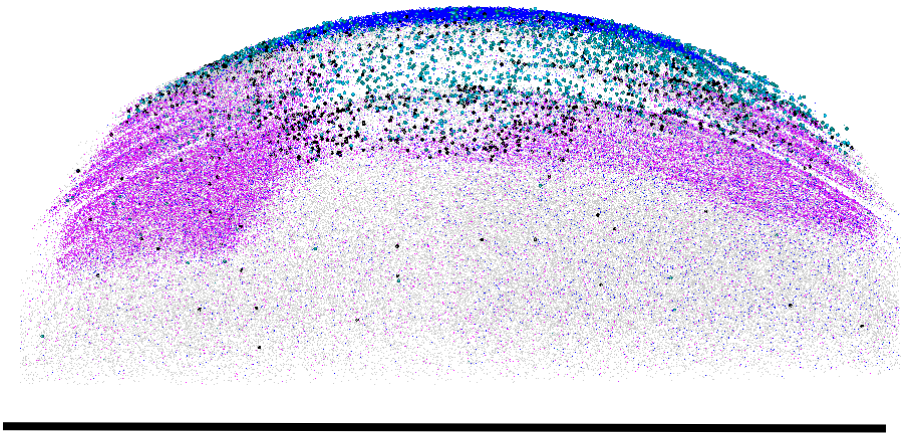


Figure 5.28 – Atom map of silicon phosphide precipitate with oxygen rich region in centre. Oxygen in light blue. Cobalt in dark blue, phosphorus in purple. Species at 36 Da shown in black.

A 50 at.% cobalt iso-concentration surface was used to generate a proximity histogram to plot the concentration profiles of cobalt, phosphorus, oxygen and silicon oxide (Figure 5.29).

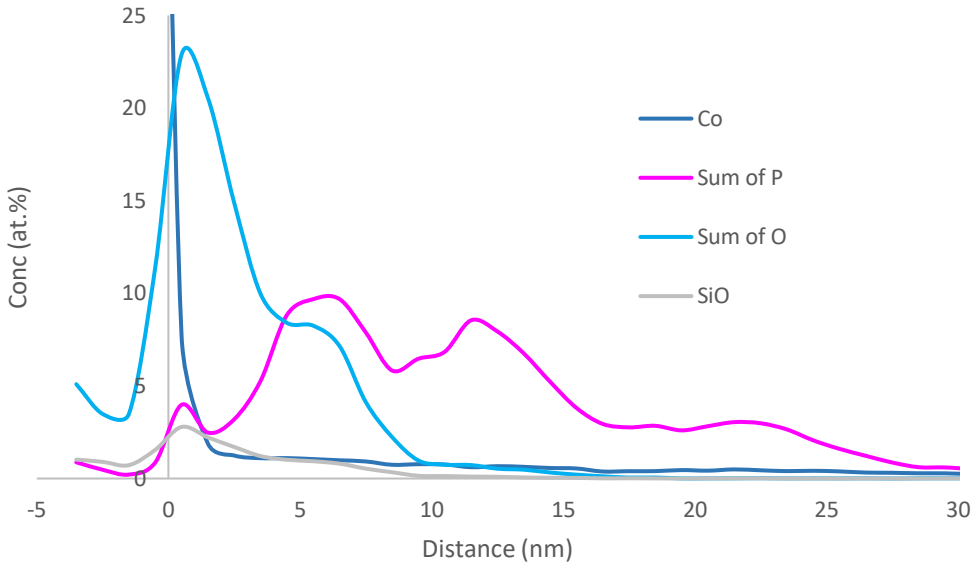


Figure 5.29 – Concentration profiles from a 50 at.% cobalt iso-concentration surface. Decomposed profiles of phosphorus and oxygen are shown along with silicon oxide.

There are two distinct phosphorus concentration peaks at approximately 7 nm and 13 nm. This corresponds to the depth of the two main silicon phosphide precipitates. The oxygen profile shows a distinct ‘shoulder’ region between 5 and 10 nm in depth, which corresponds to the depth of the first precipitate but is not found on the second precipitate (Figure 5.30).

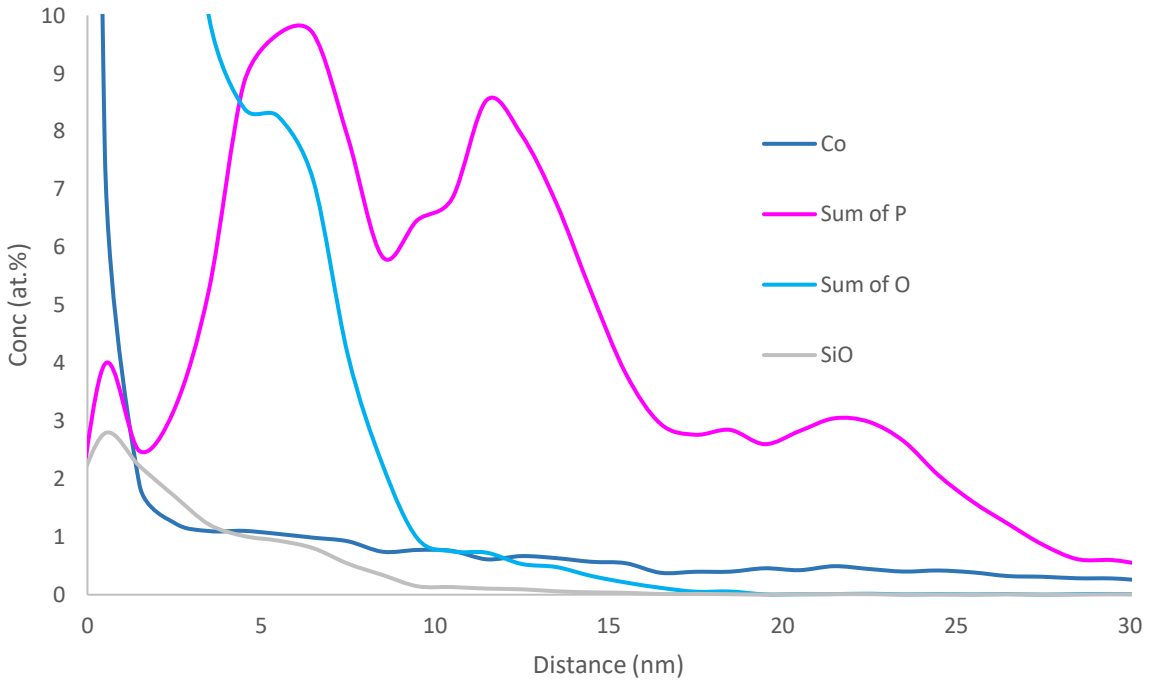


Figure 5.30 - Concentration profiles from a 50 at.% cobalt iso-concentration surface. Same data at Figure 5.29 but rescaled for clarity of low concentration species. Decomposed profiles of phosphorus and oxygen are shown along with silicon oxide.

It is interesting to note that although there two distinct silicon phosphide precipitates, only one has an associated oxygen rich region despite their similar size and composition. The two measured phosphorus precipitate regions are almost perpendicular to each other and, as such precipitates have been previously seen to lay on specific crystallographic orientations, it is likely this is here [126]. There may be a relationship between the orientation of the precipitate and the segregation of oxygen to these precipitates but the behaviour that is observed here seems to be a function of depth and proximity to the surface rather than crystallographic orientation.

5.2 Atom probe analyses using LEAP 5000 XR of silicon with no iron contamination

5.2.1 Atom probe analysis of uncontaminated, phosphorus diffused silicon. Laser energy 75 pJ

In order to determine if oxygen rich features at the surface or in proximity to silicon phosphide precipitates, could be observed in phosphorus diffused silicon without iron contamination, a number of samples were analysed alongside those with iron contamination (Figure 5.31). Despite the analysis of some tens of samples, none were found to have any silicon phosphide precipitates present. It can be visually seen that the concentration of phosphorus in the surface regions of this sample are much lower than those iron contaminated samples previously shown. This should not be taken as an indication that they are not present in the non-iron contaminated substrate as they were processed in the same conditions as that of the iron contaminated substrate. TEM analyses of similar materials also show the presence of silicon phosphide precipitates in phosphorus diffused silicon with no deliberate iron contamination [126] [258]. The lack of observation of these precipitates should then be linked to their number density compared to the nanoscale sampling that is carried out through atom probe.

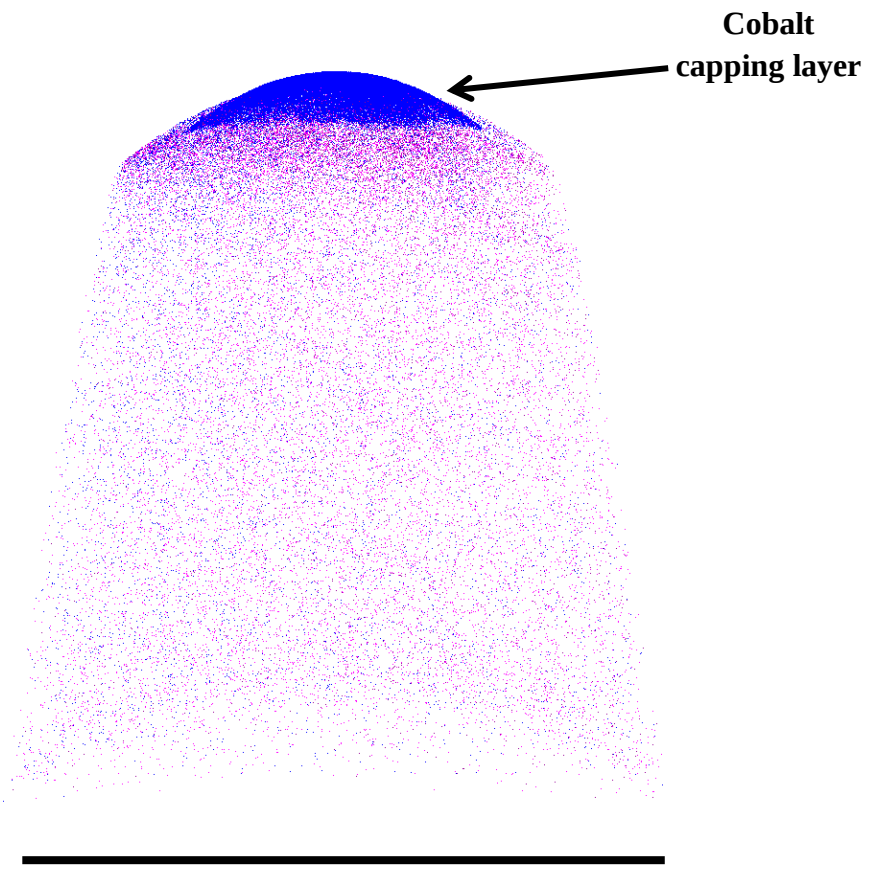


Figure 5.31 – Atom map with cobalt (blue), phosphorus (purple) and silicon (grey) of phosphorus diffused silicon with no iron contamination.

Despite the lack of silicon phosphide precipitates, heterogeneous regions rich in oxygen were found at the surface of the silicon, capping layer interface (Figure 5.32). These were also found in iron contaminated, phosphorus diffused samples which contained no silicon phosphide precipitates. Analysis of these are given in Appendix F.

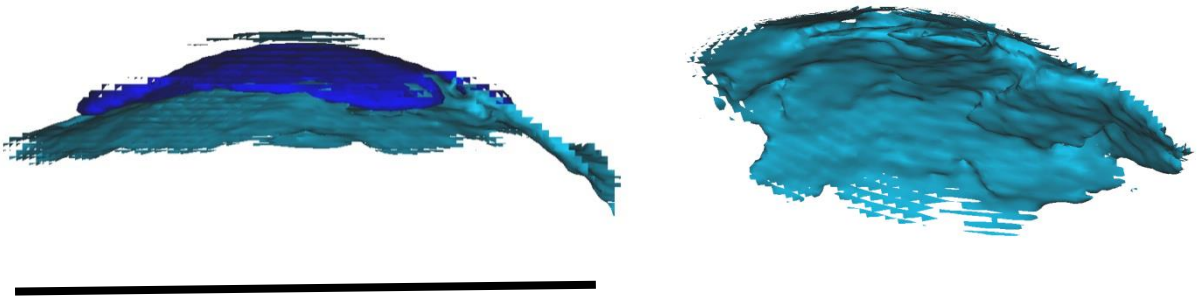


Figure 3 – Left – Iso-concentration surfaces of 10 % cobalt and 15 % oxygen side on view Right – Iso-concentration surface of 15 % oxygen tilted to view from below.

An iso-concentration surface of 15 % cobalt was used to generate a proximity histogram of concentration profiles of phosphorus, oxygen and silicon oxide (Figure 5.33).

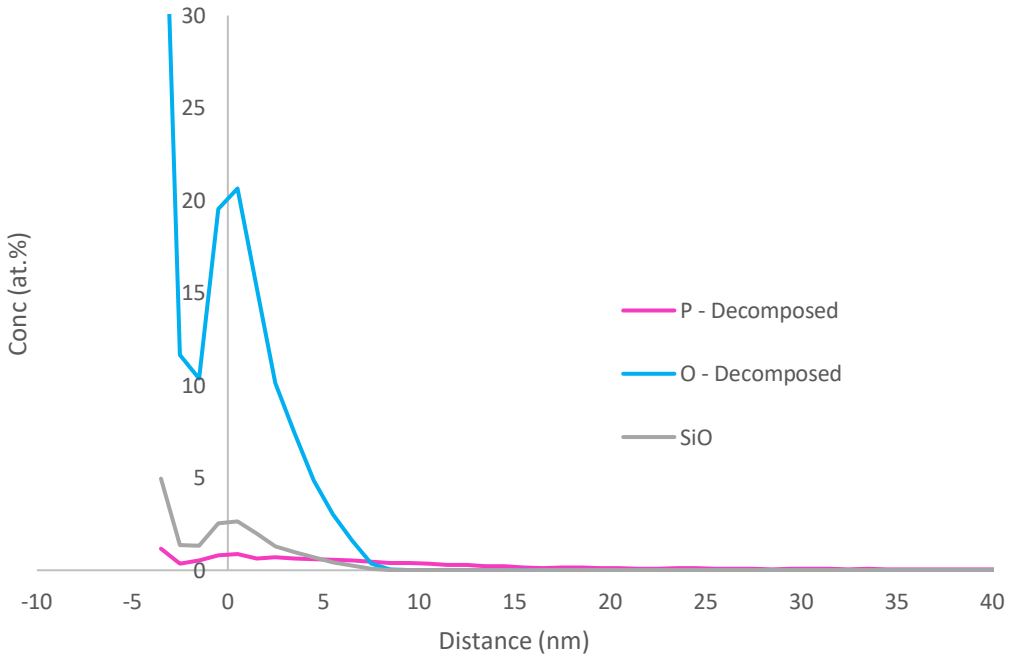


Figure 5.33 – Profiles of phosphorus, oxygen and silicon oxide from 10 at.% cobalt iso-concentration surface in a phosphorus diffused silicon with no iron contamination.

There are a number of comparisons that can be made between the concentration profiles obtained from samples both analysed using 75 pJ laser pulses, from the iron contaminated

phosphorus diffused sample in Figures 5.29 and 5.30 and the non-iron contaminated phosphorus diffused sample in Figure 5.33. The decomposed oxygen profile peaks at approximately the same concentration for both samples but extends to a far greater extent in the iron contaminated sample (~ 20 nm compared to ~ 7 nm). The decomposed oxygen profile also matches spatially with the silicon oxide profile in both samples whilst the phosphorus concentration peaks at ~ 1 at.% at the capping layer interface and decreases smoothly from there on. The species at 36 Da was plotted alongside known carbon species in a similar manner to that used for the iron contaminated analysed with 50 pJ in Figure 5.10 and presented below in Figure 5.35.

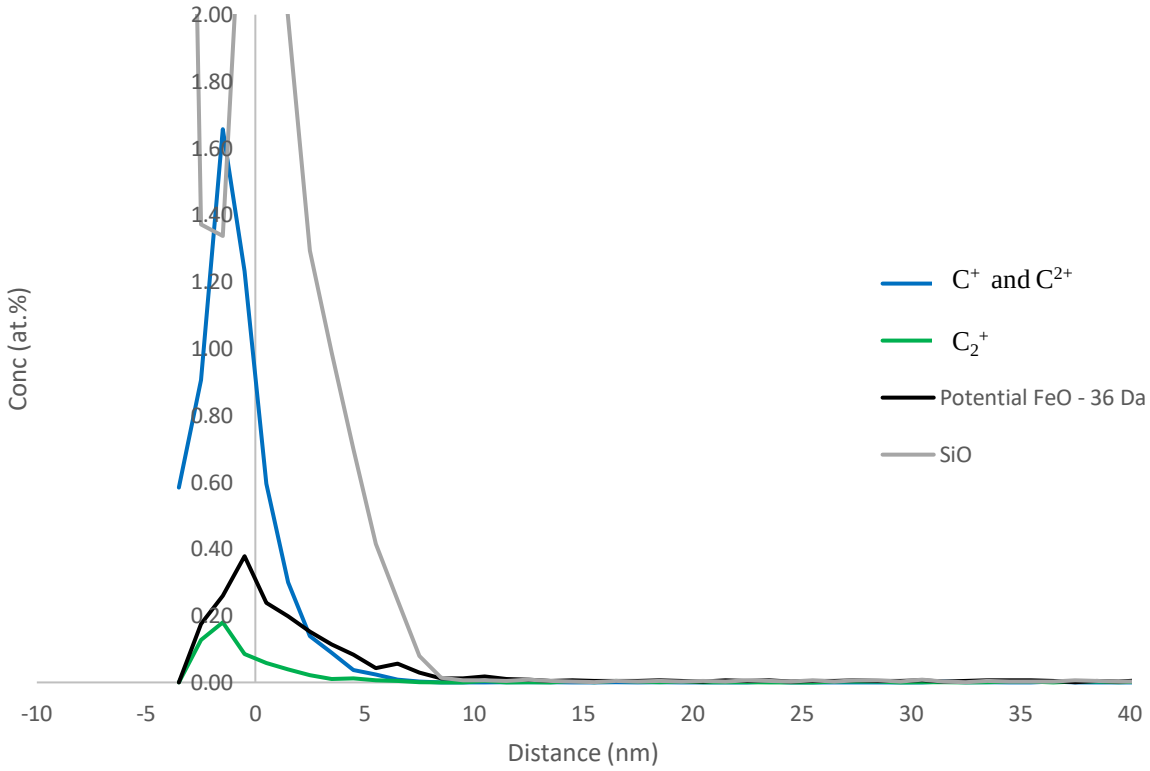


Figure 5.35 – Profiles of silicon oxide and carbon species and species at 36 Da from 10 at.% cobalt iso-concentration surface in a phosphorus diffused silicon with no iron contamination.

Species relating to the C^{2+}, C^{+} and C_2^{+} were observed to all be present within the region containing the silicon oxide layer, as was the species at 36 Da. As there was no iron contamination, the species at 36 Da will likely consist of C_3^{+} and $(^{28}Si_2{}^{16}O)^{2+}$. Species at 56 Da were also observed in this sample and as there was no intentional iron contamination, it is most likely that these species are $^{28}Si_2^{+}$ ions rather than $^{56}Fe^{+}$.

In this sample the concentration of the 36 Da species corresponding to the C_3^{+} ion is higher than that of the peak at 24 Da, which corresponds to the C_2^{+} ion. The singly charged carbon ions C^{2+} and C^{+} at 6 Da and 12 Da respectively are still the preferential species. As it would be expected that the largest complex ion to have the lower number of ions, this suggests that the peak at 36 Da does not only contain C_3^{+} species.

This could indicate that there is an increased contribution to the $(^{28}Si_2{}^{16}O)^{2+}$ complex ion concentration in this surface region, likely due to the laser pulse energy of 75 pJ used in this analysis compared to the 50 pJ used in the similar analysis in Figure 5.10. This indicates that the species at 36 Da found spatially segregated to the oxygen rich regions and silicon phosphide precipitates (which was not found with corresponding peaks at 6 Da, 12 Da and 24 Da) is not carbon based.

5.3 Discussion

5.3.1 Silicon phosphide precipitates.

Optimised atom probe sample preparation using ex situ deposited cobalt capping layers was successfully used to analyse the surface and near surface regions of iron contaminated, phosphorus diffusion gettered silicon.

It was found that at the surface of iron-contaminated, phosphorus-diffused silicon, small oxygen rich regions were identified in close proximity to phosphorus rich regions with crystalline structure. These phosphorus rich regions were identified as silicon phosphide precipitates [124] and have been previously predicted to facilitate gettering [26] through interstitial generation during precipitation.

These phosphorus precipitates have previously been observed in phosphorus diffused silicon materials when sufficient surface concentrations are present [258] and have been determined to be silicon phosphide through TEM based diffraction analysis of the crystal structure [250]. Silicon phosphide precipitates have been shown via TEM in two main forms, those of long orthorhombic precipitates with up to micron scale lengths and tens of nm in cross section and small spherical precipitates of approximately 2 nm in diameter [259]. Only the long precipitates at the very surface of the silicon were observed in samples shown in this work. Small spherical precipitates seen previously via TEM, were not observed [124], although cluster based analysis of APT data could potentially be used to test for this and has been previously used to analyse nanoscale boron clusters in silicon [260].

The silicon phosphide precipitates have been shown to extend approximately 30-40 nm in depth below the capping layer surface, which corresponds to the depth of both the measured oxygen and iron profiles previously observed [24] [115]. As the phosphorus concentration has been measured to decrease significantly as a function of depth over the initial tens of nm, it is reasonable to assume that the size and density of silicon phosphide precipitates within this region will also decrease.

Silicon phosphide precipitates were not found in all iron contaminated samples and none were found in samples with no intentional iron contamination. However, due to the small

numbers of viable samples for both materials, this does not mean that they were not present in the non-iron contaminated samples. Due to the nanoscale APT sample volumes involved, a lower local number density of precipitates could readily reduce the likelihood of observing one during analysis. Cross sectional images of phosphorus diffused silicon which not had the PSG layer removed have shown a non-uniform surface layer which is due to the non-uniform island growth of the PSG (images of these substrates can be found in Appendix D). This has been previously shown in the literature by Solmi et al. [251] who demonstrated that the size and distribution of these islands can be altered by varying the temperature of the diffusion process. This local variation in PSG thickness may lead to local nanoscale variations in phosphorus concentration and thus vary local concentrations of silicon phosphide precipitation.

The size and shape of the silicon phosphide precipitates, as measured by atom probe, are distorted through evaporation field artefacts due to differences between the evaporation field requirements of silicon phosphide and silicon. The stoichiometry of these precipitates was found to be significantly lower in phosphorus than predicted. This is likely due to lateral blurring of the preferentially evaporating precipitates, mislabelling of complex ions and dissolution of cluster ions in flight [237].

5.3.2 Oxygen rich regions

Oxygen rich regions have been observed in close proximity to higher densities of silicon phosphide precipitates and were not observed to have any crystal structure in the form of visible atomic planes, as seen in the silicon phosphide precipitates in Figure 5.17. This lack of apparent crystallinity may be a real effect, or can be a result of the low density of the oxygen rich regions in the reconstruction caused by local field variations from the silicon phosphide precipitate. Due to these density variations, and the irregular shape of the

oxygen rich regions, it was not possible to directly confirm the ratio of silicon and oxygen species within them and thus confirm if the regions are oxide particles as predicted by [24], or just oxygen rich. In each case when these oxygen rich regions were found below the silicon oxide surface layer, they were found in direct contact with silicon phosphide precipitates, yet always connected to the silicon oxide surface layer. Oxygen precipitates have been previously observed segregating to silicon phosphide precipitates in phosphorus diffused silicon via TEM [25].

Oxygen rich features in the form of nanoscale variations in the texture of oxygen iso-concentration surfaces were also observed at the surface silicon oxide/silicon interface in both iron contaminated, phosphorus diffused silicon and phosphorus diffused silicon with no iron contamination. These features were parallel to native silicon oxide/silicon interface. This indicates that such features do not need intentional iron contamination to form and thus could be formed due to oxygen precipitation based on vacancies caused by the phosphorus diffusion process. It is also possible that some oxide from the phosphorus gettering process was not removed during the HF etching prior to the thermal evaporation of the capping and remained on the surface to be analysed in this manner. It was not possible to determine the level of iron segregation, if any, to these features due to mass spectra overlaps with silicon, silicon oxide and carbon in the surface regions.

Oxygen rich regions below the surface oxide, which are not parallel to the surface, were only observed in conjunction with the silicon phosphide precipitates if there was a direct physical connection from oxygen rich regions at the silicon oxide surface layer. This indicates that the oxygen profile as measured by SIMS by Syre et al. [24], in samples processed in a similar manner, likely composes of discrete, nanoscale oxygen rich regions rather than laterally uniformly dispersed oxygen.

5.3.3 Atom probe identification of potential iron species

Due to mass spectra overlaps between majority iron and silicon species in single ion form, the main candidates for visible iron containing species were in form of the complex species $(^{54}Fe^{16}O)^{2+}$ and $(^{56}Fe^{16}O)^{2+}$ at 35 and 36 Da [208]. However, there also are overlaps between C_3^+, $^{28}Si_2{}^{16}O^{2+}$ and $(^{54}Fe^{16}O)^{2+}$ ions at 36 Da. The species at 36 Da was also found at the surface regions of phosphorus diffused silicon with no iron contamination and was spatially segregated with known carbon species of C_2^+ at 24 Da and C^+ at 12 Da. In iron contaminated samples, the species at 36 Da below the surface layers did not spatially segregate with known carbon species and therefore it is unlikely to have significant contributions from the C_3^+ species in these regions.

The distribution of satellite peaks around 36 Da in at 36.5 Da and 37 Da, from the regions containing the species at 36 Da but not C_2^+ at 24 Da and C^+ at 12 Da, indicate that the majority of the 36 Da species in the iron contaminated samples away from the surface is in fact $(^{28}Si_2{}^{16}O)^+$. The 36.5 Da and 37 Da peaks are therefore mostly likely $(^{28}Si^{29}Si^{16}O)^{2+}$and $(^{29}Si^{29}Si\,^{16}O)^{2+}$/$(^{28}Si^{30}Si\,^{16}O)^{2+}$ respectively.

The majority $(^{56}Fe^{16}O)^+$ species at 72 Da and $(^{56}Fe^{16}O)^{2+}$ at 36 Da are also potentially detectable in the APT analysis of a silicon sample without significant overlaps although there is a potential overlap with the silicon oxide complex ion $(^{28}Si_2{}^{16}O)^+$ and $(^{28}Si_2{}^{16}O)^{2+}$ species at 72 Da and 36 Da, respectively, and also with the complex carbon species C_3^+ at 36 Da for $(^{56}Fe^{16}O)^{2+}$. In order to distinguish iron oxide species conclusively despite the above overlaps, minority complex species of $(^{54}Fe^{16}O)^+$ and $(^{54}Fe^{16}O)^{2+}$ at 70 Da or 35 Da are required. However as these minority isotope species, $^{54}Fe^+$ consisting of only ~ 5% of the natural isotopic abundance of iron, of an already very low concentration species, it is unlikely that they will be visible even when spatially segregated in a silicon matrix.

Atom probe analysis parameter optimisation showed that 35 K was the lowest temperature at which these samples would reliably survive the capping layer/silicon interface transition. Laser energies of 75 pJ were shown to produce a measurable peak at 56 Da that is likely due to complex Si ions rather than Fe^{+} ions, as this laser energy was found to produce an identical peak in non iron contaminated pure silicon samples.

Overall, due to the low concentration of iron predicted to be present in the surface regions (even after phosphorus diffused gettering induced segregation), it was not possible to directly confirm the presence of iron species in this material system using APT.

5.3.4 Phosphorus diffusion gettering mechanisms

If the presence of silicon phosphide particles are required for the gettering process to proceed, then this would imply that, if the phosphorus concentration was not above the solid-solubility limit after diffusion and cooling, then precipitation would not occur and thus the gettering effect would be reduced. This proposal would fit with the observations by Syre et al., [24] that there is a minimum level of phosphorus required in the diffusion treatment that will cause gettering, before this level there is no appreciable gettering and above this level there is no appreciable increase in gettering.

An optimal gettering treatment would, therefore, be tailored to allow the minimum amount of silicon phosphide particles to form at the surface and provide the required gettering level, whilst not increasing their number such that they will affect the overall surface resistivity [255]. As the phosphorus diffusion process for silicon photovoltatic materials is used to both form the n-doped region of the device, and to simultaneously getter transition metals, the optimal diffusion parameters for gettering may not be the same for optimal device performance, even if not all the transition metals had been gettered [255].

The variation in initial phosphorus concentration and subsequent diffusion profiles that were found between atom probe samples, compared to the relatively smooth profiles as reported by SIMS in the literature, indicates that the large analysis area of SIMS is indeed averaging the concentration of phosphorus over a range of initial concentrations. This averaging also affects oxygen and iron species and, as the APT analyses shown in this chapter have demonstrated, there are heterogeneously distributed nanoscale features in the form of oxygen rich regions that are present in the material that are not observed during SIMS analysis. Therefore, APT has been shown to be a viable method for investigating surface, nanoscale segregation of species in gettered silicon when the species of interest are within a concentration range suitable for the technique and do not have significant mass spectra overlaps.

5.3.5 Future work

The analysis of atom probe samples containing silicon phosphide precipitates relies on there being a sufficient number density such that there is a reasonable probability of capturing them within the technique's nanoscale volume of analysis. If FIB lift outs were placed upon supports that would be suitable for complementary TEM and atom probe analysis, the samples could be screened first via TEM to determine if any silicon-phosphorus precipitates or oxide rich regions were present within the surface regions [261]. This would also allow the crystallinity of such precipitates and oxide rich regions to be determined. EDX and EELS based chemical analysis could also be carried out on such a sample, allowing the potential detection of iron species spatially segregated to these regions. Due to the reconstruction artefacts that will be present with the surface regions of such a sample, from variation in evaporation field requirements of the capping layer and the silicon phosphide particles, the exact dimensions of the precipitates will be more

difficult to measure and will have likely been underestimated in atom probe. TEM will allow more accurate measurements that can be then used to calibrate the atom probe reconstruction parameters.

In order to confirm the local segregation of iron oxide species to the silicon phosphide particles or oxygen rich regions using atom probe, it is proposed that the experimental procedure be repeated using isotopically purified ^{54}Fe instead of pure natural abundance iron containing the majority isotope ^{56}Fe. This would have the effect of shifting the majority iron oxide mass spectra peaks to $(^{54}Fe^{16}O)^{2+}$ at 70 Da and $(^{54}Fe^{16}O)^{2+}$ at 35 Da, thus removing potential overlaps with silicon oxide complex ions and complex carbon ions.

The iron contamination process used here [246] would need to be altered, as obtaining sufficient ^{54}Fe to form a sharp point to mechanically break the silicon oxide layer was found to be prohibitively expensive. However, it is possible to carry out energy filtered ion implantation of the ^{54}Fe isotope from a natural abundance iron source and so carry out the bulk contamination via ion implantation instead of diffusion. The ion implanted substrate would then be furnace treated in order to anneal the radiation damage and uniformly diffuse the implanted species throughout the bulk, the subsequent phosphorus diffusion and atom probe sample preparation could then be carried out as described in this work.

The effect of iron on carrier lifetimes in silicon photovoltaic materials has been well documented in the literature, in particular it is possible to readily detect very low concentrations of interstitial iron in the bulk, and so it was a natural choice for investigation using APT. However, as it has been shown in this thesis, detection of low concentration iron in silicon using APT is extremely difficult and, therefore, other contamination using other transition metal species of interest should be explored in order

to increase the likelihood of obtaining useful information on gettering processes. Repeating the process shown in this thesis of contaminating silicon crystal silicon with a number of different transition metals, such as copper [262], which do not have mass spectra overlaps with silicon, in concentrations just below their solubility limit and then subjecting them to gettering processes would increase the likelihood of observing them using APT. In order to increase the likelihood of obtaining the surface regions within an atom probe tip, low temperature wafer bonding [242] could be used to fix two surfaces of gettered silicon together to form a dual layer system which could then be centred in an atom probe tip. To further increase the amount of surface material analysed within a tip and to reduce the chance of fracture due to analysing through a planar capping layer/silicon interface, APT analysis could be carried out parallel to the gettered surface using side on lift out techniques [243].

6. Conclusions

Focused Ion Beam (FIB) sample preparation for the surface and near surface regions of single crystal silicon was optimised through a combination of ex-situ deposited capping layers and milling parameters. Metal capping layers of nickel and cobalt were both found to be suitable to preserve and delineate the surface of the silicon during FIB sample preparation and atom probe analysis.

Atom Probe Tomography (APT) laser pulsed analyses of 14 kV P^+ phosphorus implantation profiles of peak concentrations 0.1 at.% - 0.2 at.% with a predicted peak depth of ~22 nm were analysed through direct implantation into pre-fabricated silicon micro posts. Comparisons between implantation profiles from as-implanted planar substrate lift outs and implanted micro posts showed good agreement. Rapid thermal annealing of implanted micro posts showed a greater segregation of phosphorus to the surface than predicted, which may be due to the change in thermal behaviour of the high aspect ratio micro post to that of the typical planar substrate. However, mass spectra overlaps from the metal capping layers extended over ~ 5 nm into the silicon, preventing quantification of low concentration phosphorus species in that region.

Stopping and Range of Ions in Matter simulations matched the implanted profile shape and peak concentration best when analysed with lower laser energies (25 pJ) using the LEAP 5000 XR. In order for the simulation to match the depth profile, the simulation had to be started from the depth at which silicon oxide was first detected. This was ~ 5 nm offset away from the surface defined by the end of the capping layer, indicating evaporation field artefacts may be artificially enlarging the measurement of the silicon oxide layer. Direct implantation into silicon micro posts did reduce FIB sample preparation time but also

increased the number of delamination events from the capping layer material surrounding the sharpened posts. This damaged local electrodes and made the process less cost effective.

The limit of detection for phosphorus in these atom probe analyses was orders of magnitude away from the requirements that would best inform implantation parameters for quantum arrays. However, the process can readily be applied to high concentration profiles used in modern nanoelectronics.

The surface regions of iron contaminated, phosphorus diffused silicon substrates were analysed using laser pulsed APT. Phosphorus diffusion profiles as measured by SIMS and APT showed good agreement. Silicon phosphide precipitates were observed touching the surface regions and within the top tens of nm of the surface. Oxygen rich regions at the surface of the silicon were observed in both iron contaminated and uncontaminated phosphorus diffused samples. These regions were also seen away from the surface in close proximity to silicon phosphide precipitates in iron contaminated silicon samples, extending to the same depth as these precipitates. This confirms that oxygen is heterogeneously distributed within the silicon surface regions and these local concentration may be linked to the distribution of silicon phosphide precipitates laterally and in depth. Small numbers of potential iron containing species in the form of $^{54}Fe^{16}O^{2+}$ at 35 Da were identified as segregating to these oxygen rich regions, with higher laser powers making them more visible. However due to the low concentration of iron and mass spectra overlaps between iron and silicon species, it was not possible to use these species quantify iron segregation to these regions.

Appendix A

Focused Ion Beam lift out parameters

The following procedure was optimised for producing a FIB lift-out bar for a surface protected by the application of ~ 200 nm of thermally evaporated nickel or cobalt, followed by 20 minutes of electron beam deposited tungsten and 10 minutes of FIB deposited tungsten as described in section 3.2.2 of this thesis. These parameters were calibrated using a Zeiss Nvision40 system and so using a different instrument may require some recalibration of parameters.

1) The sample was tilted to 54° (normal to the FIB column)

A rectangular trench was cut perpendicular to the bar, approximately 10 – 15 µm x 5 µm, starting 1 µm away from the edge with a 30 kV, 6.5 nA beam to the depth of 8 µm using the 'Mill for depth' function. A further cut was made using the same length box with a 1 µm width up to the edge of the bar with a 30 kV, 700 pA beam using the 'Deposition Mode' function.

2) The sample was tilted to 24°, resulting in a 30° angle with respect to the FIB column.
3) A trapezium-shaped trench with a length of ~30 µm and a height of 8 µm was cut using a 30 k, 6.5 nA beam parallel to the longitudinal axis of the bar, with the edge of the trench located 1 µm away from the required final edge of the bar. Once completed, another trapezium-shaped trench was cut using a 30 kV, 3 nA beam overlaid on the initial trench with a height of 4 µm and located in direct contact with the final bar edge. A final polishing cut was made using 30 kV 700 pA and the 'Deposition Mode' function for a 1 µm thick box extending the entire length of the bar, also in direct contact with the bar.

4) The sample is rotated by 180° and the process is carried out again for the other side of the lift out bar.

Appendix B

Rapid Thermal Annealing (RTA) conditions

Sample ramped from room temperature (~ 25°C) to 600°C in 12 seconds and from 600C to 1000°C in 5 seconds and held for 5 seconds. The sample was then allowed to cool naturally back to room temperature, having dropped from 1000°C to 500°C within a couple of seconds.

Scattering and Range of Ions in Matter (SRIM) simulation parameters

14 kV P^+ implant (peak concentration 0.2 at.%) with a dose of 2.68 x 10^{14} ions/cm^2.

14 kV P^+ implant (peak concentration 0.1 at.%) with a dose of 1.34 x 10^{14} ions/cm^2.

14 kV P^+ implant (peak concentration 0.01 at.%) with a dose of 1.34 x 10^{13} ions/cm^2.

28 kV P_2+ implant (peak concentration 0.2 at.%) with a dose of 1.35 x 10^{14} ions/cm^2.

SRIM calculations were carried out by Dr Brett Johnson of the University of Melbourne with the following parameters.

"Ion = P Energy = 14 keV

Layer Width = 1.E+03 A Layer # 1- Density = 4.976E22 atoms/cm3 = 2.321 g/cm3

Layer # 1- Si = 100 Atomic Percent = 100 Mass Percent

Total Ions calculated =50000.00

Ion Average Range = 231.0E+00 A Straggling = 107.5E+00 A

Ion Lateral Range = 716.4E-01 A Straggling = 925.3E-01 A

Ion Radial Range = 112.5E+00 A Straggling = 666.1E-01 A"

In order to scale the number of simulated implanted ions to give the required peak concentrations of 0.2 at.%, 0.1 at.% and 0.01 at.% they were scaled using the known fluences and converted to atomic % with the known density of silicon of ~ 5 x 10^{22} at/cm^3. T

For convenience in comparing with atom probe measured profiles, these have been converted to at.% and plotted in Figure B.1. The predicted range for each profile was ~ 22 nm and the predicted depth straggle was ~ 11 nm.

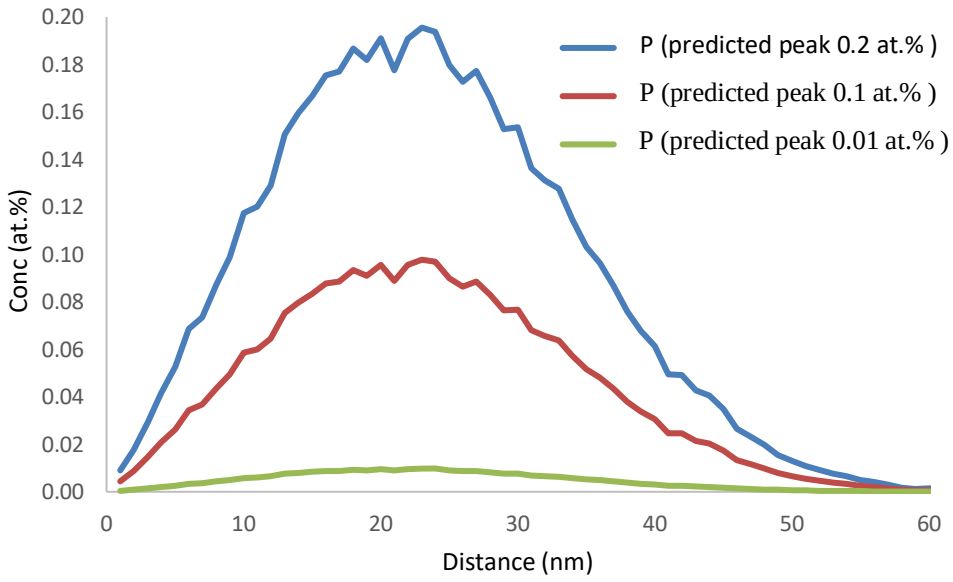


Figure B.1 – SRIM profiles of 14 kV P1 implant with peak concentrations of 0.2 at.%, 0.1 at.% and 0.01 at.%

Appendix C

Analysis of implanted micro post with nickel capping layer.

Predicted peak phosphorus concentration 0.1 at.%.

Analysis conditions: LEAP 3000X HR, 50 K, 200 kHz pulse frequency, 0.5 nJ pulse energy throughout, 0.3% detection rate in capping layer, 0.5% below capping layer.

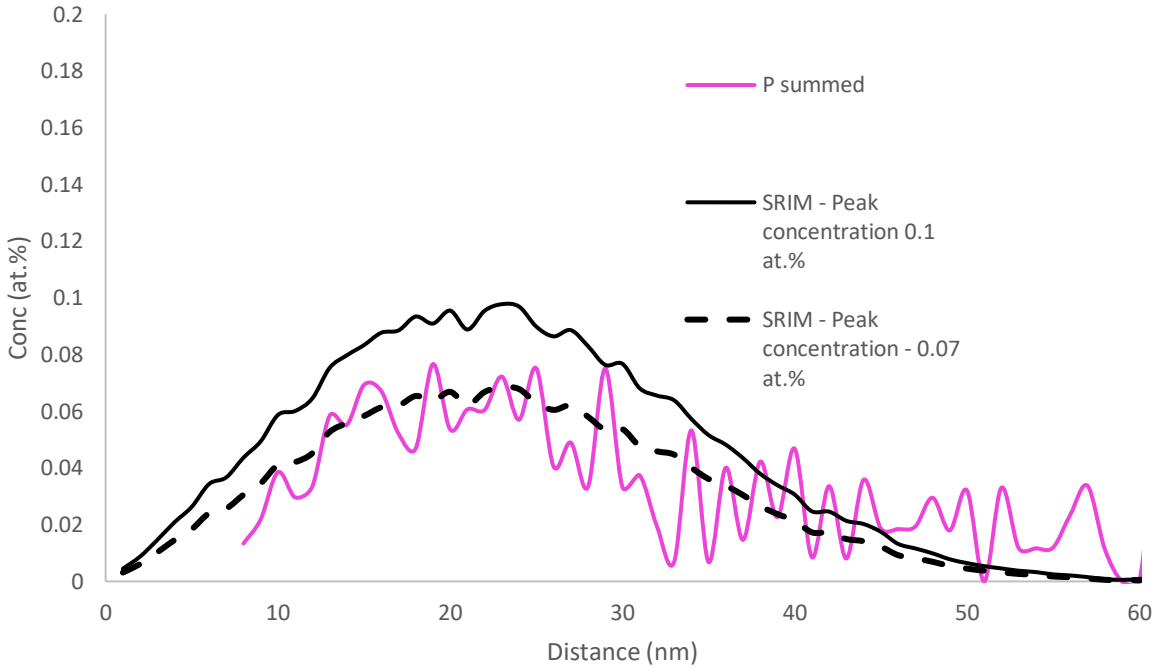


Figure C.1 – Summed phosphorus concentration profile overlaid with SRIM profiles of 0.1 at.% and 0.07 at.% predicted peak phosphorus concentration.

SRIM profiles of 0.1 at.% and 0.07 at.% predicted peak phosphorus concentrations were overlaid (Figure C.1) over the summed phosphorus concentration profile that has been normalised for depth using the starting point of the silicon oxide signal. The 0.1 at.% SRIM profile underestimates the peak concentration, whilst the 0.07 at.% SRIM profile matches the measured peak concentration and profile shape more closely.

Comparison between APT measured phosphorus profile of implanted micro posts with predicted 0.1 at.% and 0.2 at.% peak phosphorus concentrations and lift out with 0.2 at.% peak phosphorus concentration

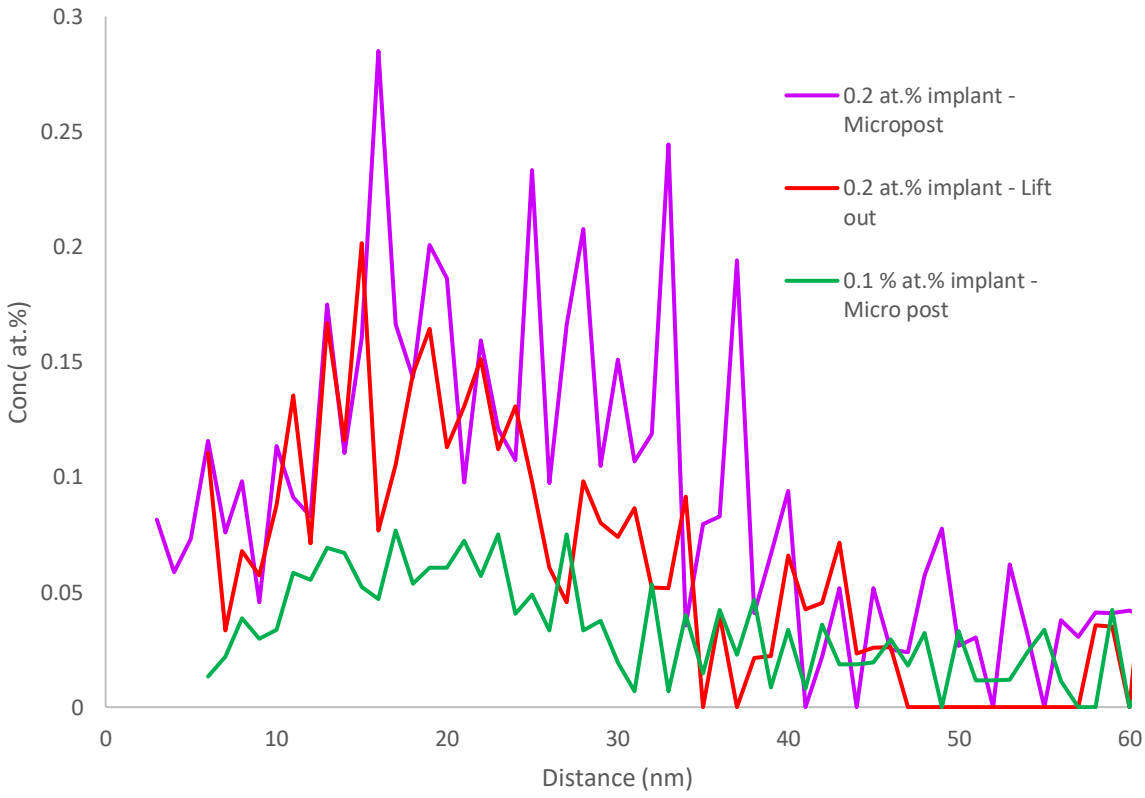


Figure C.2 – Phosphorus concentration profiles from 0.2 at.% lift out and micro post samples and 0.1 at.% lift out sample.

Concentration profiles of the micro post implanted with peak concentration of 0.1 at.% are overlaid (Figure C.2) with concentration profiles from micro posts and lift out data taken from Figure 4.21 and Figure 4.22 respectively.

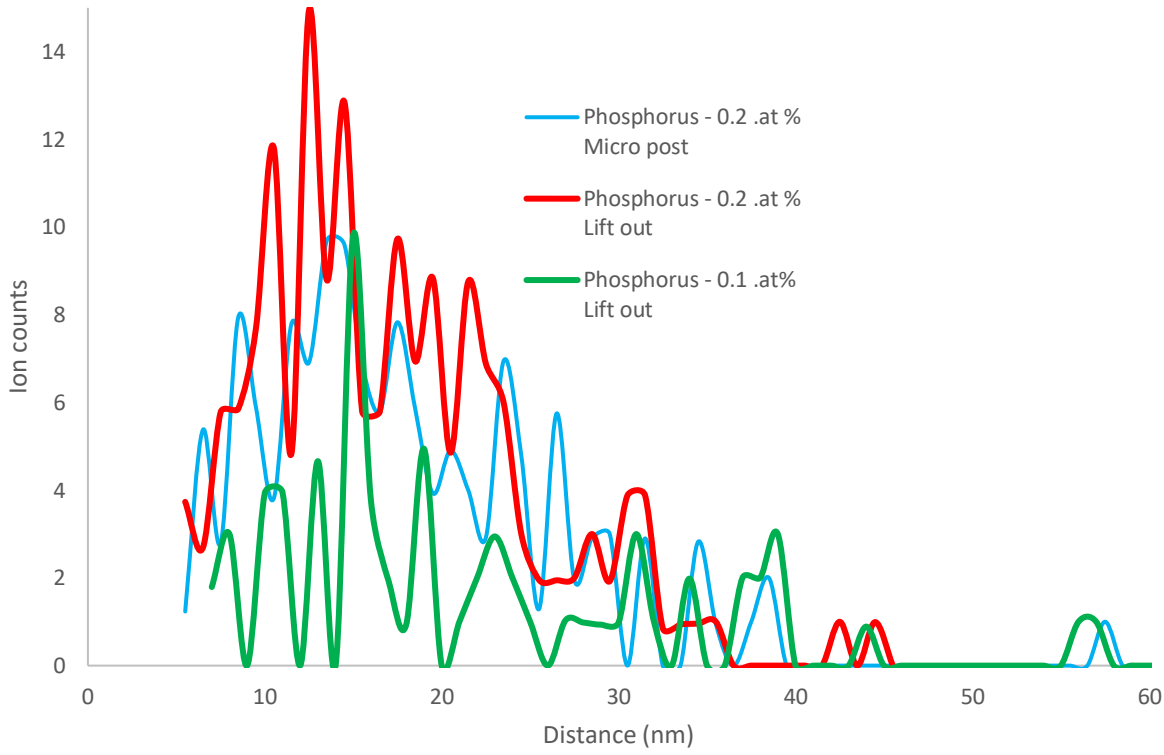


Figure C.3 – Comparison between ion counts from 30 nm x 30 nm x 100 nm ROIs from implanted micro posts and lift out samples with varying implant doses.

Summation of phosphorus ion counts from identical volumes (30 nm x 30 nm x 40 nm : 7.5 nm to 47.5 nm in depth) from the same section of the implantation profile are shown in Figure C.3. The summed phosphorus ion counts for these volumes from the 0.2 at.% peak concentration micro post, 0.2 at.% peak concentration lift out and 0.1 at.% peak concentration lift out were 133 ions, 163 ions and 65 ions respectively.

The ion count from the 0.1 at.% peak concentration micro post samples is 49% of the ion count of the 0.2 at.% peak concentration micro post sample. This indicates that the implantation doses were accurately scaled to give the end peak concentrations that were required as measured by APT analyses on comparable samples.

Appendix D

Cross sectional analyses of phosphorus diffused substrates

Scanning electron microscope (SEM) images were taken of phosphorus diffusion gettered substrates in both surface and cross section to determine if any micro or nanoscale variation in the microstructure could be observed. These variations could affect the representativeness of a nanoscale atom probe analysis volume, potentially explaining observed variation in phosphorus concentrations and thus inform future site specific sample preparation.

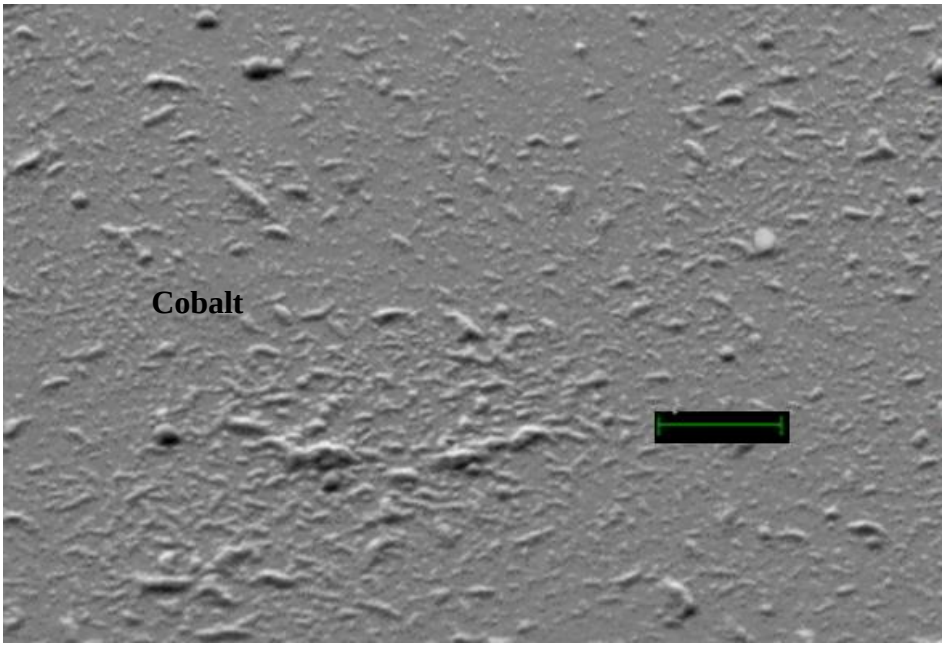


Figure D.1 – Plan view SEM micrograph of silicon surface after iron contamination and phosphorus diffusion, PSG removal by HF dip and coating with cobalt. Scale bar 2µm.

Figure D.1 is a plan SEM view of a silicon substrate that has been contaminated with iron and subjected to phosphorus diffusion gettering, dipped in HF to remove the phosphorus

silicate glass (PSG) and then coated with ~100 nm of thermally evaporated cobalt. When the same sample is observed in cross section in Figure D.2, the surface roughness appears to be due to the deposition of the cobalt capping layer. As the final atom probe tip will only retain some tens of nm of the capping layer, variation in the surface topography of the capping layer in excess of that size will have little impact.

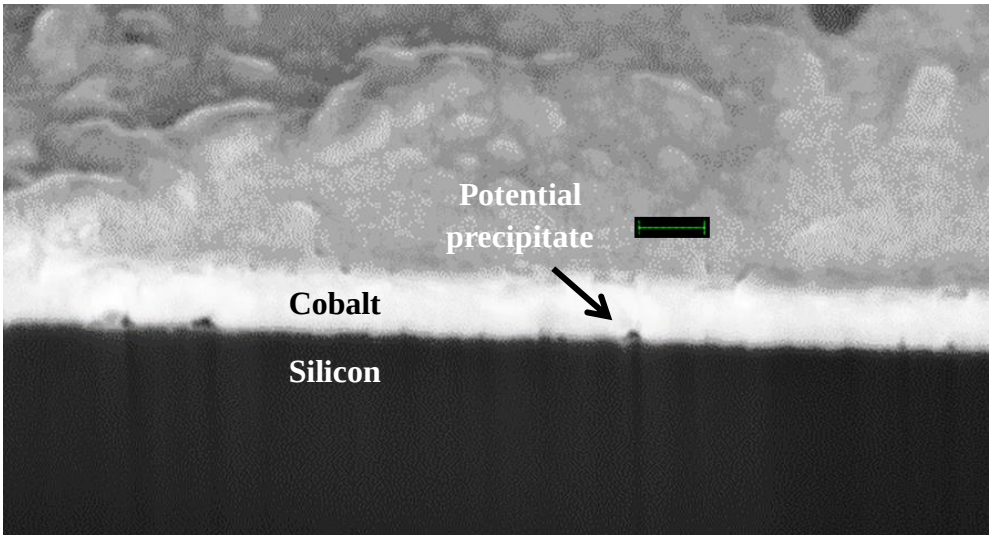


Figure D.2 – Cross sectional SEM micrograph of silicon surface after iron contamination and phosphorus diffusion, PSG removal by HF dip and coating with cobalt. Scale bar 200 nm.

The PSG layer has been removed via HF but a thin layer can be seen just above the silicon layer which may be linked to the residual phosphorus rich layer. Dark regions can be seen just above this thin layer which could be related to the phosphorus deposition but they are somewhat larger than would be expected for a cross-sectional view of nanoscale known silicon phosphide precipitates [258]. These dark regions are also linked to a FIB 'curtaining' effect due to non-uniform milling rates and could be particles related to the phosphorus diffusion or more likely debris on the surface prior to deposition of the cobalt layer.

Cross sectional SEM analyses of phosphorus diffused silicon substrates with no intentional iron contamination with their phosphorus silicate glass layer intact

In order to determine the level of uniformity of the deposition of the PSG prior to its removal, it was decided to carry out SEM surface analysis of silicon substrates that retained the PSG layer. It was not possible to obtain an identical sample to those described above but it was possible to obtain a similar sample that had been originally fabricated for optimised Secondary Ion Mass Spectrometry (SIMS) analysis.

This sample had not been contaminated with iron, had undergone a 14 min phosphorus diffusion at 875°C rather than 28 minutes and a ~ 20 nm silicon oxide layer deposited prior to thermal evaporation of the cobalt capping layer. The silicon oxide layer had been deposited via a low temperature Plasma Enhanced Chemical Vapour Deposition (PECVD) process in order to provide a region in which equilibrium SIMS sputtering could be reached prior to analysing the PSG layer.

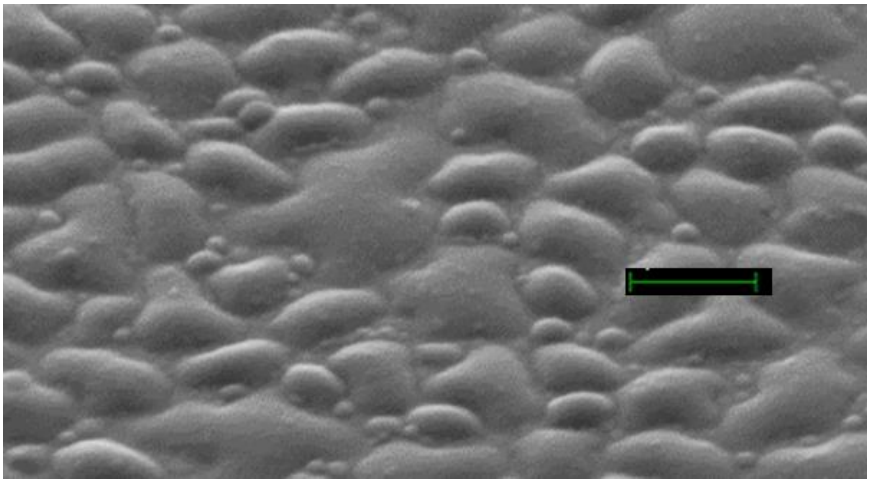


Figure D.3 – Plan view SEM micrograph of silicon surface after phosphorus diffusion, PECVD deposition of silicon oxide and coating with cobalt. Scale bar 1 µm.

A plan view of the sample fabricated for SIMS analysis be can be seen in Figure D.3. The surface can be seen to have a non-uniform, bubble like topography. These raised regions are generally oval in shape and between approximately 100 nm – 1 micron along the long axis. As the thermal evaporation of cobalt used has been observed to deposit uniformly on flat surfaces in control samples, the variation in surface uniformity is unlikely due to the cobalt layer.

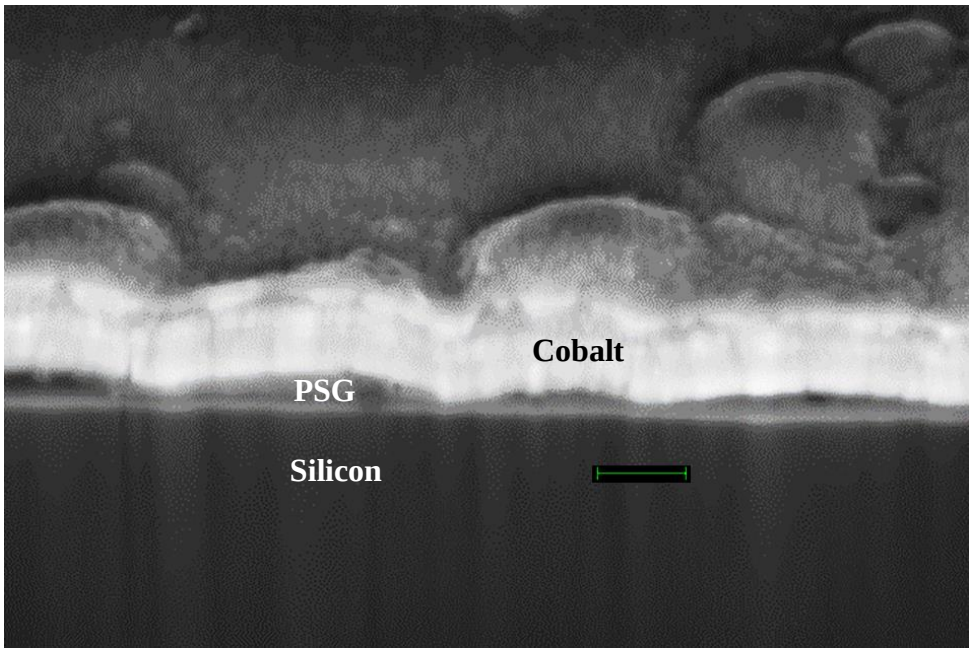


Figure D.4 – Cross sectional SEM micrograph of silicon surface after phosphorus diffusion, PECVD deposition of silicon oxide and coating with cobalt. Scale bar 200 nm.

A Focused Ion Beam (FIB) milled cross section of this substrate is presented in Figure D.4. The multilayer structure of the system can be seen to comprise (bottom to top), the darker silicon, a thin bright layer, a repeating raised section with dark spots and a bright surface layer.

This bubbled surface region has been previously seen in furnace based phosphorus diffusions and has previously linked to non-uniform deposition of the PSG [125]. This

non-uniformity is not always observed, with uniform PSG layers being confirmed through atomic force microscopy measurements [263] and TEM [258].

As the initial concentration and thus shape of the phosphorus diffusion profile is linked to surface concentration of the initial phosphorus silicate glass [264], this non-uniformity in surface thickness of the PSG will likely affect the local phosphorus concentration in close proximity to these regions. Cross sectional SEM of these bubbled regions indicate their true length scale, without the size exaggerating effect of the deposited layers above, is in the 100 nm – 200 nm range. This has implications for the use of any surface analysis technique that has a lateral resolution limit less than this, as it will result in a blurring and averaging of any data collected.

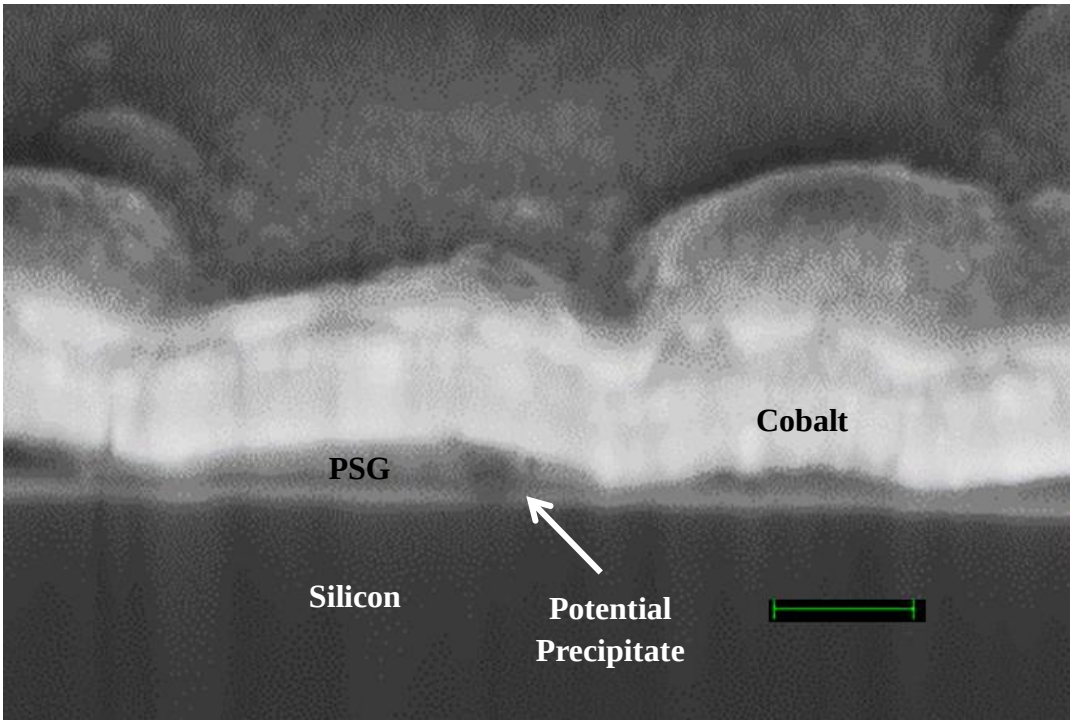


Figure D.5 – Cross sectional SEM micrograph of silicon surface after PDG/Fe process, no HF dip and deposition of silicon oxide. Scale bar 100 nm.

When greater magnification is used on the raised regions in the cross sectional image, small dark sections can be seen within that raised region in Figure D.5. These dark regions could be due to local density variations or porosity, or could be due to silicon phosphide precipitates in the PSG [258] and PSG/silicon interface [126].

Cross sectional SEM analyses of phosphorus diffused silicon substrates with their phosphorus silicate glass intact, processed using spin coating

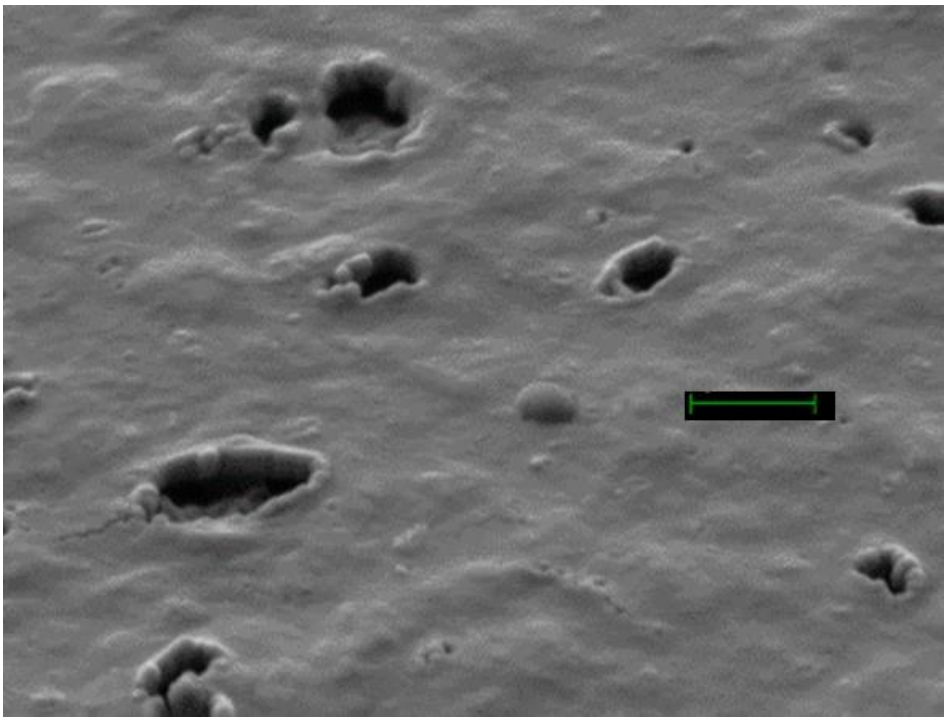


Figure D.6 – Plan view SEM micrograph of silicon surface after phosphorus diffusion via spin on dopant and coating with cobalt layer. Scale bar 1μm.

Liquid phosphorus dopant was spun onto a silicon substrate and baked on a hot plate. After the deposition of the spin on dopant, a section of the silicon was coated in thermally evaporated cobalt without first removing the PSG. A plan view of the surface of the silicon

surface with the spin on phosphorus dopant and cobalt is shown in Figure D.6. Compared to the furnace diffused sample, the surface does not show any indication of bubbles but it does show significant porosity.

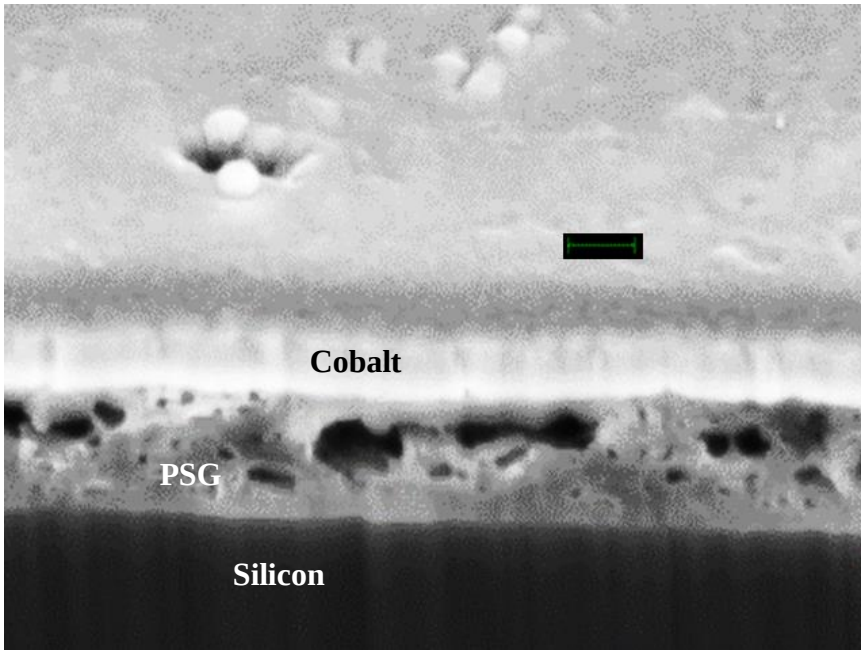


Figure D.7 – Cross sectional SEM micrograph of silicon surface after phosphorus diffusion via spin on dopant and coating with cobalt. Scale bar 200 nm.

A cross sectional view of the same substrate is shown in Figure D.7, the porosity seen in the plan view extends below the surface layer.

Due to the increased porosity and predicted reduced control of surface phosphorus concentration on the length scales required for atom probe analysis, it was decided that spin on phosphorus dopant was not suitable for these experiments in this thesis.

Appendix E

SIMS profile of phosphorus diffused silicon

SIMS analysis was carried out by Aystorm Scientific, Cheshire, UK on the phosphorus diffused silicon shown in Figure D.3 that had undergone a 14 min phosphorus diffusion at 875˚C. In order to analyse the local composition around the PSG/silicon interface and also determine how the phosphorus diffusion profile extends after this, analyses on two samples were carried out.

One sample was specially prepared to allow high depth resolution analysis of oxygen, phosphorus and silicon species in the PSG and within tens of nanometres either side of the PSG/silicon interface. An extra layer of PECVD amorphous silicon oxide (~ 20 nm) was deposited on the surface of the PSG. This was deposited in order to allow steady state SIMS sputtering to begin prior to the analysis of the PSG/silicon interface. Ultra Low Energy (ULE) SIMS analysis was carried out with a depth sampling step of ~ 0.3 nm and was used to analyse the concentrations of silicon, oxygen and phosphorus species over a total depth of ~ 250 nm.

The other sample was prepared to allow high mass resolution of the phosphorus diffusion profile over a greater depth. As the PSG/silicon interface was not required for this profile, an identical sample to that used above was dipped in HF to remove the PSG prior to SIMS analysis. High Mass Resolution (HMR) SIMS was then carried out using a depth sampling step of ~7 nm to a total depth of ~ 1.5 µm. A larger bin width was used than in the previous sample in order to allow greater depths to be analysed within a reasonable time frame [119].

A region of this analysis centred upon the PSG/silicon interface is given in Figure E.1 and the analysis including the extended phosphorus profile is given in Figure E.2. The SIMS data for phosphorus, oxygen and silicon are all displayed in counts per second as a function of depth. The phosphorus profile has also been converted into units of concentration in at/cm^3.

The initial 20 nm of the analysis in Figures E.1 and E.2 shows high concentrations of both silicon and oxygen and this can be linked to the PECVD deposited silicon oxide layer. This region is then followed by a large increase in phosphorus, slight increase in oxygen and a large decrease in silicon and extends for approximately 30 nm. This can be linked to the phosphorus rich PSG layer and this thickness is comparable to similarly processed materials in the literature [263] [249]. At approximately 40 nm, the phosphorus concentration reduces briefly and then overshoots the initial constant concentration over a 10 nm depth to reach a peak of approximately 5 x10^{21} at/cm^3. After this point, the phosphorus concentration decreases swiftly by an order of magnitude over the first 5 nm and then decreases more slowly over the rest of the profile.

This swift drop and rise in phosphorus concentration is known as ‘phosphorus pile up’ [265] [266] [267] and is due to the segregation of the phosphorus to the silicon oxide/silicon layer during thermal processing of high concentration phosphorus in silicon [249] [255].

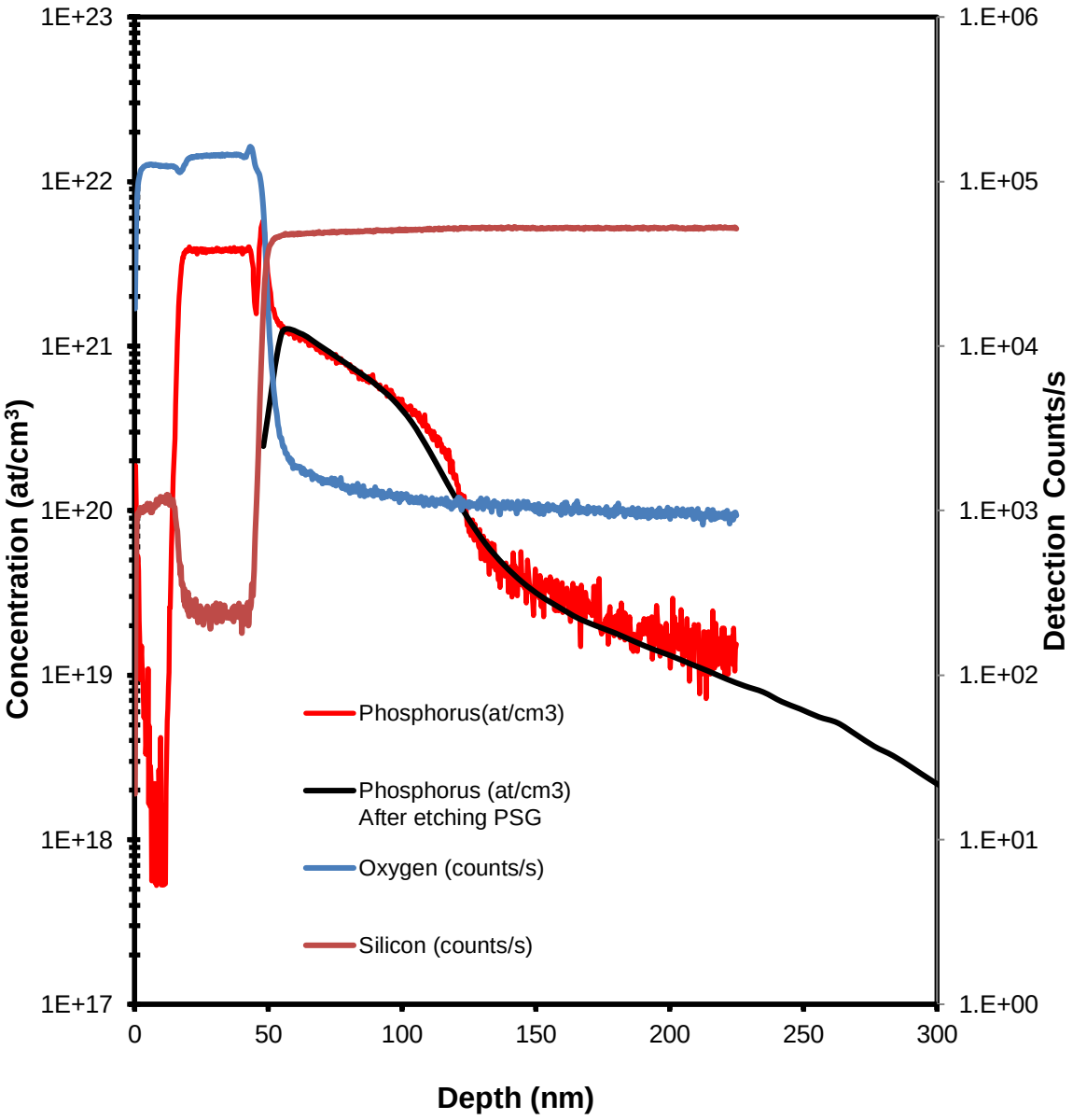


Figure E.1 – ULE and HRM SIMS analysis of phosphorus diffusion silicon (50 nm – 100 nm) with retained PSG (20 nm – 50 nm) and PECVD deposited silicon oxide layer (0 – 20 nm). Phosphorus, silicon and oxygen displayed in counts/s. Phosphorus also shown in at/cm^3.

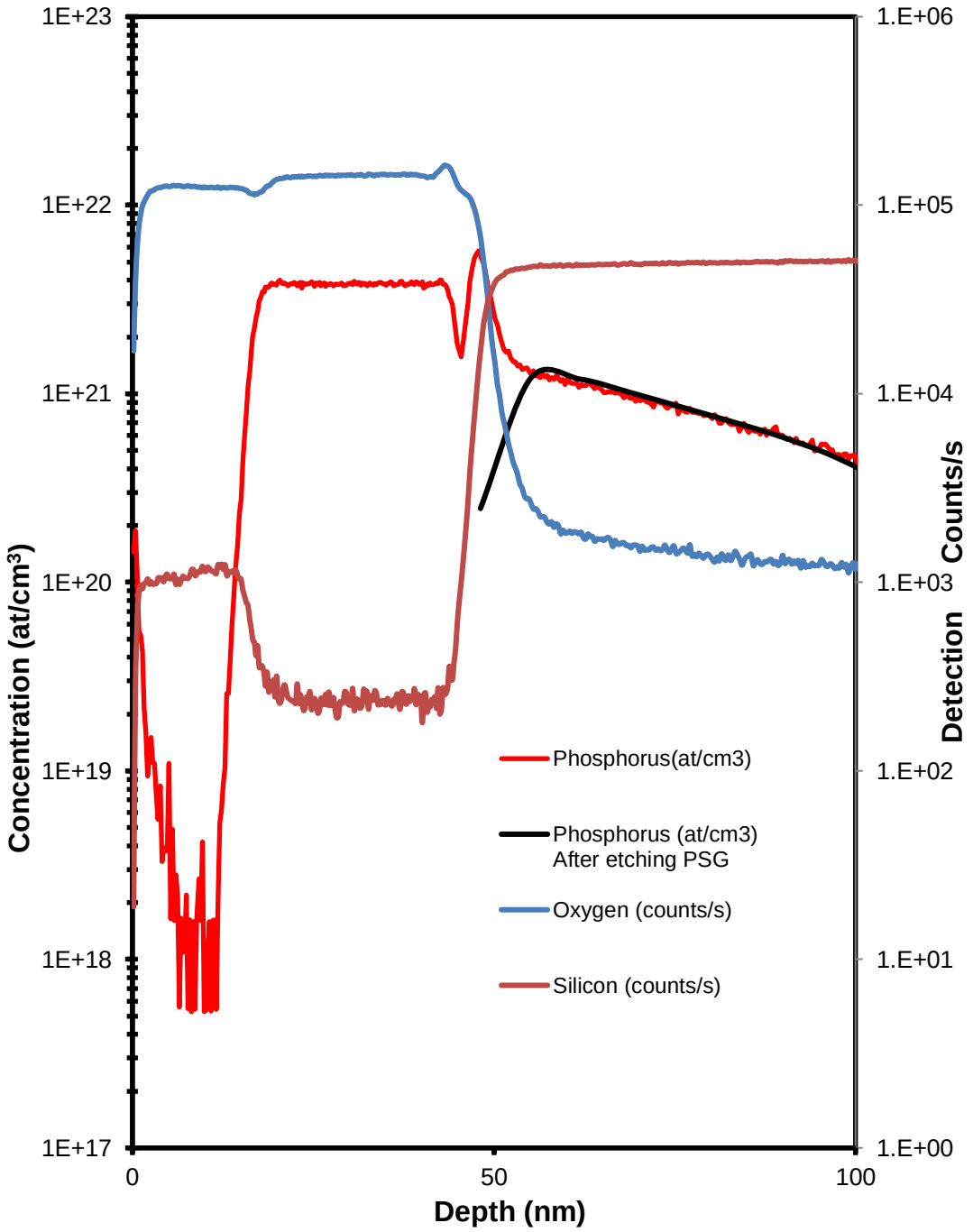


Figure E.2 – ULE and HMR SIMS analysis of phosphorus diffusion silicon (50 nm – 100 nm) with retained PSG (20 nm – 50 nm) and PECVD deposited silicon oxide layer (0 – 20 nm). Phosphorus, silicon and oxygen displayed in counts/s. Phosphorus also shown in at/cm^3.

The phosphorus concentration profile for both of the SIMS analyses was converted to atomic percent using for ease of comparison with atom probe data (Figure E.3).

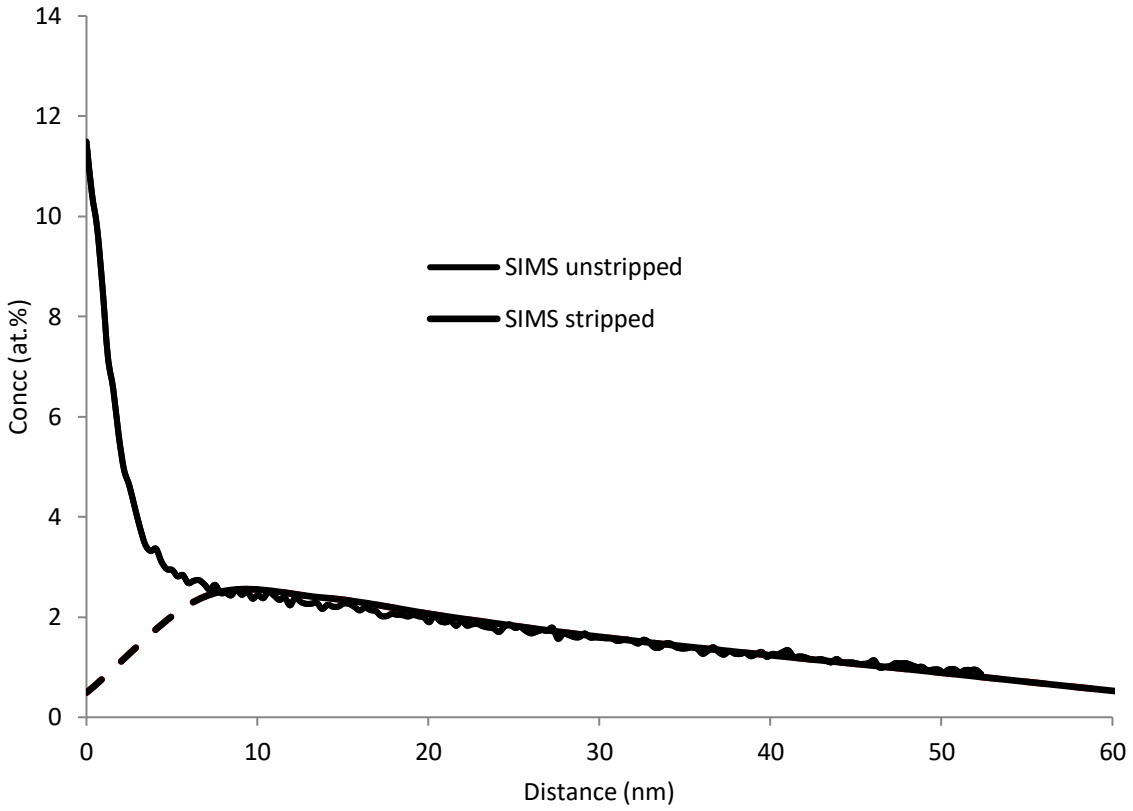


Figure E.3 – Phosphorus profiles as analysed through ULE and HMR SIMS converted to at.%..

Comparison between SIMS and APT of phosphorus profiles of phosphorus diffused silicon

Initial APT Samples were analysed from the following substrates using the LEAP 3000X HR system at 50 K, 0.5 nJ, 200 kHz and a 0.5% detection rate throughout the analysis.

- Iron contaminated, phosphorus diffused silicon with the PSG removed through HF. 28 minute phosphorus diffusion.

- Phosphorus diffused silicon with no iron contamination with the PSG retained and additional ~20 nm silicon oxide on top of the PSG. 14 minute phosphorus diffusion.

Whilst there were no visible indications of oxygen or iron segregation in any of these initial samples or any silicon phosphide precipitates, it was possible to obtain a number of phosphorus diffusion profiles that allowed a comparison with SIMS. There is good agreement between phosphorus concentration as measured by APT and SIMS in those samples for the entire profile where the phosphorus silicate has been removed and for all samples after approximately 5 nm in depth (Figure E.4).

For those samples with retained PSG, both APT and SIMS measurements indicate a large increase in concentration in the first few nm. It is possible that this is due to local variations in phosphorus concentration due to variations in initial PSG thickness as was shown in cross sectional analysis of these substrates [123].

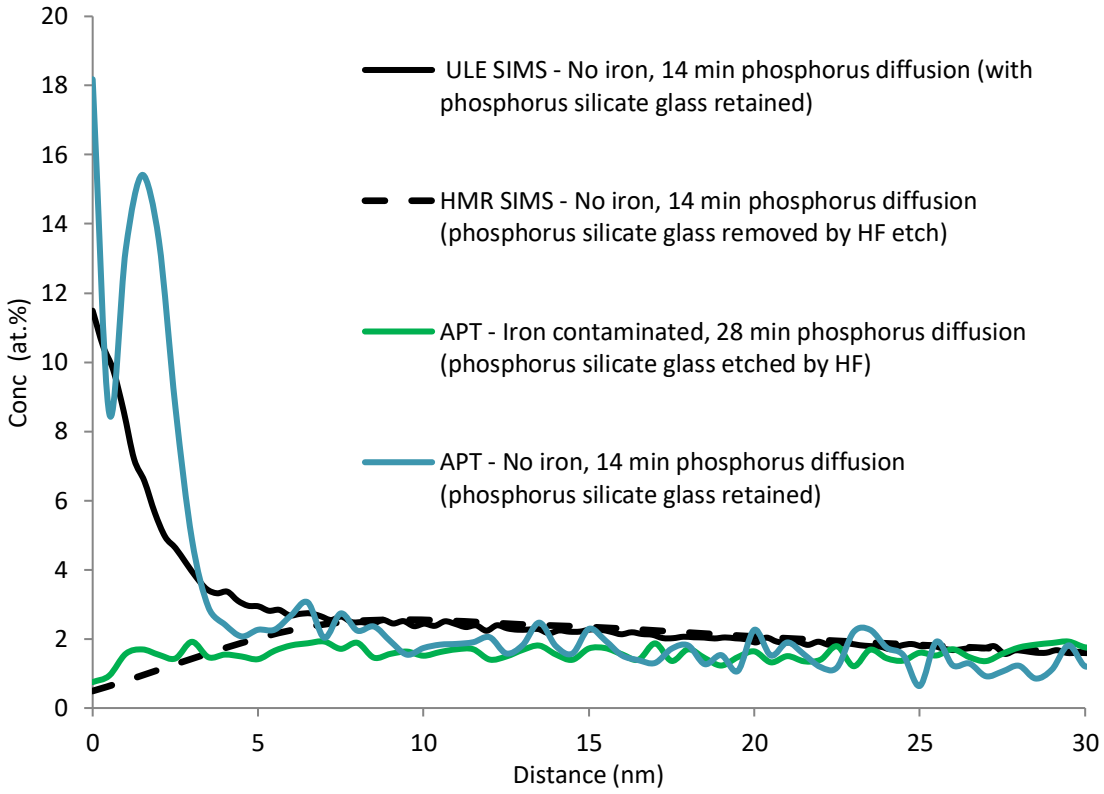


Figure E.4 – Comparison of phosphorus concentration profiles as measured by APT and SIMS.

Both SIMS and APT samples that retained the PSG and had the 14 minute phosphorus diffusion show a distinct increase in phosphorus concentration in the first 5 nm of the profile. The SIMS profile peaks at a slightly lower concentration at the surface than the APT profile and the APT profile also shows a slightly higher peak that is offset by ~ 2 nm. The difference in concentration between the two is likely due to small variations in surface concentration that is averaged out through the larger SIMS analysis area as shown through the non uniform deposition of the PSG.

The zero point for the ULE and HMR SIMS profiles in Figure E.4 started from the 50 nm depth point from the data shown in Figures E.1 and E.2. The start of the APT profile could not be clearly defined through iso-concentration surfaces of the capping layer or silicon

oxide due to an apparent microfracture after the capping layer. Immediately after this microfracture, a high concentration of phosphorus was detected and was used as the starting point of the profile. This indicates that the microfracture removed the silicon oxide layer and the majority of the PSG before leaving a small amount of PSG onto the silicon substrate.

The micron and sub micron scale surface variation seen through SEM micrographs (Figure D.4) of the substrate analysed by SIMS is significantly smaller than the lateral resolution of the SIMS beam used. This indicates that the thicknesses reported will be that of an average of the actual thickness of the PSG and local concentration variations not observable in SIMS may have an impact in the APT analyses.

It should be reiterated that the SIMS analysis is on silicon that was subjected to a 14 minute phosphorus diffusion rather than the 28 minute diffusion that was used for all other atom probe analysis in this chapter. Therefore this reduction in processing time will result in the phosphorus concentration at the surface regions being lower in the 14 minute diffusion [249]. This does however show the initial APT depth profiles of phosphorus concentrations are in reasonable agreement with those obtain by SIMS.

Appendix F

Atom probe analysis of iron contaminated, phosphorus diffused silicon. Laser energy 50 pJ

To determine what role the silicon phosphide precipitates play in the gettering process, an iron contaminated, phosphorus diffused sample without any precipitates is shown here (Figure F.1). A number of iron contaminated, phosphorus diffused silicon samples were

found to not contain silicon phosphide precipitates. The peak concentration of phosphorus at the surface was found to be approximately 1 at.% and the general concentration is significantly lower than that found in those samples containing silicon phosphide precipitates. A 10 at.% cobalt iso-concentration surface was used to delineate the surface for a proximity histogram.

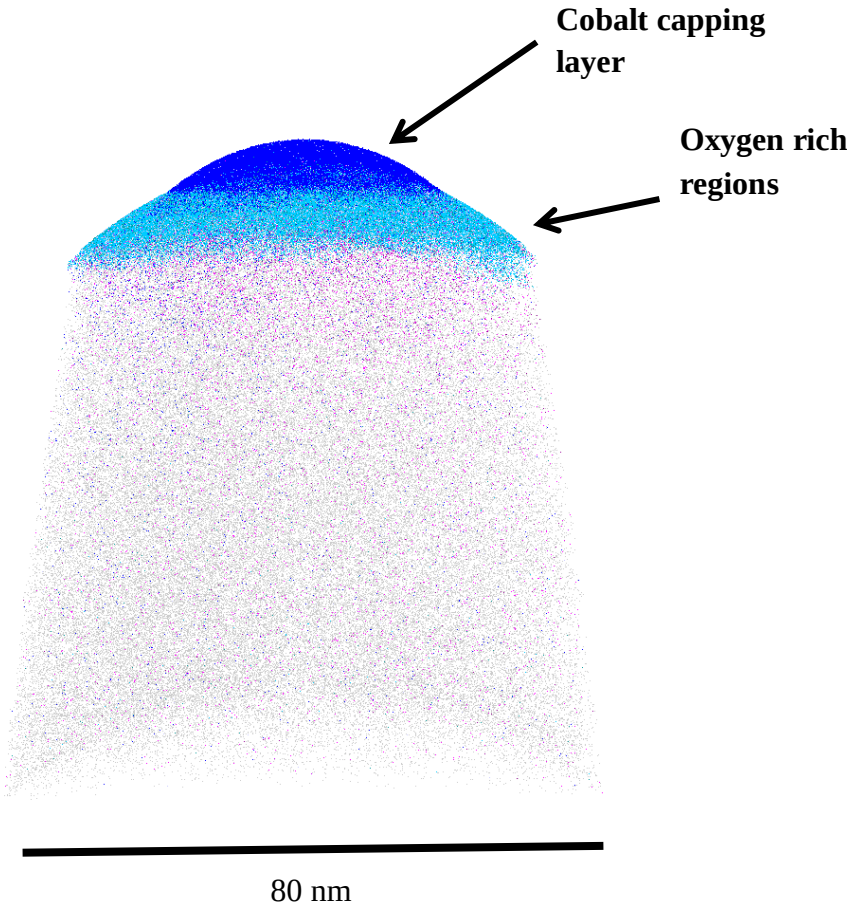


Figure F.1 – Atom map of cobalt capping layer (dark blue), oxygen (light blue) and silicon (grey)

Through close inspection of oxygen iso-concentration surfaces, it was found that there was significant variation in the spatial distribution of oxygen species at the capping layer interface (Figure F.2).

APT analysis of heterogeneous oxygen rich regions found at the silicon surface

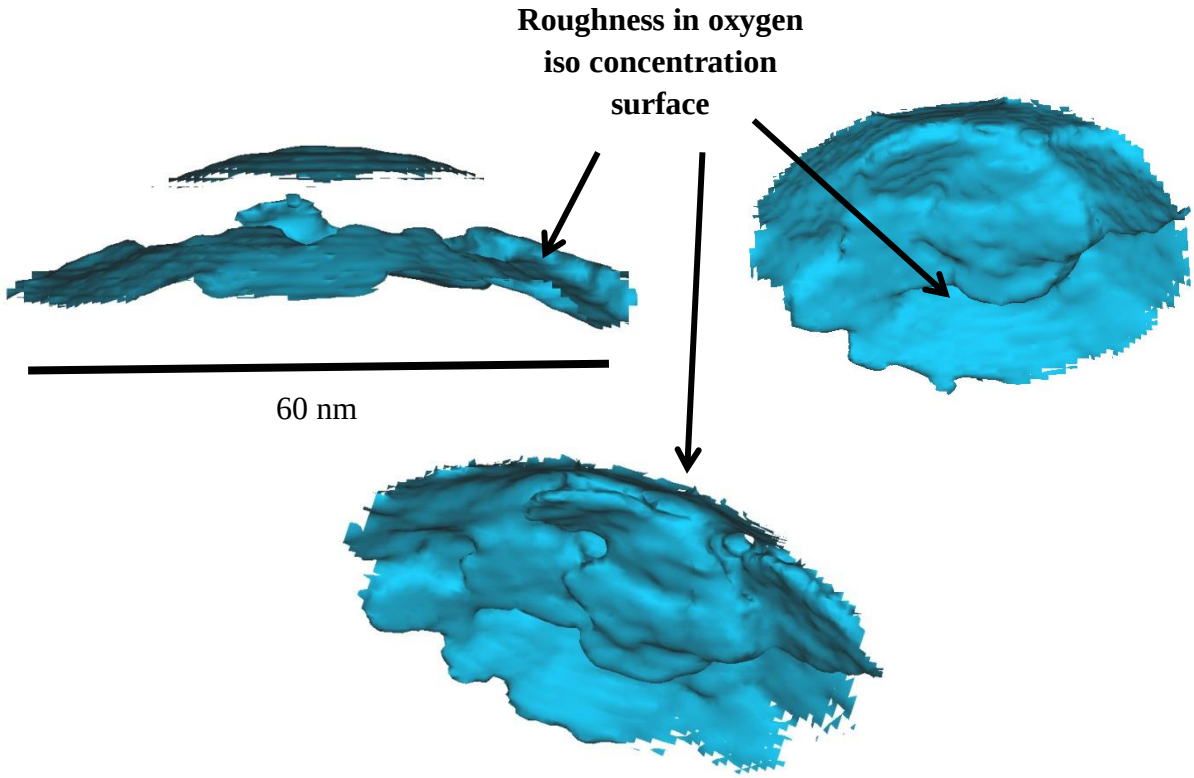


Figure F.2 – 5 at.% oxygen iso-concentration Left – 5 at.% oxygen iso-concentration parallel to capping layer. Right – 5 at.% oxygen iso-concentration tilted to view from below Bottom –15 at.% oxygen iso-concentration tilted to view it from below.

This local enrichment of oxygen could indicate the presence of oxygen precipitation without the requirement of a local high concentration of phosphorus. This surface enrichment was not readily visible in those samples containing silicon phosphide precipitates, this was likely due to the analysis artefacts caused by these precipitates in the surface regions.

As each of the oxygen rich regions in those samples with silicon phosphide precipitates were also found to have direct physical link to the surface regions, it is possible that this direct link was to such an oxygen rich feature at the surface oxide.

References

[1] B. Gault, M. P. Moody, J. M. Cairney, and S. P. Ringer, *Atom Probe Microscopy*. Springer-Verlag New York, 2012.

[2] P. J. Turner, B. J. Regan, and M. J. Southon, "Field-ion atom probe analysis," *Surface Science*, vol. 35, pp. 336–344, 1973.

[3] K. Hono, T. Ohkubo, Y. M. Chen, M. Kodzuka, K. Oh-ishi, H. Sepehri-Amin, F. Lia, T. Kinno, S. Tomiya, and Y. Kanitani, "Broadening the applications of the atom probe technique by ultraviolet femtosecond laser," *Ultramicroscopy*, vol. 111, no. 6, pp. 576–583, 2011.

[4] T. F. Kelly, D. J. Larson, K. Thompson, R. L. Alvis, J. H. Bunton, J. D. Olson, and B. P. Gorman, "Atom Probe Tomography of Electronic Materials," *Annual Review of Materials Research*, vol. 37, no. 1, pp. 681–727, 2007.

[5] K. Inoue, F. Yano, A. Nishida, H. Takamizawa, T. Tsunomura, Y. Nagai, and M. Hasegawa, "Dopant distributions in n-MOSFET structure observed by atom probe tomography," *Ultramicroscopy*, vol. 109, no. 12, pp. 1479–1484, 2009.

[6] K. Thompson, D. Lawrence, D. J. Larson, J. D. Olson, T. F. Kelly, and B. Gorman, "In situ site-specific specimen preparation for atom probe tomography," *Ultramicroscopy*, vol. 107, no. 2–3, pp. 131–139, 2007.

[7] D. J. Larson, T. J. Prosa, R. M. Ulfig, B. P. Geiser, and T. F. Kelly, *Local Electrode Atom Probe Tomography - A User's Guide*, 1st ed. Springer-Verlag New York, 2013.

[8] S. Wolf and R. Tauber, *Silicon Processing for the VLSI Era, Vol. 1: Process Technology*. Lattice Press, 1999.

[9] J. Van Donkelaar, C. Yang, A. D. C. Alves, J. C. McCallum, C. Hougaard, B. C. Johnson, F. E. Hudson, A. S. Dzurak, and A. Morello, "Single atom devices by ion implantation," *Journal of Physics: Condensed Matter*, vol. 27 154204, 2015.

[10] R. W. Keyes, "Physical limits of silicon transistors and circuits," *Reports on Progress in Physics*, vol. 68, no. 12, pp. 2701–2746, 2005.

[11] C. Qiu, Z. Zhang, M. Xiao, Y. Yang, D. Zhong, and L. Peng, "Scaling carbon nanotube complementary transistors to 5-nm gate lengths," *Science*, vol. 355, no. 6322, pp. 271–276, 2017.

[12] B. E. Kane, "A Silicon-Based Nuclear Spin Quantum Computer," *Nature*, vol. 393, pp. 133–137, 1998.

[13] J. T. Muhonen, J. P. Dehollain, A. Laucht, F. E. Hudson, R. Kalra, T. Sekiguchi, K. M. Itoh, D. N. Jamieson, J. C. McCallum, A. S. Dzurak, and A. Morello, "Storing quantum information for 30 seconds in a nanoelectronic device," *Nature Nanotechnology*, vol. 9, pp. 986–991, 2014.

[14] M. Fuechsle, J. A. Miwa, S. Mahapatra, H. Ryu, S. Lee, O. Warschkow, L. C. L. Hollenberg, G. Klimeck, and M. Y. Simmons, "A single-atom transistor," *Nature Nanotechnology*, vol. 7, pp. 242–246, 2012.

[15] B. Y. J. Preskill, "Reliable quantum computers," *Proceedings of the Royal Society of London A - Mathematical Physical and Engineering Sciences*, vol. 454, pp. 385–410, 1998.

[16] J. A. V Donkelaar, A. D. Greentree, A. D. C. Alves, L. M. Jong, L. C. L. Hollenberg, and D. N. Jamieson, "Top-down pathways to devices with few and single atoms placed to high precision," *New Journal of Physics*, vol. 12 065016, 2010.

[17] T. Schenkel, C. C. Lo, C. D. Weis, A. Schuh, A. Persaud, and J. Bokor, "Critical issues in the formation of quantum computer test structures by ion implantation," *Nuclear Instruments and Methods in Physics Research Section B*, vol. 267, no. 16, pp. 2563–2566, 2009.

[18] A. A. Istratov, H. Hieslmair, and E. R. Weber, "Iron contamination in silicon technology," *Applied Physics A*, vol. 70, no. 5, pp. 489–534, 2000.

[19] J. Hofstetter, J. F. Lelièvre, C. del Cañizo, and A. Luque, "Acceptable contamination levels in solar grade silicon: From feedstock to solar cell," *Materials Science and Engineering B*, vol. 159–160, pp. 299–304, 2009.

[20] S. Philipps, "Photovoltaics Report." Fraunhofer ISE and Werner Warmuth, PSE Conferences & Consulting GmbH, 2016.

[21] D. Macdonald and L. J. Geerligs, "Recombination activity of interstitial iron and other transition metal point defects in p- and n-type crystalline silicon," *Applied Physics Letters*, vol. 85, no. 18, pp. 4061–4063, 2004.

[22] A. Bentzen and A. Holt, "Overview of phosphorus diffusion and gettering in multicrystalline silicon," *Materials Science and Engineering B*, vol. 159–160, pp. 228–234, 2009.

[23] R. Chen, B. Trzynadlowski, and S. T. Dunham, “Phosphorus vacancy cluster model for phosphorus diffusion gettering of metals in Si,” *Journal of Applied Physics,* vol. 115 054906, 2014.

[24] M. Syre, S. Karazhanov, B. R. Olaisen, A. Holt, and B. G. Svensson, “Evaluation of possible mechanisms behind P gettering of iron,” *Journal of Applied Physics,* vol. 110 024912, 2011.

[25] Y. Zeng, X. Ma, D. Tian, W. Wang, L. Gong, D. Yang, and D. Que, “Oxygen precipitation heterogeneously nucleating on silicon phosphide precipitates in heavily phosphorus-doped Czochralski silicon,” *Journal of Applied Physics,* vol. 105 093503, 2009.

[26] A. Ourmazd and W. Schröter, “Gettering of Metallic Impurities In Silicon,” *Materials Research Society Symposia Proceedings*, vol. 36, pp. 25–30, 1985.

[27] M. Morita, T. Ohmi, E. Hasegawa, M. Kawakami, and M. Ohwada, “Growth of native oxide on a silicon surface,” *Journal of Applied Physics,* vol. 68, no. 3, pp. 1272–1281, 1990.

[28] B. E. Deal and A. S. Grove, “General relationship for the thermal oxidation of silicon,” *Journal of Applied Physics,* vol. 36, no. 12, pp. 3770–3778, 1965.

[29] J.-P. Joly, “Metallic contamination assessment of Silicon wafers,” *Microelectronic Engineering*, vol. 40, no. 3–4, pp. 285–294, 1998.

[30] E. G. Seebauer and K. W. Noh, “Trends in semiconductor defect engineering at the nanoscale,” *Materials Science & Engineering R*, vol. 70, no. 3–6, pp. 151–168, 2010.

[31] L. Arnberg, M. Di Sabatino, and E. J. Øvrelid, “State-of-the-art growth of silicon for PV applications,” *Journal of Crystal Growth*, vol. 360, pp. 56–60, 2012.

[32] J. D. Murphy, R. E. McGuire, K. Bothe, V. V. Voronkov, and R. J. Falster, “Minority carrier lifetime in silicon photovoltaics: The effect of oxygen precipitation,” *Solar Energy Materials and Solar Cells*, vol. 120, pp. 402–411, 2014.

[33] A. G. Aberle, M. B. Boreland, B. Hoex, and T. Mueller, “Industrial Silicon Wafer Solar Cells – Status and Trends,” *GREEN*, vol. 2, no. 4, pp. 135–148, 2012.

[34] R. C. Newman, “Defects in silicon,” *Reports on Progress in Physics*, vol. 45, pp. 1163–1210, 1982.

[35] E. Fourmond, M. Forster, R. Einhaus, H. Lauvray, J. Kraiem, and M. Lemiti, “Electrical properties of boron , phosphorus and gallium co-doped silicon,” *Energy Procedia*, vol. 8, pp. 349–354, 2011.

[36] W. Maly, “Cost of Silicon Viewed from VLSI Design Perspective,” *Proceedings of the 31st Conference on Design Automation, San Diego, CA, USA*, pp. 135–142, 1994.

[37] S. Pizzini, M. Acciarri, and S. Binetti, “From electronic grade to solar grade silicon: Chances and challenges in photovoltaics,” *Physica Status Solidi A*, vol. 202, no. 15, pp. 2928–2942, 2005.

[38] Y. Delannoy, “Purification of silicon for photovoltaic applications,” *Journal of Crystal Growth*, vol. 360, pp. 61–67, 2012.

[39] T. Buonassisi, A. A. Istratov, and M. D. Pickett, “Metal precipitation at grain boundaries in silicon : Dependence on grain boundary character and dislocation decoration,” *Applied Physics Letters*, vol. 89 042102, 2006.

[40] S. M. Myers, M. Seibt, and W. Schröter, “Mechanisms of transition-metal gettering in silicon,” *Journal of Applied Physics*, vol. 88, pp. 3795–3819, 2000.

[41] S. Riepe, I. E. Reis, W. Kwapil, M. A. Falkenberg, J. Schön, H. Behnken, J. Bauer, D. Kreßner-Kiel, W. Seifert, and W. Koch, “Research on efficiency limiting defects and defect engineering in silicon solar cells - results of the German research cluster SolarFocus,” *Physica Status Solidi C*, vol. 8, no. 3, pp. 733–738, 2011.

[42] T. Buonassisi, A. A. Istratov, M. D. Pickett, M. Heuer, J. P. Kalejs, G. Hahn, M. A. Marcus, B. Lai, Z. Cai, S. M. Heald, T. F. Ciszek, R. F. Clark, D. W. Cunningham, A. M. Gabor, R. Jonczyk, S. Narayanan, E. Sauar, and E. R. Weber, “Chemical natures and distributions of metal impurities in multicrystalline silicon materials,” *Progress in Photovoltaics: Research and Applications*, vol. 14, no. 6, pp. 512–531, 2006.

[43] A. Haarahiltunen and H. Savin, “Effect of Thermal History on Iron Precipitation in Crystalline Silicon,” *Energy Procedia*, vol. 8, pp. 355–359, 2011.

[44] J. S. Williams, “Ion Implantation in Semiconductors,” *Materials Science and Engineering A*, vol. 253, no. 1–2, pp. 8–15, 1998.

[45] M. Posselt, B. Schmidt, T. Feudal, and N. Strecker, “Atomistic simulation of ion implantation and its application in Si technology,” *Materials Science and Engineering B*, vol. 71, no. 1–3, pp. 128–136, 2000.

[46] E. Simoen, A. Satta, A. D'Amore, T. Janssens, T. Clarysse, K. Martens, B. De Jaeger, A. Benedetti, I. Hoflijk, B. Brijs, M. Meuris, and W. Vandervorst, "Ion-implantation issues in the formation of shallow junctions in germanium," *Materials Science in Semiconductor Processing*, vol. 9, no. 4–5, pp. 634–639, 2006.

[47] M. Tomita, M. Suzuki, T. Tachibe, S. Kozuka, and A. Murakoshi, "Estimation of ultra-shallow implants using SIMS , NRA and chemical analysis," *Applied Surface Science*, vol. 203–204, pp. 377–382, 2003.

[48] L. A. Marqués, L. Pelaz, and I. Santos, "Characterization of octadecaborane implantation into Si using molecular dynamics," *Physical Review B*, vol. 74 201201, 2006.

[49] B. Mizuno, I. Nakayama, M. Takase, H. Nakaoka, and M. Kubota, "Plasma doping for silicon," *Surface and Coatings Technology*, vol. 85, no. 1–2, pp. 51–55, 1996.

[50] A. Feygenson and N. Zemel, J, "Rapid Thermal Annealing of Arsenic-implanted silicon: A Review," *Metallurgical and Protective Coatings*, vol. 165, no. 1, pp. 109–138, 1988.

[51] M. Hori, T. Shinada, K. Taira, N. Shimamoto, T. Tanii, T. Endo, and I. Ohdomari, "Performance enhancement of semiconductor devices by control of discrete dopant distribution.," *Nanotechnology*, vol. 20 365205, 2009.

[52] R. S. Rai and S. Subramanian, "Role of transmission electron microscopy in the semiconductor industry for process development and failure analysis," *Progress in Crystal Growth and Characterization of Materials*, vol. 55, no. 3–4, pp. 63–97, 2009.

[53] P. Ronsheim, P. Flaitz, M. Hatzistergos, C. Molella, K. Thompson, and R. Alvis, "Impurity measurements in silicon with D-SIMS and atom probe tomography," *Applied Surface Science*, vol. 255, no. 4, pp. 1547–1550, 2008.

[54] M. M. Waldrop, "The Chips Are Down For Moore's Law," *Nature*, vol. 530, no. 7589, pp. 144–147, 2016.

[55] J. C. Ranuárez, M. J. Deen, and C. H. Chen, "A review of gate tunneling current in MOS devices," *Microelectronics Reliability*, vol. 46, no. 12, pp. 1939–1956, 2006.

[56] G. Moore, "Cramming more components onto integrated circuits," *Electronics*, vol. 38, no. 8, pp. 144–148, 1965.

[57] P. M. Koenraad and M. E. Flatté, "Single dopants in semiconductors," *Nature Materials*, vol. 10, no. 2, pp. 91–100, 2011.

[58] S. Mahapatra, H. Büch, and M. Y. Simmons, "Charge sensing of precisely positioned P donors in Si," *Nano Letters*, vol. 11, no. 10, pp. 4376–4381, 2011.

[59] D. Moraru, A. Udhiarto, M. Anwar, R. Nowak, R. Jablonski, E. Hamid, J. C. Tarido, T. Mizuno, and M. Tabe, "Atom devices based on single dopants in silicon nanostructures," *Nanoscale Research Letters*, vol. 6:479, 2011.

[60] A. Ekert and R. Jozsa, "Quantum computation and Shor's factoring algorithm," *Reviews of Modern Physics*, vol. 68, no. 3, p. 733, 1996.

[61] B. Schumacher, "Quantum coding," *Physical Review A*, vol. 51, no. 4, pp. 2738–2747, 1995.

[62] P. W. Shor, “Algorithms for quantum computation: discrete logarithms and factoring,” *Proceedings of the 35th Annual Symposium on Foundations of Computer Science*. pp. 124–134, 1994.

[63] A. D. C. Alves, J. Newnham, J. A. van Donkelaar, S. Rubanov, J. C. McCallum, and D. N. Jamieson, “Controlled deterministic implantation by nanostencil lithography at the limit of ion-aperture straggling,” *Nanotechnology*, vol. 24 145304, 2013.

[64] D. M. Toyli, C. D. Weis, G. D. Fuchs, T. Schenkel, and D. D. Awschalom, “Chip-scale nanofabrication of single spins and spin arrays in diamond,” *Nano Letters*, vol. 10, no. 8, pp. 3168–3172, 2010.

[65] M. Veldhorst, C. H. Yang, J. C. C. Hwang, W. Huang, J. P. Dehollain, J. T. Muhonen, S. Simmons, A. Laucht, F. E. Hudson, K. M. Itoh, A. Morello, and A. S. Dzurak, “A Two Qubit Logic Gate in Silicon,” *Nature*, vol. 526, no. 7573, pp. 410–414, 2015.

[66] A. Laucht, J. T. Muhonen, F. A. Mohiyaddin, R. Kalra, J. P. Dehollain, S. Freer, F. E. Hudson, M. Veldhorst, R. Rahman, G. Klimeck, K. M. Itoh, D. N. Jamieson, J. C. Mccallum, A. S. Dzurak, and A. Morello, “Electrically controlling single-spin qubits in a continuous microwave field,” *Science Advances*, vol. 1, no. 3 E1500022, 2015.

[67] K. Saeedi, S. Simmons, J. Z. Salvail, P. Dluhy, H. Riemann, N. V Abrosimov, P. Becker, H.-J. Pohl, J. J. L. Morton, and M. L. W. Thewalt, “Room-temperature quantum bit storage exceeding 39 minutes using ionized donors in silicon-28,” *Science*, vol. 342, no. 6160, pp. 830–833, 2013.

[68] J. C. McCallum, D. N. Jamieson, C. Yang, A. D. Alves, B. C. Johnson, T. Hopf, S. C. Thompson, and J. A. Van Donkelaar, "Single-Ion Implantation for the Development of Si-Based MOSFET Devices with Quantum Functionalities," *Advances in Materials Science and Engineering*, vol. 2012 27269, 2011.

[69] B. Lekitsch, S. Weidt, A. G. Fowler, K. Mølmer, S. J. Devitt, C. Wunderlich, and W. K. Hensinger, "Blueprint for a microwave trapped ion quantum computer," *Science Advances*, vol. 3, no. 2 E1601540, 2017.

[70] D. N. Jamieson, V. Chan, F. E. Hudson, S. E. Andresen, C. Yang, T. Hopf, C. I. Pakes, S. Rubanov, S. M. Hearne, S. Prawer, E. Gauja, A. S. Dzurak, and R. G. Clark, "Fabrication of single atom nanoscale devices by ion implantation," *Proceedings of the 2006 International Conference on Nanoscience and Nanotechnology, ICONN '06*, pp. 560–562, 2006.

[71] J. O'Brien, Schofield, M. Simmons, R. Clark, A. Dzurak, N. Curson, B. Kane, N. McAlpine, M. Hawley, and G. Brown, "Scanning tunnelling microscope fabrication of arrays of phosphorus atom qubits for a silicon quantum computer," *Smart Materials and Structures*, vol. 11, pp. 741–748, 2002.

[72] I. Ohdomari, "Single-ion irradiation: physics, technology and applications," *Journal of Physics D: Applied Physics*, vol. 41 43001, 2008.

[73] B. C. Johnson, "Single Ion Implantation Into Si-Based Devices," *ECS Transactions*, vol. 33, no. 11, pp. 179–189, 2010.

[74] M. Ilg, C. D. Weis, J. Schwartz, A. Persaud, Q. Ji, C. Chi Lo, J. Bokor, A. Hegyi, E. Guliyev, I. W. Rangelow, and T. Schenkel, "Improved single ion implantation with scanning probe alignment," *Journal of Vacuum Science & Technology B*, vol. 30 06FD04, 2012.

[75] D. N. Jamieson, C. Yang, T. Hopf, S. M. Hearne, C. I. Pakes, S. Prawer, M. Mitic, E. Gauja, S. E. Andresen, F. E. Hudson, A. S. Dzurak, and R. G. Clark, "Controlled shallow single-ion implantation in silicon using an active substrate for sub-20-keV ions," *Applied Physics Letters*, vol. 86 202101, 2005.

[76] C. Yang and D. Jamieson, "Investigation of avalanche silicon detectors for low energy single ion implantation applications," *Nuclear Instruments and Methods in Physics Research, Section B*, vol. 268, no. 11–12, pp. 2034–2037, 2010.

[77] S. Ruffell, P. J. Simpson, and I. V. Mitchell, "Electrical characterization of 5 keV phosphorous implants in silicon," *Journal of Applied Physics*, vol. 98 013713, 2005.

[78] S. Ruffell, I. V. Mitchell, and P. J. Simpson, "Annealing behavior of low-energy ion-implanted phosphorus in silicon," *Journal of Applied Physics*, vol. 97 123518, 2005.

[79] H. F. Wilson, S. Prawer, P. G. Spizzirri, D. N. Jamieson, N. Stavrias, and D. R. McKenzie, "P2 dimer implantation in silicon: A molecular dynamics study," *Nuclear Instruments and Methods in Physics Research, Section B*, vol. 251, no. 2, pp. 395–401, 2006.

[80] M. A. Bolorizadeh, S. Ruffell, I. V. Mitchell, and R. Gwilliam, “Quantitative depth profiling of ultra-shallow phosphorus implants in silicon using time-of-flight secondary ion mass spectrometry and the nuclear reaction 31P(α,p0)34S,” *Nuclear Instruments and Methods in Physics Research, Section B*, vol. 225, no. 3, pp. 345–352, 2004.

[81] K. M. Itoh and H. Watanabe, “Isotope engineering of silicon and diamond for quantum computing and sensing applications,” *MRS Communications*, vol. 4, no. 4, pp. 143–157, 2014.

[82] J. F. Ziegler, M. D. Ziegler, and J. P. Biersack, “SRIM - The stopping and range of ions in matter,” *Nuclear Instruments and Methods in Physics Research Section B*, vol. 268, no. 11–12, pp. 1818–1823, 2010.

[83] S. Rubanov, D. N. Jamieson, S. Prawer, J. C. McCallum, and G. Tamanyan, “TEM Study of the Damage Profiles induced by 14 keV P + Implantation in Silicon and Germanium,” *Microscopy and Microanalysis*, vol. 13 S02, pp. 654–655, 2007.

[84] P. M. Fahey and P. B. Griffin, “Point defects and dopant diffusion in silicon,” *Reviews of Modern Physics*, vol. 68, no. 2, pp. 290–380, 1989.

[85] D. J. Fisher, Ed., *Diffusion in silicon - 10 Years of Research*. Stafa-Zurich, Switzerland: Trans Tech Publications, 1997.

[86] IEA/Cédric Philibert et al (2014) Technology Roadmap Solar Photovoltaic Energy. All rights reserved..

[87] A. A. Istratov, T. Buonassisi, M. D. Pickett, M. Heuer, and E. R. Weber, “Control of metal impurities in ‘dirty’ multicrystalline silicon for solar cells,” *Materials Science and Engineering: B*, vol. 134, no. 2–3, pp. 282–286, 2006.

[88] T. Buonassisi, M. Heuer, A. A. Istratov, M. D. Pickett, M. A. Marcus, B. Lai, Z. Cai, S. M. Heald, and E. R. Weber, "Transition metal co-precipitation mechanisms in silicon," *Acta Materialia*, vol. 55, no. 18, pp. 6119–6126, 2007.

[89] D. Macdonald and A. Cuevas, "Transition-metal profiles in a multicrystalline silicon ingot," *Journal of Applied Physics*, vol. 97 033523, 2005.

[90] S. Rein and S. W. Glunz, "Electronic properties of interstitial iron and iron-boron pairs determined by means of advanced lifetime spectroscopy," *Journal of Applied Physics*, vol. 98 113711, 2005.

[91] J. R. Davies, "Impurities in Silicon Solar Cells," *IEEE Transactions on Electron Devices*, vol. 27, no. 4, pp. 677–687, 1980.

[92] M. Al-Amin and J. D. Murphy, "Increasing minority carrier lifetime in as-grown multicrystalline silicon by low temperature internal gettering," *Journal of Applied Physics*, vol. 119 235704, 2016.

[93] V. Vähänissi, H. S. Laine, Z. Liu, M. Yli-Koski, A. Haarahiltunen, and H. Savin, "Full recovery of red zone in p-type high-performance multicrystalline silicon," *Solar Energy Materials and Solar Cells*, vol. 173, pp. 120–127, 2017.

[94] D. P. Fenning, A. S. Zuschlag, M. I. Bertoni, B. Lai, G. Hahn, and T. Buonassisi, "Improved iron gettering of contaminated multicrystalline silicon by high-temperature phosphorus diffusion," *Journal of Applied Physics*, vol. 113 214504, 2013.

[95] T. Buonassisi, A. A. Istratov, M. A. Marcus, B. Lai, Z. Cai, S. M. Heald, and E. R. Weber, "Engineering metal-impurity nanodefects for low-cost solar cells," *Nature Materials*, vol. 4, no. 9, pp. 676–679, 2005.

[96] S. A. McHugo, A. C. Thompson, I. Périchaud, and S. Martinuzzi, "Direct correlation of transition metal impurities and minority carrier recombination in multicrystalline silicon," *Applied Physics Letters*, vol. 72, no. 26, pp. 3482–3484, 1998.

[97] P. Gundel, M. C. Schubert, F. D. Heinz, W. Kwapil, W. Warta, G. Martinez-Criado, M. Reiche, and E. R. Weber, "Impact of stress on the recombination at metal precipitates in silicon," *Journal of Applied Physics*, vol. 108 103707, 2010.

[98] D. P. Fenning, J. Hofstetter, M. I. Bertoni, G. Coletti, B. Lai, C. Del Cañizo, and T. Buonassisi, "Precipitated iron: A limit on gettering efficacy in multicrystalline silicon," *Journal of Applied Physics*, vol. 113 044521, 2013.

[99] A. Y. Liu and D. Macdonald, "Precipitation of iron in multicrystalline silicon during annealing," *Journal of Applied Physics*, vol. 115 114901, 2014.

[100] P. Zhang, H. Väinölä, A. A. Istratov, and E. R. Weber, "Thermal stability of internal gettering of iron in silicon and its impact on optimization of gettering," *Applied Physics Letters*, vol. 83, no. 21, pp. 4324–4326, 2003.

[101] P. A. Stolk, J. L. Benton, D. J. Eaglesham, D. C. Jacobson, J. Y. Cheng, J. M. Poate, S. M. Myers, P. A. Stolk, J. L. Benton, D. J. Eaglesham, D. C. Jacobson, J. Cheng, and J. M. Poate, "The mechanism of iron gettering in boron doped silicon," *Applied Physics Letters*, vol. 68, no. 1, pp. 51–53, 1996.

[102] A. Cuevas, M. J. Kerr, C. Samundsett, F. Ferrazza, and G. Coletti, "Millisecond minority carrier lifetimes in n-type multicrystalline silicon," *Applied Physics Letters*, vol. 81, no. 26, pp. 4952–4954, 2002.

[103] J. Hofstetter, D. P. Fenning, D. M. Powell, A. E. Morishige, and H. Wagner, "Sorting Metrics for Customized Phosphorus Diffusion Gettering," *IEEE Journal of Photovoltaics*, vol. 4, no. 6, pp. 1421–1428, 2014.

[104] R. A. Sinton and A. Cuevas, "Contactless determination of current–voltage characteristics and minority-carrier lifetimes in semiconductors from quasi-steady-state photoconductance data," *Applied Physics Letters*, vol. 69, no. 17, pp. 2510–2512, 1996.

[105] C. Ulzhöfer, B. Wolpensinger, J. Schmidt, S. Hameln, and A. Ohrberg, "Understanding the lifetime evolution in n-type multicrystalline silicon during phosphorus gettering and hydrogenation," *Proceedings of 23rd European Photovoltaic Solar Energy Conference.*, pp. 1051–1056, 2008.

[106] A. Stoffers, O. Cojocaru-Mirédin, W. Seifert, S. Zaefferer, S. Riepe, and D. Raabe, "Grain boundary segregation in multicrystalline silicon: Correlative characterization by EBSD, EBIC, and atom probe tomography," *Progress in Photovoltaics: Research and Applications*, vol. 23, no. 12, pp. 1742–1753, 2015.

[107] J. D. Murphy and R. J. Falster, "The relaxation behaviour of supersaturated iron in single-crystal silicon at 500 to 750°C," *Journal of Applied Physics*, vol. 112 113506, 2012.

[108] G. Zoth and W. Bergholz, "A fast, preparation-free method to detect iron in silicon," *Journal of Applied Physics*, vol. 67, no. 11, pp. 6764–6771, 1990.

[109] D. MacDonald, T. Roth, P. N. K. Deenapanray, T. Trupke, and R. A. Bardos, "Doping dependence of the carrier lifetime crossover point upon dissociation of iron-boron pairs in crystalline silicon," *Applied Physics Letters*, vol. 89 142107, 2006.

[110] D. H. Macdonald, L. J. Geerligs, and A. Azzizi, "Iron detection in crystalline silicon by carrier lifetime measurements for arbitrary injection and doping," *Journal of Applied Physics*, vol. 95, no. 3, pp. 1021–1028, 2004.

[111] M. D. Pickett and T. Buonassisi, "Iron point defect reduction in multicrystalline silicon solar cells," *Applied Physics Letters*, vol. 92 122103, 2008.

[112] M. Seibt, D. Abdelbarey, V. Kveder, C. Rudolf, P. Saring, L. Stolze, and O. Voß, "Interaction of metal impurities with extended defects in crystalline silicon and its implications for gettering techniques used in photovoltaics," *Materials Science and Engineering B*, vol. 159–160, pp. 264–268, 2009.

[113] J. Härkönen, V. P. Lempinen, T. Juvonen, and J. Kylmäluoma, "Recovery of minority carrier lifetime in low-cost multicrystalline silicon," *Solar Energy Materials and Solar Cells*, vol. 73, no. 2, pp. 125–130, 2002.

[114] H. B. Xu, R. J. Hong, B. Ai, L. Zhuang, and H. Shen, "Application of phosphorus diffusion gettering process on upgraded metallurgical grade Si wafers and solar cells," *Applied Energy*, vol. 87, no. 11, pp. 3425–3430, 2010.

[115] M. B. Shabani, T. Yamashita, and E. Morita, "Study of gettering mechanisms in silicon: Competitive gettering between phosphorus diffusion gettering and other gettering sites," *Solid State Phenomena*, vol. 131–133, pp. 399–404, 2008.

[116] G. Micard, A. Dastgheib-Shirazi, M. Steyer, H. Wagner, P. Altermatt, and G. Hahn, "Advances in the understanding of phosphorus silicte glass (PSG) formation for accurate process simulation of phosphorus diffusion," *Proceedings of the 27th European Photovoltaic Solar Energy Conference and Exhibition*, pp. 1355–1359, 2012.

[117] T. Y. Kwon, D. H. Yang, M. K. Ju, W. W. Jung, S. Y. Kim, Y. W. Lee, D. Y. Gong, and J. Yi, "Screen printed phosphorus diffusion for low-cost and simplified industrial mono-crystalline silicon solar cells," *Solar Energy Materials and Solar Cells*, vol. 95, no. 1, pp. 14–17, 2011.

[118] F. N. Schwettmann and D. L. Kendall, "On the nature of the kink in the carrier profile for phosphorus-diffused layers in silicon," *Applied Physics Letters*, vol. 21, no. 1, pp. 2–4, 1972.

[119] G. Stingeder, P. Pongratz, W. Kuhnert, and T. Brabec, "Investigation of high concentration effects of Sb and P in silicon by combination of SIMS and TEM," *Fresenius Zeitschrift fur Analytische Chemie*, vol. 333, no. 3, pp. 191–202, 1989.

[120] R. B. Fair and J. C. C. Tsai, "A Quantitative Model for the Diffusion of Phosphorus in Silicon and the Emitter Dip Effect," *Journal of the Electrochemical Society : Solid State Science and Technology*, vol. 124, no. 7, pp. 1107–1118, 1977.

[121] B. Bazer-Bachi, E. Fourmond, P. Papet, L. Bounaas, O. Nichiporuk, N. Le Quang, and M. Lemiti, "Higher emitter quality by reducing inactive phosphorus," *Solar Energy Materials and Solar Cells*, vol. 105, pp. 137–141, 2012.

[122] A. Bentzen, A. Holt, J. S. Christensen, and B. G. Svensson, “High concentration in-diffusion of phosphorus in Si from a spray-on source,” *Journal of Applied Physics*, vol. 99 064502, 2006.

[123] S. Solmi, A. Parisini, R. Angelucci, A. Armigliato, D. Nobili, and L. Moro, “Dopant and carrier concentration in Si in equilibrium with monoclinic SiP precipitates,” *Physical Review B*, vol. 53, no. 12, pp. 7836–7841, 1996.

[124] A. Armigliato and P. Werner, “High resolution electron microscopy observations of precipitates in p-supersaturated silicon,” *Ultramicroscopy*, vol. 15, no. 1–2, pp. 61–69, 1984.

[125] S. Solmi, G. Celotti, D. Nobili, and P. Negrini, “Predeposition in Silicon as Affected by the Formation of Orthorhombic SiP and Cubic SiO2P2O5 at the PSG-Si Interface,” *Journal of the Electrochemical Society, Solid-State Science and Technology*, vol. 123, no. 5, pp. 654–660, 1976.

[126] A. Bourret and W. Schröter, “HREM of SiP precipitates at the (111) silicon surface during phosphorus predeposition,” *Ultramicroscopy*, vol. 14, no. 1–2, pp. 97–106, 1984.

[127] A. Correia, B. Pichaud, A. Lhorte, and J. B. Quoirin, “Platinum gettering in silicon by silicon phosphide precipitates,” *Journal of Applied Physics*, vol. 79, no. 4, pp. 2145–2147, 1996.

[128] M. L. Joshi and S. Dash, “Distribution and Precipitation of Gold in Phosphorus-Diffused Silicon,” *Journal of Applied Physics*, vol. 37, no. 6, pp. 2453–2457, 1966.

[129] E. Spiecker, M. Seibt, and W. Schröter, “Phosphorous-diffusion gettering in the presence of a nonequilibrium concentrationof silicon interstitials: A quantitative model,” *Physical Review B*, vol. 55, no. 15, pp. 9577–9583, 1997.

[130] J. Schon and W. Warta, “Simulation of phosphorus diffusion and iron gettering with Sentaurus process,” *Proceedings of the 23rd European Photovoltaic Solar Energy Conference.*, pp. 1851–1854, 2008.

[131] M. C. Schubert, W. Kwapil, J. Schn, H. Habenicht, M. Kasemann, P. Gundel, M. Blazek, and W. Warta, “Analysis of performance limiting material properties of multicrystalline silicon,” *Solar Energy Materials and Solar Cells*, vol. 94, no. 9, pp. 1451–1456, 2010.

[132] A. Haarahiltunen, H. V. A. Yli-koski, and J. Sinkkonen, “Experimental and theoretical study of heterogeneous iron precipitation in silicon,” *Journal of Applied Physics*, vol. 101 043507, 2007.

[133] T. Mchedlidze and M. Kittler, “Involvement of iron-phosphorus complexes in iron gettering for n-type silicon,” *Physica Status Solidi A*, vol. 203, no. 4, pp. 786–791, 2006.

[134] B. Shen, J. Jablonski, T. Sekiguchi, and K. Sumino, “Influences of Cu and Fe impurities on oxygen precipitation in Czochralski-grown silicon,” *Japanese Journal of Applied Physics*, vol. 35, no. 8, pp. 4187–4194, 1996.

[135] J. D. Murphy, K. Bothe, M. Olmo, V. V Voronkov, and R. J. Falster, “The effect of oxide precipitates on minority carrier lifetime in p-type silicon,” *Journal of Applied Physics*, vol. 110 053713, 2011.

[136] S. Cabrini and S. Kawata, *Nanofabrication Handbook*. Boca Raton, USA: CRC Press, 2012.

[137] G. Cliff and G. W. Lorimer, "The quantitative analysis of thin specimens," *Journal of Microscopy*, vol. 103, pp. 203–207, 1975.

[138] L. A. Giannuzzi and F. A. Stevie, "A review of focused ion beam milling techniques for TEM specimen preparation," *Micron*, vol. 30, no. 3, pp. 197–204, 1999.

[139] D. W. Saxey, J. M. Cairney, D. McGrouther, T. Honma, and S. P. Ringer, "Atom Probe Specimen Fabrication Methods using a Dual FIB/SEM," *Ultramicroscopy*, vol. 107, no. 9, pp. 756–760, 2006.

[140] L. Giannuzzi and B. Kempshall, "FIB lift-out for defect analysis," *Microelectronic Failure Analysis: Desk Reference 2002 Supplement (ASM International)*, pp. 29–35, 2002.

[141] K. W. Urban, "Studying Atomic Structures by Aberration-Corrected Transmission Electron Microscopy," *Science*, vol. 321, no. 5888, pp. 506–510, 2008.

[142] R. F. Egerton, "Electron Energy-Loss Spectroscopy in the Electron Microscope," *Reports on Progress in Physics*, vol. 72 016502, 2009.

[143] S. V Baryshev, A. V Zinovev, C. E. Tripa, M. J. Pellin, I. V Veryovkin, Q. Peng, and J. W. Elam, "High resolution secondary ion mass spectrometry depth profiling of nanolayers," *Rapid Communications in Mass Spectrometry*, vol. 26, pp. 2224–2230, 2012.

[144] S. Lozano-Perez, M. R. Kilburn, T. Yamada, T. Terachi, C. A. English, and C. R. M. Grovenor, "High-resolution imaging of complex crack chemistry in reactor steels by NanoSIMS," *Journal of Nuclear Materials*, vol. 374, no. 1–2, pp. 61–68, 2008.

[145] A. M. Belu, D. J. Graham, and D. G. Castner, "Time-of-flight secondary ion mass spectrometry : techniques and applications for the characterization of biomaterial surfaces," *Biomaterials*, vol. 24, no. 21, pp. 3635–3653, 2003.

[146] W. Vandervorst, "Applied Surface Science Semiconductor profiling with sub-nm resolution : Challenges and solutions," *Applied Surface*, vol. 255, pp. 805–812, 2008.

[147] V. R. Deline, W. Katz, C. A. J. Evans, and P. Williams, "Mechanism of the SIMS matrix effect," *Applied Physics Letters*, vol. 33, no. 9, pp. 832–835, 1978.

[148] E. De Chambost, P. Monsallut, B. Rasser, and M. Schuhmacher, "Depth scale calibration of SIMS depth profiles by means of an online crater depth measurement technique," *Applied Surface Science*, vol. 204, pp. 391–395, 2003.

[149] S. Fearn and D. S. McPhail, "High resolution quantitative SIMS analysis of shallow boron implants in silicon using a bevel and image approach," *Applied Surface Science*, vol. 252, no. 4, pp. 893–904, 2005.

[150] R. Von Criegern, F. Jahnel, R. Lange-Gieseler, P. Pearson, G. Hobler, and S. Alexander, "Verification of lateral secondary ion mass spectrometry as a method for measuring lateral dopant dose distributions in microelectronics test structures," *Journal of Vacuum Science & Technology B*, vol. 16, no. 1, pp. 386–393, 1998.

[151] R. D. Leapman, “Comparison of detection limits for EELS and EDXS,” *Microscopy Microanalysis Microstructures*, vol. 2, no. 3, pp. 231–244, 1991.

[152] A. Christofi, J. F. Walker, and D. S. McPhail, “SIMS depth profiling and TEM imaging of the SIMS altered layer,” *Applied Surface Science*, vol. 255, no. 4, pp. 1381–1383, 2008.

[153] E. W. Müller, “Study of Atomic Structure of Metal Surfaces in the Field Ion Microscope,” *Journal of Applied Physics*, vol. 28, no. 1, pp. 1–7, 1957.

[154] B. Gault, F. de Geuser, L. T. Stephenson, M. P. Moody, B. C. Muddle, and S. P. Ringer, “Estimation of the Reconstruction Parameters for Atom Probe Tomography,” *Microscopy and Microanalysis*, vol. 14, no. 4, pp. 296–305, 2008.

[155] J. A. Panitz, “Field-ion microscopy - A review of basic principles and selected applications,” *Journal of Physics E*, vol. 15, no. 12, pp. 1281–1294, 1982.

[156] P. A. J. Bagot, “The Effects of Gaseous Adsorption on Pt-alloy Catalyst Surfaces studied with 3D Atom-Probe” DPhil Thesis, Department of Materials, University of Oxford, St Catherine’s College, 2005. Perm. (P.A. J. Bagot and W. J. Bean).

[157] T. T. Tsong and G. Kellogg, “Direct observation of the directional walk of single adatoms and the adatom polarizability,” *Physical Review B*, vol. 12, no. 4, pp. 1343–1353, 1975.

[158] S. C. Wang and T. T. Tsong, “Field and temperature dependence of the directional walk of single adsorbed W atoms on the W(110) plane,” *Physical Review B*, vol. 26, no. 12, pp. 6470–6475, 1982.

[159] M. Dagan, L. R. Hanna, A. Xu, S. G. Roberts, G. D. W. Smith, B. Gault, P. D. Edmondson, P. A. J. Bagot, and M. P. Moody, “Imaging of radiation damage using complementary field ion microscopy and atom probe tomography,” *Ultramicroscopy*, vol. 159, pp. 387–394, 2015.

[160] E. W. Müller, J. A. Panitz, and S. B. Mclane, “The Atom Probe Field Ion Microscope,” *The Review of Scientific Instruments*, vol. 39, no. 1, pp. 83–86, 1968.

[161] A. Cerezo, T. J. Godfrey, and G. D. W. Smith, “Application of a position-sensitive detector to atom probe microanalysis,” *The Review of Scientific Instruments*, vol. 59, no. 6, pp. 862–866, 1988.

[162] A. Cerezo, T. J. Godfrey, C. R. M. Grovenor, and G. D. W. Smith, “Surface analysis with a position-sensitive atom probe,” *Journal of Physics: Condensed Matter*, vol. 1 B, pp. 99–103, 1989.

[163] M. P. Moody, A. Vella, S. S. A. Gerstl, and P. A. J. Bagot, “Advances in atom probe tomography instrumentation : Implications for materials research,” *MRS Bulletin*, vol. 41, no. 1, pp. 40–45, 2016.

[164] P. A. J. Bagot, O. B. W. Silk, J. O. Douglas, S. Pedrazzini, D. J. Crudden, T. L. Martin, M. C. Hardy, M. P. Moody, and R. C. Reed, “An Atom Probe Tomography study of site preference and partitioning in a nickel-based superalloy,” *Acta Materialia*, vol. 125, pp. 156–165, 2017.

[165] O. Nishikawa and M. Kimoto, “Toward a scanning atom probe -computer simulation of electric field,” *Applied Surface Science*, vol. 76–77, pp. 424–430, 1994.

[166] M. K. Miller, A. Cerezo, M. Hetherington, and G. W. D. Smith, *Atom Probe Field Ion Microscopy*. Oxford: Clarendon Press, 1996.

[167] T. F. Kelly, T. T. Gribb, J. D. Olson, R. L. Martens, J. D. Shepard, S. A. Wiener, T. C. Kunicki, R. M. Ulfig, D. R. Lenz, E. M. Strennen, E. Oltman, J. H. Bunton, and D. R. Strait, "First data from a commercial local electrode atom probe (LEAP)," *Microscopy and microanalysis*, vol. 10, no. 3, pp. 373–383, 2004.

[168] P. Bas, A. Bostel, B. Deconihout, and D. Blavette, "A general protocol for the reconstruction of 3D atom probe data," *Applied Surface Science*, vol. 87–88, pp. 298–304, 1995.

[169] B. Gault, S. T. Loi, V. J. Araullo-Peters, L. T. Stephenson, M. P. Moody, S. L. Shrestha, R. K. W. Marceau, L. Yao, J. M. Cairney, and S. P. Ringer, "Dynamic reconstruction for atom probe tomography," *Ultramicroscopy*, vol. 111, no. 11, pp. 1619–1624, 2011.

[170] F. Vurpillot, M. Gruber, G. Da Costa, I. Martin, L. Renaud, and A. Bostel, "Pragmatic reconstruction methods in atom probe tomography," *Ultramicroscopy*, vol. 111, no. 8, pp. 1286–1294, 2011.

[171] F. Vurpillot, B. Gault, B. P. Geiser, and D. J. Larson, "Reconstructing atom probe data: A review," *Ultramicroscopy*, vol. 132, pp. 19–30, 2013.

[172] M. P. Moody, B. Gault, L. T. Stephenson, D. Haley, and S. P. Ringer, "Qualification of the tomographic reconstruction in atom probe by advanced spatial distribution map techniques," *Ultramicroscopy*, vol. 109, no. 7, pp. 815–824, 2009.

[173] T. F. Kelly and M. K. Miller, "Atom probe tomography," *The Review of Scientific Instruments*, vol. 78 031101, 2007.

[174] A. J. Melmed, T. Sakurai, Y. Kuk, and E. I. Givargizov, “Feasibility of ToF Atom Probe analysis of silicon,” *Surface Science Letters*, vol. 103, pp. 139–142, 1981.

[175] C. R. M. Grovenor and G. D. W. Smith, “The characterisation of silicon surfaces by time-of-flight atom probe analysis,” *Surface Science Letters*, vol. 123, pp. 686–692, 1982.

[176] K. Thompson, J. Sebastian, and S. Gerstl, “Observations of Si field evaporation,” *Ultramicroscopy*, vol. 107, no. 2–3, pp. 124–130, 2007.

[177] G. L. Kellogg and T. T. Tsong, “Pulsed-laser atom-probe field-ion microscopy,” *Journal of Applied Physics*, vol. 51, no. 2, pp. 1184–1193, 1980.

[178] J. Bunton, D. Lenz, J. Olson, K. Thompson, R. Ulfig, D. Larson, and T. Kelly, “Instrumentation Developments in Atom Probe Tomography: Applications in Semiconductor Research,” *Microscopy and Microanalysis*, vol. 12 S02, pp. 1730–1731, 2006.

[179] T. F. Kelly, A. Vella, J. H. Bunton, J. Houard, E. P. Silaeva, J. Bogdanowicz, and W. Vandervorst, “Laser pulsing of field evaporation in atom probe tomography,” *Current Opinion in Solid State and Materials Science*, vol. 18, no. 2, pp. 81–89, 2014.

[180] J. H. Bunton, J. D. Olson, D. R. Lenz, and T. F. Kelly, “Advances in pulsed-laser atom probe: instrument and specimen design for optimum performance,” *Microscopy and microanalysis*, vol. 13, no. 6, pp. 418–427, 2007.

[181] J. Bogdanowicz, M. Gilbert, S. Koelling, and W. Vandervorst, “Impact of the apex of an elongated dielectric tip upon its light absorption properties,” *Applied Surface Science*, vol. 302, pp. 223–225, 2014.

[182] T. F. Kelly, J. H. Bunton, T. J. Prosa, R. M. Ulfig, P. H. Clifton, and Larson, "Laser-Specimen Interactions in Atom Probe Tomography," *Microscopy and Microanalysis*, vol. 18 S02, pp. 584–585, 2012.

[183] A. Shariq, S. Mutas, K. Wedderhoff, C. Klein, H. Hortenbach, S. Teichert, P. Kücher, and S. S. A. Gerstl, "Investigations of field-evaporated end forms in voltage- and laser-pulsed atom probe tomography," *Ultramicroscopy*, vol. 109, no. 5, pp. 472–479, 2009.

[184] G. Sha, A. Cerezo, and G. D. W. Smith, "Field evaporation behavior during irradiation with picosecond laser pulses," *Applied Physics Letters*, vol. 92 043503, 2008.

[185] B. Gault, M. P. Moody, F. De Geuser, G. Tsafnat, A. La Fontaine, L. T. Stephenson, D. Haley, and S. P. Ringer, "Advances in the calibration of atom probe tomographic reconstruction," *Journal of Applied Physics*, vol. 105 034913, 2009.

[186] A. J. Melmed, J. J. Carroll, A. J. Melmed, and J. J. Carrolla, "An approach to realism in field ion microscopy via zone electropolishing," *Journal of Vacuum Science & Technology A*, vol. 2, no. 3, pp. 1388–1389, 1988.

[187] D. R. Turner, "Electropolishing Silicon in Hydrofluoric Acid Solutions," *Journal of the Electrochemical Society*, vol. 105, no. 7, pp. 402–408, 1958.

[188] R. A. D. Mackenzie, J. A. Liddle, and C. R. M. Grovenor, "Ultrahigh resolution characterisation of compound semiconductors using pulsed laser atom probe techniques," *Applied Surface Science*, vol. 50, pp. 196–201, 1991.

[189] D. E. Perea, E. Wijaya, J. L. Lensch-falk, E. R. Hemesath, and L. J. Lauhon, "Tomographic analysis of dilute impurities in semiconductor nanostructures," *Journal of Solid State Chemistry*, vol. 181, pp. 1642–1649, 2008.

[190] D. Larson and B. Wissman, "Advances in atom probe specimen fabrication from planar multilayer thin film structures," *Microscopy and Microanalysis*, vol. 7, no. 1, pp. 24–31, 2001.

[191] J. M. Walls, H. N. Southworth, and G. J. Rushton, "The preparation of field electron / field-ion emitters by ion etching," *Vacuum*, vol. 24, no. 10, pp. 475–479, 1974.

[192] D. J. Larson, K. F. Russell, and A. Cerezo, "Sharpening of field-ion specimens and positioning of features of interest by ion-beam milling," *Journal of Vacuum Science & Technology B*, vol. 18, pp. 328–333, 1999.

[193] A. Kvist, H.-O. Andren, and L. Lundin, "A specimen preparation technique for atom probe analysis of the near-surface region of cemented carbides," *Applied Surface Science*, vol. 95, pp. 356–361, 1996.

[194] M. K. Miller, K. F. Russell, K. Thompson, R. Alvis, and D. J. Larson, "Review of atom probe FIB-based specimen preparation methods," *Microscopy and microanalysis*, vol. 13, no. 6, pp. 428–436, 2007.

[195] H. Langfischer, B. Basnar, H. Hutter, and E. Bertagnolli, "Evolution of tungsten film deposition induced by focused ion beam," *Journal of Vacuum Science and Technology A*, vol. 20, no. 4, pp. 1408–1415, 2002.

[196] K. Thompson, B. Gorman, D. Larson, B. Van Leer, and L. Hong, "Minimization of Ga Induced FIB Damage Using Low Energy Clean-up," *Microscopy and Microanalysis*, vol. 12 S02, pp. 1736–1737, 2006.

[197] S. S. A. Gerstl, A. Morrone, and R. Kvitek, “Three-Dimensional Nanoscale Characterization of Pt Deposition from an Organometallic Precursor Induced by a Focused Ion Beam,” *Microscopy and Microanalysis*, vol. 12 S02, pp. 1252–1253, 2006.

[198] S. Kölling and W. Vandervorst, “Failure mechanisms of silicon-based atom-probe tips,” *Ultramicroscopy*, vol. 109, no. 5, pp. 486–491, 2009.

[199] K. Thompson, J. H. Bunton, T. F. Kelly, and D. J. Larson, “Characterization of ultralow-energy implants and towards the analysis of three-dimensional dopant distributions using three-dimensional atom-probe tomography,” *Journal of Vacuum Science & Technology B: Microelectronics and Nanometer Structures*, vol. 24, no. 1, p. 421, 2006.

[200] S. Mutas and C. Klein, “Importance of the Protective Layers and the Specimen Preparation for Reproducible APT Results,” *Microscopy and Microanalysis*, vol. 17 S02, pp. 730–731, 2011.

[201] D. J. Larson, A. D. Giddings, Y. Wu, M. A. Verheijen, T. J. Prosa, F. Roozeboom, K. P. Rice, W. M. M. Kessels, B. P. Geiser, and T. F. Kelly, “Ultramicroscopy Encapsulation method for atom probe tomography analysis of nanoparticles,” *Ultramicroscopy*, vol. 159, no. 2, pp. 420–426, 2015.

[202] Q. Yang, D. E. Joyce, S. Saranu, G. M. Hughes, A. Varambhia, M. P. Moody, and P. A. J. Bagot, “A combined approach for deposition and characterization of atomically engineered catalyst nanoparticles,” *Catalysis, Structure & Reactivity*, vol. 1, no. 3, pp. 125–131, 2015.

[203] E. A. Marquis, B. P. Geiser, T. J. Prosa, and D. J. Larson, “Evolution of tip shape during field evaporation of complex multilayer structures,” *Journal of Microscopy*, vol. 241, no. 3, pp. 225–233, 2011.

[204] T. F. Kelly, D. J. Larson, K. Thompson, R. L. Alvis, J. H. Bunton, J. D. Olson, and B. P. Gorman, “Atom Probe Tomography of Electronic Materials,” *Annual Review of Materials Research*, vol. 37, no. 1, pp. 681–727, 2007.

[205] D. Blavette and S. Duguay, “Atom probe tomography in nanoelectronics,” *The European Physical Journal Applied Physics*, vol. 68 10101, 2014.

[206] F. Panciera, K. Hoummada, M. Gregoire, M. Juhel, F. Lorut, N. Bicais, and D. Mangelinck, “Atom probe tomography of SRAM transistors: Specimen preparation methods and analysis,” *Microelectronic Engineering*, vol. 107, pp. 167–172, 2013.

[207] A. Grenier, S. Duguay, J. P. Barnes, R. Serra, G. Haberfehlner, D. Cooper, F. Bertin, S. Barraud, G. Audoit, L. Arnoldi, E. Cadel, A. Chabli, and F. Vurpillot, “3D analysis of advanced nano-devices using electron and atom probe tomography,” *Ultramicroscopy*, vol. 136, pp. 185–192, 2014.

[208] B. P. Gorman, H. L. Guthrey, and M. M. Al-Jassim, “Quantification of atomic scale defects in poly Si PV devices using atom probe tomography,” *2012 38th IEEE Photovoltaic Specialists Conference*, pp. 1498–1500, 2012.

[209] N. Dawahre, G. Shen, S. N. Renfrow, S. M. Kim, and P. Kung, “Atom probe tomography of AlInN/GaN HEMT structures,” *Journal of Vacuum Science & Technology B*, vol. 31 041802, 2013.

[210] G. Scappucci, W. M. Klesse, A. R. Hamilton, G. Capellini, D. L. Jaeger, M. R. Bischof, R. F. Reidy, B. P. Gorman, and M. Y. Simmons, "Stacking of 2D Electron Gases in Ge Probed at the Atomic Level and Its Correlation to Low-Temperature Magnetotransport," *Nano Letters*, vol. 12, no. 9, pp. 4953–4959, 2012.

[211] F. Tang, T. Zhu, F. Oehler, W. Y. Fu, J. T. Griffiths, F. C. P. Massabuau, M. J. Kappers, T. L. Martin, P. A. J. Bagot, M. P. Moody, and R. A. Oliver, "Indium clustering in a-plane InGaN quantum wells as evidenced by atom probe tomography," *Applied Physics Letters*, vol. 106 072104, 2015.

[212] M. Müller, D. W. Saxey, A. Cerezo, and G. D. W. Smith, "Nanoscale characterization of compound semiconductors using laser-pulsed atom probe tomography," *Journal of Physics: Conference Series*, vol. 209 012026, 2010.

[213] D. E. Perea, E. R. Hemesath, E. J. Schwalbach, J. L. Lensch-Falk, P. W. Voorhees, and L. J. Lauhon, "Direct measurement of dopant distribution in an individual vapour-liquid-solid nanowire," *Nature Nanotechnology*, vol. 4, no. 5, pp. 315–319, 2009.

[214] T. J. Prosa, D. Olson, B. Geiser, D. J. Larson, K. Henry, and E. Steel, "Analysis of implanted silicon dopant profiles," *Ultramicroscopy*, vol. 132, pp. 179–185, 2013.

[215] K. Thompson, J. H. Bunton, J. S. Moore, and K. S. Jones, "Compositional analysis of Si nanostructures: SIMS–3D tomographic atom probe comparison," *Semiconductor Science and Technology*, vol. 22 S127-S1, 2007.

[216] O. Moutanabbir, D. Isheim, D. N. Seidman, Y. Kawamura, and K. M. Itoh, "Ultraviolet-laser atom-probe tomographic three-dimensional atom-by-atom mapping of isotopically modulated Si nanoscopic layers," *Applied Physics Letters*, vol. 98 013111, 2011.

[217] O. Cojocaru-Mirédin, E. Cadel, B. Deconihout, D. Mangelinck, and D. Blavette, "Three-dimensional atom mapping of boron in implanted silicon," *Ultramicroscopy*, vol. 109, no. 5, pp. 649–653, 2009.

[218] Y. M. Chen, T. Ohkubo, and K. Hono, "Laser assisted field evaporation of oxides in atom probe analysis," *Ultramicroscopy*, vol. 111, no. 6, pp. 562–566, 2011.

[219] G. Sundell, M. Thuvander, and O.-H. Andre, "Hydrogen analysis in APT : Methods to control adsorption and dissociation of H2," *Ultramicroscopy*, vol. 132, pp. 285–289, 2013.

[220] K. Thompson, J. H. Bunton, T. F. Kelly, and D. J. Larson, "Characterization of ultralow-energy implants and towards the analysis of three-dimensional dopant distributions using three-dimensional atom-probe tomography," *Journal of Vacuum Science & Technology B*, vol. 24, no. 1, pp. 421–427, 2006.

[221] P. Felfer, S. P. Ringer, and J. M. Cairney, "Shaping the lens of the atom probe : Fabrication of site specific , oriented specimens and application to grain boundary analysis," *Ultramicroscopy*, vol. 111, no. 6, pp. 435–439, 2011.

[222] B. W. Kempshall, L. A. Giannuzzi, B. I. Prenitzer, F. A. Stevie, and S. X. Da, "Comparative evaluation of protective coatings and focused ion beam chemical vapor deposition processes," *Journal of Vacuum Science & Technology B*, vol. 20, no. 1, pp. 286–290, 2002.

[223] J. Gierak, E. Bourhis, M. N. Mérat Combes, Y. Chriqui, I. Sagnes, D. Mailly, P. Hawkes, R. Jede, L. Bruchhaus, L. Bardotti, B. Prével, A. Hannour, P. Mélinon, A. Perez, J. Ferre, J.-P. Jamet, A. Mougin, C. Chappert, and V. Mathet, "Exploration of the ultimate patterning potential achievable with focused ion beams," *Ultramicroscopy*, vol. 109, no. 5, pp. 457–462, 2009.

[224] B. Gault, A. La Fontaine, M. P. Moody, S. P. Ringer, and E. A. Marquis, "Impact of laser pulsing on the reconstruction in an atom probe tomography," *Ultramicroscopy*, vol. 110, no. 9, pp. 1215–1222, 2010.

[225] K. Hono, T. Ohkubo, Y. M. Chen, M. Kodzuka, K. Oh-ishi, H. Sepehri-Amin, F. Lia, T. Kinno, S. Tomiya, and Y. Kanitani, "Broadening the applications of the atom probe technique by ultraviolet femtosecond laser," *Ultramicroscopy*, vol. 111, no. 6, pp. 576–583, 2011.

[226] K. Thompson, D. J. Larson, and R. M. Ulfig, "Pre-sharpened and Flat-top Microtip Coupons: a Quantitative Comparison for Atom-Probe Analysis Studies," *Microscopy and Microanalysis*, vol. 11 S02, pp. 882–883, 2005.

[227] G. Sha and S. P. Ringer, "Effect of laser pulsing on the composition measurement of an Al-Mg-Si-Cu alloy using three-dimensional atom probe," *Ultramicroscopy*, vol. 109, no. 5, pp. 580–584, 2009.

[228] M. D. Giles, "Transient Phosphorus Diffusion Below the Amorphization Threshold," *Journal of The Electrochemical Society*, vol. 138, no. 4, pp. 1160–1165, 1991.

[229] N. E. B. Cowern, D. J. Godfrey, and D. E. Sykes, “Transient enhanced diffusion of phosphorus in silicon,” *Applied Physics Letters*, vol. 49, no. 25, pp. 1711–1713, 1986.

[230] G. S. Oehrlein, S. A. Cohen, and T. O. Sedgwick, “Diffusion of phosphorus during rapid thermal annealing of ion implanted silicon,” *Applied Physics Letters*, vol. 45, no. 4, pp. 417–419, 1984.

[231] H. Bracht, “Advanced dopant and self-diffusion studies in silicon,” *Nuclear Instruments and Methods in Physics Research B*, vol. 253, no. 1–2, pp. 105–112, 2006.

[232] M. E. Law and S. M. Cea, “Continuum based modeling of silicon integrated circuit processing: An object oriented approach,” *Computational Materials Science*, vol. 12, no. 4, pp. 289–308, 1998.

[233] R. D. Chang, J. R. Tsai, and L. W. Ho, “Elucidating the mechanism of transient loss of phosphorus due to interface segregation,” *Applied Physics Letters*, vol. 88 211914, 2006.

[234] S. K. Suram and K. Rajan, “Calibration of reconstruction parameters in atom probe tomography using a single crystallographic orientation,” *Ultramicroscopy*, vol. 132, pp. 136–142, 2013.

[235] B. P. Geiser, T. F. Kelly, D. J. Larson, J. Schneir, and J. P. Roberts, “Spatial Distribution Maps for Atom Probe Tomography,” *Microscopy and Microanalysis*, vol. 13, no. 6, pp. 437–447, 2007.

[236] S. Mutas, C. Klein, and S. S. A. Gerstl, “Investigation of the analysis parameters and background subtraction for high-k materials with atom probe tomography,” *Ultramicroscopy*, vol. 111, no. 6, pp. 546–551, 2011.

[237] M. Müller, B. Gault, G. D. W. Smith, and C. R. M. Grovenor, “Accuracy of pulsed laser atom probe tomography for compound semiconductor analysis,” *Journal of Physics: Conference Series*, vol. 326 012031, 2011.

[238] S. Koelling, M. Gilbert, J. Goossens, A. Hikavyy, O. Richard, and W. Vandervorst, “High depth resolution analysis of Si/SiGe multilayers with the atom probe,” *Applied Physics Letters*, vol. 95 144106, 2009.

[239] A. J. London, D. Haley, and M. P. Moody, “Single-Ion Deconvolution of Mass Peak Overlaps for Atom Probe Microscopy,” *Microscopy and Microanalysis*, vol. 23, no. 2, pp. 300–306, 2017.

[240] Y. Shimizu, Y. Kawamura, M. Uematsu, K. M. Itoh, M. Tomita, M. Sasaki, H. Uchida, and M. Takahashi, “Atom probe microscopy of three-dimensional distribution of silicon isotopes in Si28/Si30 isotope superlattices with sub-nanometer spatial resolution,” *Journal of Applied Physics*, vol. 106 076102, 2009.

[241] M. Tomita, M. Koike, H. Akutsu, S. Takeno, Y. Kawamura, Y. Shimizu, M. Uematsu, and K. M. Itoh, “Investigation of the factors determining the SIMS depth resolution in silicon-isotope multiple layers,” *Journal of Vacuum Science & Technology B*, vol. 30 011803, 2012.

[242] T. Plach, K. Hingerl, S. Tollabimazraehno, G. Hesser, V. Dragoi, and M. Wimplinger, “Mechanisms for room temperature direct wafer bonding,” *Journal of Applied Physics*, vol. 113 094905, 2013.

[243] S. Koelling, N. Innocenti, G. Hellings, M. Gilbert, A. K. Kambham, K. De Meyer, and W. Vandervorst, “Characteristics of cross-sectional atom probe analysis on semiconductor structures,” *Ultramicroscopy*, vol. 111, no. 6, pp. 540–545, 2011.

[244] A. Stoffers, O. Cojocaru-Miredin, O. Breitenstein, W. Seifert, S. Zaefferer, and D. Raabe, “Grain boundary characterization in multicrystalline silicon using joint EBSD, EBIC, and atom probe tomography,” *Photovoltaic Specialist Conference (PVSC), 2014 IEEE 40th*, pp. 42–46, 2014.

[245] B. P. Gorman, H. L. Guthrey, and M. M. Al-Jassim, “Quantification of atomic scale defects in poly Si PV devices using atom probe tomography,” *Photovoltaic Specialists Conference (PVSC), 2012 38th IEEE*, pp. 1498–1500, 2012.

[246] J. D. Murphy and R. J. Falster, “Contamination of silicon by iron at temperatures below 800°C,” *Physica Status Solidi RRL*, vol. 5, no. 10, pp. 370–372, 2011.

[247] A. Thøgersen, M. Syre, B. Retterstol Olaisen, and S. Diplas, “Studies of the oxidation states of phosphorus gettered silicon substrates using X-ray photoelectron spectroscopy and transmission electron microscopy,” *Journal of Applied Physics*, vol. 113 044307, 2013.

[248] A. Oastgheib-Shirazi, M. Steyer, G. Micard, H. Wagner, P. Altermatt, and G. Hahn, “Effects of Process Conditions for the n + -Emitter Formation in Crystalline Silicon,” in *Photovoltaic Specialists Conference, 2012 38th IEEE*, 2011, pp. 1584–1589.

[249] R. Chen, H. Wagner, A. Dastgheib-Shirazi, M. Kessler, Z. Zhu, V. Shutthanandan, P. P. Altermatt, and S. T. Dunham, "A model for phosphosilicate glass deposition via POCl3 for control of phosphorus dose in Si," *Journal of Applied Physics*, vol. 112 124912, 2012.

[250] C. G. Beck and R. Stickler, "Crystallography of SiP and SiAs single crystals and of SiP precipitates in Si," *Journal of Applied Physics*, vol. 37, no. 13, pp. 4683–4687, 1966.

[251] A. Armigliato, D. Nobili, M. Servidori, and S. Solmi, "SiP precipitation within the doped silicon lattice, concomitant with phosphorus predeposition," *Journal of Applied Physics*, vol. 47, no. 12, pp. 5489–5491, 1976.

[252] K. Thompson, P. L. Flaitz, P. Ronsheim, D. J. Larson, and T. F. Kelly, "Imaging of arsenic Cottrell atmospheres around silicon defects by three-dimensional atom probe tomography.," *Science*, vol. 317, no. 5843, pp. 1370–1374, 2007.

[253] R. J. Jaccodine, "Precipitates formed by high-concentration phosphorus diffusion in silicon," *Journal of Applied Physics*, vol. 39, no. 7, pp. 3105–3108, 1968.

[254] D. Blavette and S. Duguay, "Investigation of dopant clustering and segregation to defects in semiconductors using atom probe tomography," *Journal of Applied Physics*, vol. 119 181502, 2016.

[255] H. Wagner, A. Dastgheib-shirazi, B. Min, A. E. Morishige, M. Steyer, G. Hahn, T. Buonassisi, P. P. Altermatt, H. Wagner, A. Dastgheib-shirazi, B. Min, A. E. Morishige, and T. Buonassisi, "Optimizing phosphorus diffusion for photovoltaic applications: Peak doping, inactive phosphorus, gettering, and contact formation," *Journal of Applied Physics*, vol. 119 185704, 2016.

[256] A. J. London, S. Lozano-Perez, S. Santra, S. Amirthapandian, B. Panigrahi, C. Sundar, and C. R. M. Grovenor, “Comparison of atom probe tomography and transmission electron microscopy analysis of oxide dispersion strengthened steels,” *Journal of Physics: Conference Series*, vol. 522 012028, 2013.

[257] M. Thuvander, J. Weidow, J. Angseryd, L. K. L. Falk, F. Liu, M. Sonestedt, K. Stiller, and H.-O. Andrén, “Quantitative Atom Probe Analysis of Carbides,” *Ultramicroscopy*, vol. 111, no. 6, pp. 604–608, 2011.

[258] A. Armigliato, D. Nobili, S. Solmi, G. Blendin, B. Schum, A. Lachowicz, and J. Horzel, “Characterization of the PSG/Si interface of H3PO4 doping process for solar cells,” *Solar Energy Materials and Solar Cells*, vol. 95, no. 11, pp. 3099–3105, 2011.

[259] D. Nobili, A. Armigliato, M. Finnetti, and S. Solmi, “Precipitation as the phenomenon responsible for the electrically inactive phosphorus in silicon,” *Journal of Applied Physics*, vol. 53, no. 3, pp. 1484–1491, 1982.

[260] T. Philippe, O. Cojocaru-Mirédin, S. Duguay, and D. Blavette, “Clustering and nearest neighbour distances in atom probe tomography: The influence of the interfaces,” *Journal of Microscopy*, vol. 239, no. 1, pp. 72–77, 2010.

[261] M. Herbig, P. Choi, and D. Raabe, “Combining structural and chemical information at the nanometer scale by correlative transmission electron microscopy and atom probe tomography,” *Ultramicroscopy*, vol. 153, pp. 32–39, 2015.

[262] A. Zuschlag, M. Schwab, D. Merhof, and G. Hahn, “Transition metal precipitates in mc Si: a new detection method using 3D-FIB,” *Solid State Phenomena*, vol. 205–206, pp. 136–141, 2014.

[263] M. Steyer, A. Dastgheib-Shirazi, H. Wagner, G. Micard, P. P. Altermatt, and G. Hahn, “A study of various methods for the analysis of the phosphosilicate glass layer,” *Proceedings of the 27th European Photovoltaic Solar Energy Conference and Exhibition*, pp. 1325–1328, 2012.

[264] J. Schön, A. Abdollahinia, R. Müller, J. Benick, M. Hermle, W. Warta, and M. C. Schubert, “Predictive simulation of doping processes for silicon solar cells,” *Energy Procedia*, vol. 38, pp. 312–320, 2013.

[265] H. Sato, Y. Yanagisawa, M. Ogasawara, H. Kojima, H. Masuda, and N. Natsuaki, “Inactivation of Low-Dose Implanted Phosphorus Pileup in the Silicon Side of an Si / SiO 2 Interface after Oxidation,” *Journal of The Electrochemical Society*, vol. 146, no. 1, pp. 367–371, 1999.

[266] R. Duffy, V. C. Venezia, J. Loo, M. J. P. Hopstaken, M. A. Verheijen, J. G. M. Van Berkum, G. C. J. Maas, Y. Tamminga, T. Dao, and C. Demeurisse, “Low-temperature diffusion of high-concentration phosphorus in silicon, a preferential movement toward the surface,” *Applied Physics Letters*, vol. 86 081917, 2005.

[267] P. B. Griffin, S. W. Crowder, and J. M. Knight, “Dose loss in phosphorus implants due to transient diffusion and interface segregation,” *Applied Physics Letters*, vol. 67, no. 4, pp. 482–485, 1995.